UNIVERSIDAD DE LA RIOJA

TESIS DOCTORAL

Título
Strategies for sustainable photocatalysis: hybrid organometallo-silica materials and BODIPYs
Autor/es
Monica Martínez Aguirre
Director/es
Miguel Angel Rodríguez Barranco y Jesús Rubén Berenguer Marín
Facultad
Facultad de Ciencia y Tecnología
Titulación
Departamento
Química
Curso Académico
2023-2024

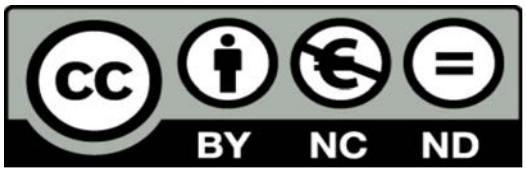

publicaciones.unirioja.es
E-mail: publicaciones@unirioja.es

UNIVERSIDAD DE LA RIOJA

TESIS DOCTORAL

2023

Programa de Doctorado en Química

ESTRATEGIAS PARA EL DESARROLLO DE SISTEMAS FOTOCATALÍTICOS SOSTENIBLES: ORGANOMETALOSÍLICAS HÍBRIDAS Y BODIPYS

STRATEGIES FOR SUSTAINABLE PHOTOCATALYSIS: HYBRID ORGANOMETALLO-SILICA MATERIALS AND BODIPYS

Mónica Martínez Aguirre

Director: Prof. Dr. Miguel Ángel Rodríguez Barranco

Director: Prof. Dr. Jesús Rubén Berenguer Marín

UNIVERSIDAD DE LA RIOJA

MIGUEL A. RODRÍGUEZ BARRANCO, Catedrático de Química Orgánica del Departamento de Química de la Universidad de La Rioja.

JESÚS R. BERENGUER MARÍN, Catedrático de Química Inorgánica del Departamento de Química de la Universidad de La Rioja.

CERTIFICAN:

que la presente memoria titulada ***Estrategias para el desarrollo de sistemas fotocatalíticos sostenibles: Organometalosílicas híbridas y BODIPYs*** ha sido realizada bajo su supervisión por la graduada en química **MÓNICA MARTÍNEZ AGUIRRE** en el Departamento de Química de la Universidad de La Rioja, y autorizan su presentación para que sea calificada como Tesis Doctoral.

Logroño, diciembre de 2023

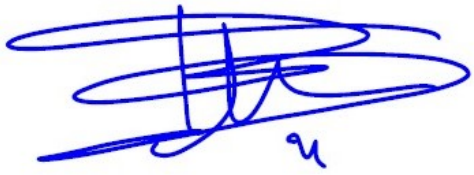

Fdo.: Miguel A. Rodríguez Barranco

Fdo.: Jesús R. Berenguer Marín

Esta tesis está dedicada a mi madre.

Te echo de menos.

"You can never know everything, and part of what you know is always wrong. Perhaps even the most important part. A portion of wisdom lies in knowing that. A portion of courage lies in going on anyway"

Robert Jordan, Winter's Heart

"There is nothing like looking, if you want to find something. You certainly usually find something, if you look, but it is not always quite the something you were after."

J.R.R. Tolkien, The Hobbit

Agradecimientos

Cuando hace cuatro años empecé la tesis, no me podía imaginar todo lo que estaba por venir. Ha habido momentos muy buenos y malos. Pero lo mejor es que no se viven en solitario, y Dios ha puesto en mi camino a personas maravillosas, y le doy gracias por ello. Quiero dar las gracias a todos los que me han acompañado en esta aventura, y han hecho posible que esta tesis saliera adelante.

En primer lugar, me gustaría agradecer a **Juan Diego Flórez**. Porque en verano del 2017, en la antesala de un concierto suyo en Pamplona, pude hablar con mis futuros directores de tesis sobre ópera, química, y proyectos de investigación, y ese momento fundó las bases de seis años y medio de colaboración y mucha química.

Gracias a esas dos personas que han hecho todo esto posible. A mis dos directores, los mafiosos jefes, por enseñarme no sólo a investigar, sino a disfrutar en el proceso. Por tantos momentos de cerveza, vermuts, o pintxos. Por esas calles Laurel, las óperas con vinito, y el bocata de después. La búsqueda del mejor txuletón de La Rioja. Y porque si me volviera a meter a esto, os elegiría a vosotros de directores sin pensármelo dos veces.

Muchas gracias, **Chuchi**. Porque desde la primera semana de laboratorio, en la que me enseñaste a montar mi primera reacción de puentes cloro de iridio, hasta las últimas correcciones de tesis; no sólo has sido un director estupendo, que siempre tienes la puerta abierta (figurada y literalmente), sino que también has sido un gran amigo, y uno de mis padres en esto de la investigación. Gracias por todos los buenos momentos, por estar siempre disponible, tanto para temas de investigación como para hablar de la última de Marvel, o cualquier tema que me inquietara. Y porque has puesto el listón muy alto para mis jefes en el futuro, que pocas personas van a poder llegar.

Y muchas gracias al segundo jefe mafioso, y mi segundo padre en esto. A **MA**. Porque todo lo que se puede decir de Chuchi se puede decir de ti también (salvo de las frikadas, aunque estoy convencida de que poco a poco te estamos convirtiendo). Gracias porque cuando algo iba mal en el laboratorio, podía ir un momento al despacho y tú me ayudabas a ver las cosas con perspectiva. Desde que empecé el doctorado, el número de bares y restaurantes que conozco se han multiplicado con creces. Y porque gracias a ti, he aprendido un poco más de la filosofía de trabajar mucho, pero disfrutar de los frutos del trabajo.

I would also like to thank Prof. **Eli Zysman-Colman** for the wonderful opportunity to have worked in your group. It was a pleasure to meet you and an honour to be part of your team for a little while. Thank you for always being available for questions and for all the support and good advice.

Por supuesto, quiero también agradecer a **Elena** y a **Mayte**, las dos jefazas del grupo, por todo su apoyo, sus consejos, y su cercanía, y por hacer los cafés memorables. A **Eduardo**, a **Pedro**, y a tantos profesores que me habéis inspirado con vuestras enseñanzas y pasión por la química.

Mil gracias a la gente con la que he tenido el privilegio de estar tantas horas en el laboratorio. Hemos pasado muchas cosas juntos, empezando por una pandemia mundial, mudanzas, o inundaciones. En primer lugar a mi tocaya de nombre y apellido, a **Mónica**. Por todos esos momentos en los que alguien nos llamaba, y sabíamos perfectamente a quién de las dos se refería. Por ser siempre la optimista que ve lo mejor en cualquier situación o persona. Por aquellas veces en las que la reacción era claramente negra, pero podíamos contar con tu "bueno, yo la veo un poco amarilla", con el que por lo menos podíamos echarnos unas risas, y seguir adelante.

A **Gonzalo**, el DJ del grupo, gracias también por estar siempre ahí, porque tienes un corazón enorme. Nunca te he oído decir que no si alguien pedía ayuda, o te preguntaba algo. Gracias por todos los buenos momentos en la huerta, en el laboratorio poniendo "temazos", o los arranques de limpieza, tan necesarios a veces. Por ser el extrovertido en un grupo de gente muy introvertida.

A mi italo-ucraniana favorita, **Katerina**, por todas las charlas frikis, de DnD, libros, series, o juegos de mesa. Gracias, porque siempre que necesitaba un abrazo podía contar contigo, y porque eres una de esas personas con la que siento que puedo hablar de lo que sea. Por tantos cumpleaños tuyos memorables, y tantos reportajes fotográficos que tenemos gracias a ti.

A **David**, el alberitense del grupo. Por ser siempre el alma de la fiesta. Gracias por todas las charlas, los cotilleos, por estar siempre dispuesto a ayudar. Por tener siempre el refrán adecuado en cada momento, o la contestación justa. Has estado ahí casi desde el principio de todo, y me llevo en el corazón muchos momentos inolvidables, como en el congreso de Granada (siempre meteré activador de rizos en todas mis maletas gracias a ti), o el de Alsacia (he oído que había una plaza muy bonita. Una pena que no la viéramos).

A **Janira**. Porque desde el primer momento, siento que has sido una gran amiga por encima de todo, siempre dispuesta a escuchar cuando lo necesitaba, y la otra gran friki del grupo. Gracias por ser mi psicóloga y consejera particular, así como mi estilista. Admiro un montón tu gran capacidad para superar obstáculos, y ser una trabajadora innata. Aunque pasen los años, siempre tendrás una "Mellon" en mí.

A **Andrea**, por ser siempre la alegría personificada. Por traer siempre una sonrisa de oreja a oreja. Siento que estos últimos meses de compartir despacho, he podido conectar más contigo, y me encanta tu personalidad. Por ser tan práctica, y estar siempre dispuesta a ofrecer consejo. No dejes que nunca nadie ni nada cambie tu forma de ser.

A las que terminaron hace más tiempo, **Cintia**, **Rebeca** y **Nora**, por vuestra gran acogida al grupo, los consejos, y todo lo que pude compartir al principio con vosotras. A **Mattia**, que llegó revolucionándolo todo, pero que cuando estaba de capa caída, eras el primero que se acercaba a preguntar "¿estás bien?". A **Julio**, porque sólo hemos coincidido más en este último año, pero me has ayudado un montón, y creo que el grupo ha hecho un gran fichaje contigo. A **Raúl**, por ser la voz de la razón, y porque siempre he podido contar contigo, tanto para preguntas, como para montajes, manualidades en el laboratorio, o simplemente para hablar. A **Laura**, por ser la más cuerda de todos los que estamos en ese despacho, y porque hablar contigo siempre me alegra el día.

Agradecer también a todas las personas del resto de grupos de investigación, presentes y antiguos. Porque a pesar de ser un departamento muy pequeño, se siente más grande gracias a todos vosotros. A todos los integrantes de los grupos GEIMA (**Quintana**, **Dani**, **Inés**, **David**, **Ainhoa**, **Alba**, **Oliver**, **María**, **Sonia**), GRUFOR (**Edu**, **Elena**, **Iris**, **David**, **Alberto**, **Bea**, **Víctor**, **Leo**, **Nil**, **Jacobo**, **Lucien**), y QUIBIS (**Paula**, **Carmen**, **Óscar**, **Marina**, **Mattia**, **Fayna**, **Ester**, **Foivos**, **Alicia**, **Pablo**, **Isma**).

A los miembros del servicio de laboratorios **Nines**, **Ernesto**, **Jorge**, **Amaya**, **Monste**, por toda vuestra ayuda, paciencia, y siempre saludar con una sonrisa.

I would also like to thank all the people from St. Andrews, for making my placement unforgettable, and in the best of ways. Many thanks to all the people at the lab, because from the very first moment, I felt very welcome by everyone. To all the wine-Friday people, you guys are the best. To **Callum**, **Fran**, **Moya**, **Oli**, **Tom**, **Megan**, **Dave**, **Lea**, **Sultan**, **Ettore**, **Manhi** and **Jasmin**. I'll always remember you fondly, and I hope our friendship will endure, even as time passes. Also to the people from the homegroup/DnD

group, **Carmen**, **Clay**, **Noah**, **Cam**, **Clayton**, **Charis**, **Jenny**, **Victoria**, **Hanna**, or **Mat**. And a special mention to **Janine**. For all the good times, the sunsets watching the moon rise, eating Dr. Noodle's boxes. For our mutual love of the Ceilidh, and Scotland in general. And because, despite the distance, I feel that the friendship has not diminished, and I am convinced that it will continue for many years to come.

También quiero mencionar a mis amigos del grupo de viejóvenes de la iglesia, porque habéis tenido una paciencia infinita, especialmente en la locura de los últimos meses. Gracias por haber estado ahí, por las oraciones, por apoyarme en todos los momentos. A **Estefany**, **Max**, **Valeria**, **Valerian**, **Nusha**. Porque somos un grupo de personas muy diferentes, pero no se puede tener un mejor grupo de amigos que todos vosotros.

Muchas gracias, **Ada**, porque has sido la mejor amiga que podía tener. Gracias por todas las conversaciones, en persona o por teléfono, a carcajada limpia o con cajas de pañuelos al lado. Porque tu amistad me ayudó a superar el momento más difícil de todo este tiempo, y todos los que vinieron después. Por ser esa amiga que siempre me recuerda qué es lo más importante, tanto con tu ejemplo como con tus consejos.

Muchas gracias a mi familia. A ti, **papá**. Porque siempre has sido para mí un ejemplo de cómo hacer las cosas bien, de tratar de conseguir lo que te propones. De constancia, dedicación, y de seguir adelante, pase lo que pase. Gracias por apoyarme en cada paso que he dado, y por aguantarme todos los días que llegaba del laboratorio de mal humor si algo no iba bien. Por la paciencia que has tenido, y el amor y cariño constante que me has dado. Y gracias al otro gran pilar de mi familia, a **Víctor** mi hermano, **Maddy**, y mis sobrinos, por sólo estar a una llamada de distancia. Por saber sacarme siempre una sonrisa incluso en los peores momentos, y aguantarme cuando hablo de química hasta en la sopa.

Y por último, gracias a ti, **mamá**. Porque tú fuiste la primera persona que me enseñó a disfrutar de aprender nuevas cosas, de ver el mundo con curiosidad. Gracias, porque no me exigías ser la mejor, sino dar lo mejor de mí, independientemente de los demás. Porque vas a ser siempre mi ejemplo de superación, de cómo afrontar los tiempos y las circunstancias más difíciles. Gracias, porque a pesar de todo lo que estabas pasando, fuiste la que más me animó a empezar este camino. Has sido también mi gran ejemplo en la fe, y gracias a eso tengo la firme certeza de que nos vamos a ver de nuevo en el cielo. Porque me viste empezar, pero no me vas a ver terminar. Pero estoy convencida de que, si estuvieras aquí, estarías muy orgullosa. Te quiero, mamá.

Index

Abbreviations and acronyms

^{1}H-NMR	proton nuclear magnetic resonance
^{4}CzIPN	1,2,3,5-tetrakis(carbazol-9-yl)-4,6-dicyanobenzene
a.u.	arbitrary units
Abs	absorption
ACQ	aggregation-induced quenching
ATR	attenuated total reflectance
B3LYP	Becke, 3-parameter, Lee-Yang-Parr functional
BODIPY	boron-dipyrromethene
bpy	2,2'-bipyridine
COFs	covalent organic frameworks
COSY	correlation spectroscopy
CT	charge transfer
CTAB	hexadecyltrimethylammonium bromide
d	doublet
D-A	donor-acceptor
dasipy	N,N'-dipropiltriethoxysilane-2,2'-bipyridine-4,4'-dicarboxamide
DCA	9,10-dicyanoanthracene
DCM	dichloromethane
DET	Dexter energy transfer
dfppy	2-(2,4)-difluorophenyl-pyridine
DMDES	dimethyldiethoxysilane
DMF	dimethylformamide
DPBF	1,3-diphenylisobenzofuran
DRUV	diffuse reflectance ultraviolet-visible
EDG	electron donating group
EDX	energy dispersive X-ray spectroscopy
Em	emission
EnT	energy transfer
ESI	electrospray ionization
et al.	and co-workers

EWG	electron withdrawing group
Ex	excitation
f	oscillator strength
FESEM	field emission scanning electron microscopy
FRET	Föster resonance energy transfer
FT-IR	Fourier transform infrared spectroscopy
HMBC	heteronuclear multiple bond correlation
$h\nu$	energy of a photon of frequency ν
HOMO	highest occupied molecular orbital
HR-ICP-MS	high resolution inductively coupled plasma mass spectrometry
HSQC	heteronuclear single quantum correlation
IC	internal conversion
ICP	inductively coupled plasma
IL	intraligand
IR	infrared
ISC	intersystem crossing
k'	pseudophotocatalytic constant
$\mathbf{K_{nr}}$	non-radiative decay constant
$\mathbf{K_r}$	radiative decay constant
LC	ligand centered
LE	locally excited
LED	light emitting diode
LEEC	light-emitting electrochemical cells
LLCT	ligand to ligand charge transfer
LUMO	lowest unoccupied molecular orbital
m	multiplet
MALDI-TOF	matrix-assisted laser desorption ionization-time of flight
MC	metal centered
MLCT	metal to ligand charge transfer
MO	molecular orbital
MOFs	metal-organic frameworks
NLDFT	non-local density functional theory

NMR	nuclear magnetic resonance
OLED	organic-light emitting devices
PC	photocatalyst
PC*	excited state photocatalyst
$PC^{\bullet+}$	oxidized photocatalyst
$PC^{\bullet-}$	reduced photocatalyst
PCM	polarizable continuum model
PDT	photodynamic therapy
PEnT	photoinduced energy transfer
PLQY	photoluminescence quantum yield
PMO	periodic mesoporous organosilica
ppy	2-phenylpyridine
pst	pseudotriplet
PXRD	powder X-ray diffraction
q	quadruplet
RGB	red-green-blue
rISC	reverse intersystem crossing
ROS	reactive oxygen species
rpm	revolutions per minute
RT	room temperature
s	singlet
S_0	single ground state
S_1	first single excited state
SET	singlet electron transfer
sh	shoulder
S_n	any singlet excited state
SOMO	singly occupied molecular orbital
Sub	substrate
t	triplet
T_1	first triplet excited state
TADF	thermally activated delayed fluorescence
TD-DFT	time-dependent density-functional theory

TEA	triethanolamine
TEM	transmission electron microscopy
TEOS	tetraethyl orthosilicate
THF	tetrahydrofuran
TLC	thin layer chromatography
Tol	toluene
UV	ultraviolet
UV-vis	ultraviolet visible
Z	atomic number
δ	NMR chemical shift
ε	molar extinction coefficient
λ	wavelength
τ	lifetime
ϕ	quantum yield

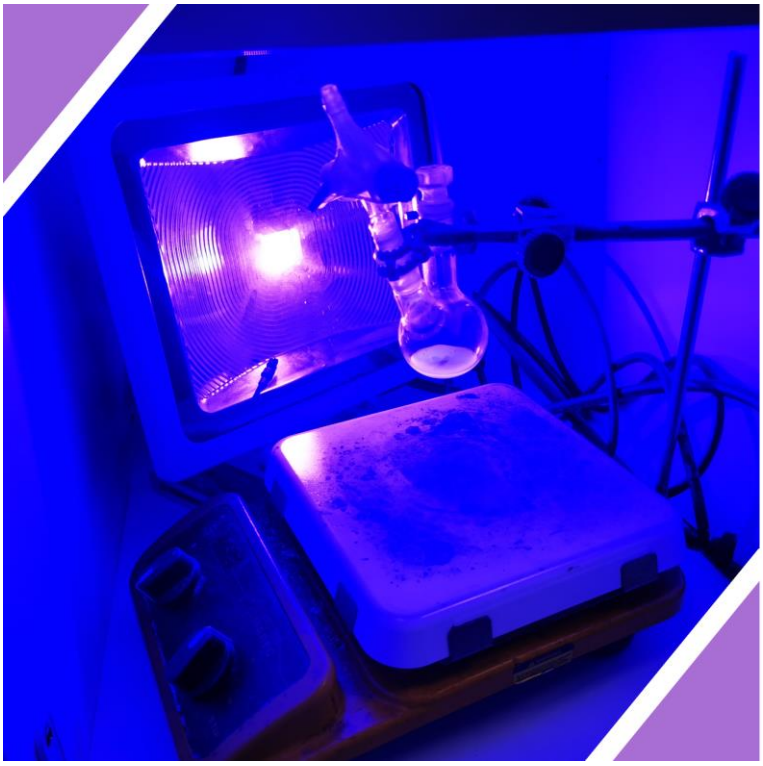

Introduction

Introduction

Photocatalysis has emerged as a field of great interest over the past few decades (Figure I.1), due to its potential in diverse applications ranging from environmental remediation to energy conversion.[1] Using the abundant energy source of light, chemists can explore a wide range of synthetic routes previously inaccessible by traditional thermal methods. Photocatalysis offers several advantages, including the ability to achieve the total synthesis of complex molecules more efficiently, requiring fewer synthetic steps and minimizing unwanted secondary reactions.[2]

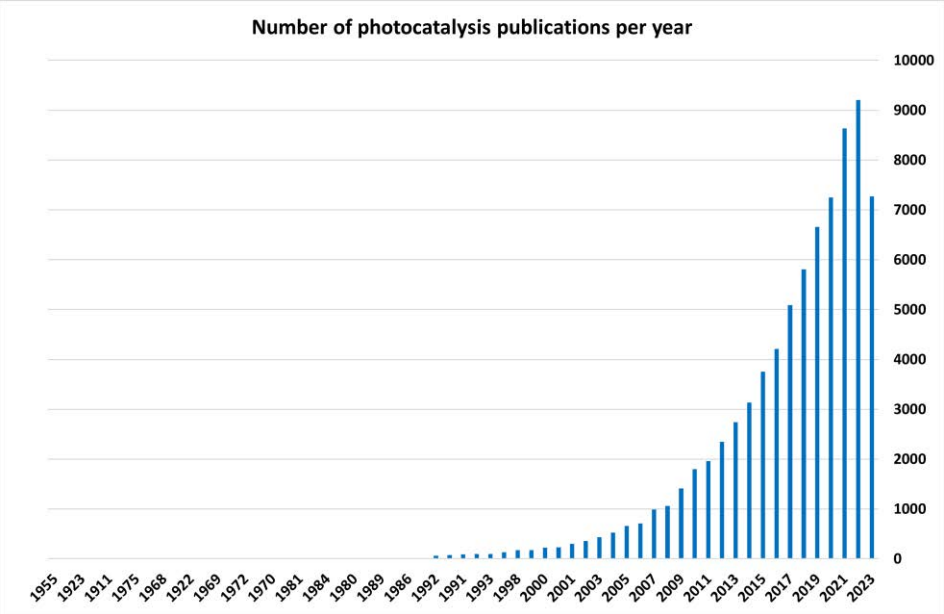

Figure I.1. Number of photocatalysis publications per year. Keyword: "photocatalysis" Web of Science search conducted 29/11/2023.

The first recorded instance of a chemist observing the effect of light on organic molecules dates from 1834, when Johann Bartholomew Trommsdorff (1770-1837) documented how crystals of α-santonin turned yellow and "burst" when exposed to sunlight.[3] However, the origins of organic photochemistry are generally attributed to the pioneering work of two chemists: Giacomo Ciamician (1857-1922) and Paul Silber (1851-1932), who were the first to systematize the study of the interaction of light with organic compounds. Ciamician and Silber explored various photoreductions in alcoholic media, including aldehydes, ketones, quinones, and nitro compounds. In addition, they studied the photoisomerization of alkenes, the dimerization of olefins, and, in particular, the intramolecular [2+2] cycloaddition of carvone under sunlight.[4]

The use of sunlight to drive chemical reactions is highly desirable because of the potential for free use of this abundant energy source. Of the total direct solar radiation received, only about 5% of the UV light reaches the Earth's surface after being filtered by the ozone layer. The remaining composition is approximately 45% visible light and 50% infrared radiation.

The main problem with organic synthesis is that most organic molecules absorb light primarily in the ultraviolet (UV) region of the electromagnetic spectrum, although the use of visible light for photocatalysis is highly recommended. Using a lower energy light source minimizes unwanted side reactions and product degradation and eliminates the need for specialized equipment and glassware (quartz/pyrex), as standard borosilicate glassware is not transparent to UV radiation. It is also more cost-effective to use visible light. Today, energy-efficient high-power light-emitting diodes (LEDs) are widely available, reducing energy costs and making them a practical and economical choice.

To overcome this limitation and expand the range of chemical reactions that can be achieved, molecules known as photocatalysts are employed. A photocatalyst (PC) can be defined as a molecule that absorbs light to promote a chemical transformation without undergoing any permanent changes itself.[5] Early examples of chemists utilizing photocatalysts can be traced back to the beginning of the 20th century. However, it was the pioneering work of the research groups of Yoon,[6] MacMillan[7] and Stephenson[8] that fully revealed the enormous potential of photocatalysis in organic synthesis.

For the photocatalytic process to be effective, two crucial steps must be carefully studied: the absorption of light by the photocatalyst, and the subsequent interaction between the photocatalyst and the substrate that allows the desired chemical reaction to occur.[9]

The behavior of a molecule upon light absorption can be effectively illustrated using a Jablonski diagram (Figure I.2). When a molecule is irradiated with light, a photon of sufficient energy is absorbed, resulting in the excitation of an electron from the singlet ground state (S_0) to a higher energy singlet state (S_n), following the spin-selection rule and the Frank-Condon principle. Although multiple singlet excited states with varying vibrational energies may be accessible, these states typically relax within picoseconds to the first singlet excited state (S_1) in accordance with Kasha's rule.[5] This relaxation occurs through non-radiative vibrational relaxation and internal conversion (IC). Once in the S_1

excited state, the molecule can return to its ground state via a non-radiative decay process (IC), or by emitting a photon in a phenomenon known as fluorescence. Alternatively, the molecule can undergo a spin-forbidden, non-radiative process called intersystem crossing (ISC) to a lower-energy triplet excited state (T_1). The probability of ISC is enhanced if there is an overlap between the vibrational levels of the two excited states. Several factors can favor a good ISC.[10] One example is the presence of heavy atoms in the molecule, that leads to strong spin-orbit coupling which is proportional to the atomic number (Z^4, Z = atomic number).[11] From the T_1 state, two general processes can occur: the non-radiative decay, and the radiative process called phosphorescence.

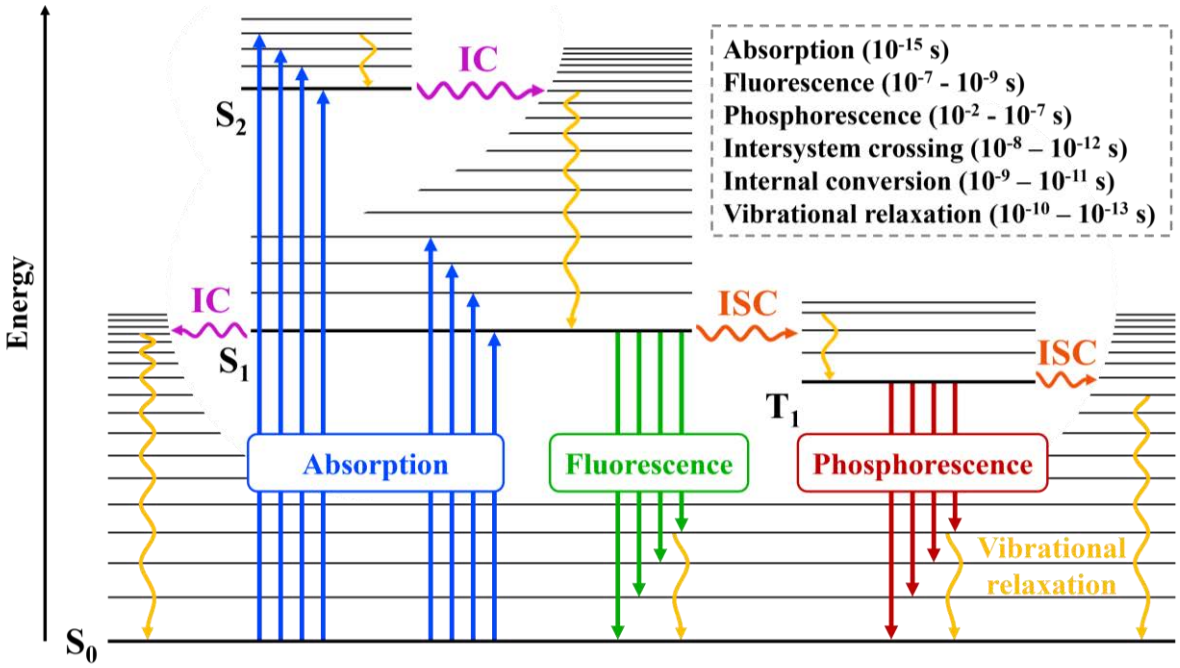

Figure I.2. Jablonski diagram.

In both radiative processes (fluorescence and phosphorescence), the emitted light has a lower energy than the absorbed photon due to vibrational relaxation, resulting in a red-shift of the emission maximum with respect to the absorption maximum. The difference between these two maxima is referred to as the Stokes shift. Fluorescence is characterized by small Stokes shifts and short lifetimes (on average between 10^{-9} and 10^{-7} s).[12] On the other hand, phosphorescence lifetimes are longer, in some cases significantly so (on average from 10^{-7} to $>10^{-2}$ s), and the Stokes shift is larger than that of fluorescence. The lifetime of the excited state plays a crucial role in photocatalytic processes and must be evaluated when considering a photocatalyst. Long-lived excited states are desirable as

they allow sufficient time for the photocatalyst to interact with the substrate before radiative or non-radiative decay occurs. If the lifetime is too short, the excited state will decay faster than the diffusion limit in solution, preventing bimolecular processes. For this reason, the most commonly employed photocatalysts are those capable of effectively populate their triplet state upon visible light absorption.

After the absorption of light, an interaction between the photocatalyst and the substrate takes place. Within the context of this thesis, two mechanisms of interaction are of particular interest: single electron transfer (SET) and photoinduced energy transfer (PEnT).[13]

Single electron transfer (SET), also known as photoredox catalysis, relies on the increased reduction and oxidation potential of the photocatalyst in its excited state compared to its ground state. This phenomenon can be explained by looking at a simplified orbital diagram of the PC (Figure I.3). Upon irradiation, an electron from the highest occupied molecular orbital (HOMO) is excited to the lower unoccupied energy orbital (LUMO). Consequently, the PC now has an increased oxidation potential, and gains the ability to reduce organic molecules (often referred to as acceptors $\mathbf{A^n}$ within the photocatalytic cycles) that in their ground state present higher oxidation potentials than the PC in its ground state. In addition, the excitation also creates a vacancy in the HOMO of the PC increasing its reduction potential and allowing it to easily oxidize donor organic molecules ($\mathbf{D^m}$).

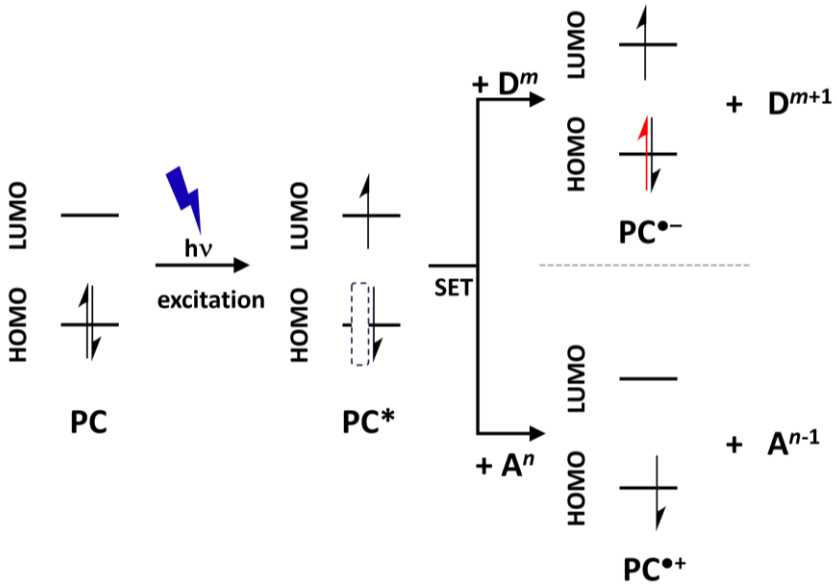

Figure I.3. Photoinduced electron transfer processes: D^m = electron donor, A^n = electron acceptor, SET = single electron transfer. The indices *m* and *n* denote the oxidation state of the donor and the acceptor respectively.

Thus, two SET photocatalytic cycles can be distinguished (Figure I.4).[9] In the oxidative quenching cycle, the photocatalyst in its excited state (PC*) gives an electron to an acceptor molecule, leading to its reduction. This newly reduced species can then proceed along a new synthetic pathway. The oxidized form of the photocatalyst ($PC^{\bullet+}$) accepts an electron from a donor molecule, closing the catalytic cycle. Similarly, in the reductive quenching cycle the PC* now is reduced, and a donor molecule is oxidized. The cycle closes with the reduced form of the photocatalyst ($PC^{\bullet-}$) donating an electron to an acceptor. In both cycles, the reaction substrates (acceptors and donors) become activated, generating highly reactive radicals (anions, cations, or neutral radicals) capable of participating in subsequent reactions.[14]

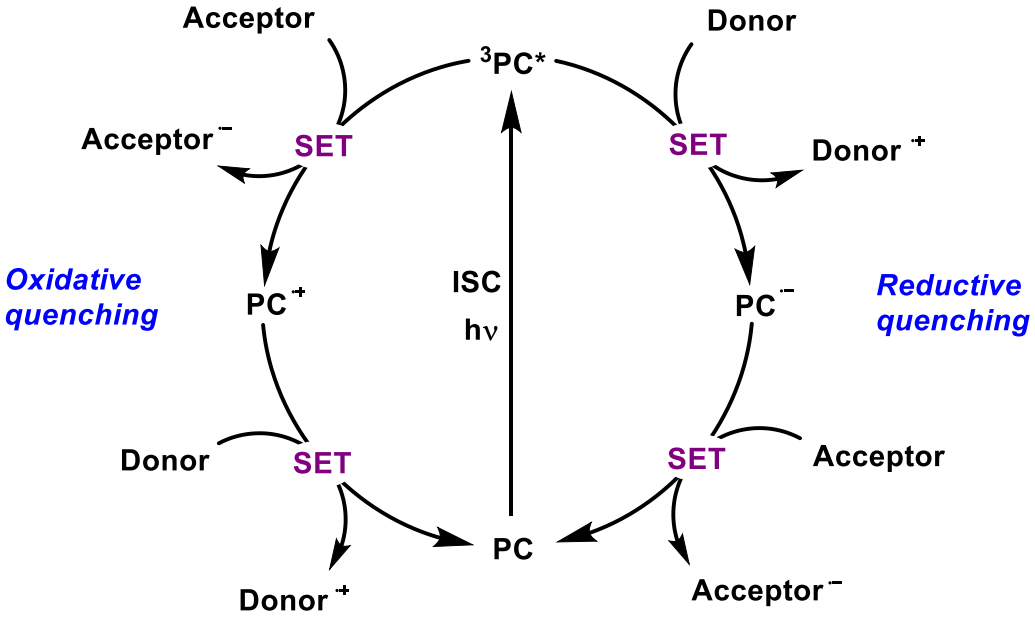

Figure I.4. Oxidative and reductive quenching cycles.

On the other hand, photoinduced energy transfer (PEnT, Figure I.5), also known as photosensitization, operates through a different mechanism than single electron transfer (SET). In PEnT, the long-lived excited state of the photocatalyst decays to its ground state by transferring energy to the substrate.

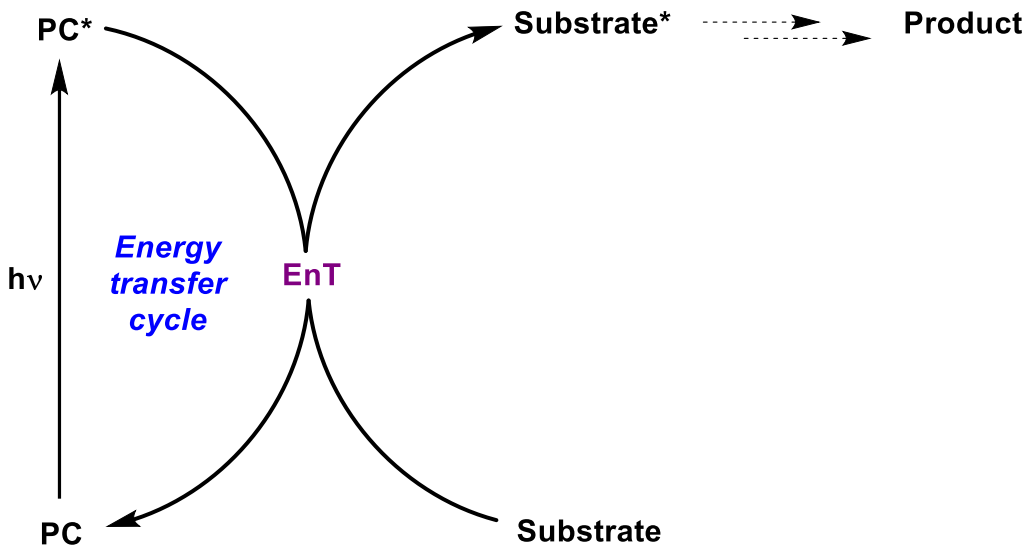

Figure I.5. Energy transfer cycle.

Two main mechanisms can occur in PEnT processes: Föster resonance energy transfer (FRET) and Dexter energy transfer (DET) (Figure I.6).[15] The first mechanism operates through dipole-dipole (coulombic) interactions, where electronic oscillation in the excited state of the photocatalyst PC* induces a dipole in the ground state of the substrate due to charge repulsion.[16] This interaction leads to the simultaneous relaxation of the photocatalyst and the excitation of the substrate. However, FRET is disfavored if the PC* is in a triplet state, because it would require two spin-forbidden processes: T_1 to S_0 for the PC, and S_0 to T_1 for the substrate. In cases where PC* is predominantly in its triplet state, the second mechanism, Dexter energy transfer (DET), becomes more likely. This mechanism involves the simultaneous intermolecular exchange of excited-state and ground-state electrons from the photocatalyst and the substrate respectively.[17] In this process, an orbital overlap is required, which experimentally can be observed if there is an overlap between the $S_0 \rightarrow T_1$ absorption spectrum of the substrate and the $T_1 \rightarrow S_0$ emission spectrum of the PC.[15] However, since obtaining such absorption spectra is quite difficult, a comparison between the triplet energies can be utilized as a rough predictive guide. If the T_1 energy of the photocatalyst is higher than that of the substrate, a Dexter mechanism is more likely to take place.

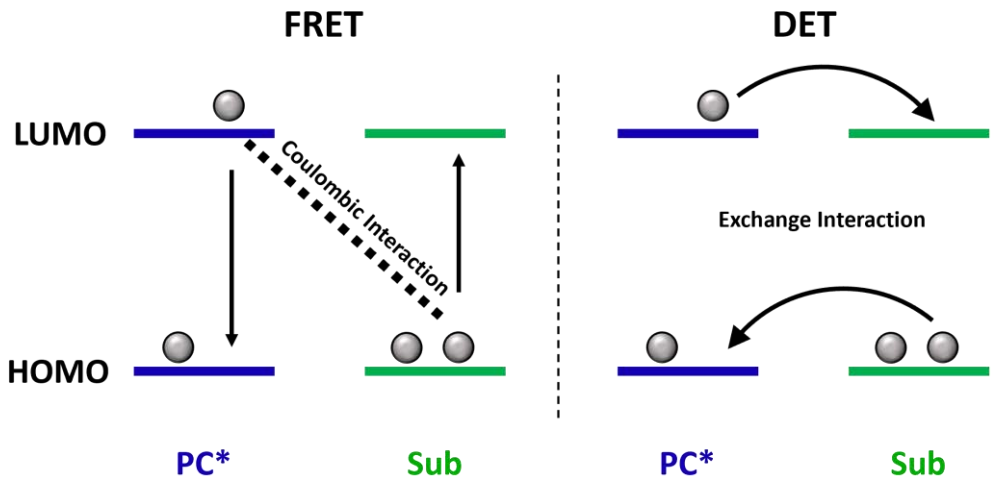

Figure I.6. Föster resonance energy transfer (left) and Dexter energy transfer mechanism (right).

Based on the information presented so far, an ideal photocatalyst should have the following characteristics:

- Good absorption in the visible region of the electromagnetic spectrum (>400 nm).
- Long-lived excited state that allows the interaction with the substrate before it deactivates.
- Photostability in solution.
- Easily modifiable molecular structure that has an impact on its photophysical properties.
- For a SET reaction: higher excited state oxidation or reduction potential than the substrate.
- For a PEnT reaction: higher triplet excited state energy than the substrate.

Considering the ideal properties of a good photocatalyst, it is indeed not surprising to find that transition metal complexes have been widely used as photocatalysts, such as ruthenium(II) polypyridyl or cyclometalated iridium(III) complexes.[14a, 18] Moreover, modifications in the ligands allow a controlled tuning of their redox and photophysical properties.[19] Figure I.7 illustrates some of the most commonly used photocatalysts based on these metals.

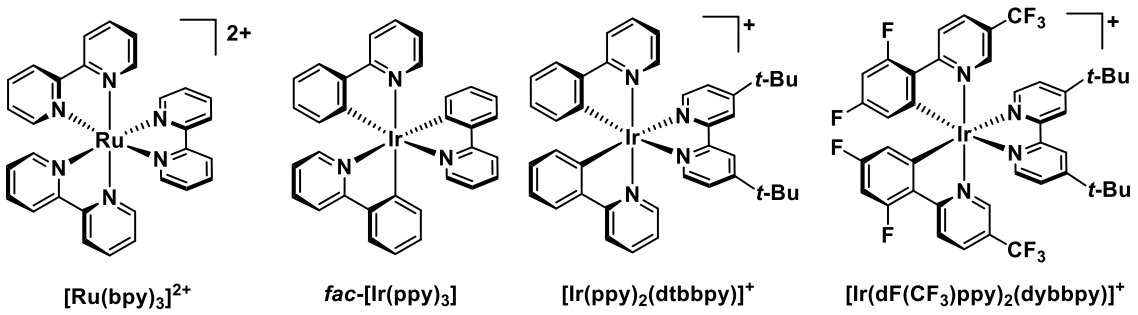

Figure I.7. Examples of organometallic photocatalysts.

However, iridium and ruthenium are rare metals found in small amounts within the Earth's crust,[20] which makes them very expensive options for the growing demand for PCs in the pharmaceutical and chemical industry.[21] To address this issue, several strategies have emerged in recent years:

- Heterogenization: one approach is the heterogenization of iridium or ruthenium complexes onto porous surfaces such as silica-based materials, titanium, or zeolites.[22] This approach preserves the properties of these compounds to a greater extent, while at the same time improving the recovery and recyclability of the PC. Various techniques have been explored to heterogenize these complexes, including grafting onto the surface of the material, vapor deposition, or ion exchange. However, many of these techniques can be defined as post-synthetic approaches, and usually lead to leaching issues or pore blocking for porous materials.[23]
- Metal-Organic Frameworks (MOFs): As part of the heterogenization strategy, metal-organic frameworks have emerged as a distinct category.[24] In MOFs, the same PCs complex molecules can be incorporated as building blocks in the structures or encapsulated within the regular pores of the MOFs, offering a unique platform for photocatalysis.[25]
- Semiconductors: Another approach to heterogenizing the photocatalytic process is the use of semiconductor materials.[24a, 26] Titanium dioxide, zinc oxide, and various metal oxides are extensively studied photocatalysts in this category. These materials possess a band gap (between the valence band and the conduction band) similar to the HOMO/LUMO separation in a traditional PC. Moreover, by introducing doping agents, these materials can be modified to absorb light in the visible region of the electromagnetic spectrum.[27]

- Earth-abundant complexes: The substitution of expensive noble metal complexes with earth-abundant transition-metal-based complexes has gained considerable attention in recent studies.[28] Among the earth-abundant transition metals, copper(I) represents the most thoroughly investigated.[29] Diimine complexes, both homoleptic and heteroleptic with a diphosphine ligand, exhibit long-lived excited states and have shown promising results (Figure I.8).[30] However, the challenge of achieving sufficient photostability in solution remains an ongoing concern for their use as photocatalysts.

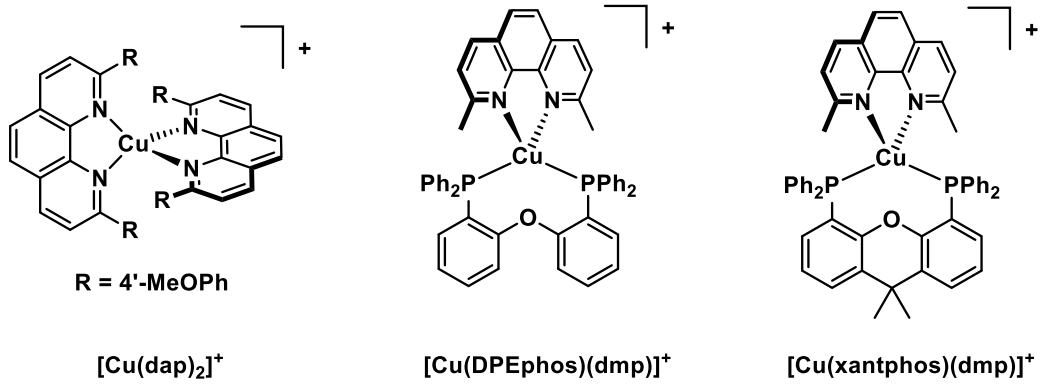

Figure I.8. Representative copper(I) photocatalysts.

- Organic photocatalysts: With the growing interest of the pharmaceutical industry in photocatalysis, organic PCs offer several advantages.[31] They are often more cost-effective and possess lower toxicity and greater biocompatibility compared to metal-based PCs.[14a, 32] Some examples in this category include acridinium and pyrylium salts, cyanoarenes, and organic dyes such as eosin Y, Rose Bengal, fluorescein, and rhodamine (Figure I.9).[33] Much progress has been made in this area in recent years, although the difficulty of tuning their redox potentials, their lower photostability, and their shorter excited-state lifetimes still leave much room for improvement. Another emerging example is the utilization of molecules exhibiting thermally activated delayed fluorescence (TADF), which possess long excited-state lifetimes that enable interactions with substrate molecules while exhibiting fluorescence emissions.[34]

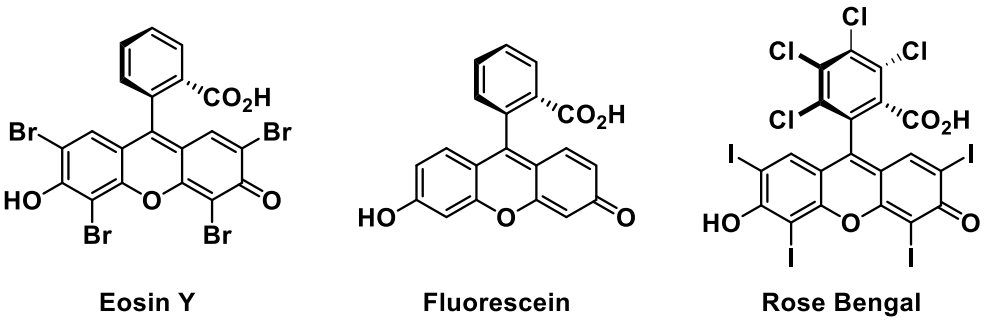

Figure I.9. Examples of organic PCs.

Within the context of this thesis, the focus is on the heterogenization strategy of cyclometalated iridium(III) complexes, taking advantage of the extensive experience of our research group in the synthesis and emissive properties of these complexes, as well as in the synthesis of mesoporous silica functionalized materials.[35] The aim is to investigate the heterogenization of previously synthesized compounds by *in-situ* techniques in a way that offers improved protection compared to post-synthetic techniques, while maintaining photocatalytic properties similar to those observed under homogeneous conditions. Two chapters of this work have been dedicated to this strategy. Nevertheless, the last chapter of this thesis is dedicated to the synthesis of a new type of organic PCs. From the initial idea of incorporating BODIPY dyes onto functionalized phenyl-pyridines, which are commonly used as cyclometalated ligands in our research group, we have obtained new organic compounds that we have studied as photocatalysts in their own right.

Objectives

Objectives

The general objectives of this doctoral thesis are framed within the search for new forms of sustainable photocatalysts, both in the heterogenization of emissive transition metal complexes and in the study of organic photocatalysts. They can be summarized in the following specific points:

- Incorporation of a cationic iridium(III) complex in different silica-based materials, by means of post-synthetic and *in-situ* techniques, with different types of morphology and degrees of incorporation of the complex.

- Study of the textural and photophysical properties of the materials obtained, comparing them with the properties of the complex used for functionalization.

- Study of the photocatalytic activity of the materials, covering different mechanisms of photocatalytic reactions. In addition, the reaction conditions of the complex in homogeneous medium will also be optimized.

- Establish mechanisms for recovering and cleaning the materials for use in successive catalytic cycles.

- Comparison of the different functionalization methods on the photocatalytic activity and reuse of the materials.

- Synthesis of a new material based on the self-condensation of the cationic iridium complex used previously, to obtain a new organometallo-ionosilica, and study of its textural, photophysical and photocatalytic properties.

- Synthesis of new BODIPYs based on phenylpyridine ligands for their subsequent incorporation in organometallic complexes as cyclometalated ligands, studying the methods to obtain a good ISC. Study of the photophysical properties of the BODIPYs.

- Study of the generation of singlet oxygen using the synthesized BODIPYs, as well as their use in a photocatalytic reaction that takes place by means of singlet oxygen sensitization.

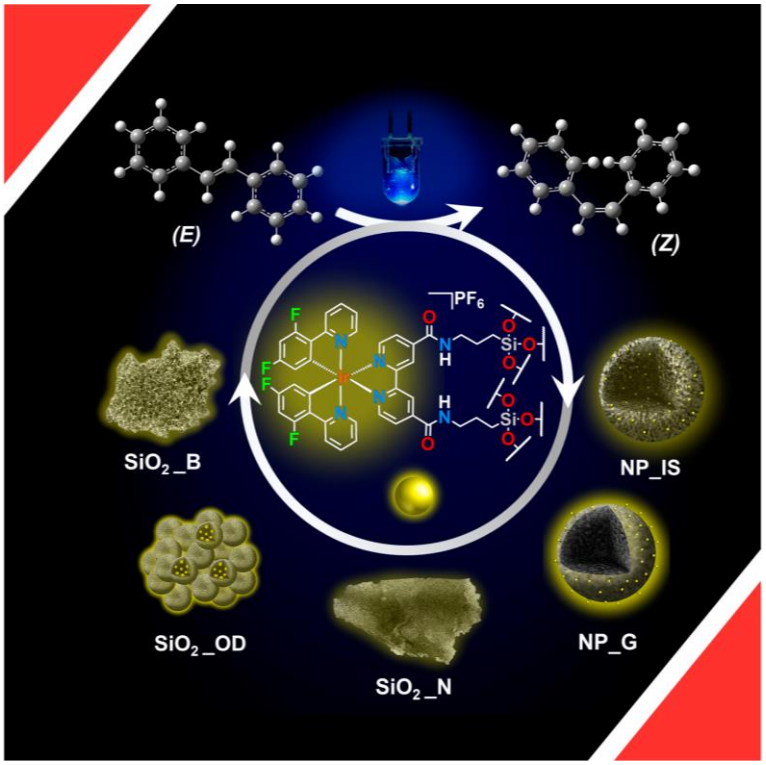

Chapter 1. Hybrid organometallo-silica photocatalysts for olefin isomerization

1.1 Introduction

As already mentioned in the general introduction, cyclometalated iridium(III) complexes have been widely used as photocatalysts in both SET and PEnT processes, due to their tunable photophysical properties, good photostability, and high ISC efficiencies resulting in highly populated triplet excited states. Among the various iridium complexes, the family of $[Ir(C^N)_2(N^N)]^+$ compounds (**IrC_2N_4**, where C^N is an anionic cyclometalated group and N^N is a neutral functionalized bipyridine) has been extensively studied. This family is particularly noteworthy due to the presence of two Ir-C bonds, that delocalize the HOMO onto the cyclometalated ligand framework (C^N) thanks to its σ-donating ability, increasing the chances of obtaining different efficient emissive excited states compared to other Ir(III) complexes (Figure 1.1).

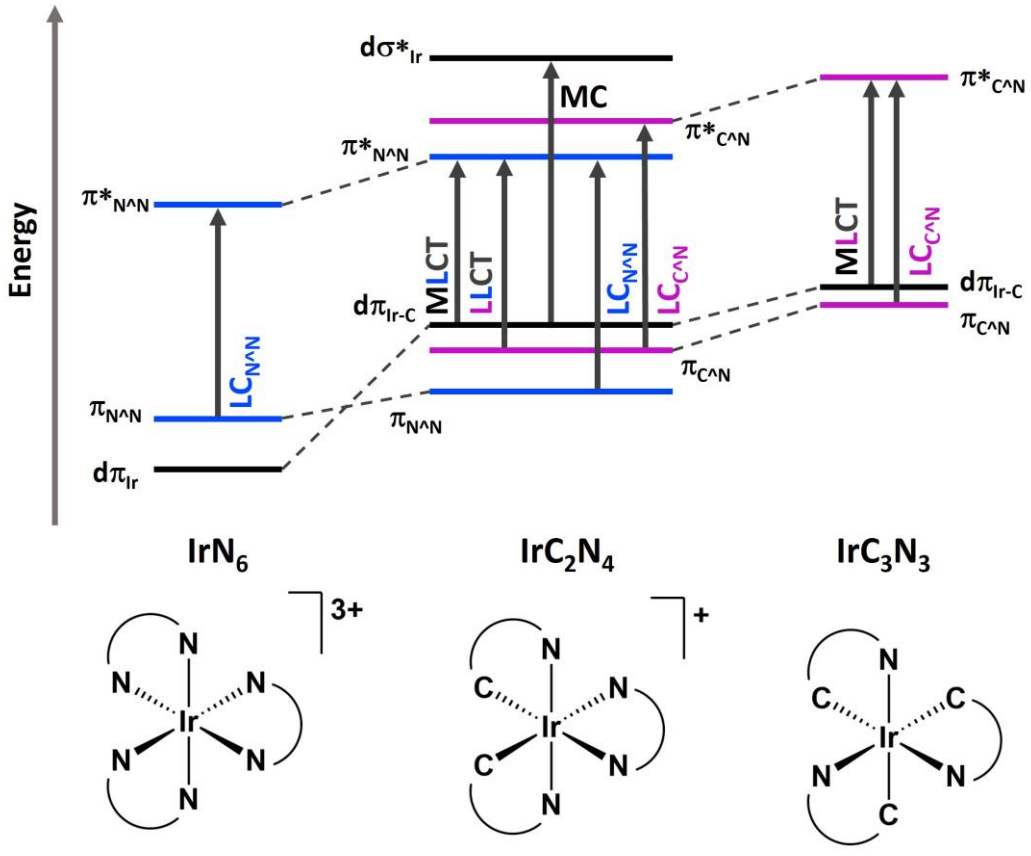

Figure 1.1. Influence of the number of Ir-C bonds on the electronic configuration and the absorption transitions of Ir(III) complexes.

This delocalization of the HOMO from the metal center to the ligands allows for the strategic modification of these ligands to stabilize or destabilize this orbital. In addition, the LUMO in these complexes is typically located in the bipyridine (N^N) ligand. This spatial separation of each frontier orbital enables independent tuning and provides the ability to modify the HOMO/LUMO energy gap, allowing for control over the emission wavelength and achieving photoluminescence over a wide range (Figure 1.2).[18a, 36] In general, the functionalization of C^N ligands with electron-donating groups (EDG) destabilizes the HOMO, whereas electron-withdrawing groups (EWG) stabilize the orbital.[37] The opposite is true for the N^N ligand, where electron-donating groups stabilize the LUMO, resulting in a blue-shift in the emission, and electron-withdrawing groups destabilize the orbital, resulting in lower energy emissions.[38] Examples of common electron-withdrawing groups include fluorides and nitriles, while electron-donating groups include amines, alcohols, and thiols, among others. The localization of the orbitals results often in the description of the emissive excited states of these complexes as a mixture of metal-to-ligand charge transfer (^{3}MLCT), between the metal and the N^N ligand, and ligand-to-ligand charge transfer (^{3}LLCT), between the C^N ligands and the N^N ligands.

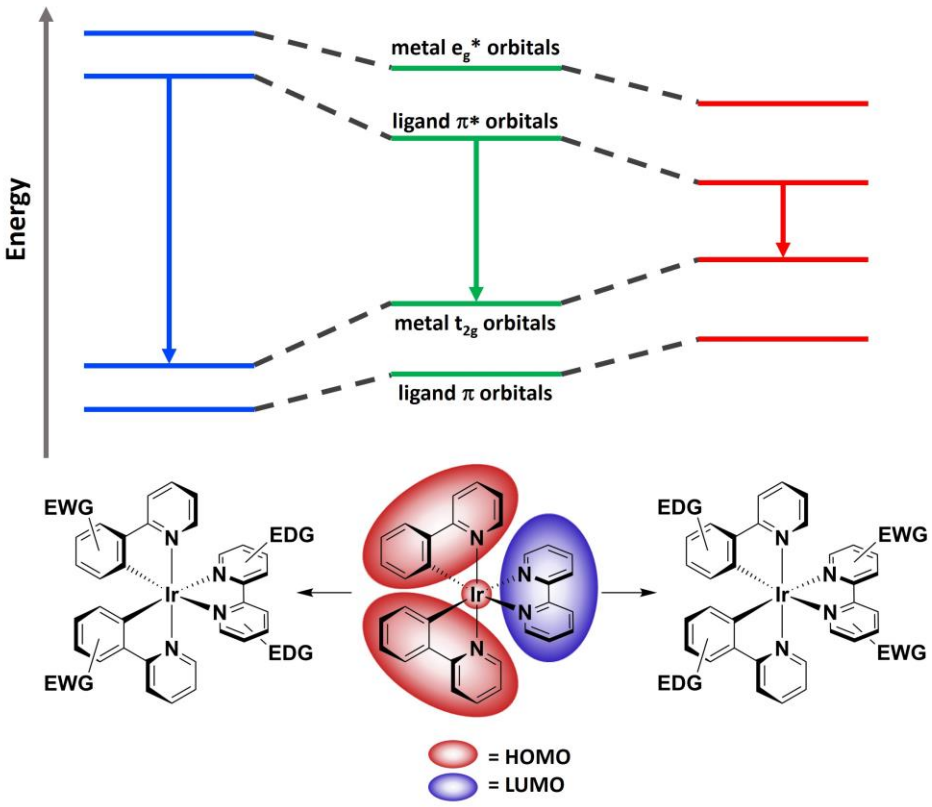

Figure 1.2. Strategies for the modulation of the luminescence in IrC_2N_4 complexes.

As previously mentioned, although the photophysical properties of these complexes have been well studied, and there is a growing library of compounds with a wide range of excited reduction/oxidation potentials, the application of cyclometalated iridium(III) complexes as homogeneous PCs in the pharmaceutical and chemical industries has been limited due to their high cost and the need for purification steps in the final product. To overcome these drawbacks, the strategy explored in this chapter is the heterogenization of the photocatalysts onto high surface area solid matrices.

Various materials have been used to support different chromophores. Examples of these can be found in the encapsulation of metal complexes within zeolite cavities, MOFs, or ion-exchange resins; their grafting onto mesoporous inorganic oxides or plasmonic metal nanoparticles; or their intercalation within layered materials such as graphene or nano C_3N_4 sheets.[27a, 39] Among these matrices, silica has been used extensively over the past few decades for the incorporation of organometallic compounds in a wide range of applications, including optical sensing, bioimaging, phototherapy, and hydrogen generation.[35a, 35b, 40] Silica offers several key properties that make it an excellent choice for heterogenizing luminescent compounds.

First, silica exhibits optical transparency, making it suitable for optical applications. It also possesses chemical and thermal stability in both aqueous and organic solvents, increasing its versatility for different reaction conditions.[41] In addition, the cost of its precursors, such as tetraethyl orthosilicate (TEOS), is relatively low (1 L for synthesis = 110 €, Sigma-Aldrich, search done on 07/13/2023).

But silica is particularly advantageous and versatile compared to other solid matrices due to the wide range of materials that can be synthesized using sol-gel synthetic strategies (Scheme 1.1). For example, mesoporous silica materials (pore diameters from 2 to 50 nm) can be synthesized by varying the surface area and pore size by selecting specific surfactants and adjusting their concentration during synthesis. The morphology of the material can also be modified, leading to the formation of monodisperse nanoparticles with different shapes, aggregates or macroscopic nanostructured gels. In addition, and taking advantage of the abundant hydroxyl (-OH) groups present on the silica surface, surface functionalization can also be tailored, providing the opportunity to introduce new chemical functions capable of interacting with a wide range of functional groups (Figure 1.3).[42]

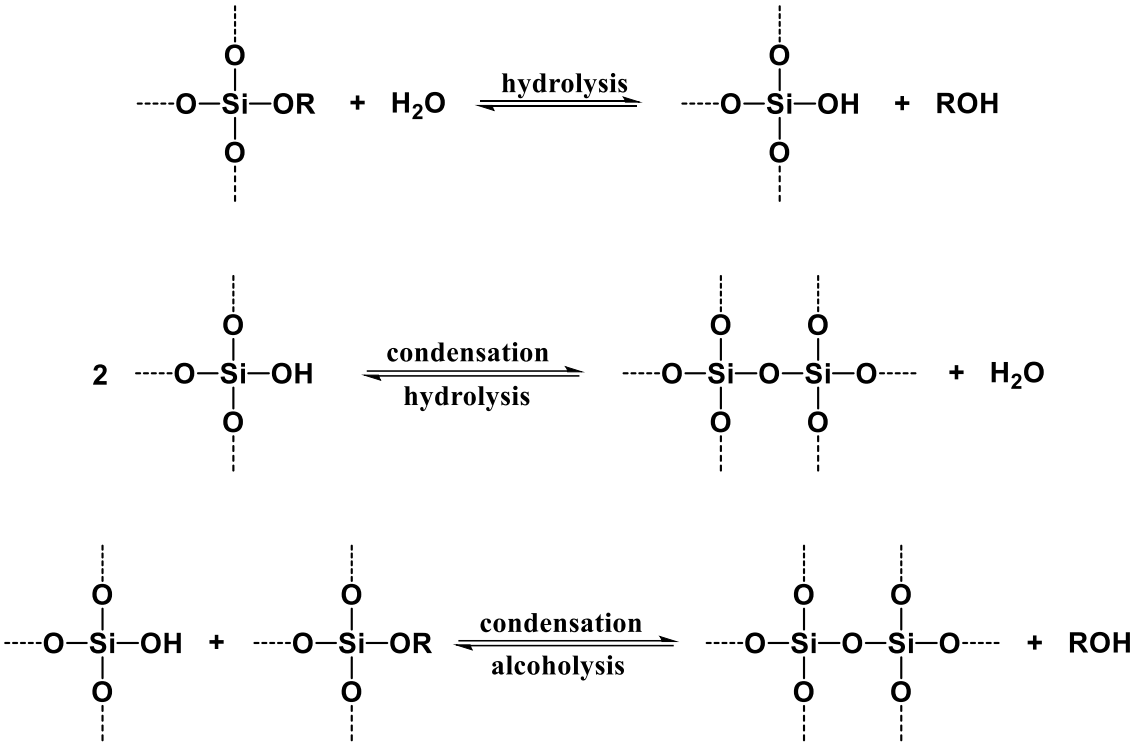

Scheme 1.1. Main reaction steps occurring in the sol-gel process of alkoxysilanes.

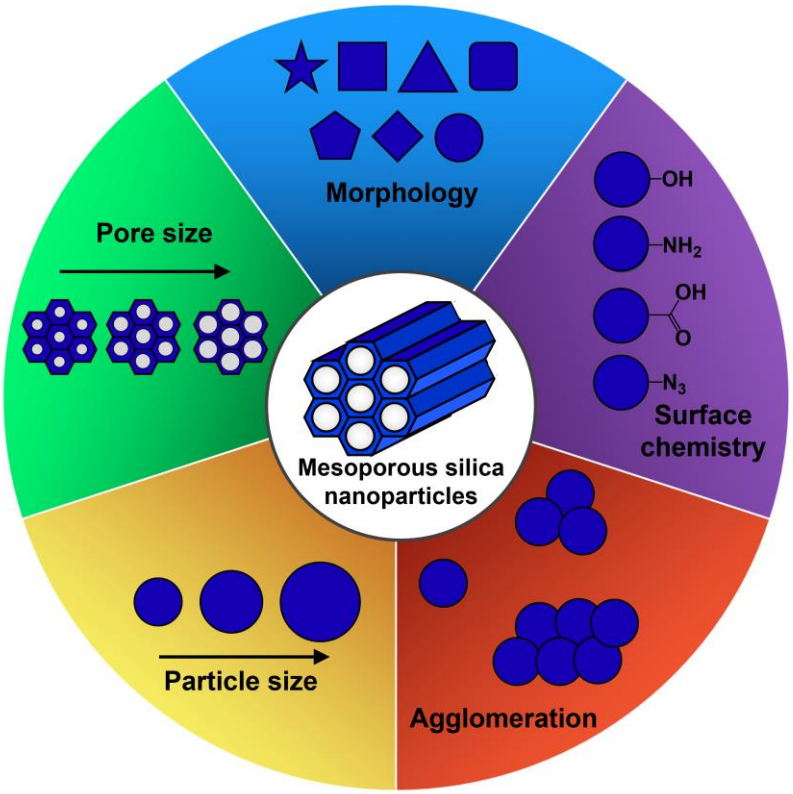

Figure 1.3. Variations that can be introduce in the synthesis of new mesoporous silica materials.

Heterogenization methods for silica materials can be distinguished into two main categories:

- Post-synthetic functionalization: traditionally, this has been the most commonly used method for functionalizing mesoporous silica materials. It involves non-covalent dye uptake by impregnation or inclusion, or the attachment of molecules to the surface by covalent bonds, a process known as grafting. [42a, 42c, 42f, 43] In a common grafting process, molecules containing terminal trialkoxysilane groups ($Si(R'O)_3R$) react with the silanol groups remaining on the silica surface through condensation/hydrolysis reactions (Figure 1.4).

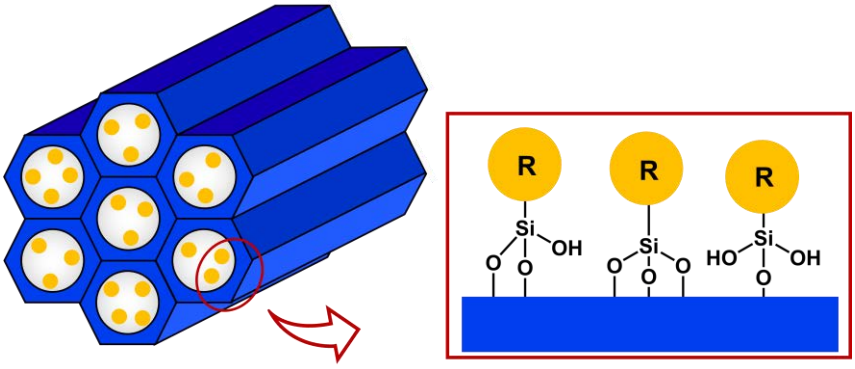

Figure 1.4. Representation of a grafted material.

These methods offer the advantage of enabling easy binding of molecules to preformed materials without affecting their textural characteristics, resulting in high incorporation percentages. However, despite their widespread use, these techniques have several drawbacks. For instance, the active phase may aggregate on the surface of the material, partially blocking the mesopores and reducing the total available surface area. In addition, the exposure of the active phase to the medium can lead to leaching problems, reducing the amount of molecules bound to the surface and reducing the recyclability of the material after each use.

-*In-situ* functionalization: in recent years, there has been a growing interest in developing more straightforward strategies to better incorporate the chromophores into the support. The *in-situ* synthesis strategy has emerged as a solution to this challenge, based on the incorporation of a previously functionalized chromophore with anchoring groups during the sol-gel preparation of the silica. This results in the simultaneous

co-condensation of the chromophore and the silica precursor, leading to the direct incorporation of the active phase into the silica network (Figure 1.5).

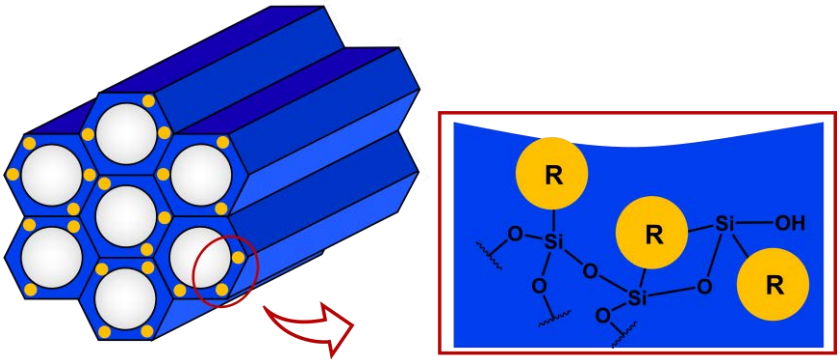

Figure 1.5. Representation of an *in-situ* material.

This synthetic approach has been explored in our group since 2011,[44] with the initial functionalization of coordination and organometallic complexes with alkoxysilane terminal groups, the so-called "Sol-Gel Coordination Chemistry" approach,[42g] although in recent years we have also used functionalized perovskite nanocrystals[45] or even luminescent proteins[35c] as chromophores. This has led to the preparation of a series of organometallo-silica hybrid materials that have demonstrated successful applications in catalysis, illumination, and bioimaging.[35a, 35b, 40] These *in-situ* methods offers improved stability of the chromophores compared to post-synthetic functionalization, thanks to the protection provided by the silica matrix, which prevents leaching problems. It also ensures a better distribution of the molecules throughout the material, preventing agglomeration on the surface and mimicking the photophysical properties of the cyclometalated complex in solution.[42g, 46] However, it may reduce the number of chromophores available to the medium, requiring the synthesis of materials with high porosity to enhance the chromophore accessibility.

Regardless of the method employed for functionalization, in the context of photocatalysis, these systems offer the well-known advantages of heterogeneous catalysis such as easy recovery and reusability, while maintaining the high selectivity that is typically observed with homogeneous catalysts.[46a] However, their use in the heterogenization of photocatalysts (PCs) has not been explored as extensively as in other

areas. Pioneering examples can be found in the work of Professors Wu[47] and Yamashita.[48] Both research groups reported the grafting of different platinum(II) and iridium(III) complexes onto silica gels with surfaces modified with amino groups, which can then bind to the metal center. These materials were successfully employed in oxidation reactions requiring the production of singlet oxygen (Scheme 1.2).

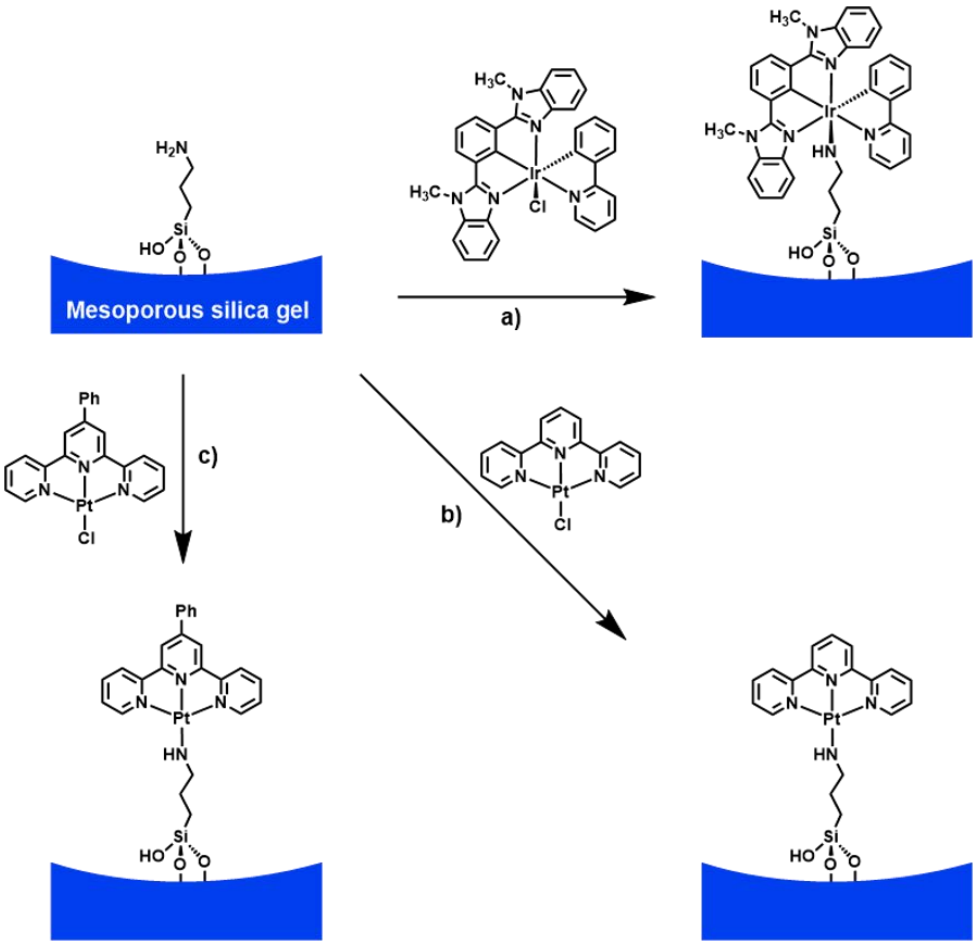

Scheme 1.2. Functionalizations performed by the groups of Prof. Yamashita (a, b) and Prof. Wu (c).

An *in-situ* functionalization method applied for photocatalysis can be found in the work of Prof. Zhao and co-workers in 2015.[43f] They introduced two trialkoxysilane terminal groups into the structure of a 2,2'-bipyridine, and synthesized a ruthenium(II) polypyridyl complex bearing six anchoring groups. This complex was then reacted with the silica precursor to obtain a mesoporous gel (Scheme 1.3). The resulting material was used in three photocatalytic reactions: oxidative dehydrogenation of dihydropyridine derivatives, reductive dehalogenation of alkyl halides, and oxidative halogenation of alcohols, achieving good yields and recyclability values.

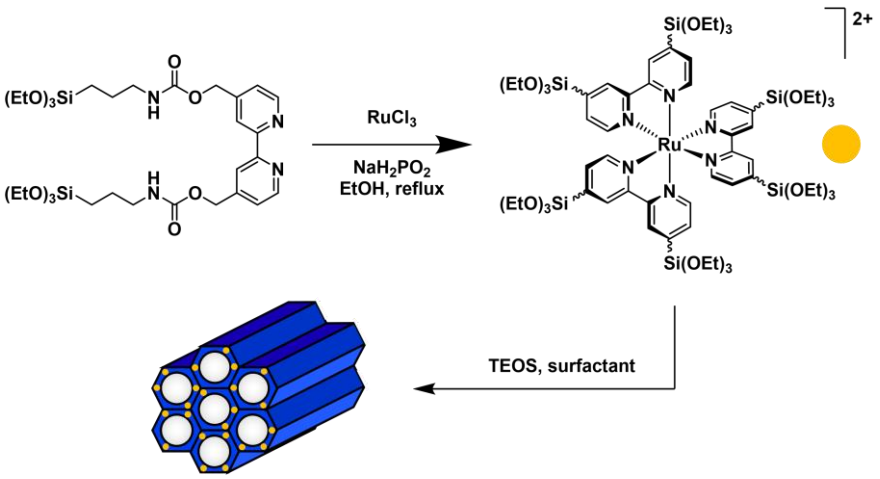

Scheme 1.3. *In-situ* functionalization carried out by Prof. Zhao and co-workers.

A more recent example, utilizing the two functionalization methods described above, can be found in the work of Prof. Romero-Salguero and co-workers,[49] who synthesized a Periodic Mesoporous Organosilica (PMO) incorporating an N-chelating ligand through *in-situ* co-condensation techniques. After obtaining the material, the available ligands on the surface were reacted with the respective chloride complexes of iridium(III) or ruthenium(II). This resulted in the grafting of the complexes onto the surface, while the N-chelating ligand can be considered as part of the structure of the material (Scheme 1.4). These materials have been used for artificial photosynthesis with good results.

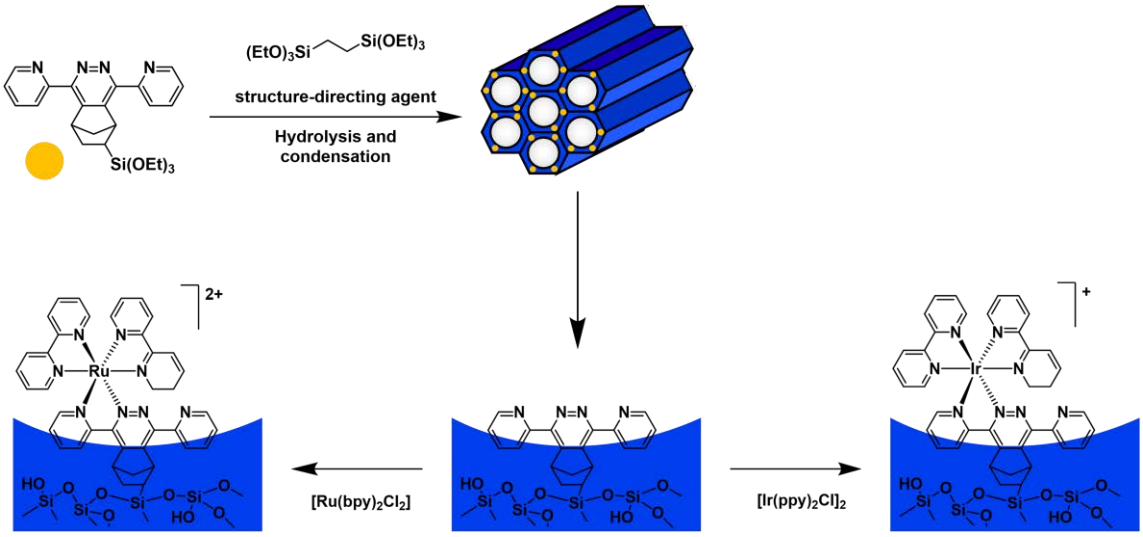

Scheme 1.4. Work of Prof. Romero-Salguero.

On the other hand, several iridium(III) cyclometalated complexes, similar to those incorporated in hybrid materials by our group, have demonstrated high efficiency in

homogeneous EnT photocatalysis.[13c, 15] One of the standard reactions in this type of mechanism, which remains a challenge in organic synthesis today, is the isomerization of alkenes to obtain the *Z*-isomer. Although this isomer is thermodynamically less stable than its *E*-isomer, it is often necessary for the preparation of anticancer drugs,[50] chromatic lasers,[51] or industrial dyes,[52] among others. Additionally, *E*-*Z* isomerization plays a crucial role in molecular switches.[53] Traditional non-photocatalytic methods to obtain the *Z*-isomer are often costly, energy-intensive,[54] and generally result in poor stereoselectivity. For this reason, the photoassisted *E* to *Z* isomerization reaction is usually carried out by irradiation under UV-light,[50, 55] but this approach is ineffective over a wide range of alkenes, and usually does not present a good selectivity. Therefore, there is an active search for new approaches to achieve this transformation under different conditions.

As just mentioned, the challenge in obtaining the *Z* isomer stems from its lower stability, making the process of obtaining it from the *E* isomer thermodynamically unfavorable. However, when an alkene molecule is excited, either by using high-energy light sources, such as UV-light, or by using a photocatalyst, it enters its S_1 or T_1 state, which have a minimum energy positioned at the maximum energy of the S_0 state between both isomers. In other words, these molecules possess a conical intersection (CI) that connects the ground state and the excited state, allowing the excited molecule to relax to either the *E* or *Z* isomer (see Figure 1.6).

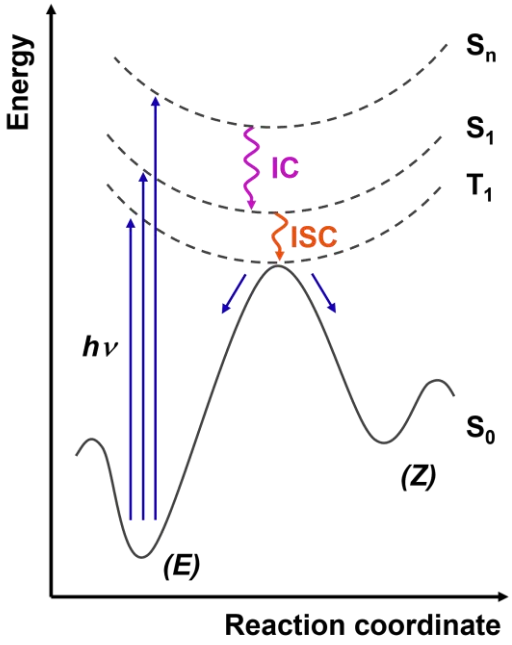

Figure 1.6. General energy profile diagram of an alkene.

The stereoselectivity of the reaction, favoring one isomer over the other, results from the difference between the triplet state energies of the two geometries. Examining the diagram in Figure 1.7, there is a 21 kJ/mol difference in the triplet states of the stilbene isomers, with *trans*-stilbene (*E*) being more stable.[56] This implies that by using a photosensitizer with a triplet energy situated between the energies of the two triplet states, it becomes capable of selectively sensitize only one of the isomers. Upon entering the excited state, the conical intersection is reached, allowing the molecule to relax to either of its two structures. However, over time, the concentration of the *Z*-isomer increases since it cannot be sensitized with the photocatalyst.[17a]

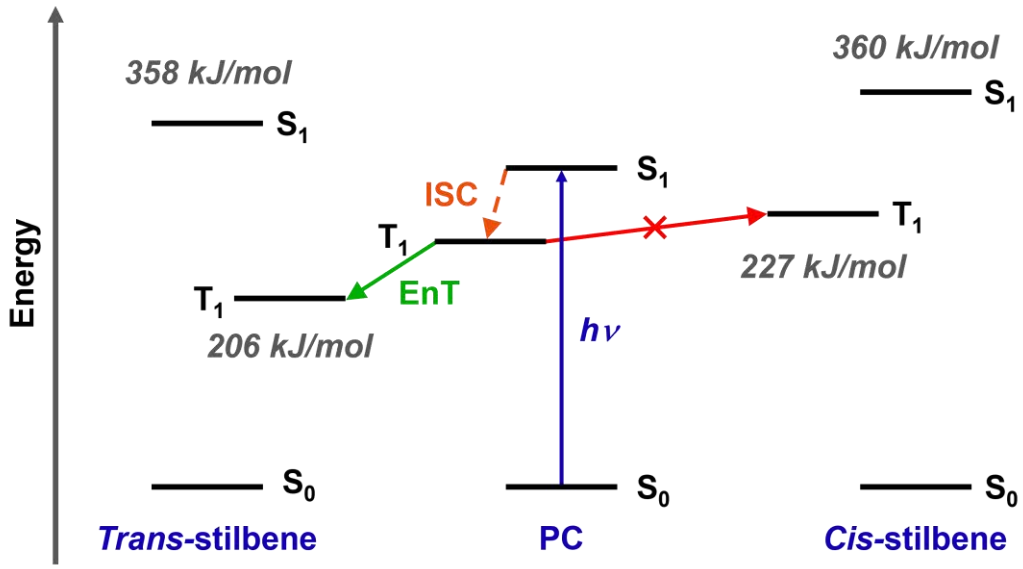

Figure 1.7. Diagram of the photosensitization of *trans*-stilbene by a photocatalyst.

In this context, we have chosen the highly phosphorescent cyclometalated complex [Ir(dfppy)$_2$(*dasipy*)]PF$_6$ (**1**, dfppy = 2-(2,4)-difluorophenyl-pyridinyl; *dasipy* = N,N'-dipropiltriethoxysilane-2,2'-bipyridine-4,4'-dicarboxamide), previously reported by our group, as it emits at 550 nm (217 kJ/mol),[40a] slightly above the triplet energy of *trans*-stilbene (580 nm, 206 kJ/mol).[57] This complex has two terminal triethoxysilane groups in its structure, allowing its co-condensation with the silica precursor using *in-situ* techniques. Moreover, since there are limited comparisons in the literature regarding the photocatalytic activity of materials functionalized by the two aforementioned techniques, we proposed the synthesis of different materials, varying their characteristics and functionalization method, to evaluate their recyclability and reusability in the isomerization reaction of the *trans*-stilbene.

All the work presented in this chapter has been published in a peer-reviewed scientific journal, and can be consulted in:

M. Martínez-Aguirre, E. Serrano, C. Ezquerro, E. Lalinde, J. R. Berenguer, J. García-Martínez, M. A. Rodríguez. Hybrid organometallo-silica catalysts for sustainable visible-light promoted olefin isomerization. *Catal. Today* **2023**, *422*, 114213.

1.2 Synthesis of the iridium(III) complex

1.2.1 Synthesis and characterization

Although the synthesis and characterization of the complex used for the functionalization of the materials have been previously carried out by our group,[40a] and they are also detailed in the PhD Thesis by Cintia Ezquerro,[58] the data are presented here again to establish its properties and to be able to compare them when introduced in silica matrices.

The highly emissive complex [Ir(dfppy)$_2$(*dasipy*)]PF$_6$ (**1**) was synthesized by reacting [Ir(dfppy)$_2$(NCMe)$_2$]PF$_6$ with the stoichiometric amount of the diimine ligand *dasipy* at room temperature, and using dichloromethane as the solvent (Scheme 1.5). The complex was obtained as a yellow solid that must be stored under inert atmosphere due to its ability to self-condensed *via* the alkoxysilane groups.

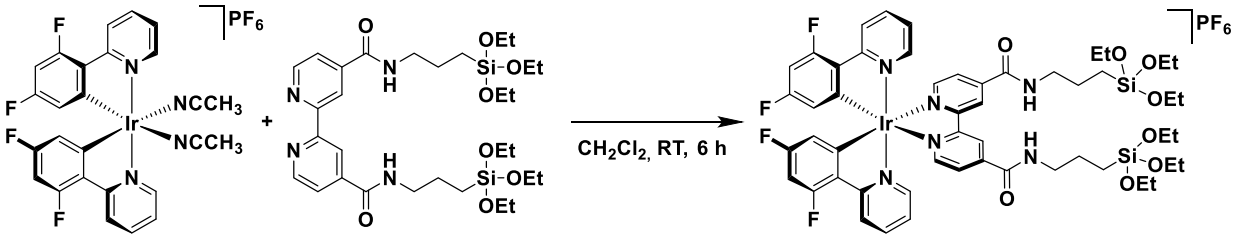

Scheme 1.5. Synthetic route of complex [Ir(dfppy)$_2$(*dasipy*)]PF$_6$.

The full characterization of the complex can be found in the experimental section of this thesis as well, and it was performed by elemental analysis, mass spectrometer, IR and NMR.

In the IR spectrum, the weak bands corresponding to the vibration modes ν(C-H) of the aromatic rings (>3000 cm^{-1}) and the aliphatic chains (<3000 cm^{-1}) can be observed, as well as the ν(N-H) bands at 3400 cm^{-1} and the stronger ν(C=O) at 1665 cm^{-1} corresponding to the amide group of the *dasipy* ligand. Other relevant bands can be observed at 1270 cm^{-1}, which is attributed to the C-F bond vibration, as well as intense bands at 1160 and 1075 cm^{-1} that correspond to the bond vibrations of the triethoxysilane group. As for the ^{1}H, ^{13}C{H} and ^{19}F{H} NMR spectra, the observed signals correspond to those already described (refer to Experimental Part).

1.2.2 Photophysical properties

According to previously published information,[40a] the absorption spectra of complex **1** exhibit distinct features in both solid state (Diffuse Reflectance UV-vis, DRUV) and in THF solution (Table 1.1 and Figure 1.8). In the high-energy region (below 300 nm), a prominent absorption peak is observed which, according to TD-DFT theoretical calculations, can be attributed to spin-allowed intraligand π-π* transitions, originated from the aromatic ligands dfppy (L: C^N) and *dasipy* (L': N^N). Additionally, a mixture of intraligand and ligand-to-ligand [C^N →N^N] charge transfer transitions (^{1}IL/^{1}LL'CT) contribute to the absorption in the range of 300-320 nm, along with a certain contribution of the metal. A less intense absorption band is observed between 340-400 nm, resulting from a combination of metal-to-ligand [M →N^N] and ligand-to-ligand charge transfers (^{1}ML'CT/^{1}LL'CT). Finally, and due to the strong spin-orbit coupling produced by the iridium center, weak absorptions are observed at lower energies (λ_{abs} 400-500 nm). These weak absorptions are typically associated with spin-forbidden ^{3}ML'CT (d(Ir) →$\pi^*_{N^N}$) and ^{3}LL'CT (π_{C^N} →$\pi^*_{N^N}$) transitions.

Table 1.1. Absorption data in THF solution ($5x10^{-5}$ M) and in solid state of complex **1**.

Sample	λ_{abs}/ nm (ε/ M^{-1} L^{-1})
[Ir(dfppy)$_2$(*dasipy*)]PF$_6$ (1)	285, 312, 380, 420, 445, 476 ***Solid***
	260 (54.0), 274$_{sh}$ (47.9), 305 (31.6), 360 (8.8), 417 (1.1), 445 (0.8), 470 (0.4) ***THF***

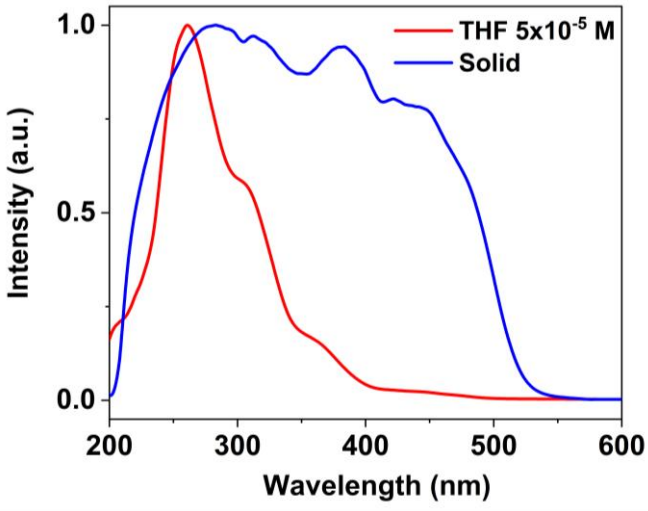

Figure 1.8. Normalized absorption spectra of complex **1** in solid state and THF solution ($5x10^{-5}$ M).

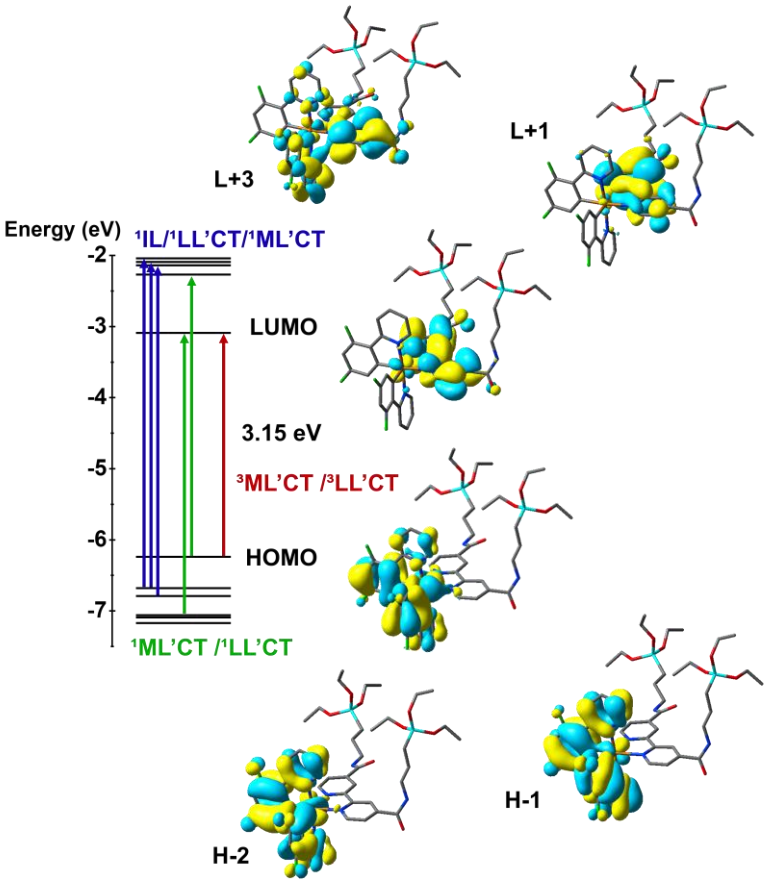

Figure 1.9. Molecular orbitals and transitions involved in complex **1** absorption.

The emissive properties of complex **1** have also been measured in solid state and in THF solution at RT, and the transitions were elucidated through theoretical calculations. In a degassed THF solution ($5x10^{-4}$ M), complex **1** exhibits a brilliant yellow structureless phosphorescence (τ = 0.71 μs, ϕ = 56%) with a maximum wavelength at 550 nm (Figure 1.10 and Table 1.2). As shown in Figure 1.11, the SOMO is located at the *dasipy* ligand, whereas the SOMO-1 is located at the dfppy ligands and the iridium center, so this emission can be attributed to a mixture of ^{3}ML'CT/^{3}LL'CT transitions, wherein the metal component plays a significant role (metal contribution to the calculated orbital = 41%). In the solid state, the emission appears slightly red-shifted (λ_{max} = 560 nm), accompanied by reduced values of lifetime (τ) and photoluminescence quantum yield (PLQY, ϕ) (τ = 0.35 μs, ϕ = 29%). This observation aligns with the higher non-radiative decay constant K_{nr} observed in the solid state compared to THF solution, indicating some degree of aggregation-induced quenching (ACQ) phenomena, resulting from π-π interactions between the ligands.

Table 1.2. Photophysical data in solid state and THF solution ($5x10^{-4}$ M) for complex **1**. All data at Room Temperature.

Sample	Medium (T/K)	λ_{em}/ nm[a)]	τ/μs[b)]	ϕ/%[c)]	K_r	K_{nr}
1	Solid	560	0.35	29.4	$8.4x10^5$	$2.0x10^6$
	THF	550	0.71	55.8	$7.9x10^5$	$6.2x10^5$

a) Data measured with λ_{exc} at 365 nm. Similar emission spectra obtained by excitation in the range 365-480 nm. b) Emissions lifetimes calculated as average of a bi-exponential decay. c) λ_{exc} at 440 nm.

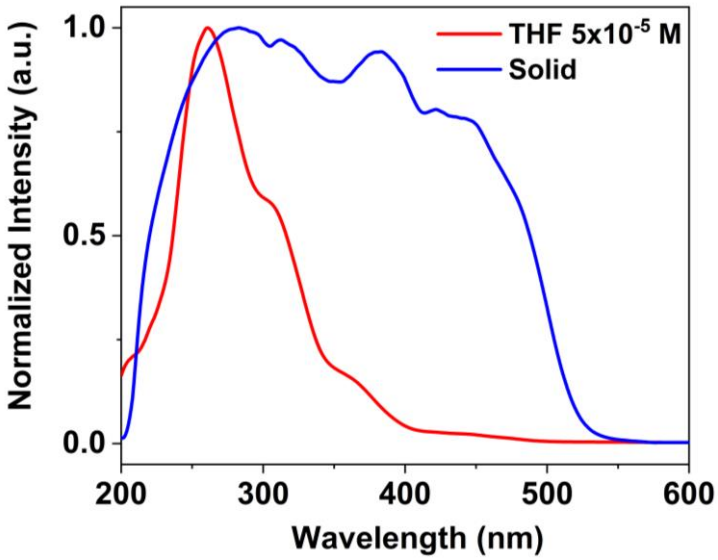

Figure 1.10. Normalized emission spectra (λ_{exc} = 365 nm) at RT for complex **1** in THF solution ($5x10^{-4}$ M) and in solid state.

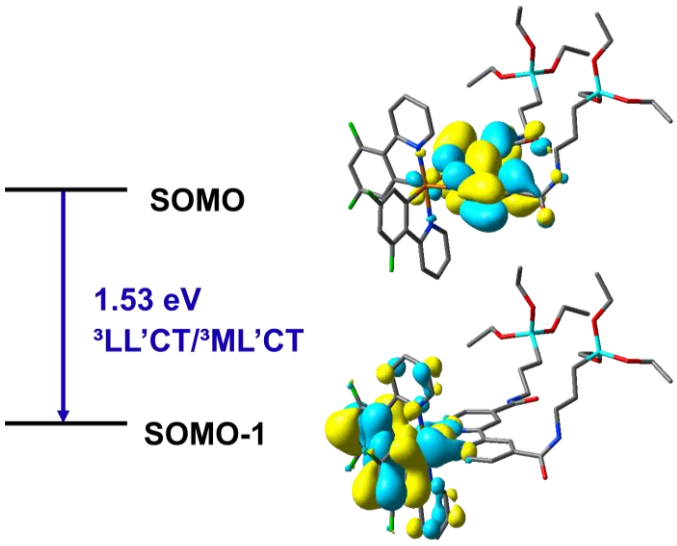

Figure 1.11. Molecular orbitals involved in complex **1** emission.

1.3 Synthesis and characterization of the hybrid organometallo-silica photocatalysts

1.3.1 Synthesis

The synthesis of silica materials was carried out based on Sol-Gel Coordination Chemistry, using TEOS as silica precursor, and CTAB (hexadecyltrimethylammonium bromide) as surfactant. Complex **1** has been used as the chromophore in the synthesis of four different materials using *in-situ* functionalization techniques, including gels (**SiO_2_N**, **SiO_2_B** and **SiO_2_OD**) and nanoparticles (**NP_IS**), and for the preparation of post-synthetic grafted silica nanoparticles (**NP_G**). These syntheses were adapted from our previously reported methodology for this type of materials.[35a, 35b, 40a]

The synthesis scheme, as well as the nomenclature used for these different hybrid organometallo-silica catalysts, is illustrated in Scheme 1.6. All syntheses were conducted under mild conditions, ranging from room temperature to 80°C. Detailed experimental procedures can be found in the Experimental Part.

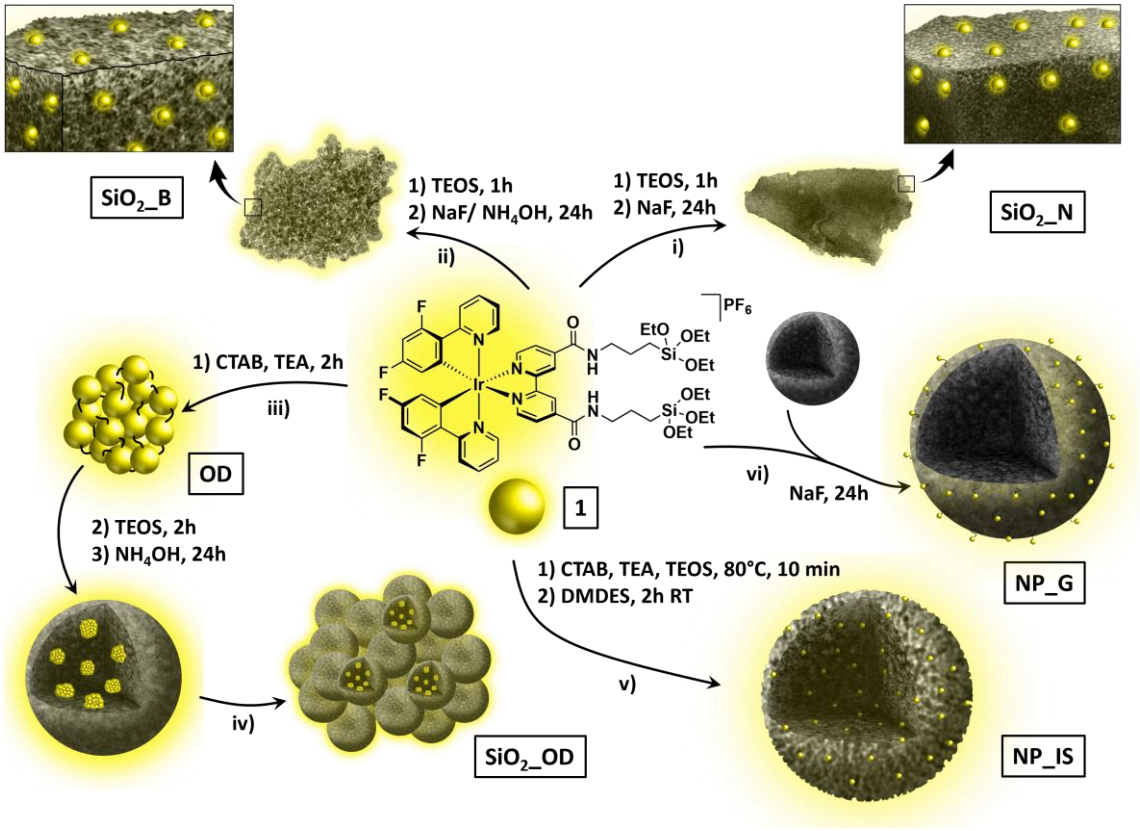

Scheme 1.6 Schematic representation of the synthesis of the hybrid organometallo-silica materials starting from complex **1**, and the nomenclature used.

The first two synthesized materials, corresponding to the hybrid silica gels **SiO_2_N** and **SiO_2_B,** were prepared in the absence of surfactant, and by using NaF as a catalyst for the co-condensation of tetraethyl orthosilicate (TEOS) with the alkoxysilane terminal groups of **1**. In both cases, a solution containing complex **1** and TEOS (in tetrahydrofuran, THF, for **SiO_2_N** or EtOH for **SiO_2_B**) was stirred in water at RT for 24 h, in a neutral media for **SiO_2_N** (i, Scheme 1.6) or basic media for **SiO_2_B** (ii, Scheme 1.6).[35a] The amount of complex **1** was carefully adjusted to achieve a nominal iridium content of 1 wt%.

The synthesis of both **SiO_2_OD** and **NP_IS** was carried out using CTAB as a surfactant and triethanolamine (TEA) as the catalyst of the sol-gel processes. The synthesis of **SiO_2_OD**, also targeting a nominal iridium content of 1 wt%, followed a one-pot two-step procedure at RT. In a first step, a solution of complex **1** in EtOH was pre-hydrolyzed in water for two hours in the presence of TEA and CTAB, leading to the formation of Organometallic Dots (**OD**, iii, Scheme 1.6).[35b] These particles consist entirely by molecules of complex **1**, covalently bonded by condensation of the terminal trialkoxysilane groups. In a second step, TEOS was added to react with these **ODs** in a basic media for an additional 24 hours, to allow the growth of the silica nanoparticles encapsulating the previously formed **ODs**. These nanoparticles do not remain discrete, but rather aggregate with each other to form the final **SiO_2_OD** material (iv, Scheme 1.6).

The nanoparticles **NP_IS** reported here were also previously synthesized in our group,[40a] but have been included in this study because of their good emissive and textural properties, and as an example of an *in-situ* material composed of discrete nanoparticles. The synthesis of these nanoparticles is carried out by the rapid addition of a solution of complex **1** in a mixture of ethanol and TEOS to a basic aqueous solution of CTAB and TEA. After 10 minutes at 80ºC, a capping agent known as dimethyldiethoxysilane (DMDES) was added and the mixture was stirred for an additional 2 hours, leading to discrete nanoparticles superficially capped with methyl groups (v, Scheme 1.6). Unlike the rest of the materials, **NP_IS** has a nominal iridium content of only 0.2 wt%. Finally, for **SiO_2_OD** and **NP_IS**, the elimination of the surfactant was achieved by ionic exchange with a saturated ethanolic solution of NH_4NO_3.

Additionally, an analogous functionalized material was synthesized by post-synthetic techniques (**NP_G**). To obtain this material, conventional silica nanoparticles without the presence of iridium complex were first prepared (**MSN**, detailed synthesis in the

Experimental Part). These nanoparticles were suspended in ethanol, and the appropriate amount of complex **1** was added to obtain a nominal iridium content of 1 wt%. The reaction was stirred at RT for 24 hours in the presence of NaF to accelerate the hydrolysis of the alkoxy groups (vi, Scheme 1.6).

To assess the successful incorporation of complex **1** into the five different materials and to confirm the preservation of its molecular structure, various analyses were performed, including infrared (FTIR), absorption, and emission spectroscopies (see the Photophysical Properties section for more detailed information on the last two techniques).

The FTIR spectra of all hybrid organometallo-silica materials, including both gels and nanoparticles, exhibit characteristic bands corresponding to the Si–O and Si–O–Si bonds, as indicated in Figure 1.12. Additionally, weak absorptions attributed to complex **1** were observed in all spectra at approximately 3280 cm^{-1}, 2900 cm^{-1} and 1500–1400 cm^{-1}. These bands can be assigned to the vibrations of the N-H and C-H bonds in the amidic moiety, as well as the vibrations of the aromatic groups, respectively. In the spectrum of the hybrid nanoparticles **NP_IS**, two additional bands were observed at around 1265 cm^{-1} and 850 cm^{-1}, which can be attributed to the presence of the Si-Me bonds originating from the DMDES capping agent used in their synthesis.

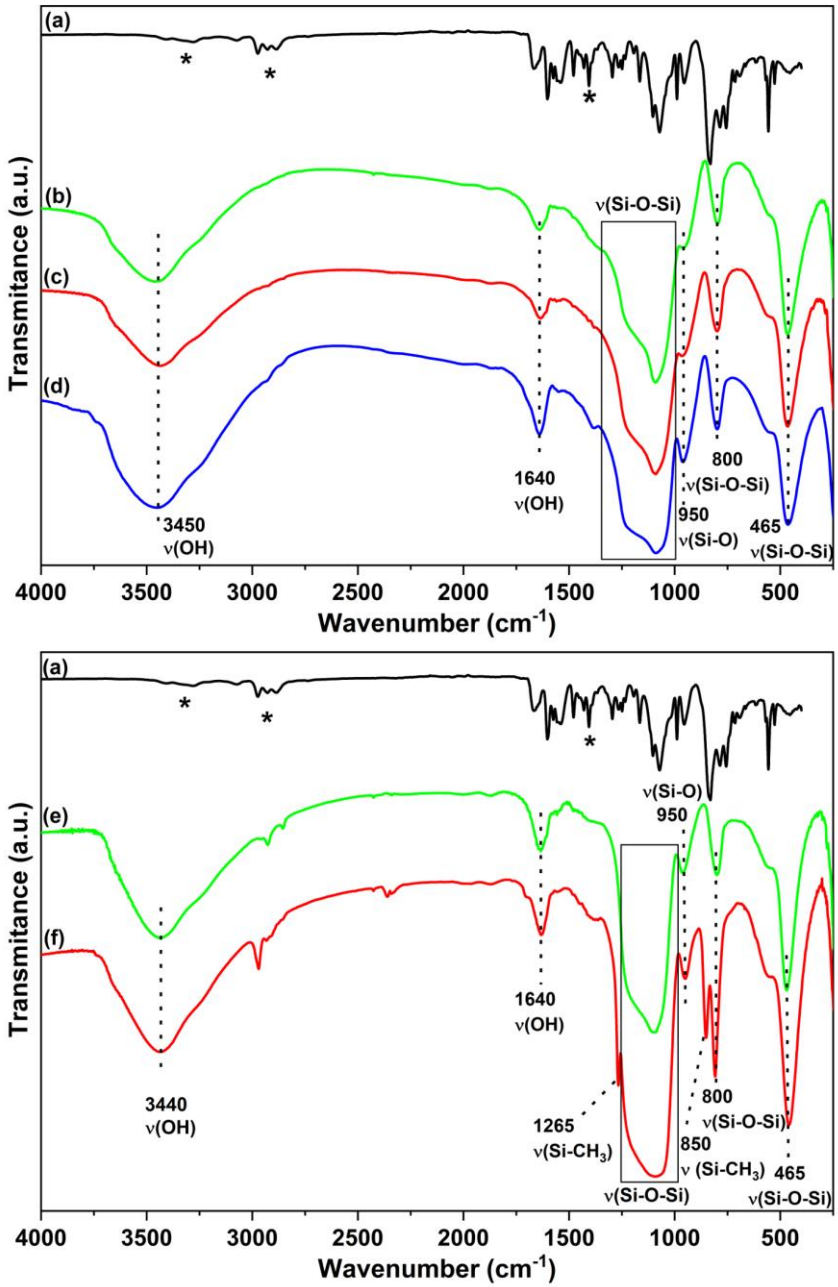

Figure 1.12. FTIR spectra of the silica materials (up; **SiO_2_N** (b); **SiO_2_B** (c); **SiO_2_OD** (d)) and nanoparticles (down; **NP_G** (e); **NP_IS** (f)) in comparison with the spectrum of the pure complex **1** (a). (*) Characteristic absorptions of complex **1** observed in the hybrid materials.

1.3.2 Textural characterization

The physisorption experiments for the textural characterization of the materials were carried out at the University of Alicante, in the Laboratory of Molecular Nanotechnology group led by Prof. Javier García Martínez.

Figure 1.13 shows the nitrogen adsorption/desorption isotherms at 77 K, and the pore size distribution obtained for the five synthetized materials. A type IV isotherm, characteristic of mesoporous materials, is observed for all samples.

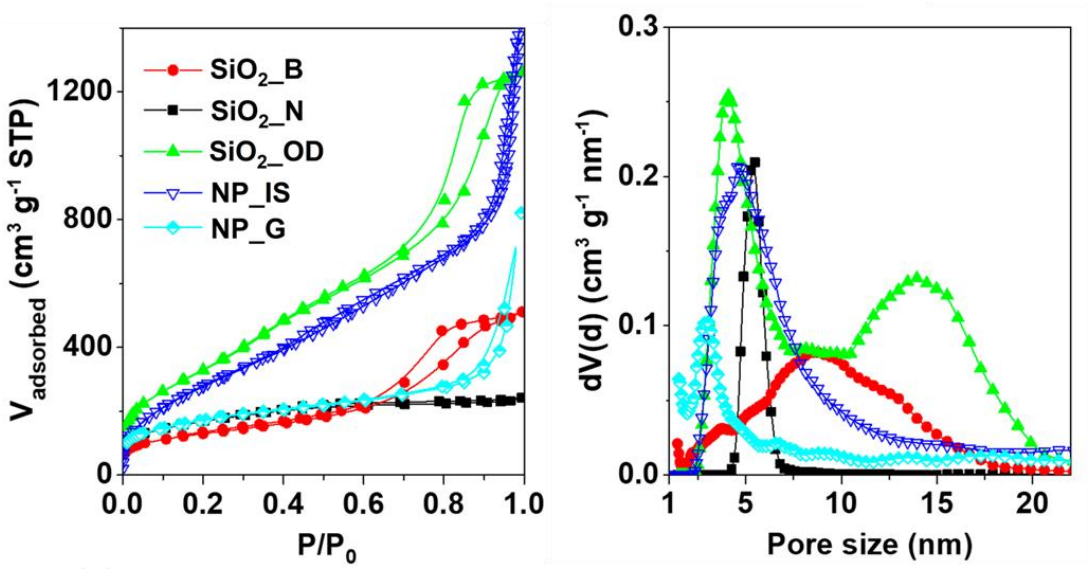

Figure 1.13. N_2 adsorption/desorption isotherms at 77 K (left) and the corresponding pore size distribution calculated using the NLDFT method (right) of the five mesoporous hybrid organometallo-silica materials.

The textural properties extracted from the adsorption/desorption isotherms, as well as the iridium metal content determined by Inductively Coupled Plasma (ICP) analysis, are shown in Table 1.3.

Table 1.3 Textural properties and metal content of the five hybrid materials.

Sample	Ir[a] (wt%)	A_{BET}[b] (m^2/g)	$V_p^{0.99}$[c] (cm^3/g)	d_p[d] (nm)
SiO_2_B	0.76 (1.0)	465	0.8	9.7
SiO_2_N	0.71 (1.0)	580	0.4	5.0
SiO_2_OD	0.38 (1.0)	1270	2.0	4.0/13.0
NP_IS[e]	0.11 (0.2)	1120	2.2	5.0
NP_G	0.89 (1.0)	610	1.3	3.0

a) Iridium content calculated from ICP mass spectroscopy analyses after treatment of the samples with diluted HF. Values in brackets represent the nominal metal content. b) Surface area estimated by the multipoint BET method using the adsorption data in the relative pressure (P/P_0) range of 0.05–0.3. c) Total pore volume read directly from the adsorption branch of the isotherm at 0.99. d) Average pore diameter determined at the maximum of the pore size distribution plot obtained applying the NLDFT equilibrium model. e) Data obtained from reference [40a]. **SiO_2_N**, **SiO_2_B** and **SiO_2_OD** were centrifuged and air dried before their textural characterization. All samples were degassed at 100ºC before gas adsorption measurements (see Experimental Part for details).

An analysis of the textural data of both **SiO_2_B** and **SiO_2_N** gels shows a surface area between 500 and 600 m^2/g, as well as very high incorporation percentages of the complex, more than 70% for both. Notably, **SiO_2_B** exhibited textural properties similar to the corresponding silica material synthesized without the presence of complex **1** under comparable basic conditions.[35a] Thus, **SiO_2_B** showed a total pore volume of approximately 0.8 cm^3/g and an average pore diameter of about 10 nm, which implies that the introduction of the chromophore in the synthesis has not affected the textural properties of the material. The images obtained by the Transmission Electron Microscopy (TEM) analysis (Figure 1.14, top) show the characteristic aspect of an amorphous material with intraparticle mesoporosity.

On the other hand, **SiO_2_N** displayed slightly reduced total pore volume (0.4 cm^3/g) and average pore diameter (5.0 nm) compared to the corresponding silica-free material,[35a] as well as to **SiO_2_B**. This behavior has previously been attributed to the weaker interaction between cationic Ir(III) complexes and the silica precursor in a neutral medium. TEM images show that this gel is formed by the aggregation of small

nanoparticles of between 5 and 10 nm (Figure 1.14, center), resulting in an amorphous material similar to the previous one, although with differences in its textural appearance.

As for the last synthesized mesoporous gel, **SiO_2_OD** shows excellent textural values, being the material with the highest BET surface area, 1270 nm, in spite of being a gel type material. Its TEM images (Figure 1.14, bottom) show that it is formed by the aggregation of nanoparticles with an average diameter of 30-40 nm. As a result, its surface area is considerably larger than the other two synthetized gels, and it presents two types of porosity. The first type is the typical mesoporosity of materials synthesized in the presence of a surfactant, with an average pore diameter of 4 nm. The second type is an interparticle porosity with a broader size distribution, ranging from 10 to 20 nm. However, despite of being the material with the most interesting textural properties, it shows the lowest incorporation yield (40%), probably due to the functionalization method. Nevertheless, these values still represent a significant iridium content, making it suitable for use as a photocatalyst.

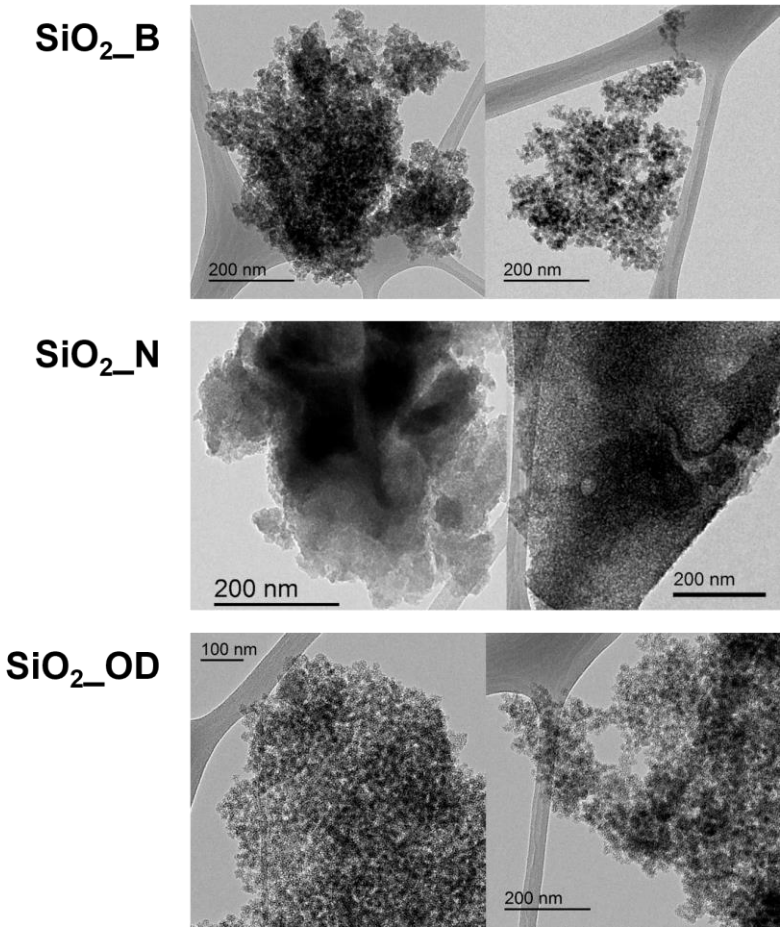

Figure 1.14. Representative TEM images of the mesoporous silica gels **SiO_2_B**, **SiO_2_N** and **SiO_2_OD**

As for the discrete nanoparticles, **NP_IS** shows a higher incorporation yield of 60%, and excellent textural properties, with a very high surface area of 1120 m^2/g, the highest pore volume value with 2.2 cm^3/g, and a pore diameter of 5.0 nm. The use of the capping agent DMDES, with two terminal methyl groups, results in a star-shaped morphology with an open mesoporosity, as can be observed in the TEM images (Figure 1.15, top). This feature also results in a homogeneous distribution of nanoparticle diameters averaging 60 nm.

Finally, the grafting-functionalized silica nanoparticles **NP_G** show a very high incorporation yield of 90%, indicating the greater ease of complex incorporation through post-synthetic techniques rather than *in-situ* methods. When comparing its textural properties to the metal-free nanoparticles (**MSN**), **NP_G** shows a surface area slightly lower than **MSN** (610 m^2/g *vs.* 760 m^2/g),[40a] probably due to a partial block of the pores. The mesoporosity of **NP_G** is very similar to that of the previously mentioned materials (pore volume of 1.3 cm^3/g and pore diameter of 3.0 nm), and the characteristic morphology of these mesoporous silica nanoparticles can be observed in the TEM images (Figure 1.15, bottom).

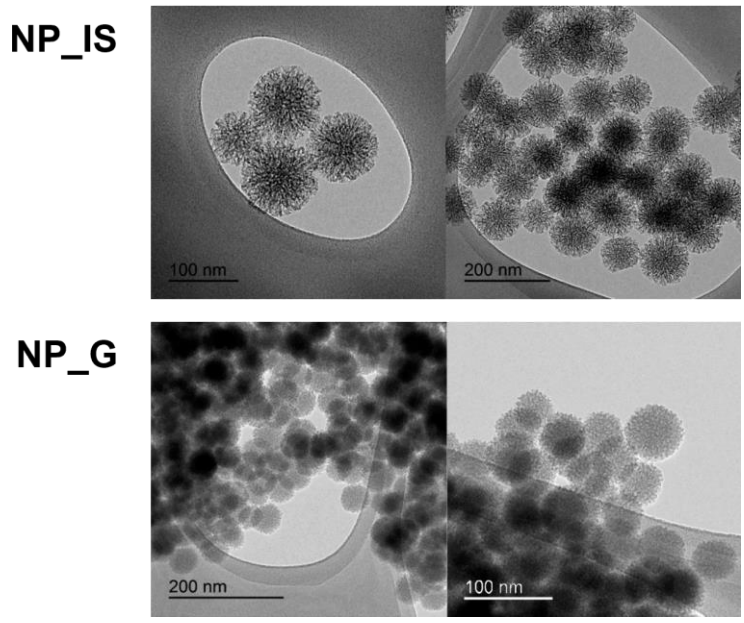

Figure 1.15. Representative TEM images of the mesoporous silica nanoparticles, **NP_IS** and **NP_G**

1.3.3 Photophysical properties

Figure 1.16 and Table 1.4 show the solid-state absorption spectra (diffuse reflectance spectra, DRUV) and the corresponding data for all the hybrid organometallo-silica materials. As shown in Figure 1.16, the DRUV spectra of all the organometallo-silica materials exhibit comparable absorptions to those observed for complex **1**, which serves as evidence that the structural integrity of the chromophore remains intact as it became incorporated into the silica matrix.

The absorption spectra of these materials exhibit a profile similar to that of the complex in solution, with lower intensity in the low-energy bands assigned to spin-forbidden transitions. This phenomenon can be attributed to the low concentration of the complex, together with its good dispersion within the silica matrix, which causes the materials to exhibit properties similar to those observed for **1** in solution.

Table 1.4. Absorption data in the solid state of the hybrid organometallo-silica materials.

Sample	λ_{abs}/ nm (ε/ M^{-1} L^{-1})
SiO_2_B	280, 293, 310, 353, 445, 471_{sh} ***Solid***
SiO_2_N	291, 311, 350, 444, 470_{sh} ***Solid***
SiO_2_OD	295, 308, 354, 444, 470_{sh} ***Solid***
NP_IS	298, 308, 345, 418, 445, 475_{sh} ***Solid***
NP_G	280, 295, 306, 345, 422, 445, 470_{sh} ***Solid***

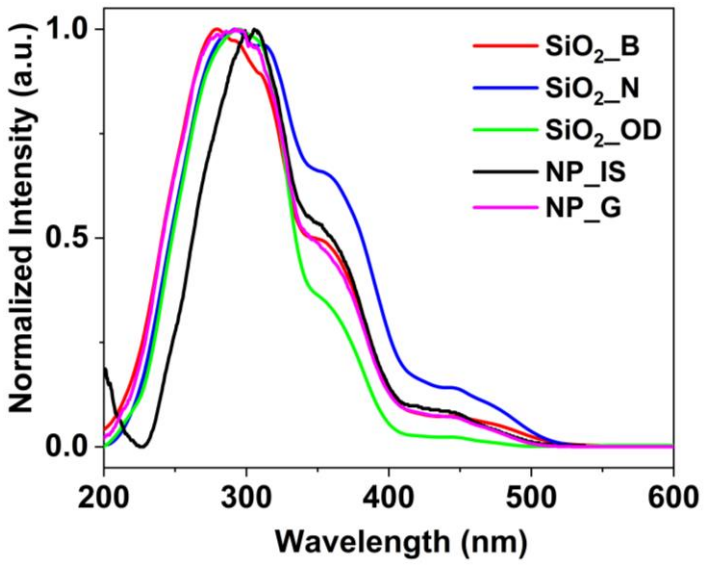

Figure 1.16. Solid state DRUV of the hybrid organometallo-silica materials

Regarding the emission and excitation spectra of the hybrid materials, they were measured both in the solid state and in $CHCl_3$ suspensions (1 mg/ml), since this is the medium in which the latter photocatalytic studies were carried out. Similar to the absorption spectra, all materials showed similar broad emission profiles, reminiscent of those measured for complex **1**, both in the solid state or THF solution. These data are presented in Table 1.5, Figure 1.17 and Figure 1.18.

Table 1.5. Photophysical data in solid state and $CHCl_3$ suspension (1 mg/ml) of the hybrid organometallo-silica materials. All data at RT.

Sample	Medium (T/K)	λ_{em}/ nm[a)]	τ/μs[b)]	ϕ/%[c)]	K_r	K_{nr}
SiO_2_B	Solid	580	0.29	10.0	$3.4x10^5$	$3.1\ x10^6$
	$CHCl_3$ Suspension	550	0.89	15.8	$1.8\ x10^5$	$9.5\ x10^5$
SiO_2_N	Solid	570	0.49	13.0	$2.7\ x10^5$	$1.8\ x10^6$
	$CHCl_3$ Suspension	565	0.57	12.5	$2.2\ x10^5$	$1.5\ x10^6$
SiO_2_OD	Solid	555	0.52	12.3	$2.4\ x10^5$	$1.7\ x10^6$
	$CHCl_3$ Suspension	565	0.77	10.4	$1.4\ x10^5$	$1.2\ x10^6$
NP_IS	Solid	550	0.72	50.1	$7.0\ x10^5$	$6.9\ x10^5$
	$CHCl_3$ Suspension	550	1.10	42.6	$3.9\ x10^5$	$5.2\ x10^5$
NP_G	Solid	555	0.42	16.3	$3.9\ x10^5$	$2.0\ x10^6$
	$CHCl_3$ Suspension	550	0.97	46.0	$4.7\ x10^5$	$5.6\ x10^5$

a) Data measured with λ_{exc} at 365 nm. Similar emission spectra obtained by excitation in the range 365- 480 nm. b) Emissions lifetimes calculated as average of a bi-exponential decay. c) λ_{exc} at 365 nm.

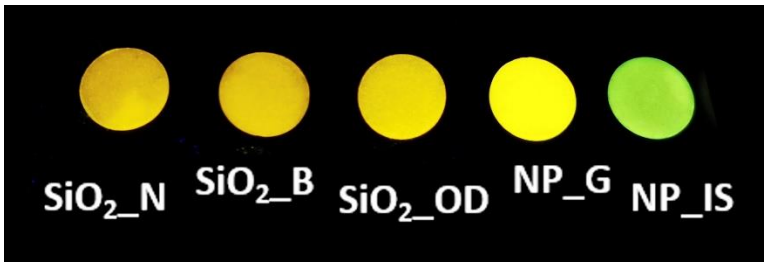

Figure 1.17. Photo of the emission of the hybrid organometallo-silica materials in solid state (λ_{ex} = 365 nm)

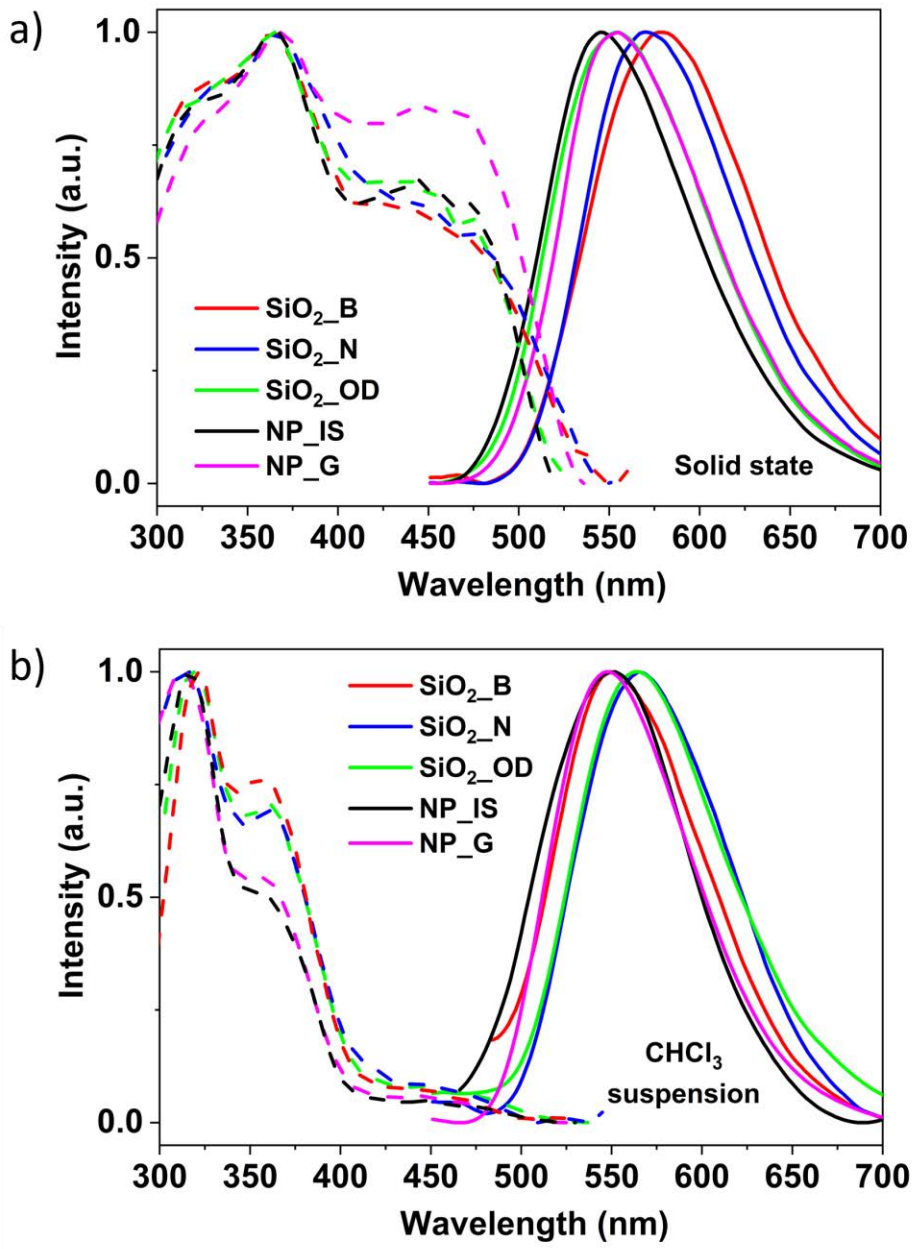

Figure 1.18. Normalized excitation (λ_{em} 450-460 nm) and emission (λ_{exc} 365 nm) spectra of the hybrid organometallo-silica materials at room temperature in (a) solid state and (b) in suspension of $CHCl_3$ (1 mg/ml).

On closer inspection of the data, the hybrid silica gel **SiO_2_B** displays in the solid state the largest bathochromic shift compared to complex **1**, with an emission maximum at 580 nm. However, the emission is blue-shifted in a chloroform suspension, appearing at the same wavelength as complex **1** in THF solution (λ_{max} = 550 nm). This indicates an interaction between the solvent and the chromophore molecules, suggesting that a significant proportion of the complex molecules are located on the surface of the material

and accessible to the medium. On the other hand, the other hybrid *in-situ* gels **SiO_2_N** and **SiO_2_OD** exhibit emission maxima in the solid state at 570 nm and 555 nm, respectively. However, in $CHCl_3$ suspension, both materials exhibit emissions at the same maxima (λ_{max} = 565 nm). These three materials (**SiO_2_B**, **SiO_2_N**, and **SiO_2_OD**) have the lowest PLQY values, ranging from 10.0% to 15.8%, both in solid state and in suspension. Considering the aggregation-caused quenching (ACQ) characteristics of complex **1** in the solid state, this fact indicates a high degree of association of the chromophore molecules in the silica gels **SiO_2_B**, **SiO_2_N**, and especially in the case of **SiO_2_OD**, where the initial formation of Organometallic Dots (**ODs**) involved the condensation of very close chromophore molecules.

On the other hand, the discrete nanoparticles **NP_IS** show a consistent emission maximum of 550 nm, regardless of the measurement medium (solid state or suspension). This suggests an excellent shielding of the chromophores in **NP_IS** and indicates similar emission characteristics to complex **1** in THF solution at room temperature (λ_{max} = 550 nm). Moreover, **NP_IS** exhibits the highest emission intensity among the *in-situ* materials, with PLQY values of 50.1% in the solid state and 42.6% in suspension, similar to complex **1** in THF (ϕ = 55.8%). These high values observed in **NP_IS** can be attributed to its low iridium content (0.11 wt%), which allows for better dispersion and protection of the complex molecules by the silica matrix, effectively preventing solid aggregation quenching and mimicking the behavior of the chromophore in solution.

Finally, the grafted nanoparticles **NP_G** display an emission maximum of 555 nm in the solid state, which is slightly blue-shifted to 550 nm in suspension. Compared to related nanoparticles synthetized by our group containing only 0.2 wt% of iridium, which exhibited a high PLQY of about 39%,[40a] **NP_G** shows a lower PLQY of 16% in the solid state. This reduction in PLQY is likely due to the higher incorporation of the iridium chromophore in **NP_G** (0.89 wt% of iridium), leading to some degree of quenching caused by the aggregation of the iridium molecules on the silica surface. However, in $CHCl_3$ suspension, the PLQY of **NP_G** significantly increases to 46%, suggesting that the interaction of the solvent with the grafted iridium(III) complexes molecules reduces both the intermolecular π-π quenching between the chromophore molecules and the non-radiative decay constant.

Regarding the lifetimes, all hybrid materials show increased values in $CHCl_3$ suspension compared to the solid state (Table 1.5). This effect is particularly pronounced for **NP_G** and **SiO_2_B**, with lifetimes in suspension more than twice the values in the solid state (τ 0.97 μs *vs*. 0.42 μs for **NP_G** and 0.89 μs *vs*. 0.29 μs for **SiO_2_B**). Furthermore, these materials exhibit absorptions in the blue region of the electromagnetic spectrum (λ_{abs}>400 nm), both in the solid state and in chloroform suspension. Therefore, considering all of the above, it can be concluded that the hybrid silica materials exhibit promising properties as potential photosensitizers.

1.4 Photocatalytic studies

1.4.1 Homogeneous tests

As indicated in the introduction to this chapter, the reaction used to measure the photocatalytic activity of the hybrid materials is the isomerization of *trans*-stilbene to *cis*-stilbene (Scheme 1.7).

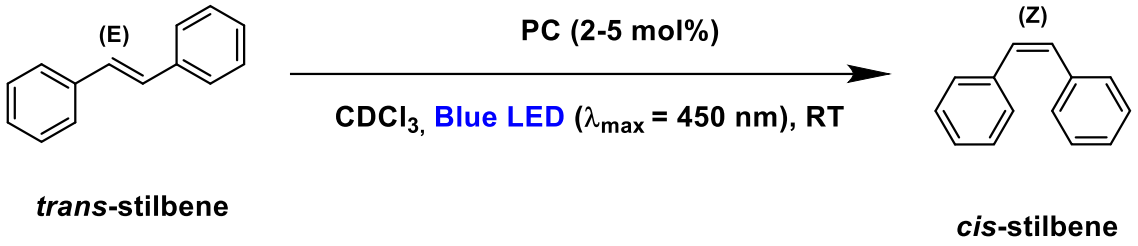

Scheme 1.7. Photocatalytic isomerization reaction.

This well-known reaction is considered a standard for EnT reactions. Its progress can be easily monitored by ^{1}H-NMR spectra (Figure 1.19), where the hydrogens on the alkene bond appear as a single singlet signal, both in regions of the spectrum where they do not overlap with other signals (~7.15 ppm for the *trans*-stilbene, and ~6.60 ppm for the *cis*-stilbene).

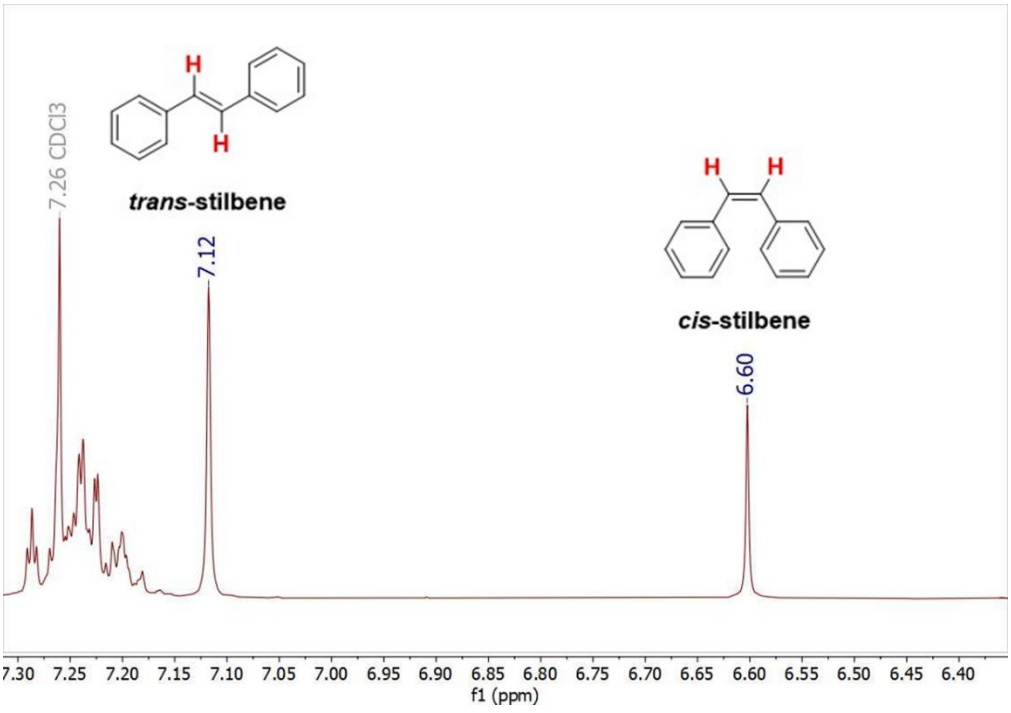

Figure 1.19. ^{1}H-NMR signals used to follow the isomerization conversions.

For this reason, the reactions were carried out using NMR tubes as reactors and deuterated chloroform as the solvent. To ensure that the iridium(III) complex was an effective PC for this reaction, preliminary tests were conducted using complex **1** in homogeneous media before proceeding with the materials. The light source for the irradiation was an RGB LED with a power of 50 W [λ_{max} (blue LEDs) = 450 nm, ~17 W], and maintaining agitation at RT (see Figure 1.21 in the next section for the set-up). Two different molar ratios of *trans*-stilbene:complex **1** were employed for this study, 1:0.05 and 1:0.02 (see Experimental Part for further details). The conversion was measured at 15-minute intervals. The results obtained are presented in Figure 1.20.

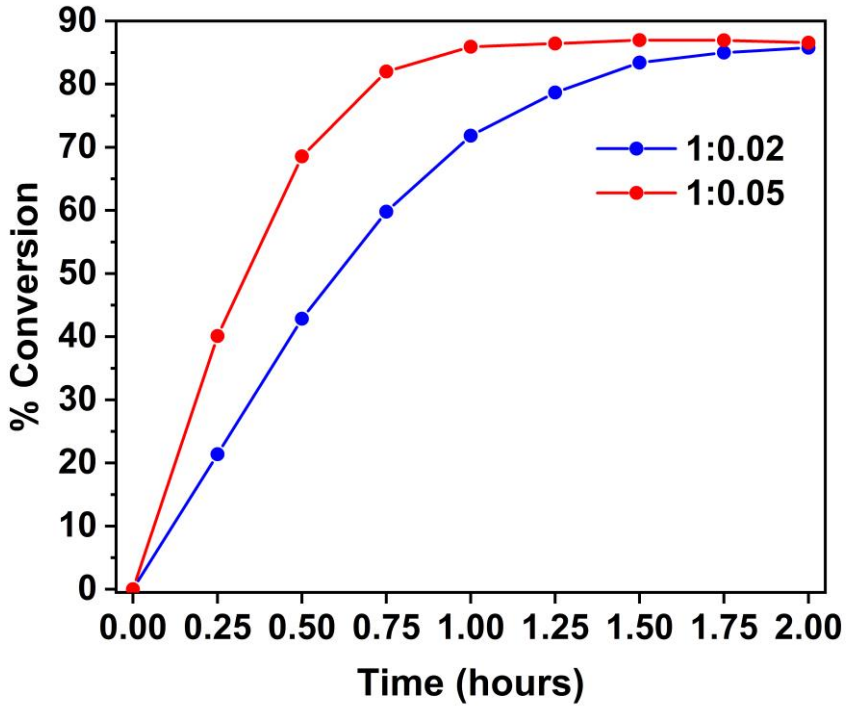

Figure 1.20. Photochemistry reaction with complex **1** as PC, in a molar proportion of *trans*-stilbene of 2 mol% and 5 mol%.

The tests reveal that the reaction rate depends on the molar ratio used, with a slightly slower rate observed when using a lower ratio ($k'_{0.05}/k'_{0.02}$ = 1.54, Table 1.6). However, in both cases a conversion of 85% to *cis*-stilbene was achieved after 1.5 hours of irradiation.

Table 1.6. Constant values of the photocatalytic activity, regression coefficients, and conversions reached at different times for complex **1**.

Molar ratio (*trans*-stilbene:PC)	**Conversion at 6 h (%)**	**Maximum conversion (%) / Time (h)**	**k' (h^{-1})[a)]**	**R[b)]**
1:0.02	85	85 / 1.0	1.337±0.021	0.9995
1:0.05	85	85 / 1.5	2.066±0.006	0.9999

a) 1st order reaction rate pseudophotocatalytic constant of the reaction of isomerization of *trans*-stilbene into *cis*-stilbene obtained as the average of three runs. b) Regression coefficient.

Two backgrounds tests were also conducted. In the first test, complex **1** was added in a molar ratio of 1:0.05 but in the absence of irradiation, while the second test was performed under blue light irradiation without adding the PC to the reaction media. In both cases, no conversion to *cis*-stilbene was observed even after 6 hours. This highlights the importance of both the photocatalyst and irradiation in driving the reaction.

1.4.2 Kinetic studies

Having established that complex **1** yielded good conversion results for this reaction, the same test was performed using each of the five silica-based materials as photosensitizer. The experimental setup remained the same as the previous one (Figure 1.21), with the corresponding amounts of material added to achieve the desired molar ratio (see Experimental Section for more details).

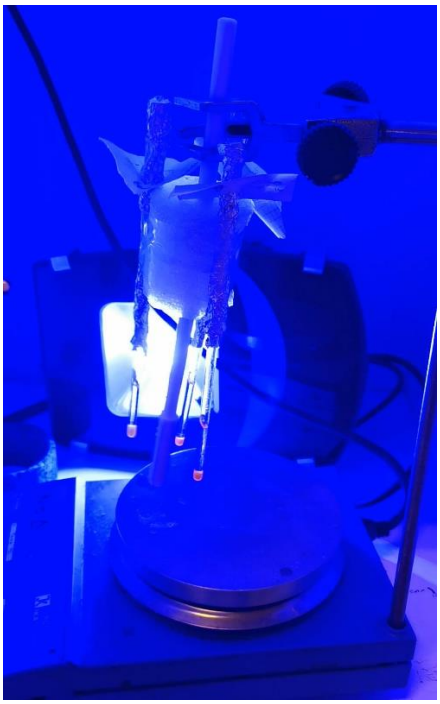

Figure 1.21. Set-up used for the photocatalytic tests.

The results obtained are presented in Figure 1.22 and Table 1.7. All materials exhibit good photoactivity, reaching a maximum conversion slightly lower than the homogeneous tests (~80%) after irradiation times ranging from 16 to 53 hours. The order of reactivity is as follows, from faster to slower: **NP_G** (16 h, 83%) > **NP_IS** (23 h, 79%) ≥ **SiO_2_B** (25 h, 82%) > **SiO_2_OD** (27 h, 80%) > **SiO_2_N** (53 h, 73%). To determine the factors that affect the reaction rate is complex, as different variables can be involved. However, these results suggest a possible synergistic contribution of two factors, the quantum yield of the materials, and the accessibility to the PC molecules, which is related to the surface areas, pore volumes and pore diameters of the materials.

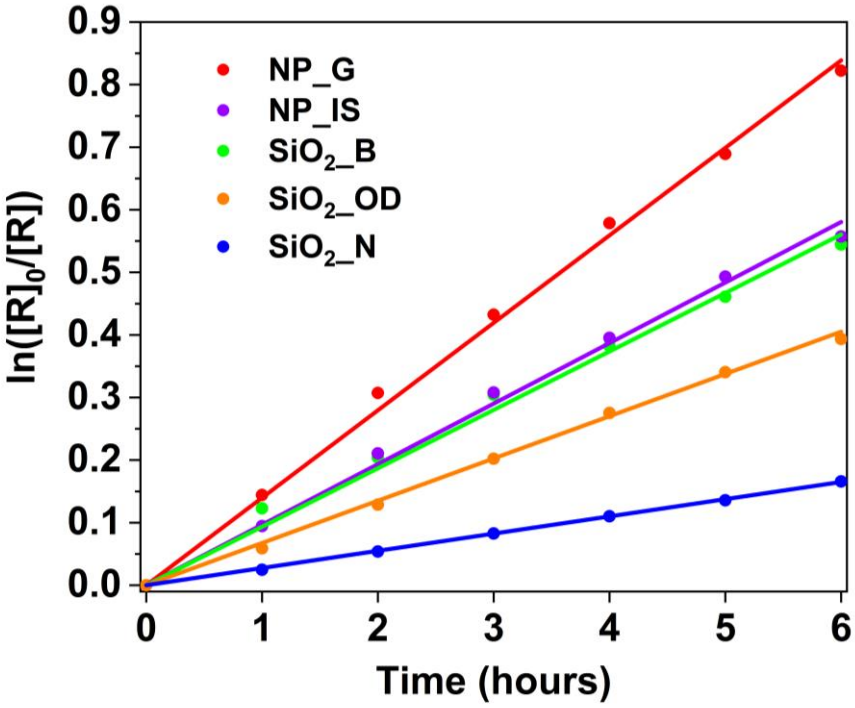

Figure 1.22. Representation of the pseudophotocatalytic constant (k') of the five hybrid materials for the first 6 hours of the reaction.

Table 1.7. Constant values of the photocatalytic activity, regression coefficients, and conversions reached at different times for each photocatalyst.

Photocatalyst	Conversion at 6 h (%)	Maximum conversion (%) / Time (h)	k' (h^{-1})[a)]	R[b)]
SiO_2_B[d)]	50	82 / 25	0.093±0.002	0.9989
SiO_2_N[d)]	20	73 / 53	0.028±0.001	0.9999
SiO_2_OD[d)]	33	80 / 27	0.068±0.001	0.9998
NP_IS[c)]	47	79 / 23	0.097±0.002	0.9992
NP_G[d)]	59	83 / 16	0.140±0.002	0.9994

a) 1st order reaction rate pseudophotocatalytic constant of the reaction of isomerization of *trans*-stilbene into *cis*-stilbene obtained as the average of three runs. b) Regression coefficient. c) *trans*-stilbene:photocatalyst molar ratio = 1:0.02. d) *trans*-stilbene:photocatalyst molar ratio = 1:0.05.

The material with the highest kinetic constant, **NP_G**, also exhibits the highest quantum yield in $CHCl_3$ suspension (ϕ = 46%), and benefits from a better accessibility of the photocatalyst molecules that are covalently grafted on the surface of the nanoparticles.

In addition, a better dispersion in the reaction medium is favored since the morphology of the material consists of discrete nanoparticles.

The next materials showing very high and similar reactivity are **NP_IS** and **SiO$_2$_B**, despite their distinct morphologies ($k'_{NP\_G}/k'_{NP\_IS \text{ or } SiO2\_B} \approx 1.5$, Table 1.7). **SiO$_2$_B** is a disordered gel with a low quantum yield in suspension ($\phi \sim 16\%$) and moderate textural properties. However, its photocatalytic activity and photophysical properties suggest that a significant fraction of complex molecules is retained on the material surface, facilitating interaction with the substrate. On the other hand, **NP_IS** consists of a material formed by discrete nanoparticles in which the chromophore is in a smaller amount (nominal iridium content of 0.2 wt% compared to 1 wt% for the rest of the hybrid catalysts), and is better protected within the silica matrix. However, this seems to be compensated by its high surface area and open porosity (A_{BET} = 1120 m^2/g, V_p = 2.2 cm^3/g), together with a very high quantum yield in suspension (ϕ = 42.6%). In addition, like **NP_G**, the discrete nanoparticle structure allows for improved dispersion in the reaction medium.

Finally, **SiO$_2$_OD** exhibits twice less photoactivity compared to **NP_G** (k'_{NP_G}/k'_{SiO2_OD} = 2.1, Table 1.7), despite having the best textural properties (A_{BET} = 1270 m^2/g, V_p = 2.0 cm^3/g). This can be attributed to a lower quantum yield in suspension (ϕ = 10.4%), and a poor photocatalyst accessibility, as the Ir(III) complex molecules were clustered in the **ODs**. As expected, **SiO$_2$_N**, which has the least favorable combination of textural (A_{BET} = 465 m^2/g, V_p = 0.8 cm^3/g) and emissive properties (ϕ = 12.5%), displays the lowest reactivity among all the hybrid materials (k'_{NP_G}/k'_{SiO2_N} = 5, Table 1.7).

1.4.3 Recyclability of the materials

Finally, a study was conducted to investigate the recyclability of the photocatalyst. To this end, a total of seven catalytic cycles, each lasting six hours, were performed using the same isomerization reaction. Conversion measurements were taken every two hours of irradiation. After each six-hour cycle, the materials were recovered by centrifugation, washed with dry dichloromethane, and then used in the next catalytic cycle (see Experimental Part for details). The results obtained for each material are presented in Figure 1.23.

All materials exhibit high photostability even after seven catalytic cycles, indicating their good recoverability and reusability for this type of photoreaction. The evolution of their photoactivity showed a clear correlation with their corresponding textural properties.

Thus, the materials that show a more pronounced decrease in their photocatalytic activity (~20%) are **NP_G** and **SiO_2_B**, which are also the ones where complex **1** is less protected into the silica matrix. This fact probably leads to a partial lixiviation of the iridium(III) molecules during the reaction or the recovery procedure of the material.

In contrast, **SiO_2_OD** and **NP_IS**, which are the hybrid materials containing the chromophore molecules in a more protected environment, show a smaller decrease in their photoactivity throughout the seven recycling cycles (~10% for **SiO_2_OD**), or even no variation (for **NP_IS**).

Although **SiO_2_N** displays the least photocatalytic activity, it exhibits a consistent increase with each catalytic cycle (~28% in total), which seems to indicate that the photocatalyst molecules gradually become more exposed to the medium with use. However, despite showing the greatest increase in activity in percentage terms, its overall reactivity remains relatively low compared to the other materials.

It is also worth mentioning that no signals corresponding to free complex **1** were detected by ^{1}H-NMR in any catalytic cycle for all the hybrid materials.

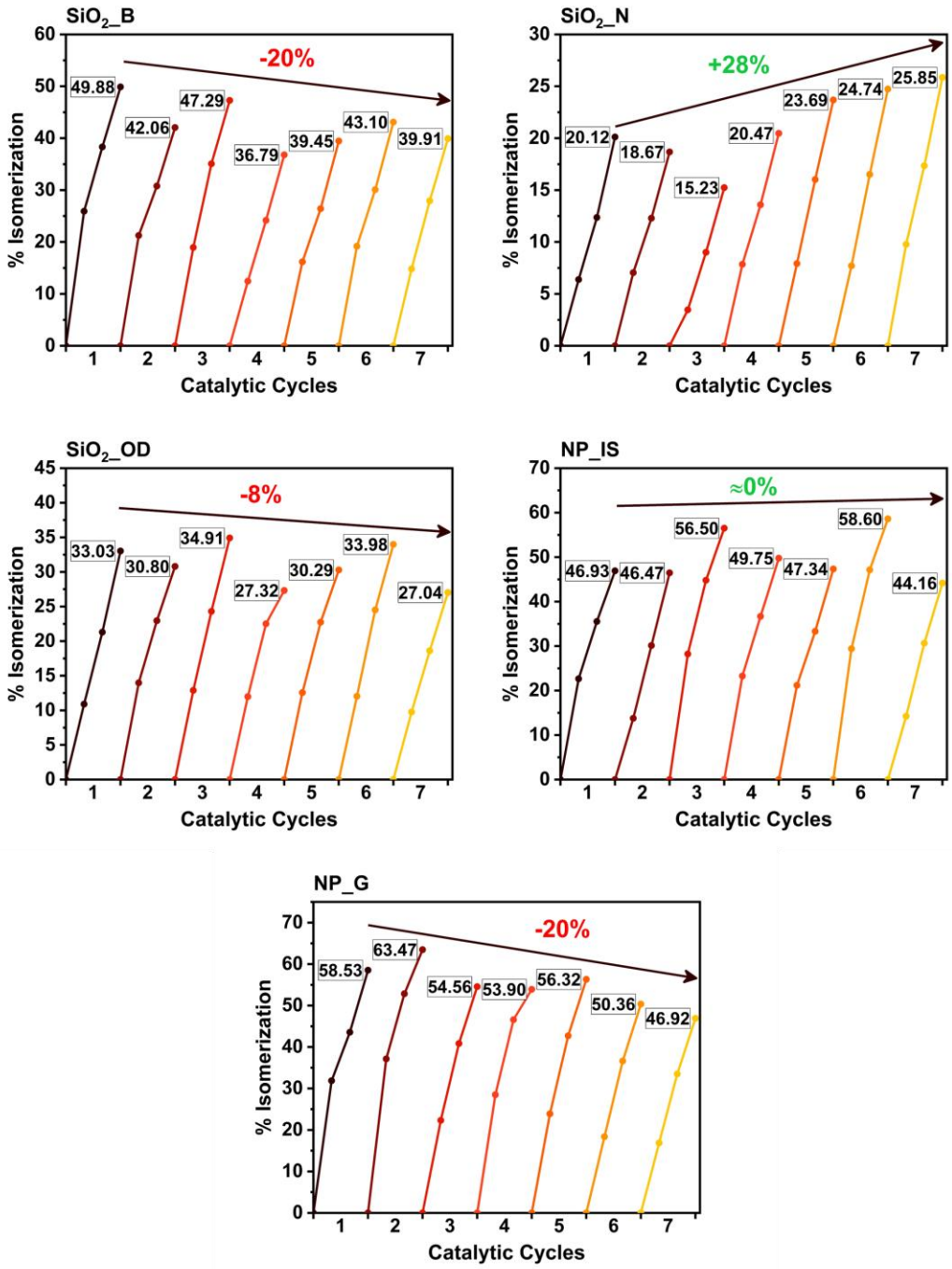

Figure 1.23. Isomerization results and evolution of the photocatalytic activity obtained after 6 h of irradiation for the hybrid materials during each of the seven catalytic cycles. Experiments were carried out under identical conditions.

After completing the recyclability studies, the two samples that exhibited the best catalytic performance (**NP_IS** and **NP_G**) were selected to evaluate their photophysical properties and compare them with their initial values. These materials serve also as archetypal examples of both *in-situ* and post-synthetic functionalization methods,

respectively. As shown in Figure 1.24 and Table 1.8, after undergoing seven catalytic cycles both materials exhibit similar emission profiles. The most notable differences are the reduction in quantum yield, which is more pronounced in the case of the grafted nanoparticles (20% for **NP_IS** vs. 30% for **NP_G**), and a slight bathochromic shift of the emission maximum for **NP_G**.

Table 1.8. Comparison of the photophysical data in $CHCl_3$ suspension (1 mg/ml) for the hybrid organometallo-silica materials **NP_IS** and **NP_G** before and after seven catalytic cycles of six hours each. All data at Room Temperature.

Sample	λ_{em}/ nm	τ/μs	ϕ/%
NP_IS	550	1.10	42.6
NP_IS after photocatalysis	552	0.77	33.0
NP_G	550	0.97	46.0
NP_G after photocatalysis	570	0.57	32.2

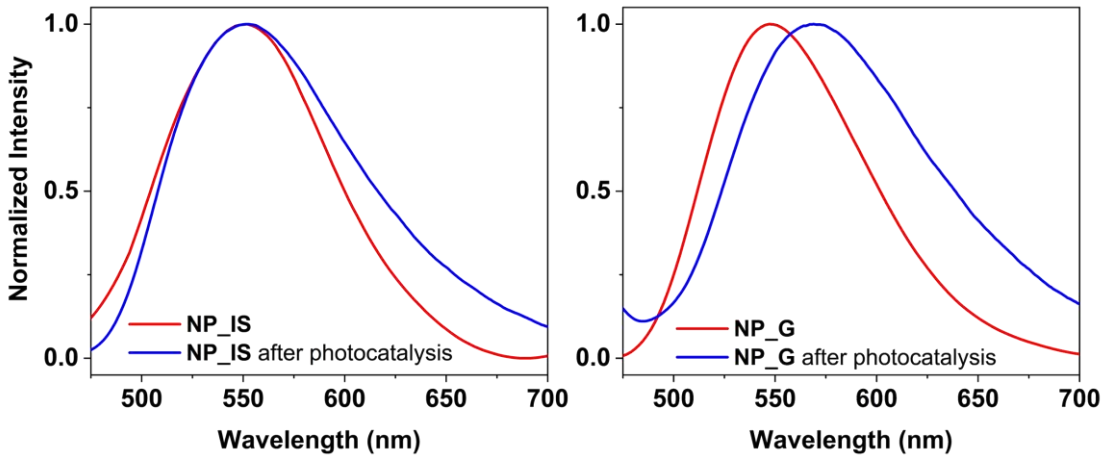

Figure 1.24. Normalized emission (λ_{exc} = 365 nm) spectra in $CHCl_3$ suspension (1 mg/ml) at RT for the hybrid organometallo-silica materials **NP_IS** (left) and **NP_G** (right) before and after seven catalytic cycles of six hours each.

Chapter 2. Heterogeneous photoredox reactions and recyclability of an iridium(III) ionosilica

2.1 Introduction

Chapter 1 is devoted to the description of several silica-based hybrid materials functionalized with the emissive iridium(III) complex [Ir(dfppy)$_2$(*dasipy*)]PF_6 (**1**), which have shown excellent photocatalytic activity for energy transfer reactions. However, when electron transfer reactions were attempted with these materials, the results were less promising. Among the five materials studied, it was observed that the deeper the chromophore **1** molecules were embedded in the silica matrix, the lower the photocatalytic performance. In fact, the four materials synthesized by *in-situ* techniques showed little or no photocatalytic activity for the photocatalytic production of phenanthridines from acyloximes, a reaction that proceeds through an oxidative quenching mechanism (Scheme 2.1). The only exception was the nanoparticles grafted with the complex, **NP_G**, which displayed some activity, obtaining a reactant:product ratio of 4:1 after 90 hours of irradiation. This is due not only to the improved exposure of the photocatalyst to the medium, which allows closer interaction with the substrate, but also to the fact that the silica used as a substrate acts as an insulator, preventing electronic transfer between the chromophore and the substrate.[59]

In light of these findings, we decided to synthesize a heterogeneous material that would exclude silica as a support for the complex. This new material, composed entirely of complex molecules co-condensed together, can be categorized as a novel variety of organometallic ionosilica. The term "ionosilica" was originally introduced by Hesemann in 2013 to describe materials resulting from the covalent bonding of ionic molecules through Si-O-Si bonds, ultimately forming a neutral material (Scheme 2.2).[60]

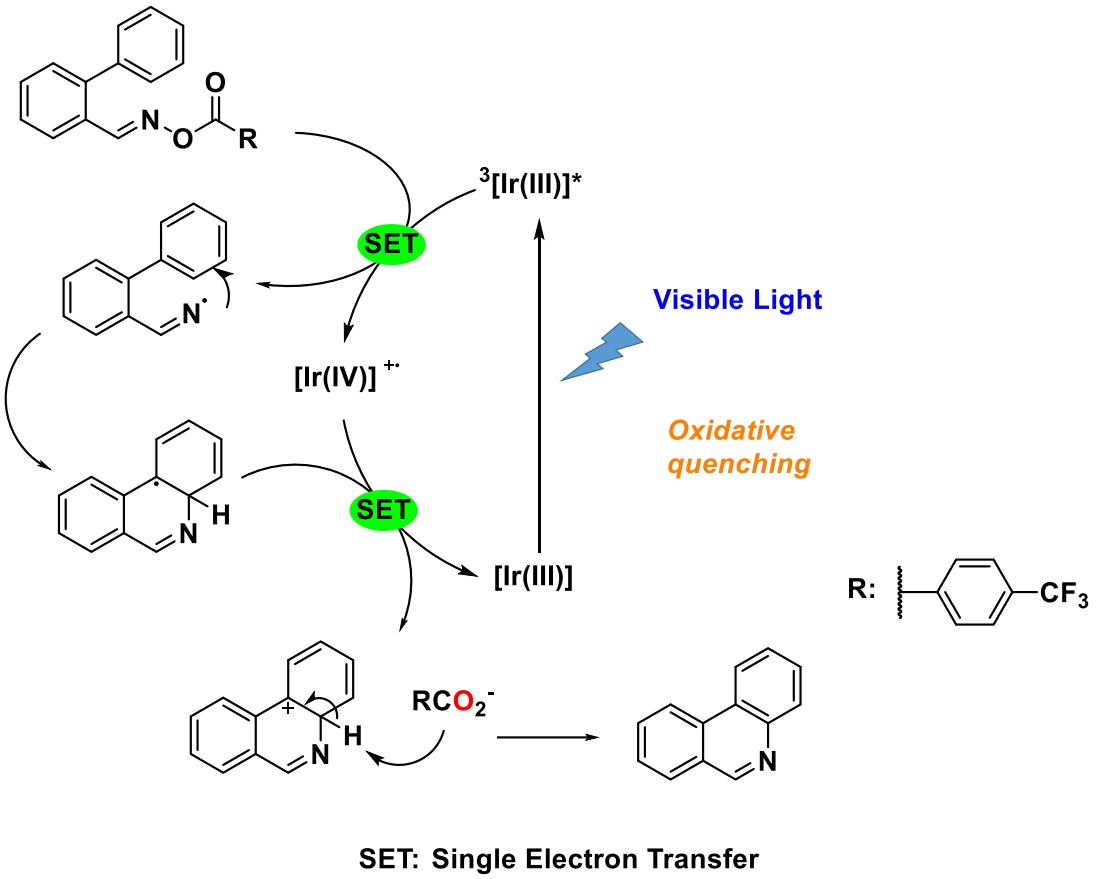

Scheme 2.1. Mechanism of the photocatalytic synthesis of phenanthridine.

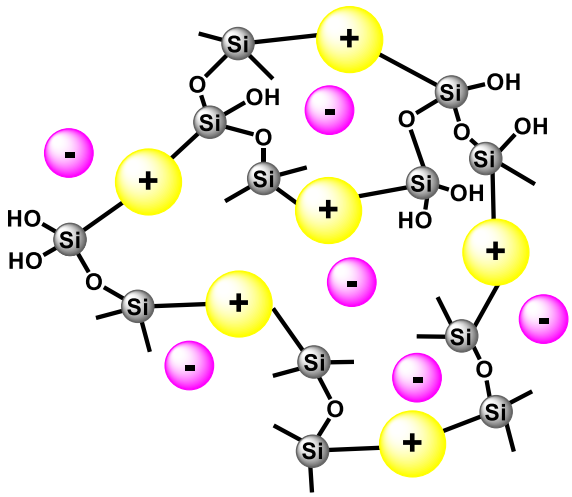

Scheme 2.2. Schematic representation of an ionosilica.

The synthesis and properties of these materials resemble those of Periodic Mesoporous Organosilicas (PMOs), which are usually obtained by hydrolysis-polycondensation reactions involving organic groups functionalized with trialcoxysilane moieties; often

with the addition of a silica precursor such as TEOS to the medium in varying proportions.[61] This process results in hybrid materials with very different compositions and structures.[62] Using this synthetic approach, it is possible to obtain PMOs with high mesoporosity and functionalization, in which the organic groups are integral constituents of the structure of the material, conferring specific physicochemical properties.

On the other hand, Hesemann et al. introduced a synthetic method that combines anionic surfactants with cationic organic molecules such as quaternary ammonium or imidazolium, to incorporate highly ionic functionalization in the core of the materials.[60, 63] This method opens the door to the successful use of anionic surfactants in obtaining ionosilicas with structures similar to those observed in PMOs. This is achieved through the formation of precursor-surfactant ion pairs in the reaction mixture, serving as growth control agents.[64] In addition, the stronger the interaction between surfactant and precursor, the higher the order of the resulting materials. Figure 2.1 illustrates some of the precursors used by Hesemann's group, along with an example of the synthesis of an ionosilica.[65]

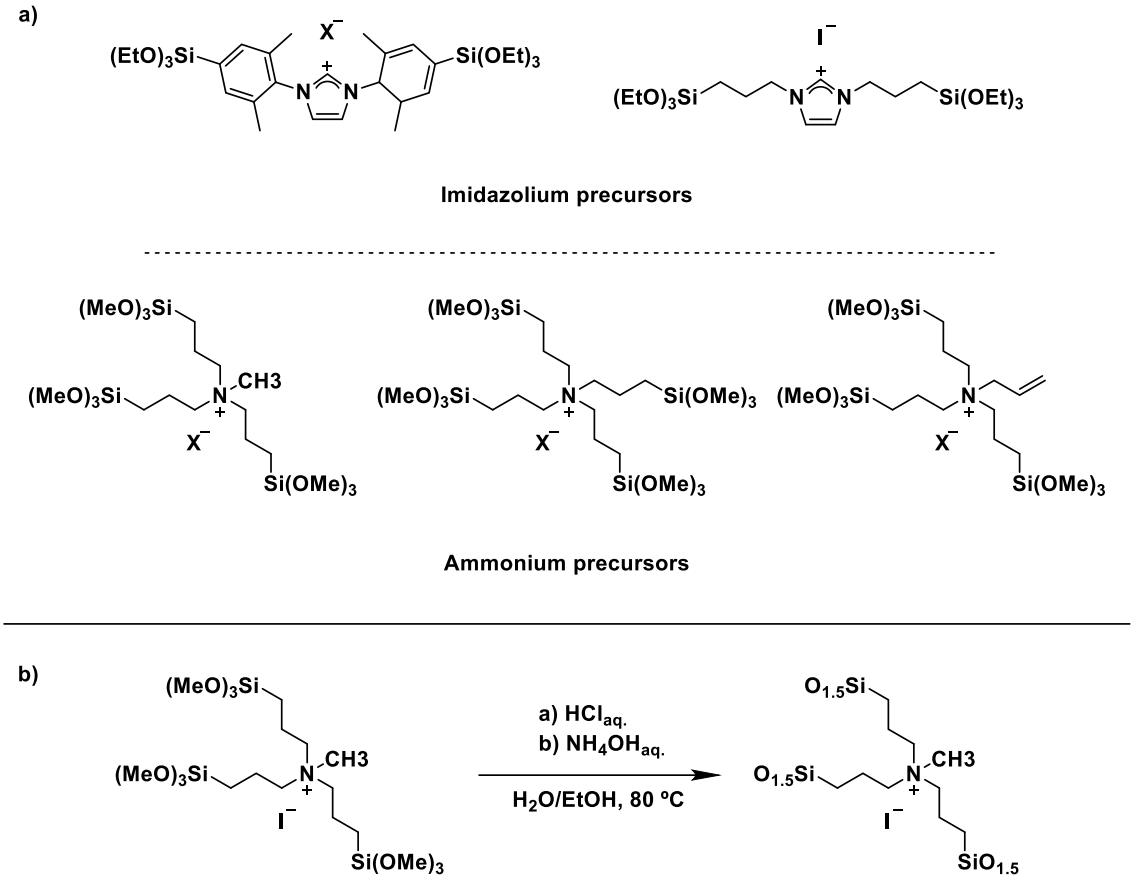

Figure 2.1. a) Examples of ionosilica precursors; b) Synthesis of an ionosilica.

The use of ionic precursors during synthesis leads to the homogeneous distribution of a multitude of ionic species within the matrix of the material. In fact, according to the definition of these ionosilicas, the silylated cation groups form bonds with each other, while the anions remain mobile within the structure. This makes them very versatile materials, positioning them at the interface between ionic liquids and hybrid silica, and giving them unique properties attributable to their ionic nature.[66] These materials have been studied for applications in areas such as catalysis, separation and purification, energy storage and heat release, or photodynamic therapy and drug carrier.[67]

Although much of the research about ionosilicas has focused on those synthesized with organic cationic groups, there are also some examples of these materials incorporating metals into their structure by post-synthetic methods. One noteworthy example in the literature include the use of chlorometalates in functionalized silica materials featuring imidazolium halide groups. Examples of this type can be found since the early 2000s, when Hölderich et al. successfully incorporated chloroaluminates using this methodology.[68] Later examples include the use of metal salts such as $InCl_3$, $FeCl_2$, $CuCl_2$, and $AuCl_3$ (Scheme 2.3), which have been used for catalytic applications.[69] However, they present serious leaching problems of the metals in solution, and generally the imidazolium groups are grafted onto the surface of other silica materials.

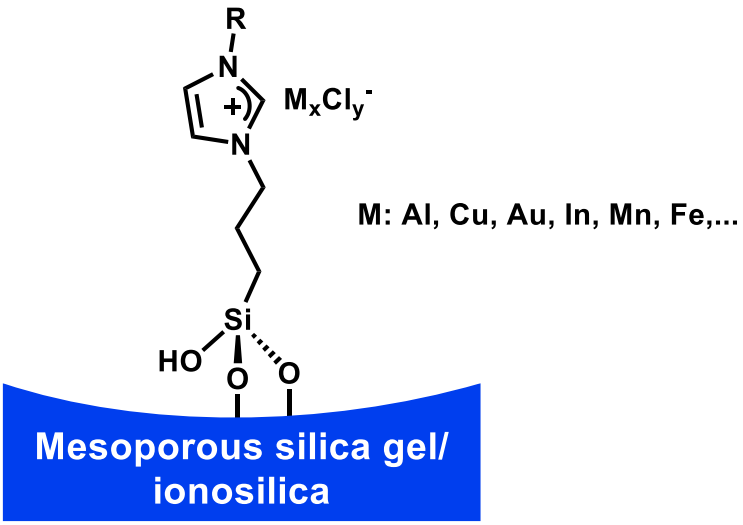

Scheme 2.3. Functionalized silica materials with imidazolium and chlorometalates.

Indeed, a number of examples of covalent integration of cationic coordination complexes of transition metals, such as Re(I), Ru(II), Ir(III) or Pt(II), into silica matrices have been described. These cases mainly involve post-synthetic grafting,[39a, 43a, 70]

although there are several examples of *in-situ* preparations.[43f, 71] However, to our knowledge, there has been no attempt to synthetize an ionosilica composed exclusively of covalently bonded ionic coordination molecules; resembling an organometallic polymer in which the monomers themselves are the complex molecules. Nevertheless, related self-condensed neutral Zn(II) porphyrin or phthalocyanine based-materials have been reported.[72] On the other hand, Metal-Organic Frameworks (MOFs) and Covalent Organic Frameworks (COFs) serve as examples of porous materials that can incorporate transition metal complexes bond by covalent bonds.[24b, 73] However, their intricate spatial arrangements and employment of secondary building units make them an entirely separate class of materials. Their synthesis is often more complex, and the resulting crystalline materials cannot be considered polymers. Furthermore, the different units within their structure are typically connected using covalent bonds that are not Si-O-Si bonds. Instead, other types of bonds are employed, such as imine groups, formed by the condensation of an aldehyde with an amine, boron condensation from the dehydration between boronic acids, and various other strategies.[74]

The introduction of Chapter 1 discussed the synthetic power and applications of energy transfer reactions. However, there is a growing interest in developing materials that are active in both energy transfer and electron transfer reactions. This is of significant synthetic interest, as the latter are an extremely versatile tool for achieving chemical reactions that are inaccessible by traditional methods. For example, Scheme 2.4 shows several molecules of interest to the pharmaceutical and agrochemical industries, where the use of photoredox catalysis is a key step in their synthesis.[14b] In addition, industry interest in the implementation of photoredox catalysis has increased due to its potential for continuous flow operation, which allows more uniform light penetration and efficient photocatalyst excitation compared to batch reactions.[75] The continuous flow process also enables the reactions to be scaled up for industrial production, reducing labor risks and industrial waste streams.[76]

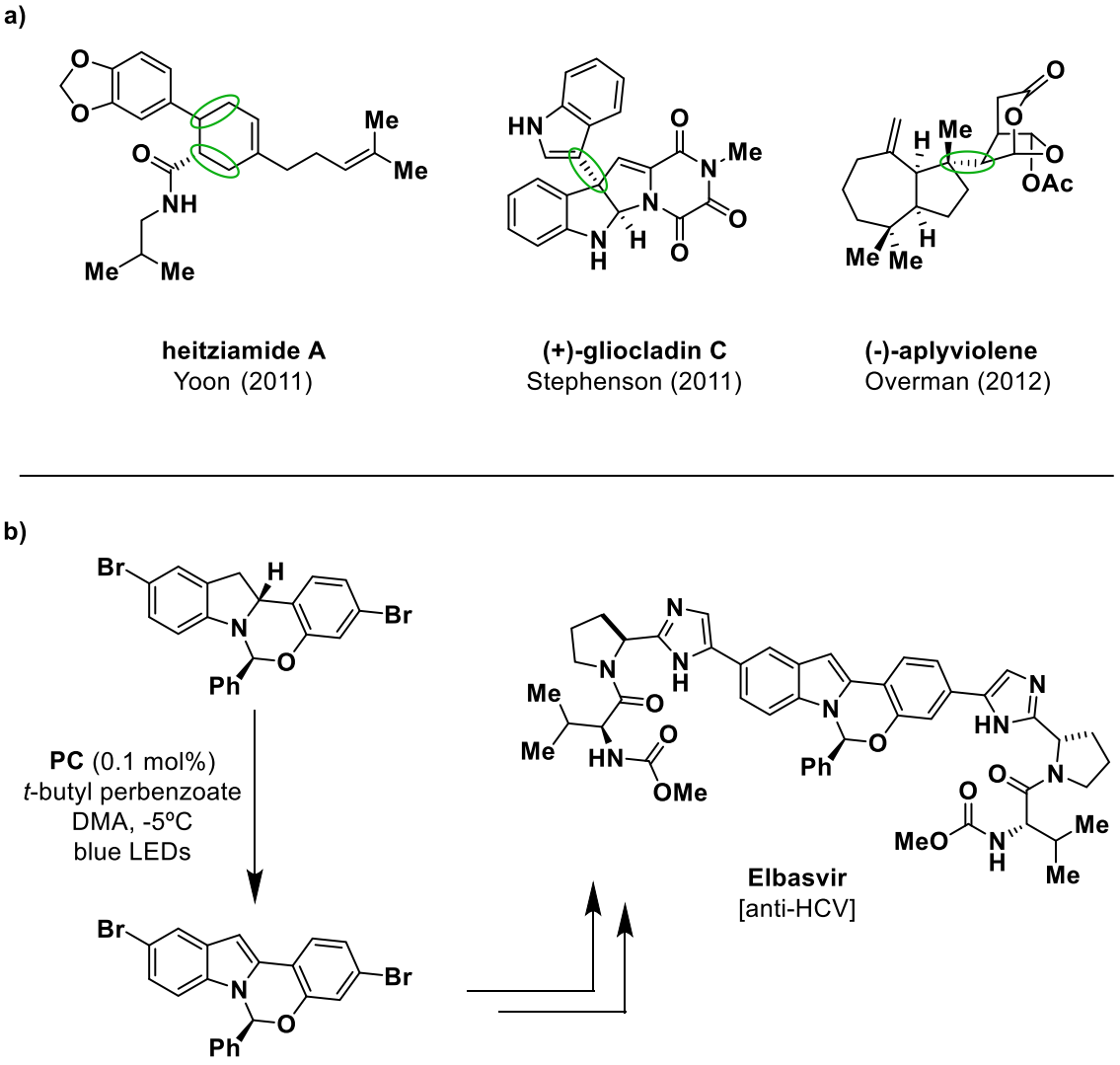

Scheme 2.4. Examples of application of photoredox catalysis in total synthesis: a) Several examples of natural products with a key photoredox catalysis step; b) Photocatalytic indoline dehydrogenation as a key step in the sustainable synthesis of Elbasvir.

The significant progress made in photoredox catalysis is mainly attributed to the advances of radical chemistry in chemical synthesis.[77] The generation of radicals by irradiation allows the activation of typically unreactive moieties of the molecules, such as C-H bonds, while also demonstrating considerable tolerance and compatibility with other functional groups within the molecule or reagents present in the medium.[78] Furthermore, unlike other ionic processes, the use of protective groups is not usually required. Additionally, it permits reactivity on highly substituted groups, including quaternary centers, making it attractive for natural product synthesis. The conversions

achieved with radical chemistry are not restricted to the familiar cyclizations; intermolecular additions, homolytic substitutions, and C-H functionalizations are also attainable.[14a, 19a] Moreover, in recent years enantioselective reactions have also been conducted via radical mechanisms, by combining enantioselective polar organocatalysis with excited-state reactivity and radical chemistry.[79]

Although there are numerous methods for producing radicals, the cleavage of a carbon-halogen bond (C-X) is a well-studied and versatile approach, primarily because of the relatively ease of breaking this bond in a wide variety of substrates.[80] However, while dehalogenations may be achieved through conventional procedures such as metal-halogen exchange,[81] stochiometric tin hydride,[82] or the utilization of other highly toxic reagents,[83] photoreductive catalysis has emerged as a highly effective and sustainable method for generating these radicals.[84] One of the earliest reactions found in literature on photocatalytic reductive dehalogenation is Fukuzumi's 1990 paper,[85] which describes the reduction of phenacyl bromides using visible light, $[Ru(bpy)_3]^{2+}$ as the photocatalyst, and 9,10-dihydro-10-methylacridine as the stoichiometric reductant. In this example, the reaction undergoes a reductive quenching mechanism, as depicted in Scheme 2.5.[18c] This straightforward and well-known reaction can achieve high yields in relatively short irradiation times, and is easily monitored by ^{1}H-NMR spectroscopy. Due to these factors, many research groups have adopted this reaction as a standard test of the efficiency of various photocatalysts under both homogeneous and heterogeneous conditions.[86] As such, it serves as one of the two reactions utilized in this chapter to evaluate the photocatalytic activity and recyclability of the new ionosilica material obtained.

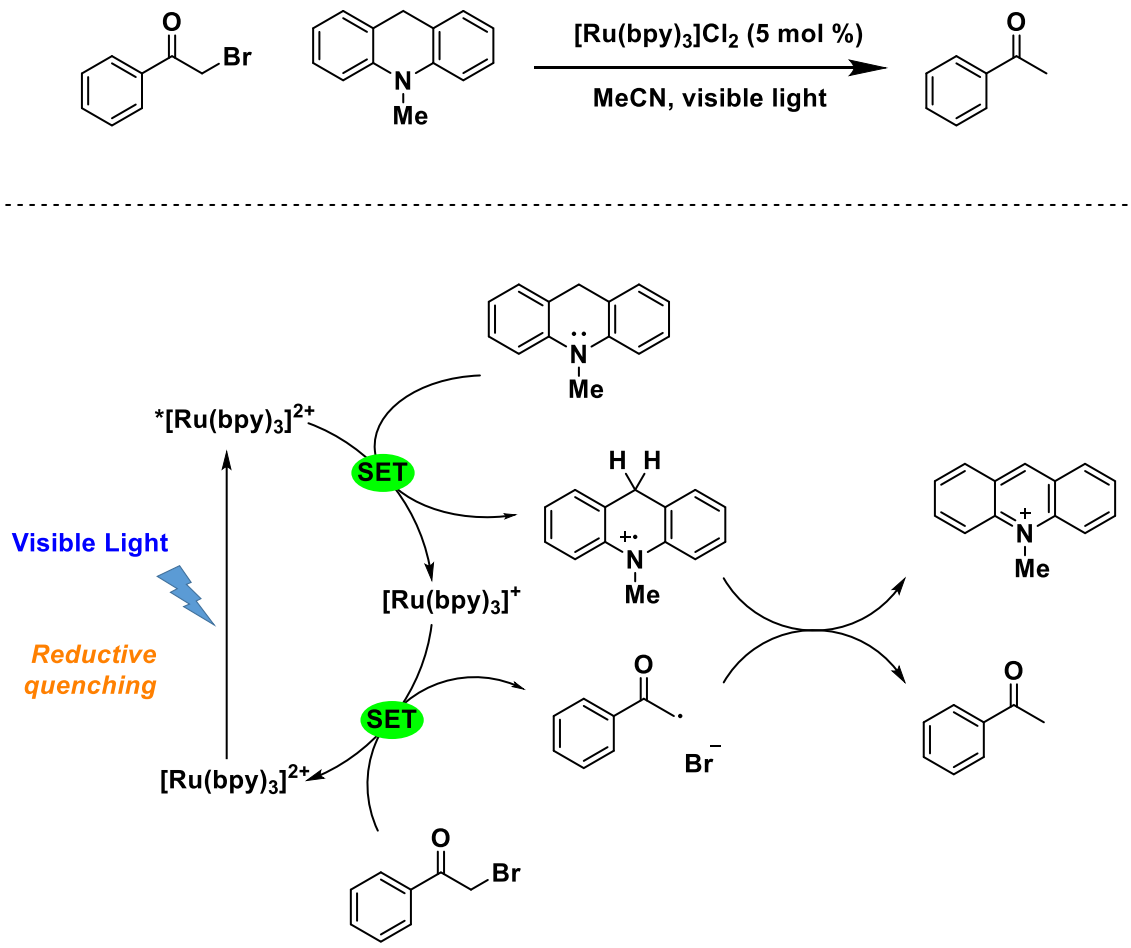

Scheme 2.5. First reported photocatalytic dehalogenation of 2-bromoacetophenone.

The other selected reaction involves obtaining phenanthridines from acyloximes by an oxidative quenching mechanism as described at the beginning of this introduction (Scheme 2.1). Phenanthridine derivatives are of considerable biological interest due to their antibacterial,[87] antifungal,[88] antiviral,[89] or anticancer activity,[90] like other molecules bearing *N*-heterocycles.[91] Not surprisingly, these compounds are present in pharmaceutical drugs and natural products, including trisphaeridine, nitidine, sanguinarine, and chelerythrine, among others (Figure 2.2).[92]

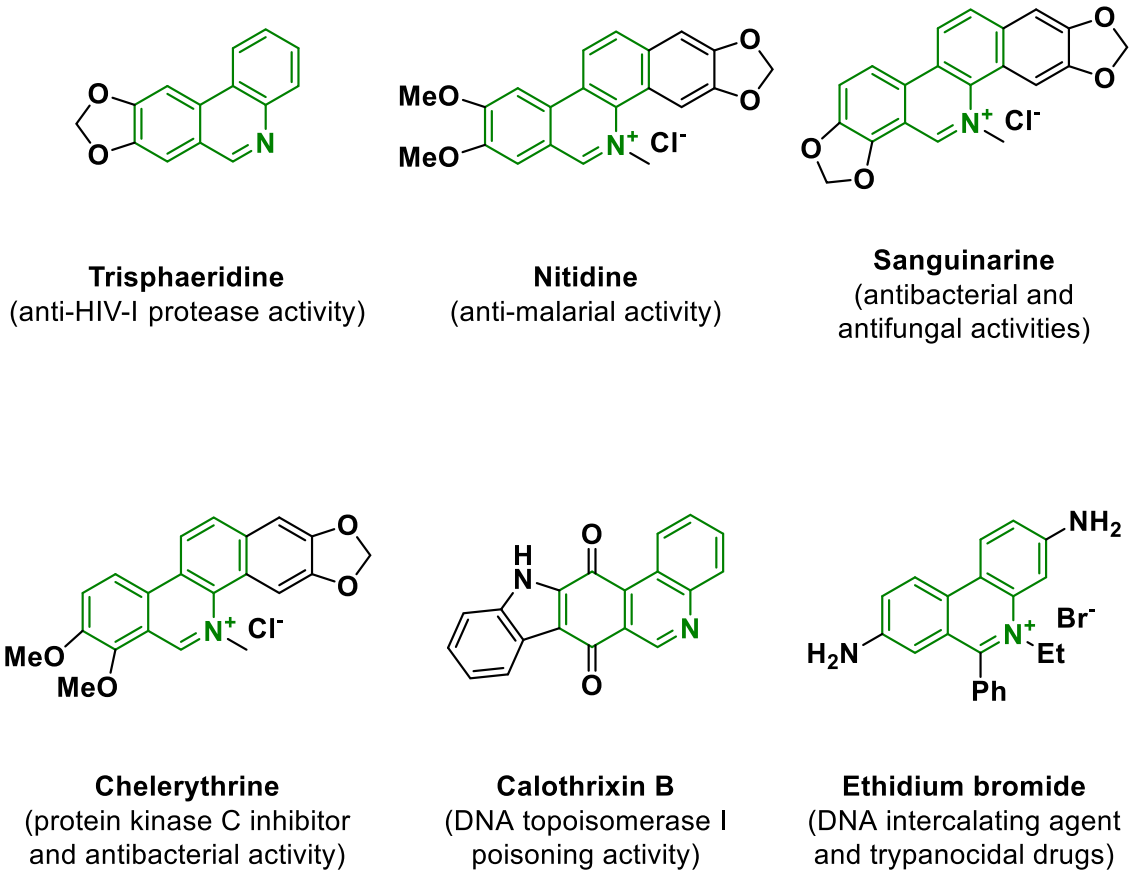

Figure 2.2. Examples of biologically active phenanthridine derivatives.

The synthesis of these derivatives typically involves multistep synthetic routes that require numerous reaction sequences and severe conditions.[93] Nevertheless, due to the ease of breaking the N-O bond in acyloximes, it is possible to obtain radicals centered on the nitrogen atom that promote intramolecular cyclization and N-C bond formation.[14c] To our knowledge, our group was the first to report the synthesis of phenanthridine derivatives using photochemical methods with ultraviolet light in 2006, by means of this strategy.[94] Additionally, our group synthesized precursors of natural derivatives including this reaction in their synthetic pathway.[95] In 2015, Yu and coworkers published this same reaction via a single electron transfer process using the photocatalyst [Ir(ppy)$_3$] under visible light and obtaining the same iminyl radical (Scheme 2.6).[96]

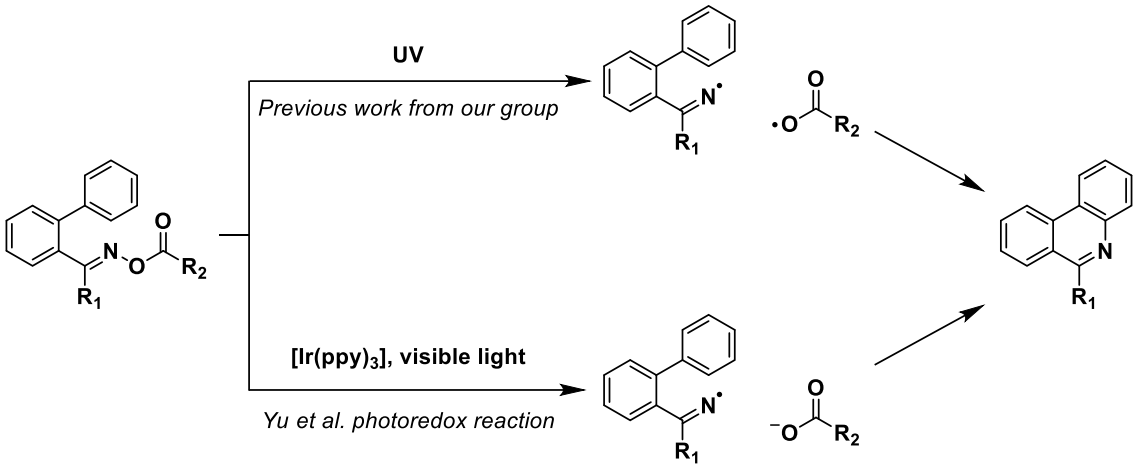

Scheme 2.6. Photochemical N-O cleavage of acyloximes to form phenanthridines.

Given the biological significance of phenanthridine derivatives and our previous experience with these systems, we decided to use this reaction for the recyclability tests of our material in an oxidative quenching mechanism, as it can also be monitored by NMR spectroscopy.

In summary, this chapter describes the preparation of an ionosilica synthetized by co-condensation reactions of the complex **1** $[Ir(dfppy)_2(dasipy)]PF_6$ used in chapter 1. The photocatalytic activity of the material will be compared with that of the complex under homogeneous conditions in two different single electron transfer (SET) photocatalytic reactions; a reductive quenching mechanism (dehalogenation of 2-bromoacetophenone) and an oxidative quenching mechanism (formation of phenanthridines).

2.2 Synthesis and characterization of the ionosilica material

2.2.1 Synthesis

The synthesis strategy of the ionosilica **SC-1** is again based on sol-gel chemistry, where the formation of intermolecular bonds mainly involves the hydrolysis and condensation of the triethoxisylane groups of complex **1**, forming Si-O-Si bonds. To achieve this, complex **1** is dissolved in a minimal volume of ethanol and gradually added to water under vigorous stirring, ensuring a uniform dispersion of the complex within the medium. To further improve homogeneity, the mixture is stirred at room temperature for 1 hour. Next, 0.7 ml of a 0.05 M aqueous solution of NaF is added as a catalyst for the hydrolysis reaction between the triethoxysilane groups. The reaction mixture is set at 80ºC and stirred continuously for a total of 4 days (96 hours). After this period, the formation of an insoluble yellow solid is observed, which can be recovered from the medium by centrifugation. The resulting material is washed once with distilled water and twice with ethanol. Finally, the solid is air dried at room temperature and subsequently ground to obtain **SC-1** as fine yellow powder.

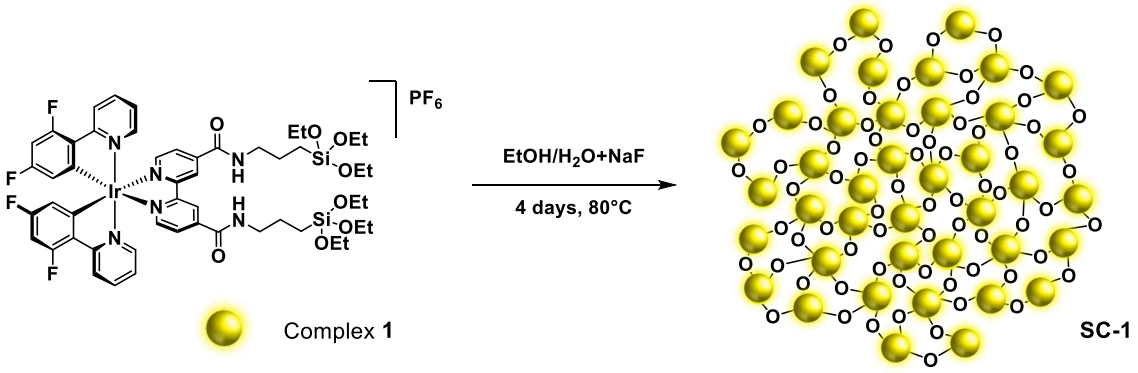

Scheme 2.7. Schematic representation of the synthesis of the new ionosilica (**SC-1**).

The residual waters from the different washing steps showed a very weak yellow coloration and luminescence, indicating that a significant portion of the complex used in the synthesis has condensed within the material. This observation was also supported by the calculated yield obtained in this reaction (74%). In addition, the complex present in the residual water can be recovered and reused in a subsequent self-condensation reaction.

2.2.2 Characterization

Chemical characterization of the material was performed using IR spectroscopy, mass spectrometry, and elemental analysis.

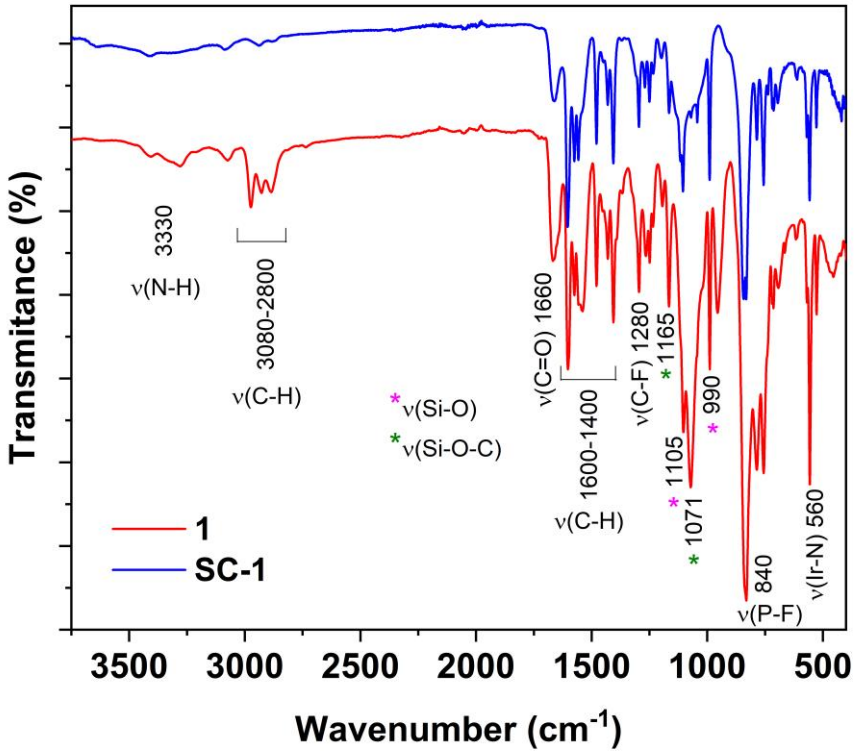

Figure 2.3. FTIR spectra of the material **SC-1** in comparison with the spectrum of the pure complex **1**.

The FTIR spectra exhibit similar bands for both complex **1** and the material **SC-1** (Figure 2.3). In the high energy region, both spectra show bands corresponding to the ν(C-H) vibration of the aromatic (>3000 cm^{-1}) and aliphatic (<3000 cm^{-1}) groups although with lower intensity in the **SC-1** spectrum. Above 3300 cm^{-1}, a low intensity band appears, due to the vibration of the amidic N-H bond of the *dasipy* ligand, together with the characteristic band of the C=O bond at 1660 cm^{-1}. In the range of 1600-1400 cm^{-1}, signals corresponding to the C-H bond tension of the aromatic groups can be observed. Other significant bands include one intense narrow absorption at ca. 560 nm, assigned to the Ir-N bond, and a very strong band at 840 cm^{-1}, corresponding to the vibration of the P-F bond of the PF_6^- anion. In fact, the presence of this absorption in the **SC-1** spectrum agrees with the preservation of the counter-anion within the structure

of the material, confirming its ionic nature. Furthermore, the fact that both spectra have the same signal fingerprint indicates that the molecular structure of the complex is preserved during the self-condensation reaction.

In addition to the characteristic bands of Si-O bonds, the spectrum of **SC-1** also shows absorptions corresponding to Si-O-C bonds, although in the latter case the intensity is much lower than in the spectrum of **1**. Particularly noteworthy is the case of the very intense band at 1071 cm^{-1} in the spectrum of complex **1**, which is observed as a weak absorption for **SC-1**. This fact suggests that although the self-condensation reaction is largely complete, reducing the number of Si-O-C bonds, unreacted ethoxysilane groups remain in the final material structure.

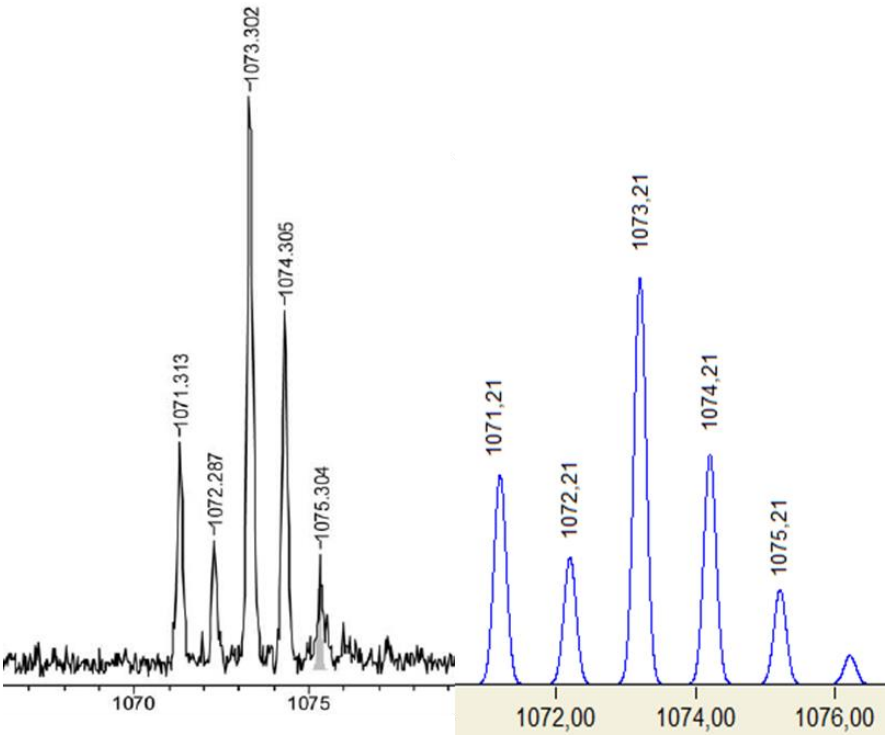

Figure 2.4. Mass spectrum of **SC-1** (left) and simulated isotopic distribution (right).

Regarding the mass spectrum of **SC-1**, due to the complexity of the sol-gel reaction and the likelihood of varying degrees of Si-O-Si bond formation among the complex molecules, assigning peaks from the material fragmentation is challenging. The observed peaks likely correspond to fragments that are more easily ionized. Specifically, the mass spectrum shows a signal at $^{m}/_{z}$ 1073 (Figure 2.4, left), which is consistent with the molecular mass of the structure shown in Figure 2.5. Its isotopic distribution is also

consistent with calculations using the *Molecular Weight Calculator* program (Figure 2.4, right). This structure can be considered as an average molecular model of how the complex is generally distributed throughout the material. This representation shows that for each complex molecule, four of the triethoxysilane groups have hydrolyzed to form Si-O-Si bonds with other complex molecules, while two groups remain unreacted. This agrees with the findings from the infrared spectra. The empirical formula of the proposed model is $C_{44}H_{42}F_{10}IrN_6O_6PSi_2$, which also aligns with the elemental analyses conducted on this material (see Experimental Part for additional information). Other signals in the positive MALDI spectrum have been assigned but are not discussed here as they do not provide further information about its composition. However, it is worth noting the presence of a single signal at $^{m}/_{z}$ 144.6 in the negative MALDI spectrum, corresponding to the PF_6^- counter-anion.

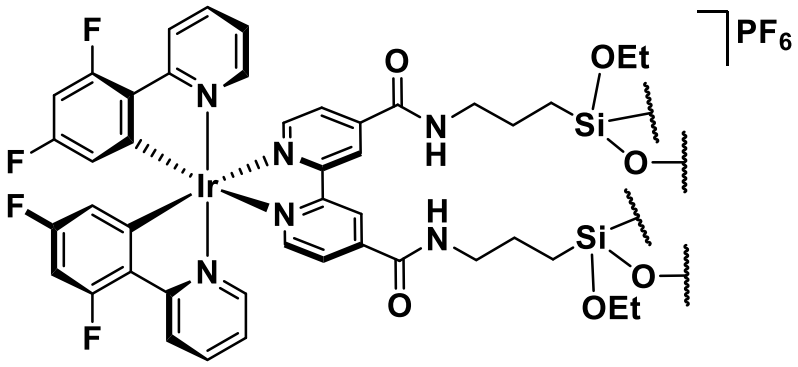

Figure 2.5. Proposed molecular structure of complex **1** in **SC-1**.

2.2.3 Textural properties

The textural characterization of the ionosilica was carried out using different techniques, including nitrogen adsorption/desorption isotherms at 77 K, Powder X-Ray Diffraction (PXRD), Transmission Electron Microscopy (TEM) and Field Emission Scanning Electron Microscopy with Energy Dispersive X-Ray Spectroscopy (FESEM-EDX). All the experiments were carried out at the University of Alicante, within the Laboratory of Molecular Nanotechnology group under the supervision of Prof. Javier García Martínez and Dr. Elena Serrano.

Figure 2.6 shows the nitrogen adsorption/desorption isotherms at 77 K (left) and the corresponding pore size distribution (right). As expected, a type II isotherm is observed due to the absence of surfactants in the synthesis process. This isotherm is characteristic of non-porous materials in which the adsorption of the nitrogen occurs at low values of the relative pressure P/P_0. Analysis of the textural data from the isotherm reveals a small surface area of 28 m^2/g, with no porosity (pore volume 0.03 cm^3/g).

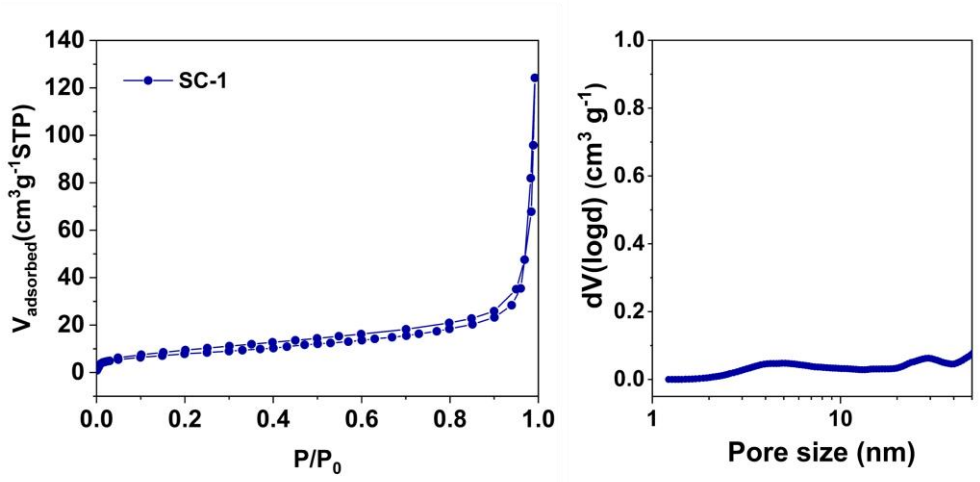

Figure 2.6. N_2 adsorption/desorption isotherms at 77 K (left) and the corresponding pore size distribution calculated using the NLDFT method (right) of **SC-1**.

Surprisingly, the TEM images show that the material consists of discrete spherical particles with a wide range of particle diameters, from 30 nm to 220 nm (Figure 2.7). The formation of these spherical structures is striking despite the absence of surfactants and structure-directing agents in the synthesis, as it was initially expected that an unstructured material would be obtained. A plausible explanation is that, since the complex is insoluble in water and is initially added dissolved in ethanol, micelles of different sizes may form

in the reaction medium. As the reaction proceeds over an extended period of time (4 days) under constant temperature and stirring conditions, uniform particle growth occurs, resulting in the formation of these spherical structures, the shape also being driven by surface energy. However, it is worth noting that the absence of surfactants is evident in the wide range of particle diameters observed.

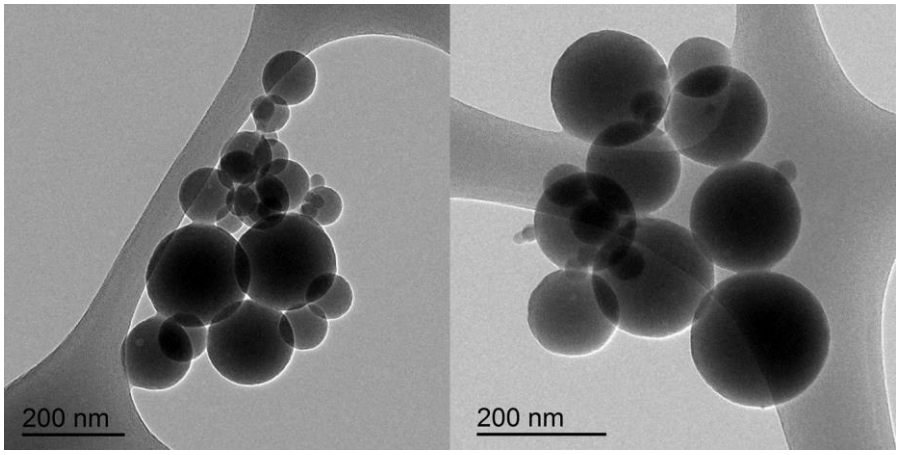

Figure 2.7. Representative TEM images of **SC-1**.

The X-ray powder diffraction spectrum confirms the absence of crystallinity in the structure, showing a pattern typical of an amorphous solid (Figure 2.8), with broad diffuse peak maxima at 2θ *ca*. 10º, 21º and 40º. These features are thought to be related to short-range ordering caused by the interactions between the Ir complex molecules. However, it should also be noted that XRD patterns of amorphous silica based materials usually show a broad peak at 2θ = 21º.[97]

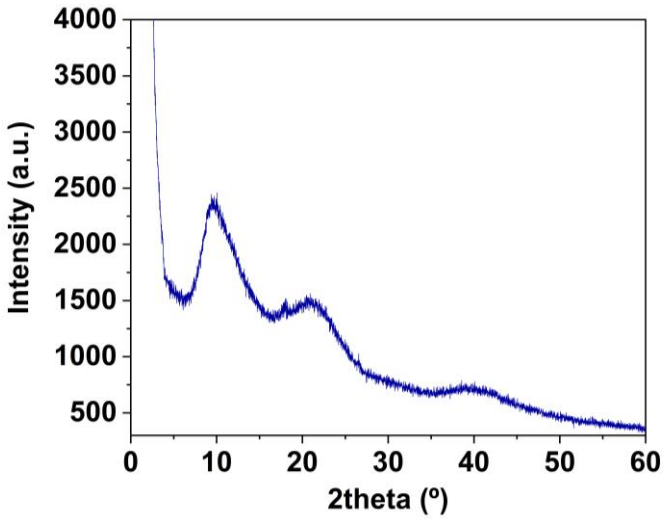

Figure 2.8. Powder X-Ray spectrum of **SC-1**.

Finally, Figure 2.9 shows the results or the FESEM-EDX analysis, where the same spherical shape of the particles can be observed. The elemental mapping for iridium, phosphorous and silicon atoms shows a homogeneous distribution of the three elements over the surface of the material. Therefore, **SC-1** appears to maintain a consistent composition throughout its structure. It is also noteworthy that phosphorous atoms are found exclusively in the counter-anion of the complex (PF_6^-). This, together with the results from the infrared spectrum and negative MALDI experiments, suggests that the counter-anion is a constituent of the material, probably located both on the surface and within the material to maintain ionic neutrality.

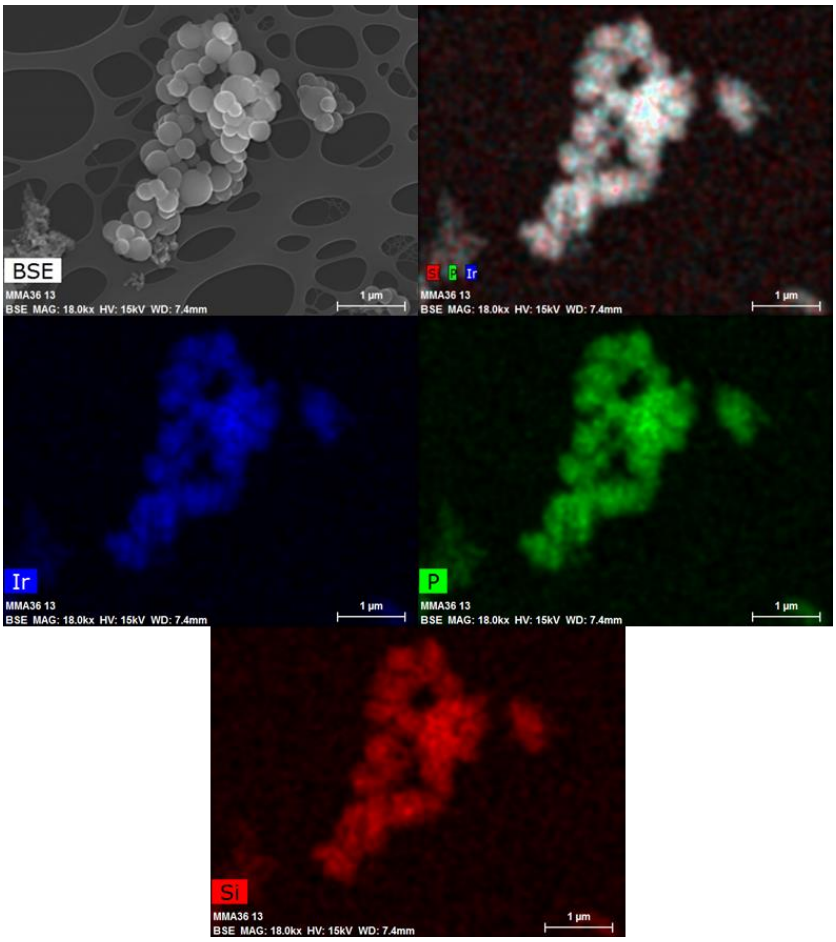

Figure 2.9. EDX analysis mapping in FESEM for **SC-1**.

In summary, this material is composed of cationic complex molecules linked by Si-O-Si bonds, with the counter-anion integrated into the structure through ionic interactions, forming an amorphous material consisting of discrete particles with varying diameters. As a result, this material can be classified as a new class of organometallic hybrid ionosilica.

2.2.4 Photophysical properties

Figure 2.10 and Table 2.1 show the solid-state absorption spectrum and associated data of material **SC-1**, together with the data of complex **1** in both solid state and THF solution (already commented on Chapter 1) for better comparison. As observed, the spectrum of the material is very similar to the spectra of complex **1**, both in solution and in the solid state. This again supports the idea that the molecules of the complex retain their structure after the material is formed. Thus, all the spectra show the high energy absorptions due to spin-allowed intraligand π-π* transitions (below 300 nm) or ^{1}IL/^{1}LL'CT contributions (300-320 nm), together with the combination of metal-to-ligand and ligand-to-ligand charge transfers (^{1}ML'CT/^{1}LL'CT) between 340 and 400 nm. Finally, weaker low-energy features typically associated with spin-forbidden ^{3}ML'CT (d(Ir) →$\pi^*_{N^N}$) and ^{3}LL'CT (π_{C^N} →$\pi^*_{N^N}$) transitions (400-500 nm) are also observed.

In particular, the shape of the spectrum of **SC-1** more closely resembles that of the THF spectrum of **1**, but with slightly stronger low-energy bands due to the spin-forbidden transitions. However, the absorption maxima align more closely with the spectra of the complex in the solid state.

Table 2.1. Absorption data in THF solution ($5x10^{-5}$ M) and in solid state of complex **1** and ionosilica **SC-1.**

Sample	λ_{abs}/ nm (ε x 10^3/ M^{-1} cm^{-1})
[Ir(dfppy)$_2$(*dasipy*)]PF$_6$ (1)	285, 312, 380, 420, 445, 476 ***Solid***
	260 (54.0), 274$_{sh}$ (47.9), 305 (31.6), 360 (8.8), 417 (1.1), 445 (0.8), 470 (0.4) ***THF***
SC-1	295, 320, 362, 423, 446, 480$_{sh}$ ***Solid***

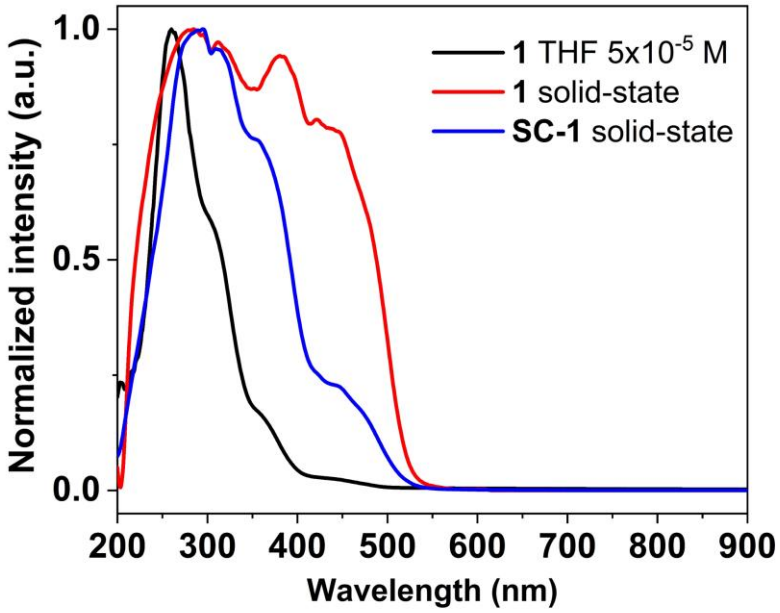

Figure 2.10. Normalized absorption spectra of complex **1** in solid state and THF solution, and of **SC-1** in solid state.

With regard to the excitation and emission data, these were obtained for the material in the solid state and in suspension (1 mg/ml) in both DMF and MeCN, as these solvents were used in the subsequent photocatalytic studies (Table 2.2 and Figure 2.11).

Table 2.2. Photophysical data in solid state and THF solution ($5x10^{-4}$ M) for complex **1** and in solid state and 1 mg/ml suspension for the self-condensed material **SC-1**. All data at Room Temperature.

Sample	Medium	λ_{em}/ nm[a)]	τ/μs[b)]	ϕ/%	K_r	K_{nr}
Complex 1	Solid	560	0.35	29[c)]	$8.29x10^5$	$2.03x10^6$
	THF	550	0.71	56[c)]	$7.89x10^5$	$6.20x10^5$
SC-1	Solid	590	0.43	12[d)]	$2.79x10^5$	$2.05x10^6$
	DMF	585	0.56	23[d)]	$4.11x10^5$	$1.38x10^6$
	MeCN	585	0.54	35[d)]	$6.48x10^5$	$1.20x10^6$

a) Data measured with λ_{exc} at 375 nm. Similar emission spectra obtained by excitation in the range 365 – 480 nm. b) Emissions lifetimes calculated as mono-exponential decay or an average of a bi-exponential decay. c) λ_{exc} at 440 nm. d) λ_{exc} at 375 nm.

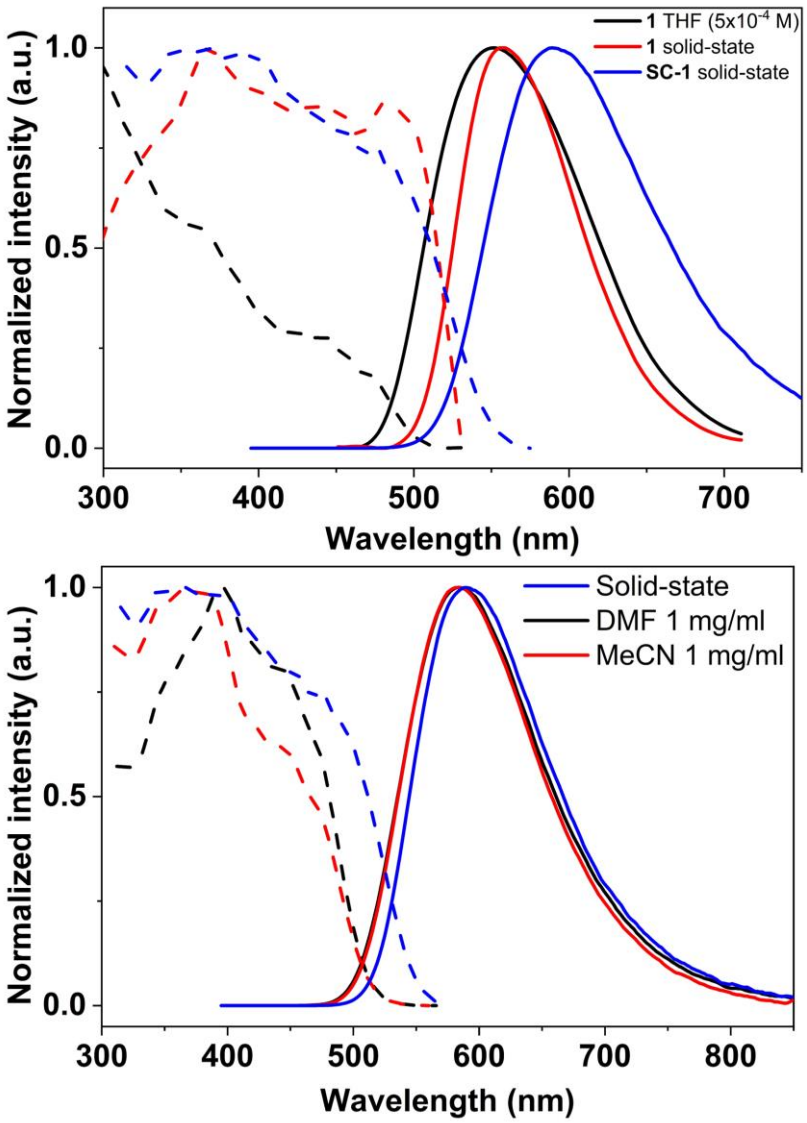

Figure 2.11. Normalized excitation (λ_{em} 550-590 nm) and emission (λ_{exc} 365 nm) spectra at room temperature of complex **1** in solid-state and THF solution, and **SC-1** in solid (up), and of **SC-1** in different media (down).

The emission profile of the material **SC-1**, both in the solid state and in suspension, exhibits an unstructured phosphorescent yellow emission, which closely resembles that of the complex **1**. As mentioned in Chapter 1, this emission is attributed to a mixture of ^{3}ML'CT/^{3}LL'CT excited states, with a remarkable metallic character. However, in all spectra, the emission maxima of the material show a notable bathochromic shift of 30-40 nm with respect to those observed for the complex. As observed for the hybrid nanomaterials described in Chapter 1, the emission of **SC-1** shows a longer lifetime compared with **1** in the solid state (τ *ca*. 0.50 μs *vs* 0.35 μs); although shorter values than that observed for the complex in THF solution (τ 0.71 μs). All these facts may be

attributed to a certain degree of distortion of the molecules of **1** in the self-condensed material **SC-1** or, more likely, to the different degree of intermolecular interactions of the molecules in the more disordered environment of **SC-1** compared to complex **1** in the solid state.

Finally, in the solid state, **SC-1** has an even lower quantum yield than that observed for complex **1** (ϕ 12% for **SC-1** vs. ϕ 29% for **1**). However, in DMF or MeCN suspension, the quantum yield of **SC-1** increases significantly (ϕ 23% or ϕ 35%, respectively) to values comparable to those of solid complex **1**. This phenomenon can be attributed to a higher light absorption in the dense **SC-1** solid material than in suspension or, perhaps, to the interactions of the solvent with the complex molecules located on the surface of the material.

2.3 Photocatalytic studies

2.3.1 Photocatalytic dehalogenation of 2-bromoacetophenone

The first photocatalytic reaction aimed to assess the photoactivity and recoverability of the material was the dehalogenation of 2-bromoacetophenone (Scheme 2.8).

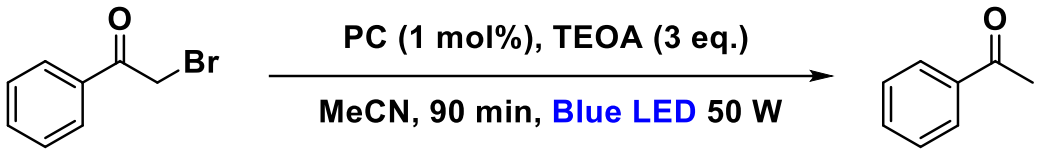

Scheme 2.8. Photocatalytic dehalogenation reaction.

This reaction requires the presence of 3 equivalents of triethanolamine (TEOA) as a sacrificial reactant. The proposed mechanism is illustrated in Figure 2.12, which is based on similar reactions found in the literature.[86d, 98] This reaction follows a reductive quenching mechanism, where the excited iridium(III) PC is reduced by taking one electron from the TEOA. This allows the reduction of 2-bromoacetophenone and the cleavage of the C-Br bond, which returns the PC to its ground state, and the two resulting radicals react with each other, yielding acetophenone and an imine salt that precipitates in the medium.

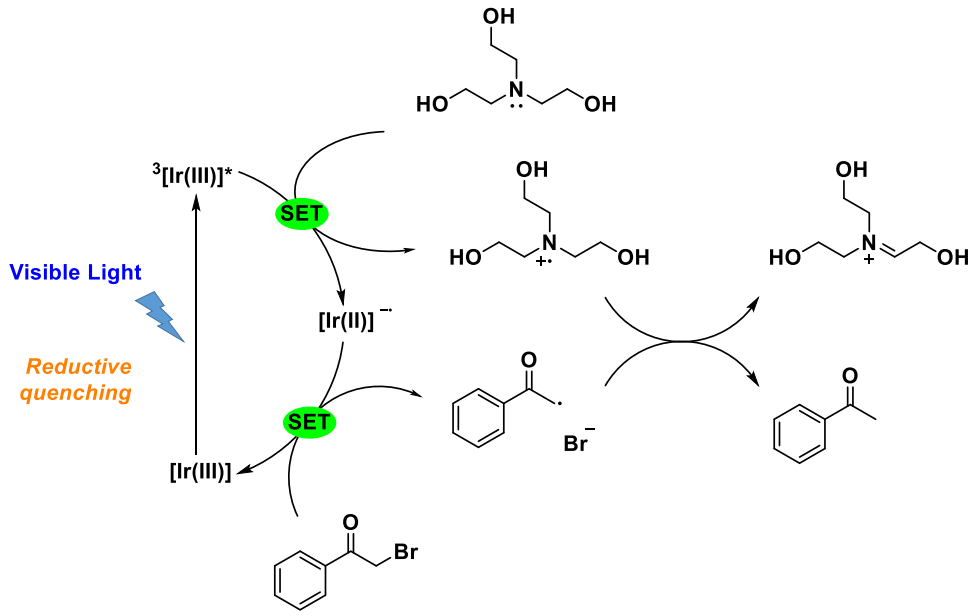

SET: Single Electron Transfer

Figure 2.12. Mechanism of the photocatalytic dehalogenation reaction.

NMR spectroscopy was employed to monitor the reaction, using known amounts of 1,3,5-trimethoxybenzene as an internal standard. Figure 2.13 shows the signals used for quantification. These signals correspond to singlets and were selected for their cleanliness and ease of a more accurate integration. The signal at 6.09 corresponding to the protons in the aromatic ring of 1,3,5-trimethoxybenzene was chosen for the internal standard.

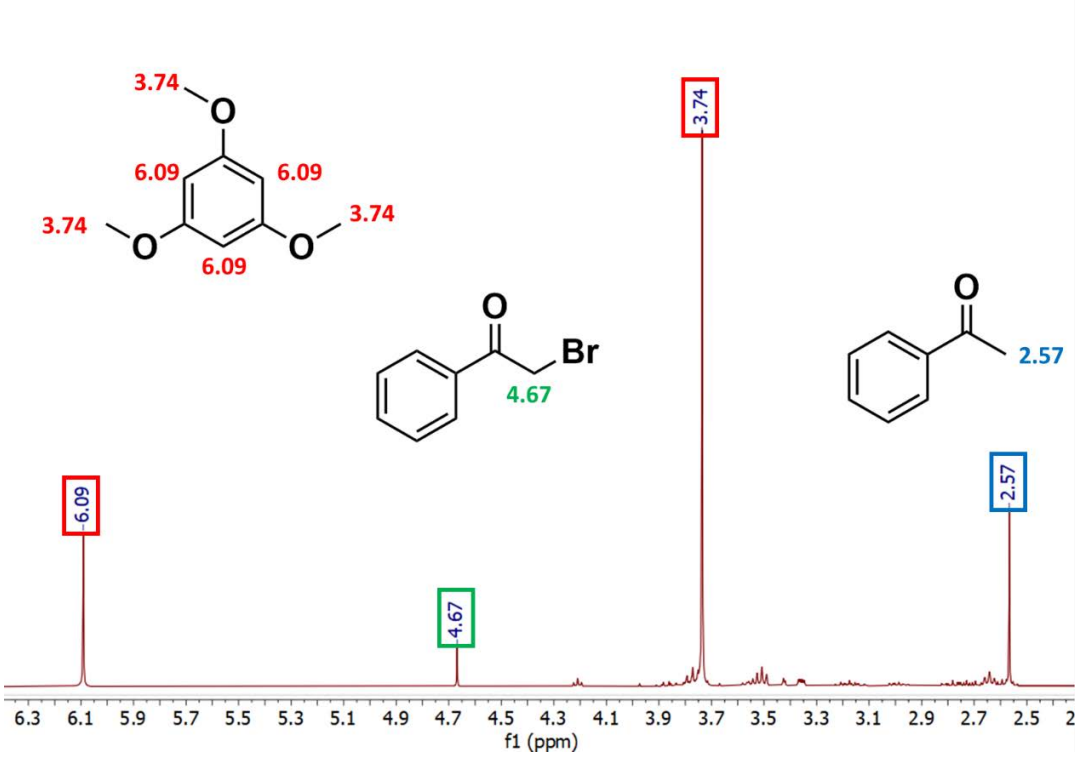

Figure 2.13. ^{1}H-NMR signals used to follow the reaction yield.

Table 2.3 displays the results of the optimization experiments carried out with complex **1** under homogeneous conditions and with **SC-1** under heterogeneous conditions, using a 50 W blue LED [λ_{max} (blue LEDs) = 450 nm]. First, the reaction conditions for the complex were optimized, using deuterated acetonitrile as solvent. After several tests using 1 mol% photocatalyst loading, it was observed that the reaction reached 100% yield in just 5 minutes, both under inert atmosphere and in the presence of oxygen (entries 1 and 2 in Table 2.3). Significantly, these results remained consistent even when the amount of catalyst was reduced to 0.02 mol% (entries 3 and 4). Subsequently, a blank test was conducted without adding catalyst, leaving the reaction under stirring and irradiation for 60 minutes (entry 5). Because the LED used in the experiments is not monochromatic and has an emission tail, a portion of this irradiation

was absorbed by 2-bromoacetophenone. Consequently, a yield of 7% was obtained in the absence of a photocatalyst after 1 hour of irradiation.

Table 2.3. Results of the dehalogenation reaction of 2-bromoacetophenone.

Entry	Catalyst loading (mol%)	PC	Time (min)	Yield (%)	Conditions
1	1	**1**	5	100	Under N_2
2	1	**1**	5	100	In presence of O_2
3	0.02	**1**	5	100	Under N_2
4	0.02	**1**	5	100	In presence of O_2
5	-	**-**	60	7	Under N_2
6	0.02	**SC-1**	60	Traces	Under N_2
7	1	**SC-1**	90	88	Under N_2
8	1	**SC-1**	60	Traces	Under N_2, no TEOA
9	1	**SC-1**	60	0	Under N_2, no light

As for the tests with the material, a preliminary attempt with 0.02 mol% catalyst loading under an inert atmosphere resulted in only traces of acetophenone traces after 60 minutes of irradiation (entry 6). For this reason, a test with 1 mol% loading was performed, resulting in a 90% yield after 90 minutes of irradiation (entry 7).

It was also confirmed that the addition of TEOA to the reaction was essential, as only traces of product were observed in its absence (entry 8). In addition, the need for irradiation to carry out the reaction was also confirmed (entry 9).

After the optimization under both homogeneous and heterogeneous conditions, tests were carried out to evaluate the recovery and recyclability of the material. For this purpose, a volumetric flask was used to set up the same reaction, increasing the amount of material to 40 mg to minimize potential losses during recovery. A constant irradiation time of 90 minutes was maintained for each cycle, to allow a representative comparison of the material activity at the same time. The reaction was conducted under an inert atmosphere, with acetonitrile previously purged with nitrogen for 20 minutes. The photocatalyst ratio was kept at 1 mol%. After each cycle, the material was centrifuged in order to separate it from the reaction medium. An aliquot of the supernatant was then subjected to ^{1}H-NMR analysis to determine the yield (further details of the procedure can be found in the Experimental Part).

Figure 2.14 summarizes the material recovery and washing procedure used. First, as mentioned above, the material was centrifuged at 20000 rpm for 15 minutes to separate it from the reaction medium. It was then washed with approximately 50 ml of distilled water to dissolve the imine salt formed during the reaction. After sonication for 10 minutes, a second centrifugation step with the same parameters successfully removed almost all of the previously precipitated salt. The material was washed a second time with absolute ethanol, and after centrifugation, transferred back to the flask used for the reaction with the aid of dry dichloromethane. The solvent was then removed using a rotary evaporator, and the flask was subsequently heated to 100ºC under vacuum for 30 minutes to ensure complete drying and to remove any residual water from the washings. The flask was then allowed to cool to room temperature under inert atmosphere, and the solvent for the new catalytic cycle (previously degassed) was added. The flask was sonicated for 1 minute, which was enough time for the material to detach from the walls of the flask and become uniformly resuspended in the reaction solvent. Finally, the remaining reagents were added, and the flask was subjected to a new irradiation cycle.

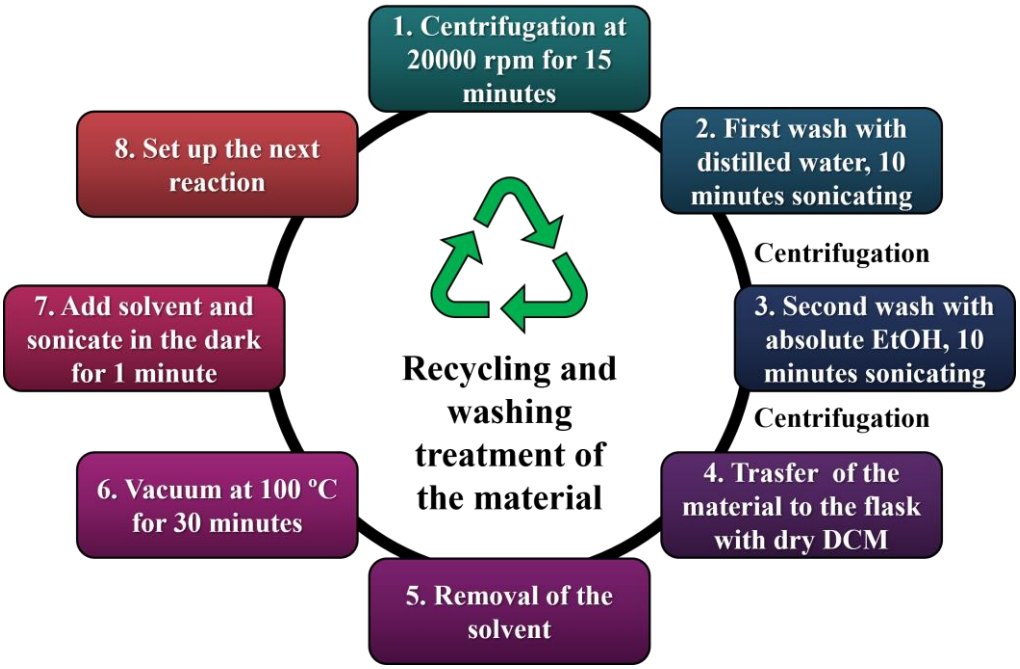

Figure 2.14. Schematic representation of the photocatalyst recovery and washing process in each of the catalytic cycle for the dehalogenation reaction.

The results of the yield obtained for each catalytic cycle are presented in Figure 2.15. Seven catalytic cycles were performed, each lasting 90 minutes. The material was recovered and cleaned according to the procedure shown in Figure 2.14. After completion

of cycle 7 and washing of the material, an additional cycle was performed. This time, the reaction was allowed to run to 100% completion, instead of the typical 90 minutes. The results obtained are very promising, showing only a 20% decrease in the photocatalytic performance of the material after seven cycles. In particular, the most significant decrease in activity occurred during the first three cycles (90% to 78%). Thereafter, stability was observed between cycles 4 and 6, and even cycle 7, considering the experimental error associated with quantifying the yield by NMR spectroscopy. Importantly, although the photocatalytic rate of the material decreased slightly in each cycle, it retained the ability to complete the reaction entirely in the eighth cycle, although this required a longer irradiation time (180 minutes). This suggests that the initial loss of activity may be attributed to possible material losses during the washing process rather than a decrease in photoactivity.

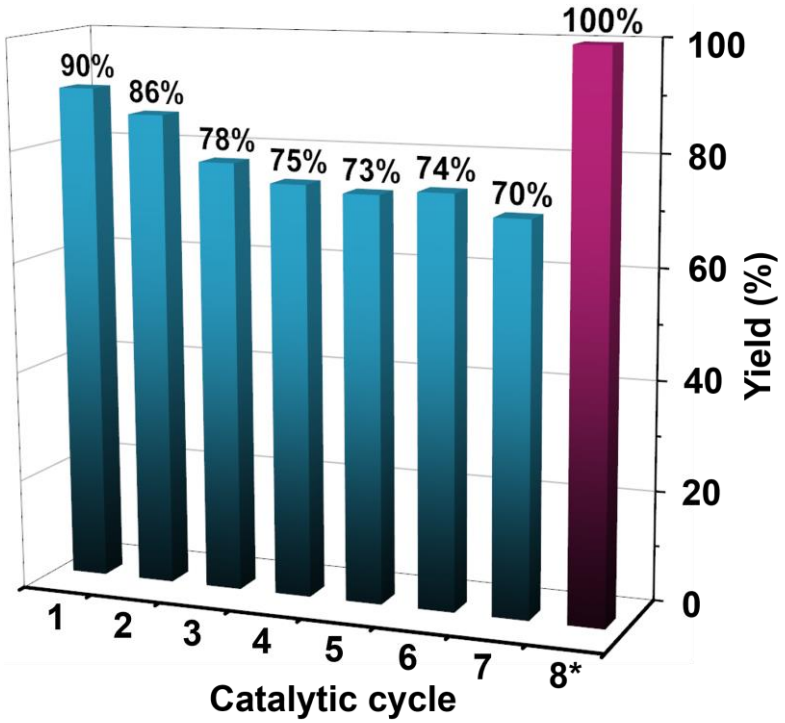

Figure 2.15. Results of the yields obtained by recovering the PC and reusing it in seven consecutive catalytic cycles. Experiments up to the 7th cycle were carried out under identical conditions, measuring the yield after 90 min. (*) For the 8th cycle, the yield is obtained after 180 min.

In conclusion, these results highlight the potential of the material as a heterogeneous photocatalyst for photoredox reactions following a reductive quenching mechanism. Furthermore, the material displays promising recoverability and reusability over eight catalytic cycles.

2.3.2 Photocatalytic synthesis of phenanthridine

The second reaction tested with the material was the synthesis of phenanthridines from acyloximes (Scheme 2.9).

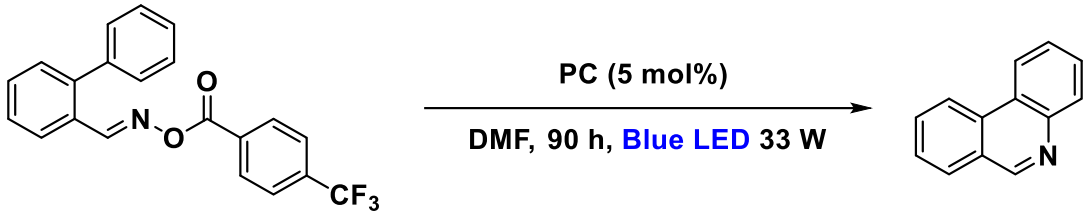

Scheme 2.9. Photocatalytic synthesis of phenanthridine reaction.

In contrast to the previous reaction, the presence of an external electron donor is not required as the same reactant acts as both the acceptor and donor in the catalytic cycle. Figure 2.16 outlines the reaction mechanism, which follows an oxidative quenching pathway.[96] Upon excitation, the photocatalyst undergoes oxidation by donating an electron to the acyloxime, breaking the nitrogen-oxygen bond and forming an iminyl radical. This radical then attacks the phenyl group, leading to intramolecular cyclization. The electron is then returned to the complex, restoring its initial oxidation state and generating a carbocation. Finally, phenanthridine is obtained by abstraction of a proton.

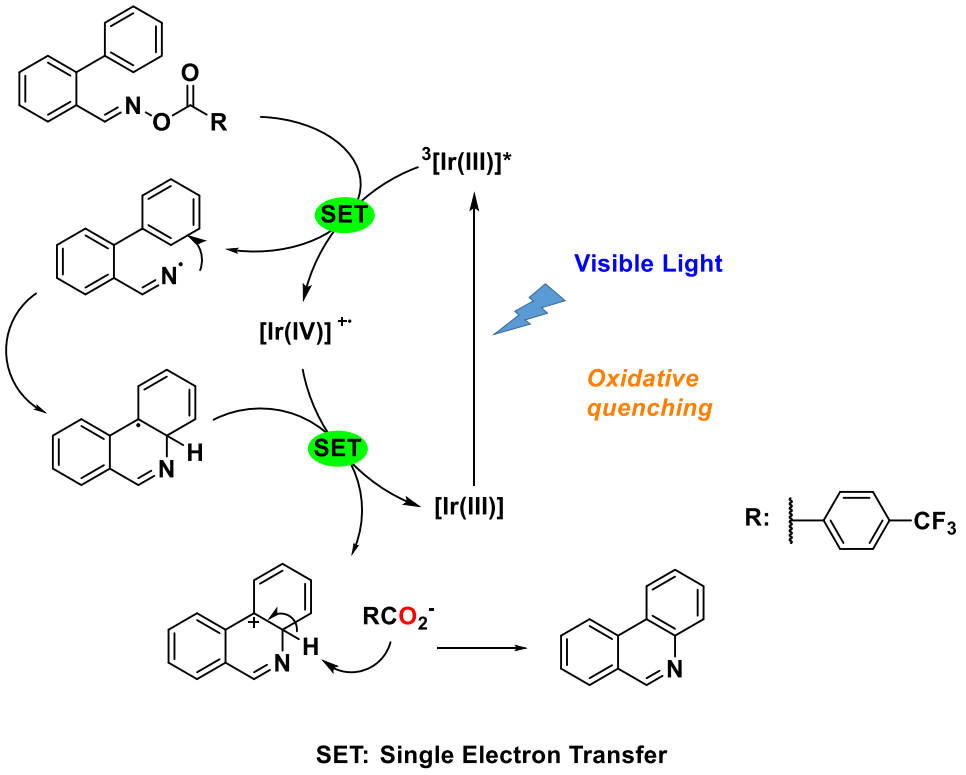

Figure 2.16. Mechanism of the photocatalytic reaction.

This reaction is extremely sensitive to the presence of traces of oxygen and water in the medium. For this reason, the reaction is carried out under strict conditions of inert atmosphere, using dry DMF stored in a dry box. The conversion of the reaction was monitored by NMR spectroscopy, and the signals used are shown in Figure 2.17. In addition to the reagent and the product, other signals corresponding to a different substance have also been observed, although their isolation and identification have proven challenging. A plausible hypothesis, which fits well with the signals observed in the NMR spectrum is that these may correspond to the *Z*-isomer of acyloxime, which is unable to undergo reduction and break the N-O bond. However, further isolation is necessary to confirm this.

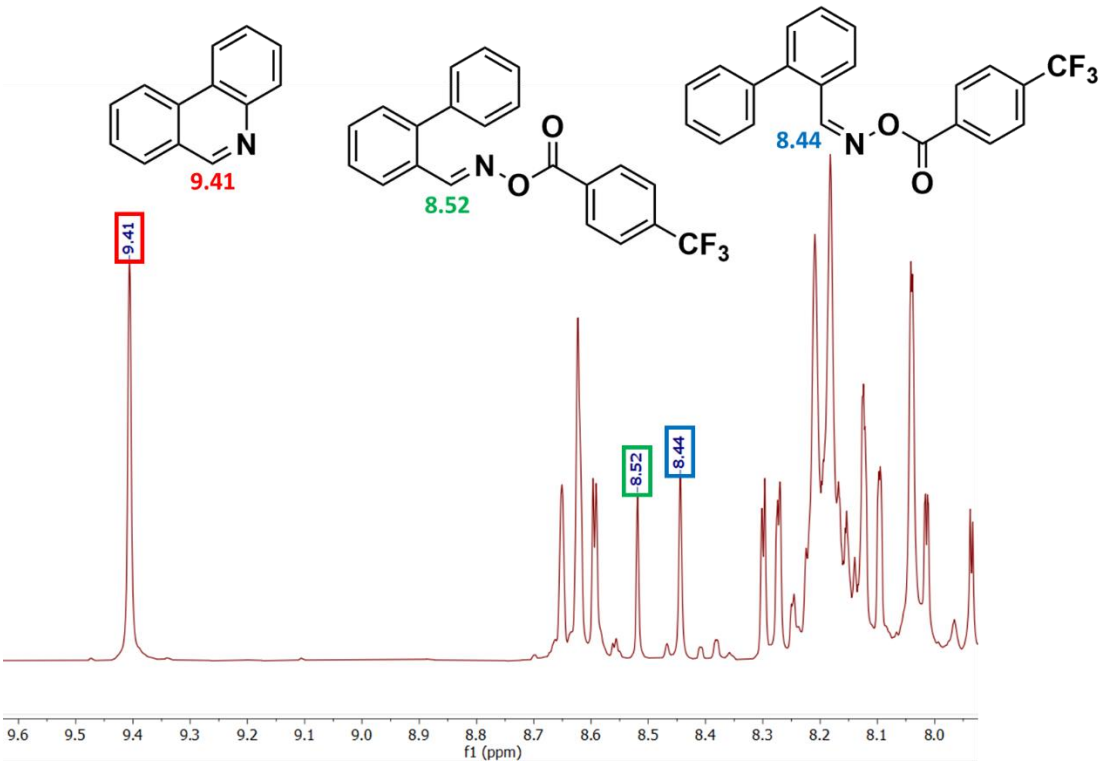

Figure 2.17. ^{1}H-NMR signals used to follow the conversion of the reaction.

The irradiation source for this reaction was a 100 W RGB LED, using only the blue light component [λ_{max} (blue LEDs) = 450 nm, ~33 W]. As previously stated, all of these tests were carried out by performing the reaction setup in a dry box using commercially available anhydrous DMF stored inside. The use of freshly opened commercially available dry DMF, compared to various DMF deoxygenation techniques such as nitrogen bubbling for 30 minutes prior to irradiation or the Freeze-Pump-Thaw method, resulted

in superior conversion rates for the homogeneous complex in previous tests. For this reason, it was decided to use the commercially anhydrous DMF as the solvent and to store it in a dry box. Table 2.4 presents the results of the optimization of this reaction, both for complex **1** and for the **SC-1** material (see Experimental Part for further experimental details).

Table 2.4. Results of the photocatalytic synthesis of phenanthridine.

Entry	Catalyst loading (mol%)	PC	Time (hours)	Conversion (%)
1	5	**1**	72	97
2	7.5	**SC-1**	88	89
3[a)]	5	**1**	24	-
4[b)]	-	**-**	72	-
5[c)]	5	**1**	24	Traces

a) No light irradiation. b) No photocatalyst added to the reaction. c) In presence of O_2.

For the optimization under homogeneous conditions, it was found that this reaction required additional loading of photocatalyst in contrast to the previous reaction, which had to be increased to 5 mol%. In addition, the irradiation time was increased to 72 hours to achieve 97% conversion (entry 1). Optimization of the reaction using the material led to an increase in catalyst loading to 7.5 mol%, and an extended reaction time of approximately 90 hours, resulting in conversion values close to 90% (entry 2). Control reactions without irradiation, without photocatalyst, and in the presence of oxygen showed no reaction (entries 3-5). As mentioned above, this reaction is sensitive to even small amounts of water which can break the imine bond of the acyloxime, producing the biphenyl-2-carboxaldehyde. It is therefore essential to maintain strict dry conditions to avoid this side reaction.

After optimizing the reaction under both homogeneous and heterogeneous conditions, studies were carried out to determine the recoverability and recyclability of **SC-1**. The reaction was set up in a volumetric flask using 10 mg of material, given the complexity and precautions required for this reaction. Irradiation was carried out for 90 hours in each catalytic cycle, with a constant photocatalyst loading of 7.5 mol%. Figure 2.18 illustrates the washing procedure optimized for material recovery in this reaction.

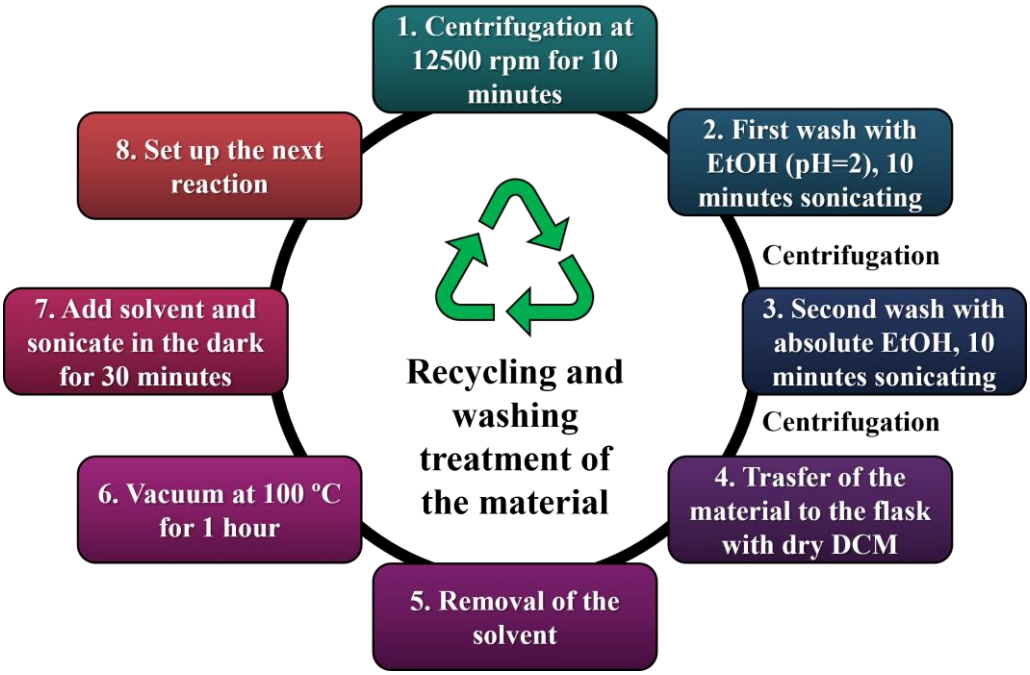

Figure 2.18. Schematic representation of the photocatalyst washing process in each of the catalytic cycle for the synthesis of phenanthridine.

This washing procedure is similar to the one described above, but incorporates some key differences. Firstly, the material is centrifuged in Eppendorf tubes to allow better recovery due to the smaller amount used for this reaction. During initial tests, it was observed that the material appeared brownish in color during recovery. To overcome this issue, the first wash is performed with acid ethanol (pH=2) to remove any organic residues that may adhere to the surface of the material. After this first wash, the yellow hue of the material is restored, so the second wash is performed with absolute ethanol to eliminate any traces of acid. After centrifugation, the material is transferred back to the reaction flask with the help of dry dichloromethane. The solvent is evaporated, and the flask is heated for one hour under vacuum at 100 °C to ensure thorough removal of any traces of water. After adding the DMF in the dry box, the flask is sonicated for 30 minutes in the dark. This step was implemented due to observed difficulties in material dispersion during this reaction, which worsened as additional catalytic cycles were performed. Increasing the sonication time from the initial cycles resolved this issue. Finally, the reagents are added, and the reaction is irradiated with stirring for a new catalytic cycle.

Figure 2.19 showcases the results of reusing the material for seven consecutive catalytic cycles. Two different results are presented for each cycle. In blue the total

percentage of acyloxime reacted is shown, accounting for both phenanthridine formation and other secondary compounds (such as the suspected *Z*-isomer of acyloxime or small amounts of aldehyde). Purple shows the conversion values for acyloxime to phenanthridine.

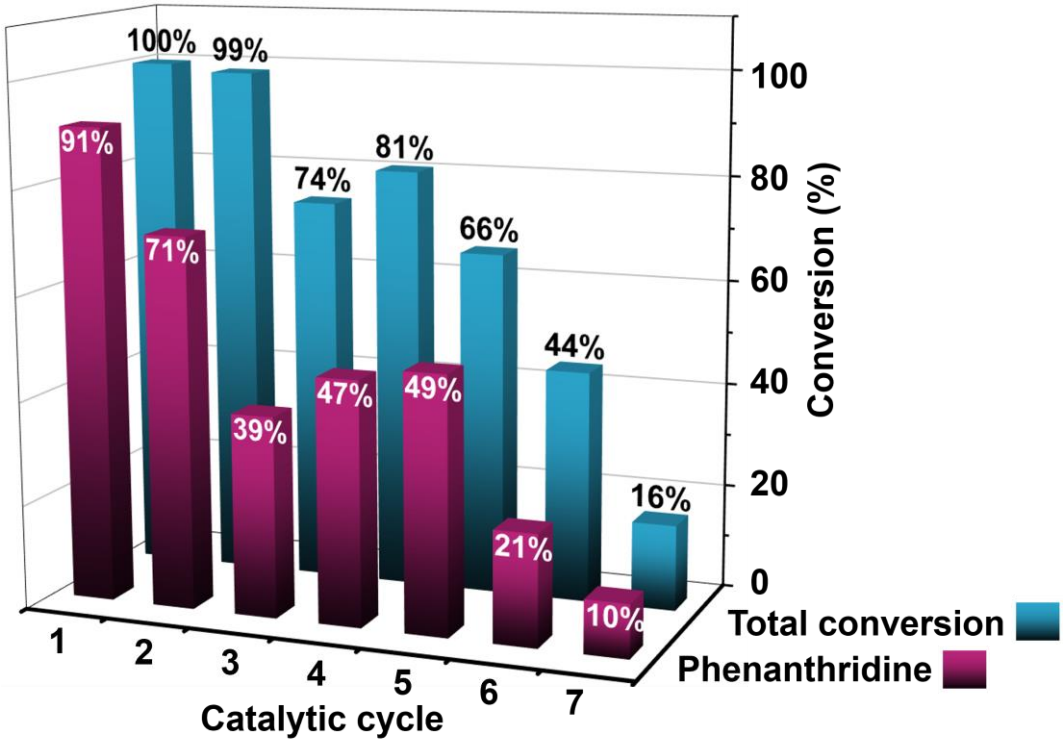

Figure 2.19. Results of the conversion values obtained recovering the PC and reusing it in seven consecutive catalytic cycles. Experiments were carried out under identical conditions.

In this case, a more pronounced decrease in the photocatalytic activity of the material is observed compared to the previous dehalogenation reaction. Conversion drops from 91% to 40% in the first three cycles, although there appears to be a slight recovery of material activity in the fourth and fifth cycles (up to 50%). However, in the sixth and seventh cycles, the values obtained for both the conversion to phenanthridine and the acyloxime reaction values are significantly lower, reaching only 10% conversion in the last cycle. This trend was confirmed by repeating the test again with new material and seven catalytic cycles. Part of this decrease in activity may be attributed to the lower initial amount of material used in this reaction compared to the dehalogenation of 2-bromoacetophenone, making small losses during washing more significant. However, it should also be considered that this reaction has a much longer irradiation time (90 hours per cycle), resulting in a total irradiation time of 630 hours for the material. In contrast,

the previous dehalogenation reaction had a total irradiation time of only 10.5 hours for the entire reuse study. Research has shown that irradiation time plays a crucial role in the photostability of the photocatalysts,[99] which could be a major factor contributing to the decline in activity. However, it is important to note that the material exhibits excellent performance for reactions that follow both reductive and oxidative quenching mechanisms. Furthermore, although this reaction is experimentally more challenging, the material maintains high activity values for the initial five catalysis cycles, corresponding to 450 hours of irradiation.

2.3.3 Photophysical properties of the material after 8 cycles

Upon completion of the material recyclability tests, **SC-1** was recovered and cleaned for a final evaluation of its photophysical properties after the photocatalytic cycles. The material used for these evaluations was obtained from the dehalogenation reaction of 2-bromoacetophenone, as it provided sufficient quantity for all required tests. Firstly, Figure 2.20 presents the plots of the solid-state diffuse reflectance UV-vis (DRUV) measurements for the recovered material compared to the initial material. The reflectance measurements are displayed on the left, along with the spectrum resulting from applying the Kubelka-Munk transform, which provides an approximate absorption spectrum on the right.

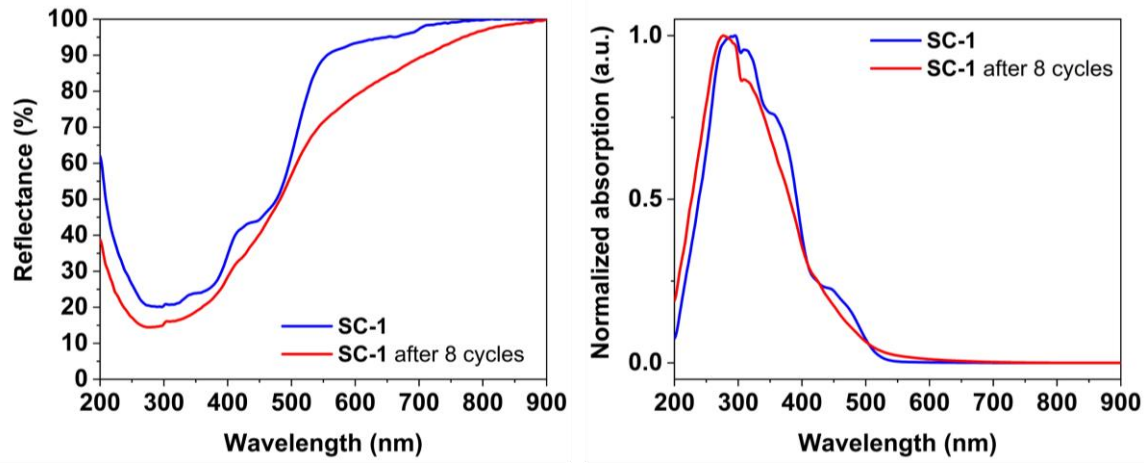

Figure 2.20. Comparison of the reflectance (left) and absorption spectra (right) of **SC-1** before and after 8 photocatalytic cycles.

The graphs show that the absorbance pattern is maintained for both samples, with slight variations in the intensity of some bands. However, as the reflectance intensities of both samples are similar, it can be concluded that there are no significant differences in the absorption of the material after the photocatalytic cycles.

The emission results of the material can be found in Table 2.5 and Figure 2.21.

Table 2.5. Emission data in solid state of **SC-1** before and after 8 photocatalytic cycles. All data at Room Temperature.

Sample	λ_{em}/ nm[a)]	ϕ/%[a)]
SC-1 solid	590	12
SC-1 solid after 8 cycles	610	2

a) Data measured with λ_{exc} at 375 nm.

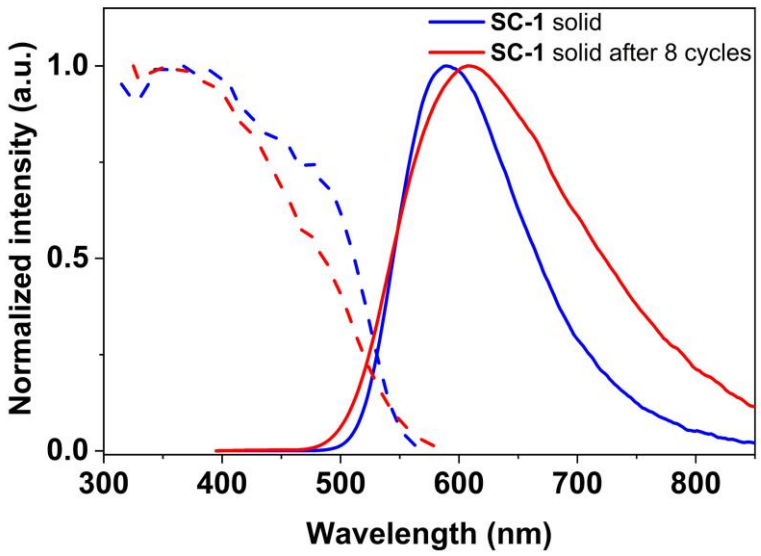

Figure 2.21. Comparison of the emission spectra of **SC-1** before and after 8 photocatalytic cycles.

In this case, a more significant difference in emission is observed before and after the use of **SC-1** in photocatalysis. Interestingly, the emission lifetime decreases, and there is a shift towards longer wavelengths in the emission, similar to what was observed for grafted nanoparticles in Chapter 1 (**NP_G**). This contrasts with the nanoparticles synthesized through *in-situ* techniques also in Chapter 1 (**NP_IS**), where no shift in the emission maximum was noted. These observations would suggest that the complex molecules present on the surface of the material may undergo degradation when involved in these types of reactions, thereby altering their emission characteristics and influencing the overall emission of the material. However, it is plausible that the complex molecules located in deeper layers of the material are less affected, as they are better shielded within the structure of the material. Furthermore, although some of the activity has been lost, the material still retains its photocatalytic capabilities. It would be worth investigating ways to gradually reach the complex molecules in the deeper layers of the material during photocatalytic cycles as a possible direction for future research, as this could improve the overall performance of the material.

Chapter 3. Synthesis of BODIPY dyes based on the phenylpyridine ligand

3.1 Introduction

Organic photocatalysis has experienced significant growth in recent years, driven by interest in finding cost-effective and sustainable photocatalysts (PCs). Although organic dyes have been known for a long time, their use in synthetic applications and as photocatalysts has only recently attracted attention. This has led to the gradual success in replacing organometallic iridium(III) and ruthenium(II) complexes by organic PCs in a wide range of reactions, either in EnT or SET processes.[32] This transition is made possible by their increasingly tunable and designable properties, which directly influence the energy of the excited states and, consequently, their oxidation and reduction potentials.[100]

A fundamental difference in their capacity as PCs between organometallic compounds and organic molecules lies in the excited states involved in the photocatalytic reactions. Ir and Ru based photocatalysts efficiently populate the T_1 state due to the presence of the metal, which significantly impacts their ISC efficiency. On the other hand, organic compounds can be rationally synthesized to operate from the S_1 or T_1 state.

In organic compounds, excitation to the S_1 state usually occurs via π-π^* transitions. As discussed in the general introduction to this thesis, the S_1 state usually exhibits very short lifetimes, often on the order of nanoseconds. However, many photoredox reactions have been described in which the organic PC acts from this excited state.[33] The higher energetic lever of S_1 compared to T_1, leading to a high reduction and oxidation potential, allows reactions to be catalyzed that are energetically inaccessible from a triplet state.

On the other hand, regarding the shorter lifetimes of singlet states compared to triplet states, it is accepted that lifetimes longer than 1 nanosecond can participate in SET processes, since the decay of the excited state is close to, but still above, the diffusion rate constant of the substrate molecules ($k_{diff} \sim 1x10^{10}$ - $2x10^{10}$ s^{-1}).[33] This allows organic dyes with fluorescence lifetimes between 2 and 20 ns to still photocatalyze SET reactions.

Regarding the character of the excited states, similar to MLCT transitions in organometallic compounds, organic compounds exhibit a marked Charge Transfer (CT) character when their HOMO and LUMO (or SOMO and SOMO-1) are spatially separated within the molecule.[101] Such systems, known as donor-acceptor systems, are widely used

as a strategy to synthetize molecules that exhibit TADF behavior. By reducing the overlap integral of the orbitals, the energy of the singlet and triplet states becomes more similar, enabling a return to the singlet state after populating the triplet state (Figure 3.1, a). A common strategy to obtain these donor-acceptor systems in a single molecule is to introduce a so-called "magic angle" between the two parts hosting the orbitals (Figure 3.1, b).[102] This breaks the conjugation and separates the donor from the acceptor, but as the angle is not strictly orthogonal, it still allows some orbital overlap and charge transfer from one side to the other. The generation of charge transfer (CT) states often results in longer excited state lifetimes compared to locally excited (LE) states.[103] However, these systems often have lower emission quantum yields due to the minimal orbital overlap. Placing the two orbitals in separate parts of the molecule allows for the rational design of these photocatalysts, and the HOMO-LUMO gap.[32]

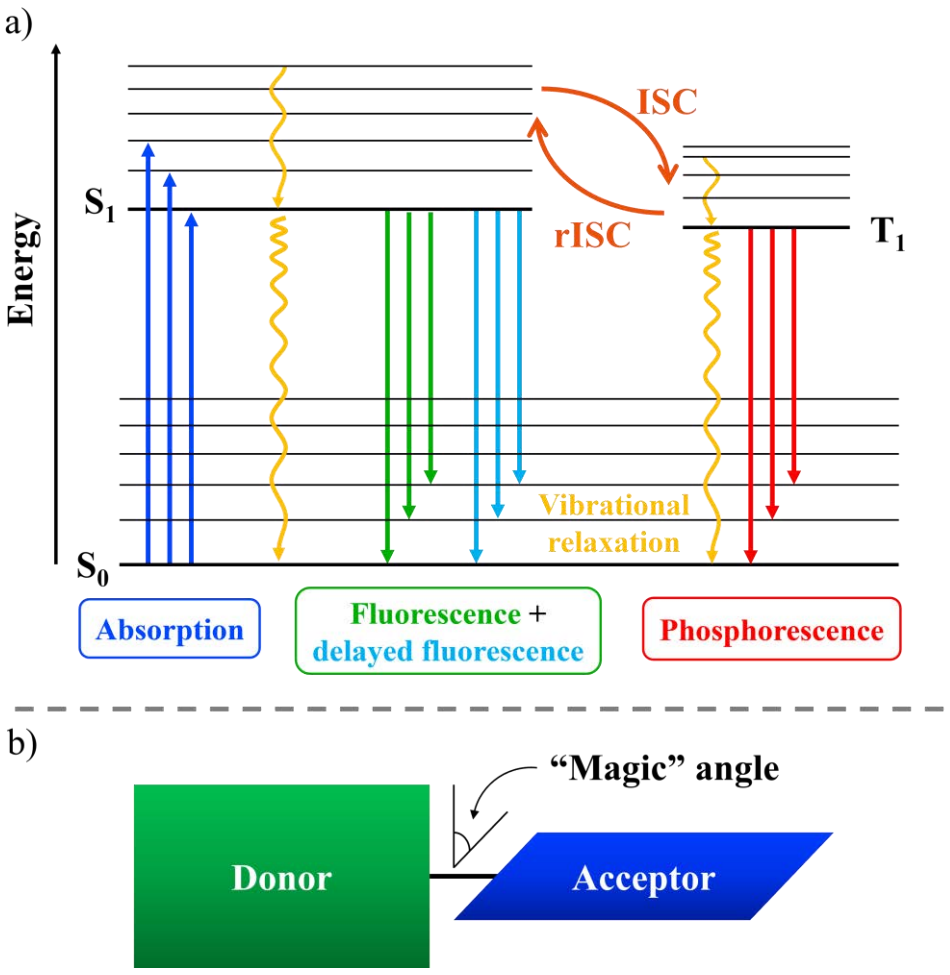

Figure 3.1. a) Simplified diagram on the mechanisms of emission (rISC: reverse intersystem crossing). b) Scheme of the donor-acceptor system.

The most commonly used organic photocatalysts are listed below, together with some of their photophysical characteristics (Figure 3.2)[33]:

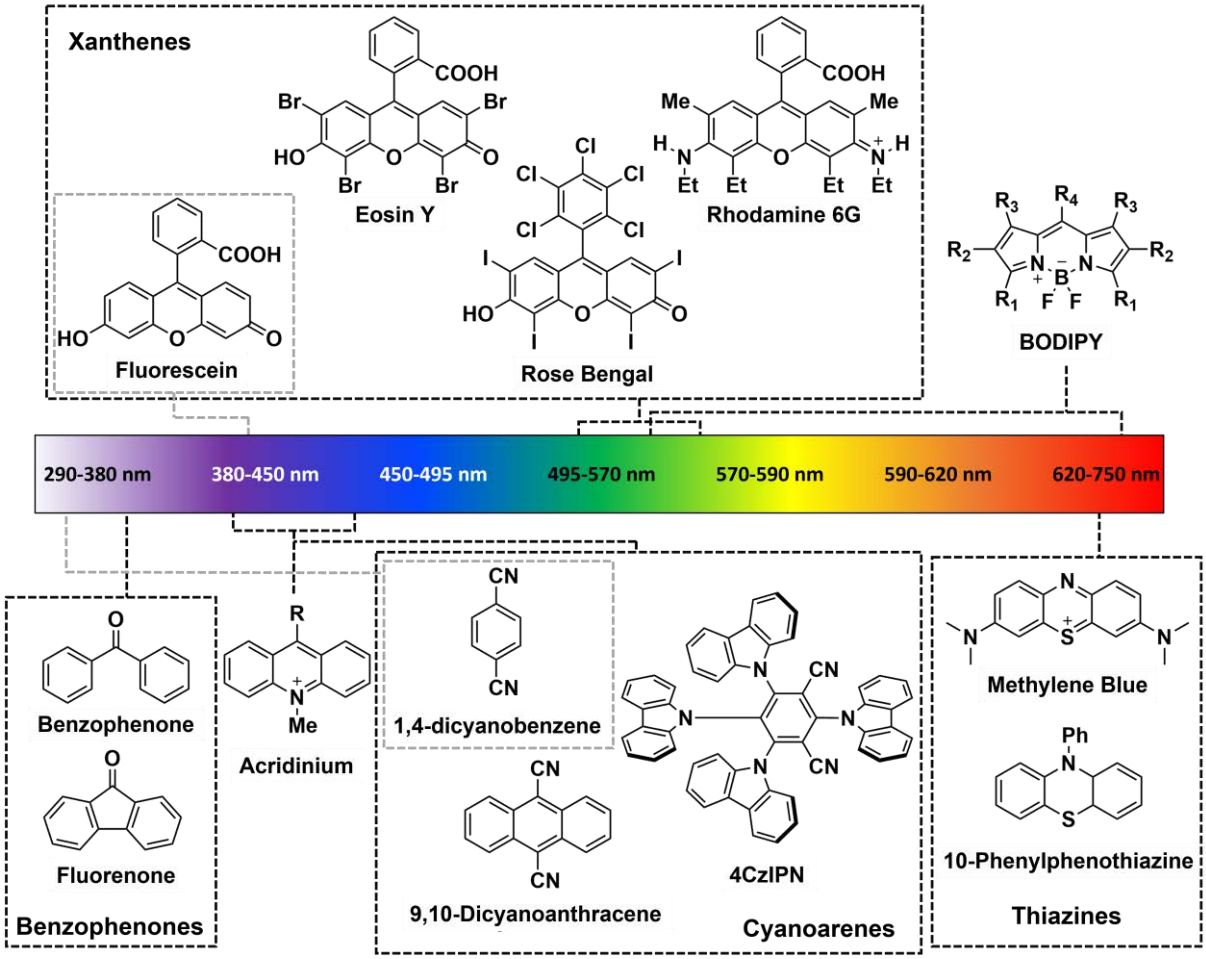

Figure 3.2. Most frequently employed organic PCs and their absorption range in the visible spectrum.

- Xanthenes: These derivatives represent a class of compounds used as dyes for more than a century, although their utilization as PCs and the investigation of their excited state behavior are relatively recent. A complicating factor in their study is the complex equilibria they exhibit between their neutral and ionized forms, which significantly affects their absorption spectra.[33] The dianionic form, typically with higher absorptivity and wider absorption ranges, is usually the preferred form for photocatalysis. This category includes Fluorescein, Eosin Y, Erythrosine, Rose Bengal or Rhodamine,[104] to name the most representative ones. Among these, Fluorescein reaches the S_1 state after irradiation, which is a moderate oxidizer and a potent reductant. It exhibits a very high fluorescence quantum yield (0.93) with a very short lifetime (~4 ns), and inefficient ISC. Its application in photocatalysis is quite limited.[33] In contrast, Eosin Y, Erythrosine and

Rose Bengal exhibit highly efficient ISC due to the halogen atoms in their structure, which induce the heavy atom effect. The singlet state lifetimes are very short (ranging from 0.5 to 2.7 ns), while those of the triplet are longer ($\tau_{Eosin\ Y}$= 24 ms).[100b] In these cases, the triplet state assumes the primary importance in photocatalysis, acting as a moderate oxidant and reductant, with the ability to generate singlet oxygen as well.[105] The latter mechanism has been the most studied with these molecules, until their recent application in electron transfer reactions.[106]

- Benzophenones: Compounds characterized by fast and highly efficient ISC, which is characteristic of carbonyl compounds with S_1 and T_1 states very close in energy.[33, 107] Although electron transfer reactions have been described,[108] their T_1 state does not exhibit such high oxidation and reduction potential values. These compounds absorb primarily in the ultraviolet region, with weaker absorptions in the near-UV.

- Cyanoarenes (dicyanoanthracenes): The family of cyanoarenes has been extensively studied for about 30 years,[109] and serves as a prominent example of photocatalysts that facilitate electron transfers from the singlet excited state.[33] Capable of oxidizing compounds with oxidation potentials exceeding +2.0 V and reaching reduction potentials between -0.7 and -1.7 V, these molecules feature an aromatic core adorned with two cyano groups.[33] A commercially available compound within this category is 9,10-dicyanoanthracene (DCA), with the appearance of a yellow crystalline solid. The DCA core is a strong singlet excited state photooxidant, although structural modifications can change its mechanism of action to EnT processes.[110]

In recent years, the most notable representative within this group of organic photocatalysts has been 1,2,3,5-tetrakis(carbazol-9-yl)-4,6-dicyanobenzene (4CzIPN) and its derivatives.[111] These compounds exhibit a marked donor-acceptor character, with the HOMO and LUMO separated into distinct regions of their structures. Although originally designed as efficient compounds for OLED and TADF applications,[34c, 112] Zhang and co-workers began to explore the potential of these donor-acceptor dyes in photocatalysis.[113] These compounds are highly valued for their flexibility in modifying their redox potentials.[114] For example, photooxidation pathways are enhanced by structural modifications of the isophthalonitrile fragment, where the LUMO is located. Conversely, photoreduction pathways are enhanced by changes in the diarylamine fragments, where the HOMO is located (Figure 3.3).[110]

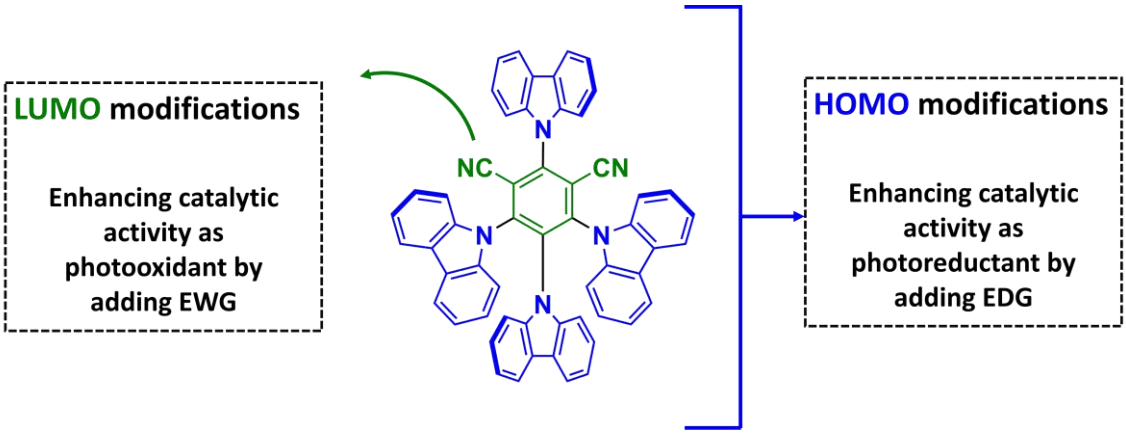

Figure 3.3. 4CzIPN structure and modifications to tune the photoredox pathway.

- Acridiniums: Acr-Me$^+$ and other 9-substituted Acr-R acridiniums are molecules considered to be good oxidizers in their singlet excited state.[32-33] The utilization of these compounds as photocatalysts dates back to the work of Fukuzumi et al. in 2004.[115] These molecules typically feature linked donor-acceptor moieties, with the substituent group at the 9-position acting as an electron donor, and the 10-alkyl/aryl acridinium cation (Acr$^+$) serving as the electron acceptor.[116] They possess charge-transfer excited states with long lifetimes due to their orthogonal structure, which prevents charge recombination.[117] These compounds also exhibit broad redox potential windows, with oxidation potentials reaching up to +2.18 V, making them the most oxidizing organic PCs known to date.[116a]

- Thiazines: Methylene blue, a well-known and widely used compound in various medical and biological applications,[118] has diverse properties that vary depending on the solvent and protonation state. Compared to other dyes mentioned above, methylene blue has an intense red absorption (650-670 nm).[119] The most relevant excited state for photocatalysis is the triplet state, characterized by relatively long lifetimes.[33] Although the energy absorption of methylene blue is comparatively low, it serves as a relatively good oxidant in its excited state, and is an efficient photosensitizer for singlet oxygen generation.[105b, 120]

In addition to these families of organic compounds, the BODIPY dye (boron-dipyrromethene, or 4,4-difluoro-4-borata-3a-azonia-4a-aza-*s*-indacene) is an attractive alternative in photoorganocatalytic applications. The first synthesis of these organoboronic compounds was reported in 1968 by Treibs and Kreuzer.[121] Although

several synthetic routes are known, one of the main strategies to obtain these compounds is the condensation of two pyrrole units with an aldehyde or an acyl chloride, in the presence of an acid such as trifluoroacetic acid. Subsequent treatment with $Et_2O{\cdot}BF_3$ yields *meso*-substituted BODIPYs (Scheme 3.1).[122]

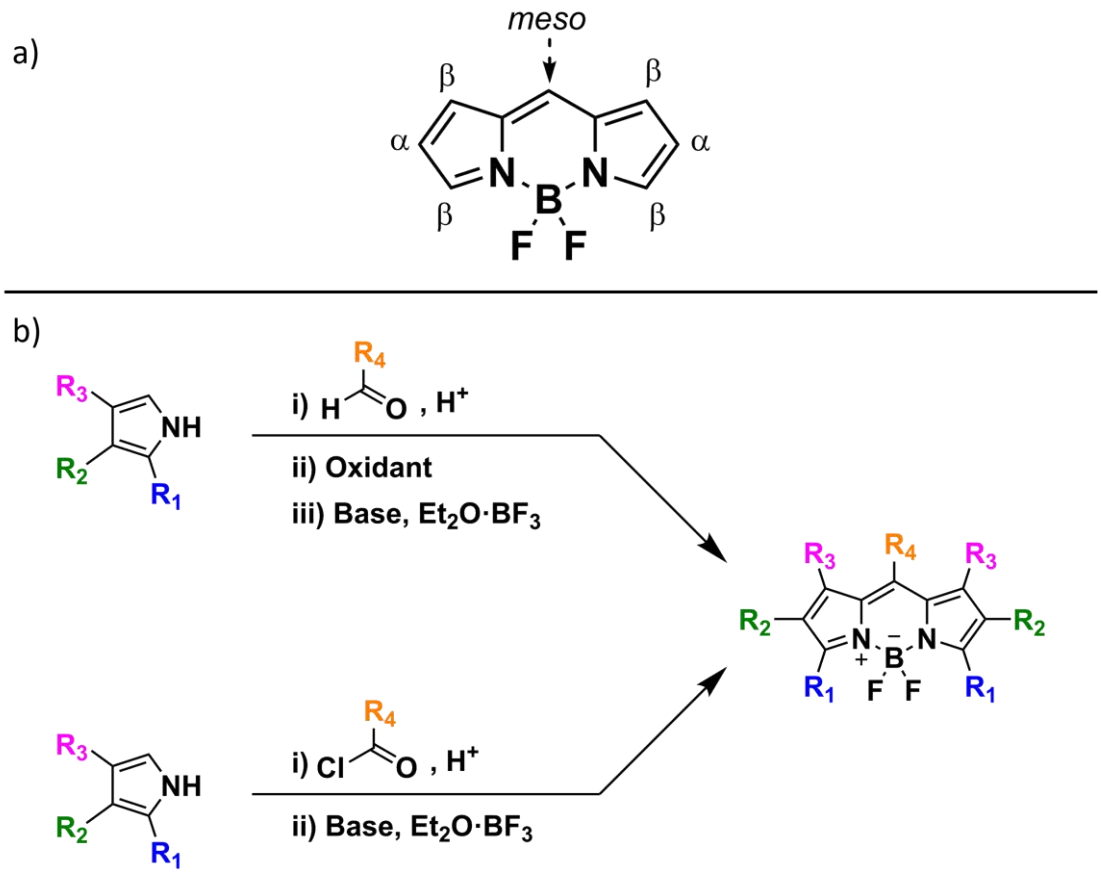

Scheme 3.1. a) General structure of the BODIPY core. b) Reaction of pyrroles with an aldehyde or an acyl chloride for the obtention of BODIPYs.

These compounds offer excellent chromophore properties, such as narrow absorption in the visible spectrum, high absorptivity values, high fluorescence quantum yields,[123] and outstanding thermal and optical stability. However, their main advantage compared to other organic dyes, is their versatility in post-synthetic structural modification due to their reactivity at the α, β and *meso*-positions (Figure 3.4).[122b, 124] This adaptability distinguishes them from other organic photocatalysts such as Rose Bengal or Methylene Blue, which, although being commercially available, are more challenging to post-modify. This ability to modify their structure makes it possible to synthetize BODIPYs with absorptions across the entire visible spectrum, ranging from 450 nm to 700 nm.[125] Due to their versatility and excellent properties, their applications have

extended to photodynamic therapy,[126] bioimaging and sensing,[127] organic-light emitting devices (OLED) or Light-Emitting Electrochemical Cells (LEEC),[125, 128] hydrogen evolution,[129] CO_2 reduction,[130] solar cells,[131] or photocatalysis.[132]

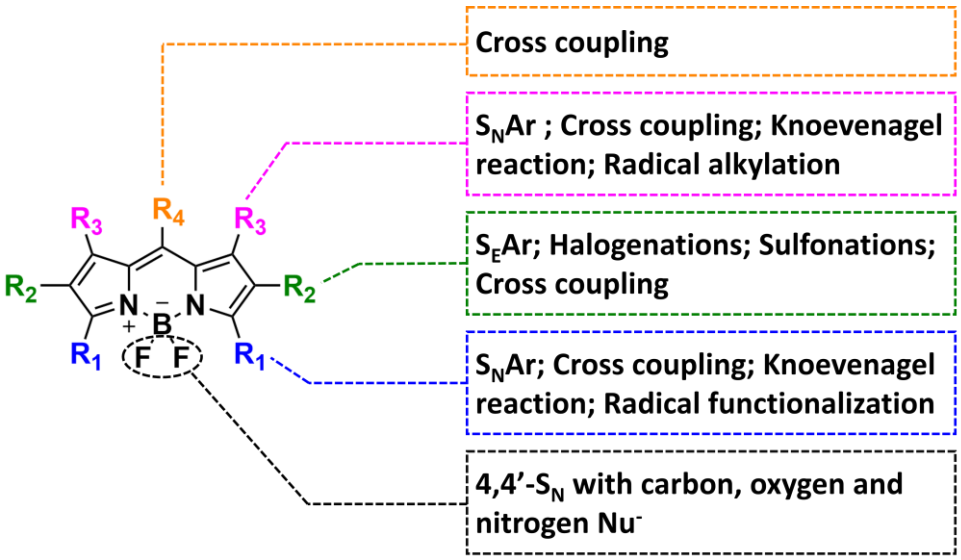

Figure 3.4. Post-synthetic structural modifications of the BODIPY core.

The application of BODIPYs in photocatalysis is limited by their short lifetime in their singlet excited states. In addition, they often exhibit low intersystem crossing efficiency, which limits their role as photosensitizers. However, structural modifications offer a promising avenue to overcome this impediment. Several strategies have been employed, including the incorporation of heavy atoms,[126d, 133] the synthesis of BODIPY dimers,[134] systems based on donor-acceptor strategies,[135] the establishment of twisted or orthogonal conformations,[136] and the formation of aggregates.[137] This chapter primarily explores two strategies, namely the incorporation of heavy atoms and donor-acceptor systems, often complemented by an orthogonal conformation, as already mentioned for other organic dyes. A brief summary of the influence of the two strategies is discussed below.

Heavy atom effect

The presence of heavy atoms favors ISC through spin-orbit coupling interactions, which often leads to the formation of long-lived triplet excited states.[133] A well-known strategy is to introduce halogens such as bromine or iodine into the α positions of the BODIPY core, which strongly affects the photophysical properties of the dye.[138] As an example (Scheme 3.2), the addition of two iodine atoms to these positions, although

producing similar absorption behavior for the two BODIPY molecules, the iodo-substituted BODIPY has a significant decrease in its fluorescence quantum yield (ϕ_F 71.2% to 2.7%).[132b] On the other hand, the lifetime of the triplet state increases to 57.1 μs.

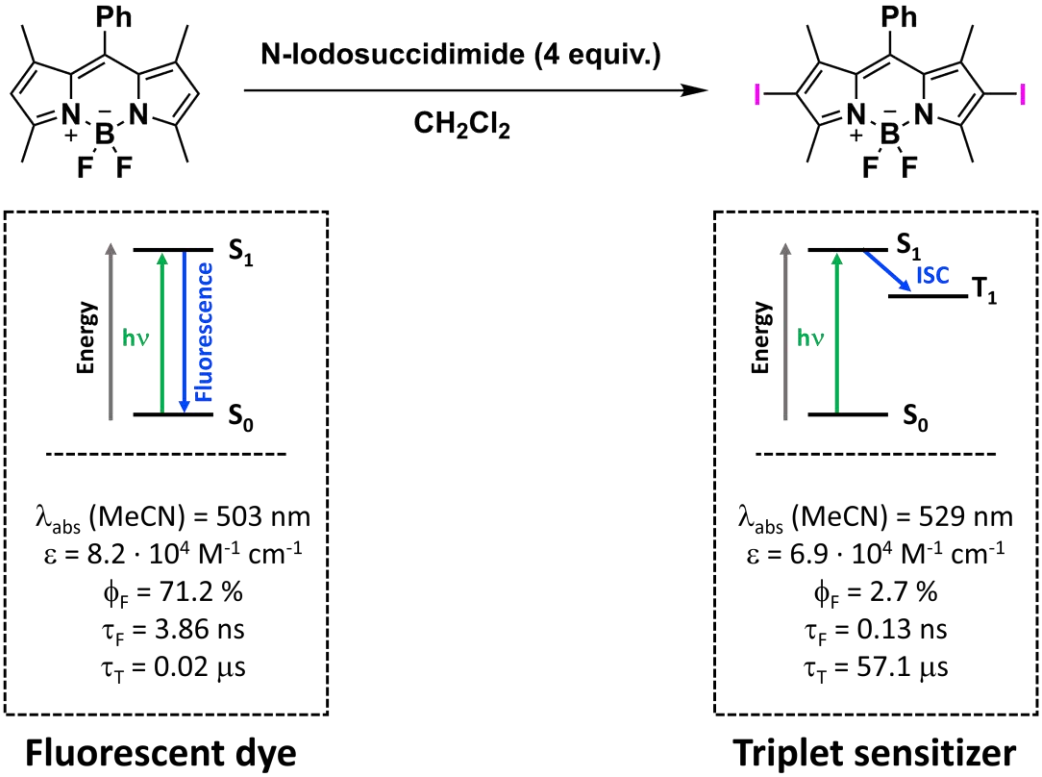

Scheme 3.2. Effect of two iodine atoms at α positions in the photophysical properties of a BODIPY.

In another example by Xie et al. (Scheme 3.3),[139] this strategy was used to synthetize different *meso*-substituted BODIPYs with and without iodine atoms at the α positions, resulting in different singlet oxygen quantum yields (ϕ_Δ). These values are often used as an indicator of the efficiency of the ISC process.

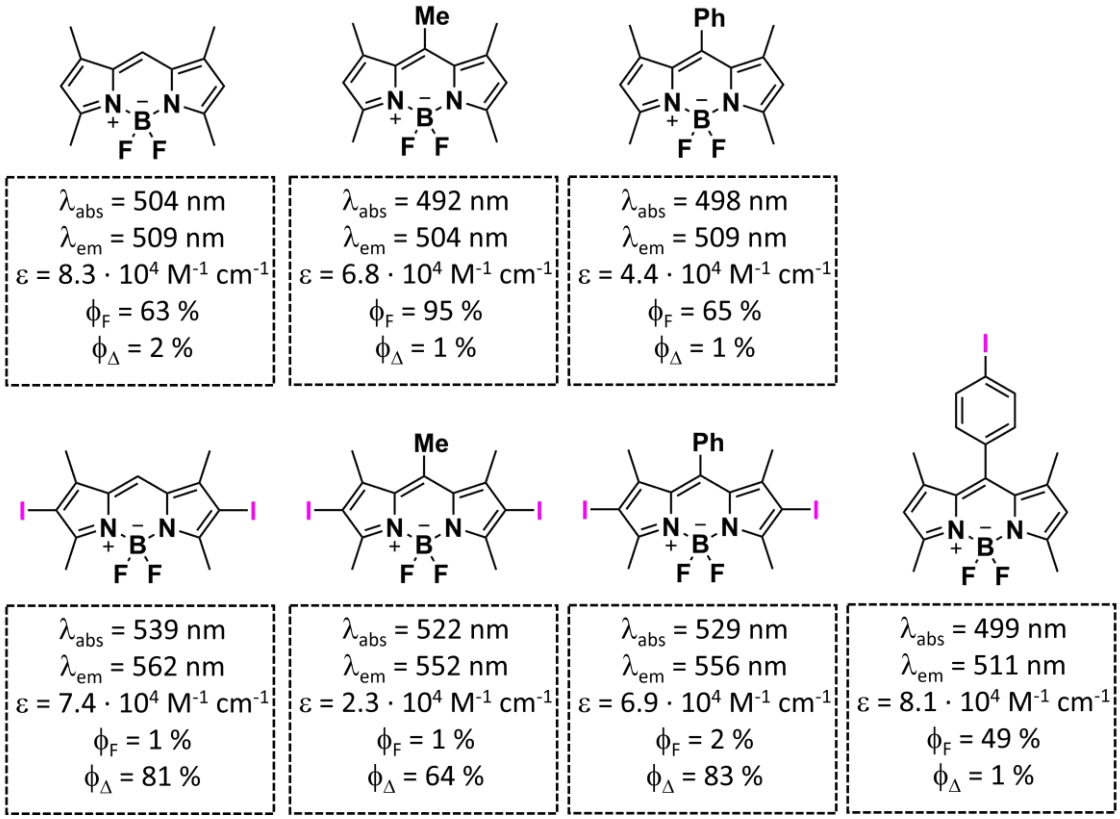

Scheme 3.3. Xie et al. work on the heavy atom effect in different *meso*-substituted BODIPYs.

As an alternative to halogen atoms, the inclusion of transition metals and one or more BODIPY moieties within the same molecule provides an intriguing synergy.[140] This approach not only improves the efficiency of ISC, but also alters the photophysical properties of both the coordination complexes and the BODIPY core in distinctive and compelling ways. Some research in this field has been carried out in the works of Sun et al.,[141] Zhang et al.,[129a] White et al.,[142] or Zhao et al.[143] (Scheme 3.4). These complexes bearing BODIPY moieties improve their absorption properties and the singlet oxygen quantum yields to respect with both the BODIPY core and the complexes. Interestingly, to our knowledge, the BODIPY moiety has not been incorporated into octahedral iridium(III) complexes through the cyclometalated ligands, but has been rather limited to the diimine ligand. Consequently, we embarked on the synthesis of phenylpyridine ligands with bonded BODIPY dyes, with the aim of exploring their properties and the potential for obtaining cyclometallated iridium(III) complexes with these ligands.

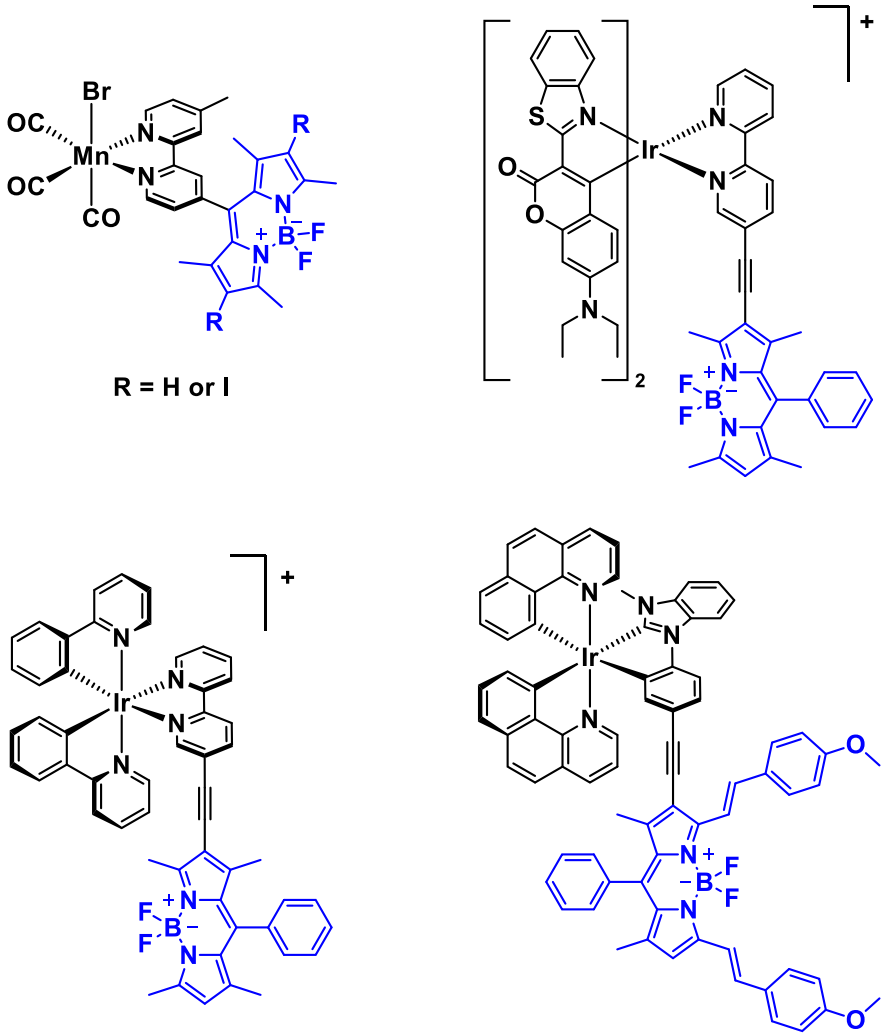

Scheme 3.4. Examples of octahedral complexes bearing BODIPY moieties.

Donor-acceptor-based BODIPYs

Although the aforementioned heavy atom strategy is widely recognized, the toxicity of heavy metals limits the biomedical applications of these BODIPYs.[135c] Consequently, the search for alternative strategies that can achieve robust ISC values is essential. In this context, BODIPY dyes based on donor-acceptor systems are synthetized by incorporating an electron acceptor or electron donor moiety at the *meso*-position. This group is also positioned orthogonally with respect to the BODIPY core, thus facilitating the spin-orbit charge transfer ISC.[135a, 135b] Yoon et al. reported the synthesis of a BODIPY molecule with a phenoxazine (PXZ, a strong electron donor) at the *meso*-position (Figure 3.5).[135c] Due to the torsion angle between the two planes, the HOMO-LUMO gap increased, and the energy difference between the singlet and triplet state was reduced. These molecules exhibited far-red/near infrared emissions and a large Stokes shift.

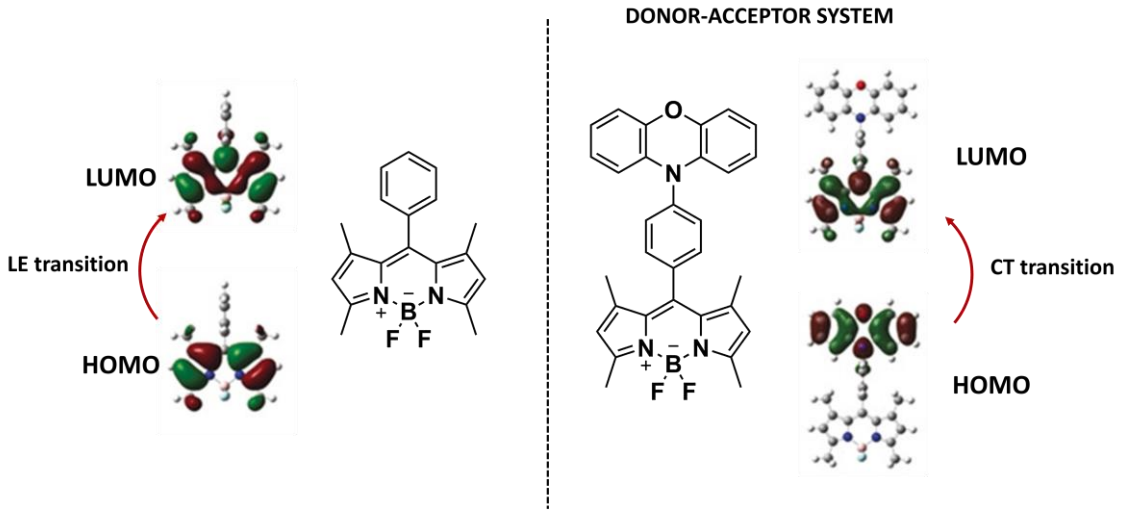

Figure 3.5. Donor-acceptor BODIPY (frontier MOs diagrams obtained from *Angew. Chem. Int. Ed.* **2020**, *59*, 8957).[135c]

In addition, a combination of these two strategies can be used to further amplify the impact on the excited states of the dyes (Figure 3.6).[124c, 144]

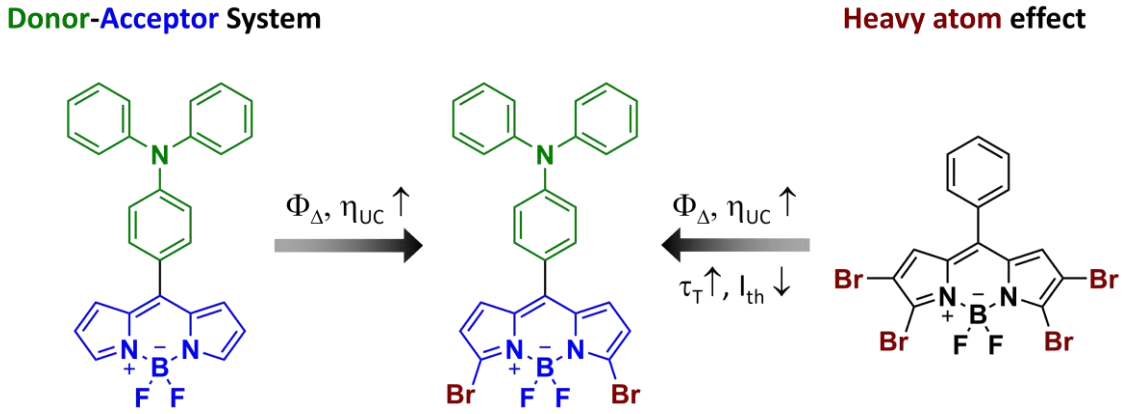

Figure 3.6. Synergistic effect on the combination of D-A system and heavy atom effect (η_{UC} denotes upconversion emission efficiency and I_{th} refers to intensity threshold).

As mentioned above, and despite the growing literature on the use of BODIPYs in various fields, their application in photocatalysis remains relatively limited in comparison. Although some examples demonstrate their effectiveness in Single Electron Transfer (SET) and Energy Transfer (EnT) processes, BODIPYs stand out in one specific EnT process: the generation of singlet oxygen. In fact, the high singlet oxygen quantum

yields of these molecules compared to other organic dyes have made them popular in photodynamic therapy (PDT). PDT is a non-invasive, selective method of treating certain types of cancer, as specific areas of the human body can be selectively targeted by irradiation in the presence of a photosensitizer and molecular oxygen.[145] When these three elements are combined, reactive oxygen species (ROS), such as singlet oxygen, are formed only in the irradiated area, leading to apoptosis or cell death.[146] However, singlet oxygen is not only useful in PDT, but also has great potential in organic synthesis,[147] as it is a highly reactive species that can oxidize compounds such as phenols, sulfides and amines.[148]

Due to the great interest in BODIPYs, and with the aim of obtaining iridium(III) compounds with BODIPY moieties in the cyclometalated ligands, we have proposed the synthesis of different compounds based on difluorophenylpyridine, which has been a recurring ligand throughout this thesis. In addition, we have explored the influence of the aforementioned strategies on the efficiency of the ISC process by measuring the singlet oxygen quantum yield, together with the performance of photocatalytic assays using the obtained photosensitizers.[149]

3.2 Synthesis and characterization of new BODIPY dyes

3.2.1 Synthesis

The synthesis of the precursors **L1** and **L2** was carried out by two different procedures. The synthesis of 2,6-difluoro-3-(pyridin-2-yl)benzaldehyde **L1** has already been described in the literature (Scheme 3.5),[150] and involves a Stille coupling, in which an organostannane nucleophilic group is coupled with an electrophilic alkyl halide, in the presence of a palladium catalyst.

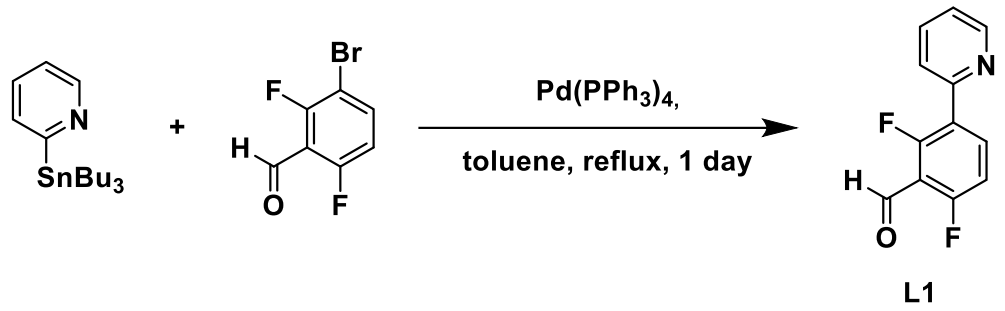

Scheme 3.5. Synthesis of **L1**.

A different procedure was used to obtain the precursor 2-fluoro-6-(N,N-dimethylamine)-3-(pyridin-2-yl)benzaldehyde (**L2**) (Scheme 3.6). For this synthesis, difluorophenylpyridine was dissolved in dry THF, and the solution was cooled to -80ºC. Next, n-BuLi was added to deprotonate the acidic proton of the difluorophenyl moiety. After 20 minutes, dry DMF was added dropwise, and the reaction was allowed to return to room temperature for 20 minutes with stirring. After this time, distilled water was added, and the compound was extracted with dichloromethane. After purification with a chromatographic column, two pure compounds **L1** and **L2** are obtained in 98% yield. Under these conditions, both compounds are obtained in about 50% yield, although the yield of either compound can be adjusted by keeping the reaction at -80°C longer after addition of DMF or by heating the reaction more rapidly to room temperature.

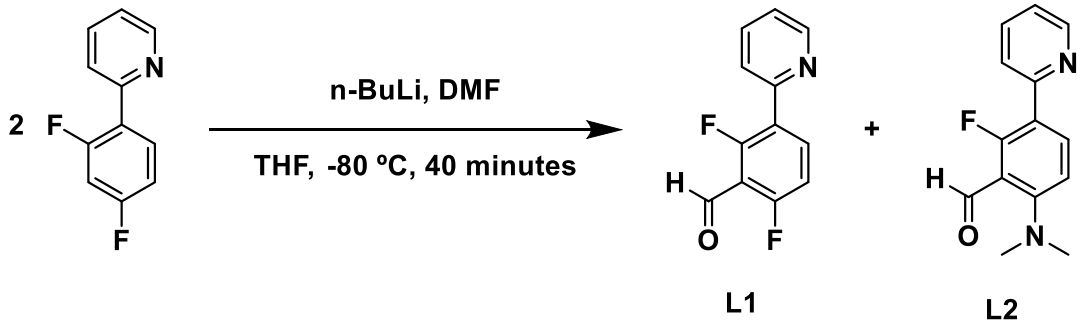

Scheme 3.6. One pot synthesis of **L1** and **L2**.

The synthesis of the BODIPYs **BD-1** and **BD-2** was carried out following a standard procedure starting from an aldehyde (Scheme 3.7).[151] For this purpose, the respective amounts of aldehyde and pyrrole were dissolved in dichloromethane under inert atmosphere. After stirring the reaction overnight at room temperature, *p*-chloranil was added as a weak oxidant to remove hydrogen from the pyrroles. After one hour, NEt_3 was added, followed by the addition of $BF_3{\cdot}OEt_2$. The color of the solution changes to a very dark bluish color. After neutralization, the compounds were extracted in dichloromethane and purified by column chromatography, gradually increasing the polarity of the eluent. The resulting compounds show very bright emissions in solution even under sunlight, while the solids have a reddish color with green iridescence. The yield of these reactions is within those observed for this type of procedure, ranging between 20% to 30%.

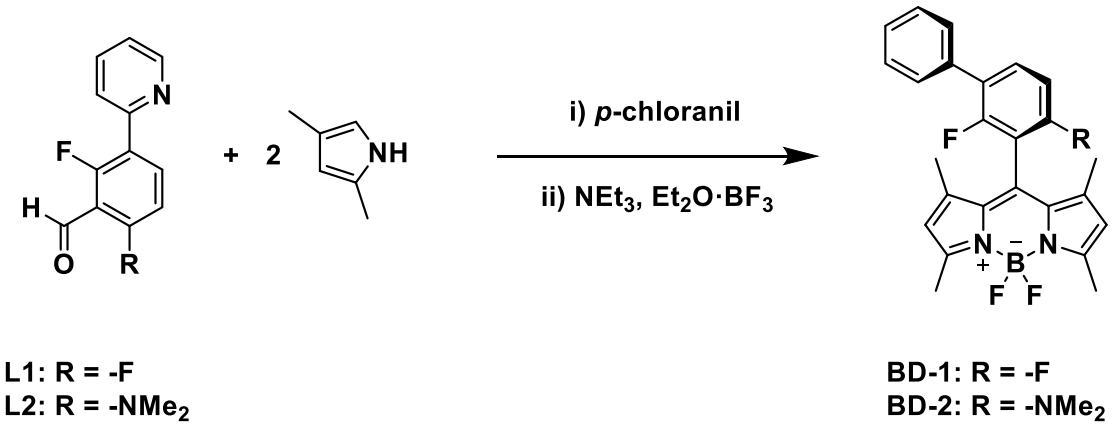

Scheme 3.7. Synthesis of **BD-1** and **BD-2** starting from their respective aldehydes.

Iodination of the α positions has been performed by a general procedure obtained from the literature (Scheme 3.8),[152] using an excess of N-iodosuccinimide (4 equivalents) as the iodinating agent. The reactions were carried out in dichloromethane, and the color of the solution changes immediately from red to dark violet when the N-iodosuccinimide is

added. After two hours of stirring, purification through chromatographic column afforded dark violet solids, which showed no luminescence under UV light.

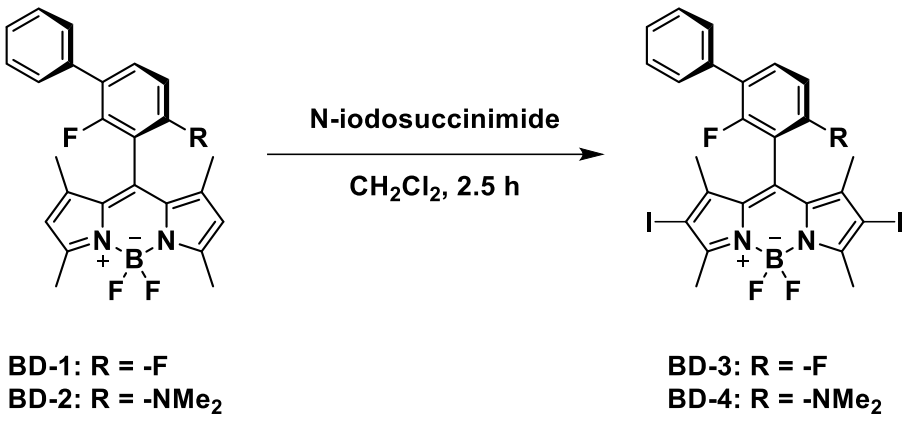

BD-1: R = -F
BD-2: R = -NMe_2

BD-3: R = -F
BD-4: R = -NMe_2

Scheme 3.8. Iodination of the α positions of the two BODIPY dyes.

3.2.2 Characterization

The synthetized BODIPY dyes were characterized by means of elemental analysis, mass spectrometry, IR and NMR spectroscopy. The most relevant data is summarized below, while the complete characterization can be found in the Experimental Part.

The mass spectra (MALDI-TOF or ESI, both positive and negative) of all the compounds show the molecular peaks corresponding to $[\mathbf{M}]^+$ or $[\mathbf{M}+H^+]$ as the base peak (100%). The IR spectra (Figure 3.7) showed similar fingerprint patterns among the BODIPYs, with very weak bands corresponding to the ν(C-H) vibrational modes of the aromatic rings (>3000 cm^{-1}) and of the methyl groups (<3000 cm^{-1}). An intense band is also observed for all compounds around 1530-1550 cm^{-1}, which is assigned to the B-F bond vibrational mode.[153] Other significant bands tentatively assigned to ν(C-F) and ν(N-B) were observed within the 1300-1310 cm^{-1} and 970-990 cm^{-1} regions of the spectra, respectively. The iodine-substituted BODIPYs **BD-3** and **BD-4** showed a very intense characteristic ν(C-I) band, located around 525 cm^{-1}.

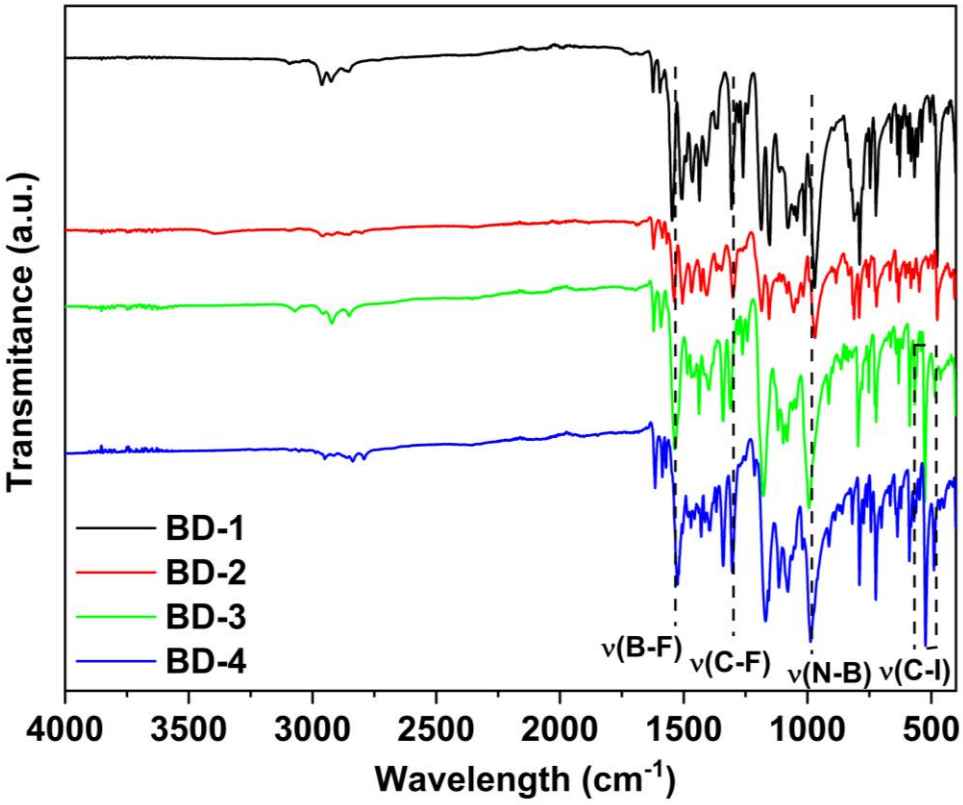

Figure 3.7. FTIR spectrum of the four BODIPY dyes.

As for the NMR spectra, all the ^{1}H, ^{13}C and ^{19}F signals were assigned via 2D experiments (see Experimental Part). The fluorine spectra of both **BD-1** and **BD-3** revealed characteristic signals of the fluorine bound to the boron atom, showing a quadruplet by coupling to ^{11}B with spin 3/2. In addition, a broadening effect was observed at the base of the signals, due to the coupling with ^{10}B (with spin 3) of lower intensity due to the lower isotopic abundance (80.35% vs. 19.65%, respectively). However, for both **BD-2** and **BD-4**, a complex second-order ABX-type system is observed (Figure 3.8). This means the inequivalence of the two fluorine atoms bound to the boron, causing an AB-type coupling between them and, subsequently, with the boron atom. The inequivalence is caused by a break in the symmetry of the molecule, possibly due to the presence of the dimethylamine group in the phenylpyridine moiety of the BODIPYs. As this group is larger than the fluorine atom in BODIPYs **BD-1** and **BD-3**, it prevents the rotation along the carbon$_{meso}$-carbon$_{phenylpyridine}$ bond, breaking the symmetry of the molecule and making the fluorine atoms non-equivalent. The same has been previously observed for BODIPYs with substituents that present a variable steric hindrance at the ortho position of the *meso*-phenyl moiety.[154]

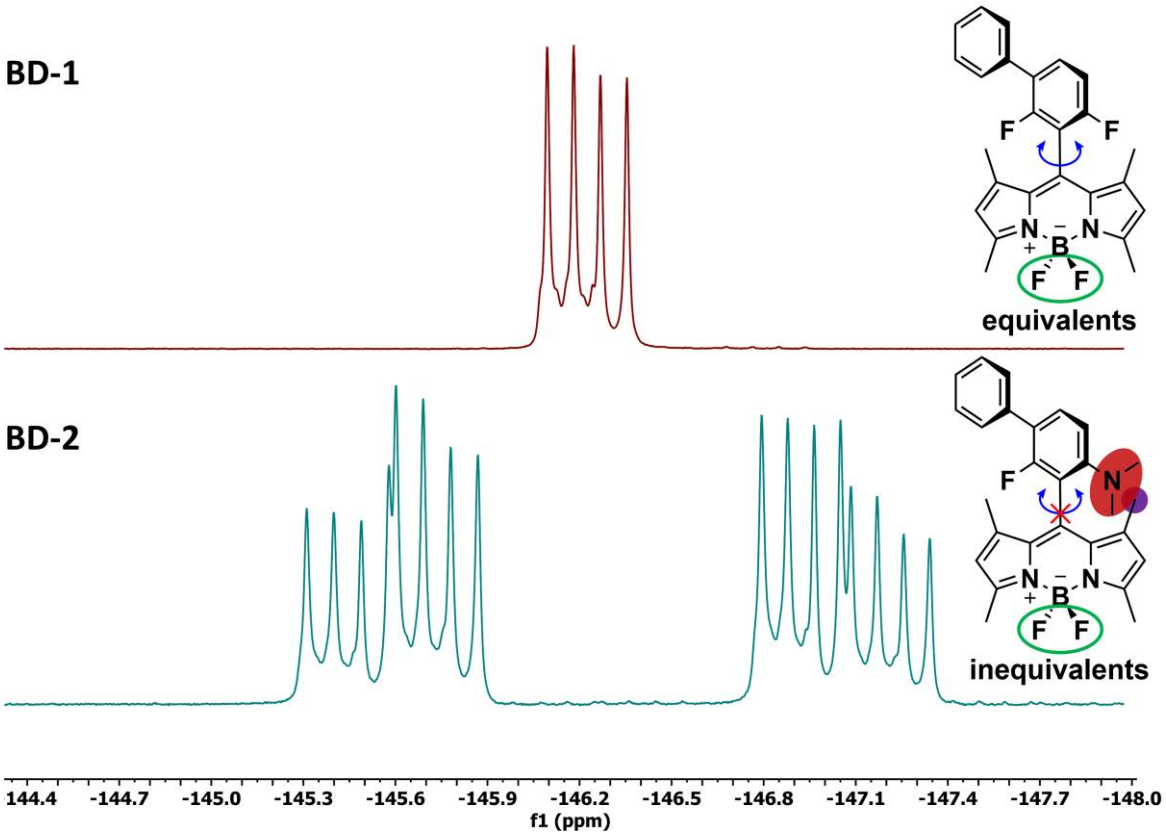

Figure 3.8. $^{19}F\{^{1}H\}$ spectra comparison of the -BF_2 signal of **BD-1** and **BD-2**.

The structure of **BD-4** was also confirmed by X-ray diffraction spectroscopy performed on a green crystal obtained by slow evaporation of the solvent in a solution of **BD-4** in deuterated chloroform. As shown in Figure 3.9, all the atoms of the BODIPY core are located in one plane, except for the two fluorine atoms attached to the boron atom, which has a tetrahedral geometry. The substituted phenylpyridine also adopts a planar arrangement, oriented at a dihedral angle of 76.65º with respect to the BODIPY core plane. The geometry exhibited by the dimethylamine group is also noteworthy. Previous studies by our research group hinted at the existence of planarity in cases where this group substituted aromatic ligands,[155] attributing it to the involvement of the two free nitrogen electrons in the aromaticity of the system. However, the geometry observed for **BD-4** shows a certain degree of pyramidalization at the nitrogen atom, resulting in a more tetrahedral geometry (C(26)-N(4)-C(27) 111.51º *vs*. tetrahedral angle = 109º), which suggests the localization of the nitrogen electron within the dimethylamine group. As commented later, density functional theory (DFT) calculations have been performed on all BODIPYs compounds, including their optimize structures for the S_0 and T_1 states (Figures A.1-2 and Table A.3 of the Annex). In particular, the calculated structural data for S_0 agree well with those observed experimentally for **BD-4**, including the pyramidalization at the nitrogen atom and the dihedral angle between the BODIPY and phenylpyridine main planes (72.91º *vs*. 76.65º, respectively).

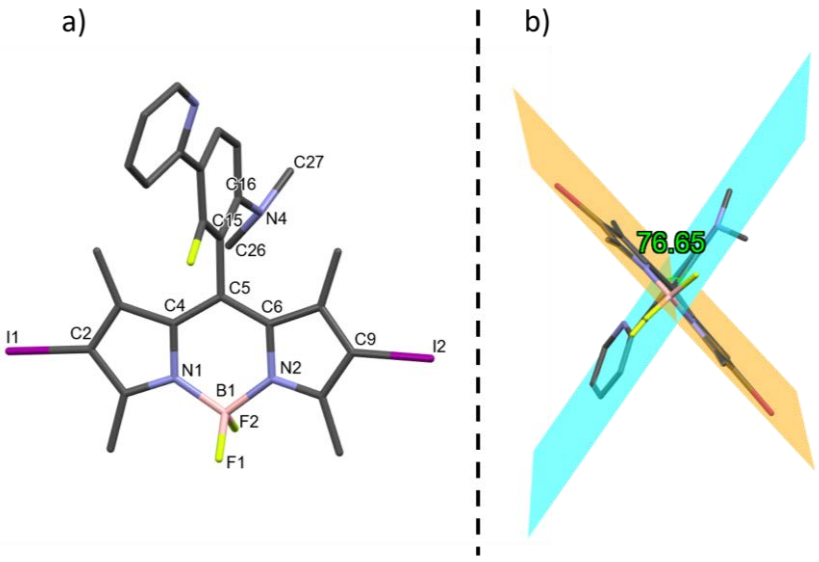

Figure 3.9. a) Molecular structure of **BD-4**. Selected bond distances and angles: C(5)-C(15) 1.493(3), B(1)-N(1) 1.546(3), B(1)-N(2) 1.553(3), B(1)-F(1) 1.392(3), B(1)-F(2) 1.388(2), N(1)-B(1)-N(2) 106.44(15)º, F(1)-B(1)-F(2) 109.55(16)º, C(26)-N(4)-C(27) 111.51(17)º. More data and the crystallographic data can be found in the Annex, Table A.1,2. b) Dihedral angle calculated between the best planes obtained for the phenylpyridine (in blue) and the BODIPY core (in orange).

3.2.3 Photophysical properties

ABSORPTION SPECTRA

Table 3.1 and Figure 3.10-Figure 3.11 show the absorption data for the four synthesized BODIPYs in $5x10^{-6}$ M THF solutions. The spectra exhibit the expected pattern for these compounds, featuring a very intense and narrow band in the low-energy region (500-550 nm). For **BD-1** and **BD-2** this maximum appears at *ca.* 515 nm, whereas a red-shift of approximately 30 nm occurs in the spectra of the two iodinated BODIPYs **BD-3** and **BD-4**, whose spectra are very similar to each other (λ_{max} = 550 nm). All compounds show remarkably high absorbance values, more intense in **BD-2** and **BD-4**. In the high-energy region, these two compounds also show a more intense band in the 300-320 nm range.

Table 3.1. Absorption data in THF solution ($5x10^{-6}$ M) of the four BODIPY dyes.

Sample	λ_{abs}/ nm (ε/ M^{-1} L^{-1})
BD-1	375 (5.3), 394 (3.8), 484_{sh} (20.2), 512 (65.6) ***THF***
BD-2	317 (27.4), 374 (5.2), 395 (4.1), 484_{sh} (21.9), 515 (77.8) ***THF***
BD-3	394 (10.9), 418 (9.4), 515_{sh} (24.9), 548 (64.5) ***THF***
BD-4	309 (53.1), 389 (12.9), 414 (9.8), 515_{sh} (28.0), 548 (77.3) ***THF***

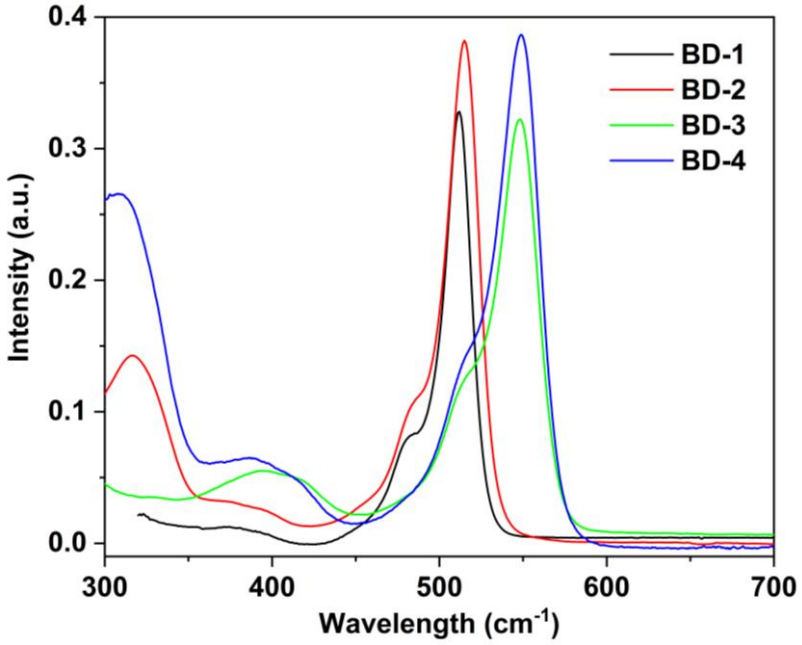

Figure 3.10. Absorption spectra of the four BODIPY dyes in THF $5x10^{-6}$ M.

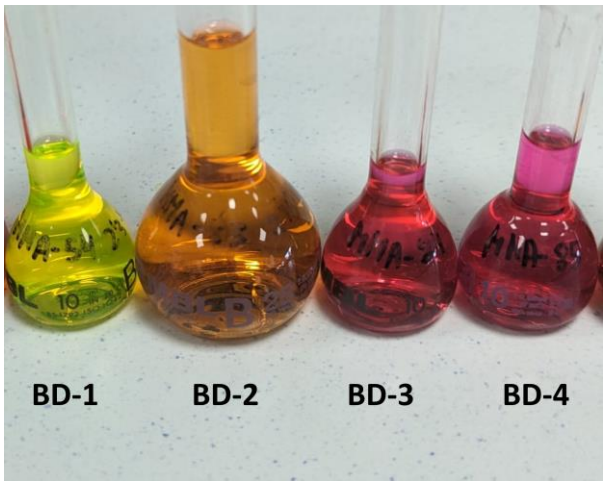

Figure 3.11. Solutions of the four BODIPYs in THF.

Typically, the strong absorptions in the low-energy region of BODIPYs are attributed to S_0-S_1 transitions, generally centered on the BODIPY core. To confirm the nature of these transitions, DFT calculations were performed on all BODIPYs compounds at the B3LYP/6-31G** level, using a PCM solvation method with tetrahydrofuran as solvent (the derived information can be found in the Annex). The calculations confirm the assignment of the $S_0 \rightarrow S_1$ transition for **BD-1** and **BD-3**, with a remarked Locally Excited (LE) character centered on the BODIPY (Figure 3.12; Tables A.4-A.6 and Figure A.9 in the Annex). However, for **BD-2** and **BD-4**, the main absorption leans toward an $S_0 \rightarrow S_2$ transition with a higher oscillator strength than $S_0 \rightarrow S_1$ (Annex, Tables A.4, A.5 and A.7) and a smaller energy difference between HOMO and HOMO-1. These transitions show a mixed character between HOMO → LUMO and HOMO-1 → LUMO excitations, the latter being more prominent in **BD-2**. In this case, the transition shows a mixed LE character centered on the BODIPY, together with a charge transfer (CT) character from the phenylpyridine to the BODIPY. The presence of the dimethylamine group significantly affects the HOMO and HOMO-1 orbitals, potentially causing their displacement towards this area of the molecule compared to their analogues with the fluorine atom (Figure 3.12). Two reasons may explain this influence: Firstly, its electron-donating character with respect to the fluorine atom, and secondly, the larger size of this group, which results in an orthogonal position of the *meso*-substituent and eliminates the possibility of rotating along the $carbon_{meso}$-$carbon_{phenylpyridine}$ bond (as it has also been observed in the $^{19}F\{^1H\}$ NMR spectra). Previous observations on BODIPYs exhibiting a donor-acceptor character, also favored by the perpendicular geometry,

indicate that the CT character of this absorption is more favored the higher the electron-donating capacity of the substituent (the phenylpyridine in this case), constituting the BODIPY core as the acceptor.[132d]

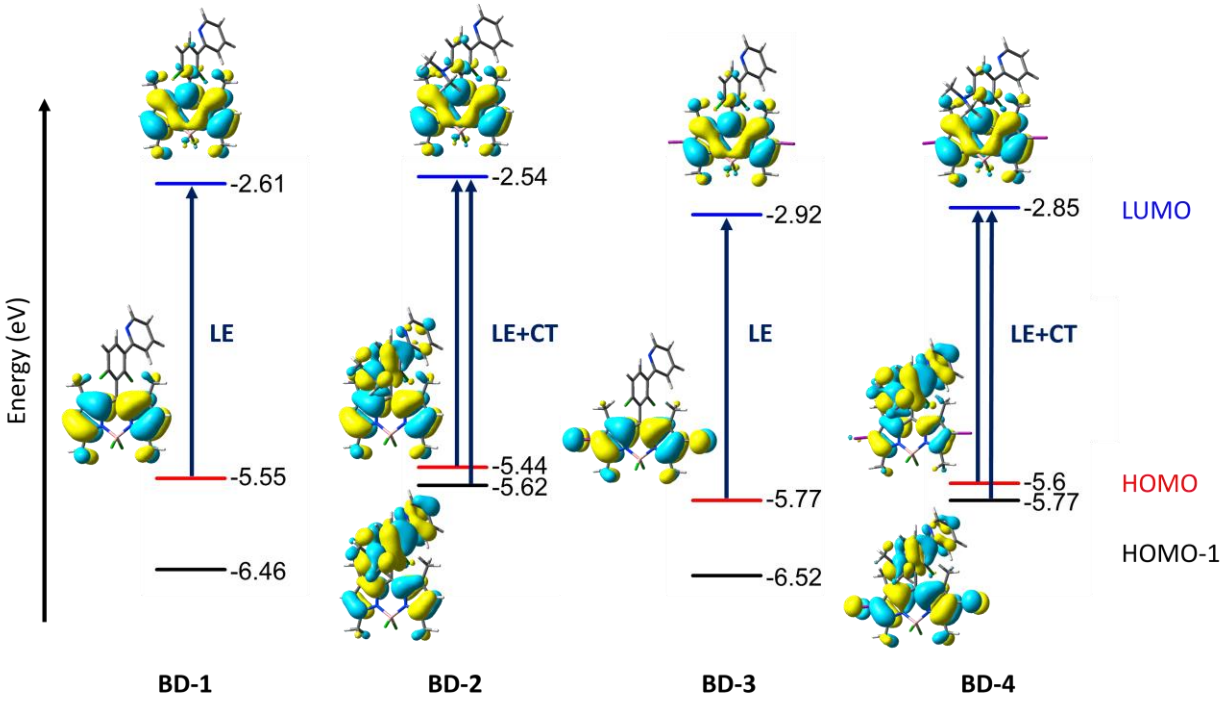

Figure 3.12. Schematic representation of the frontier MOs of the four BODIPYs.

Finally, the bands observed in the high-energy region can be assigned by theoretical calculations to phenylpyridine-centered LE transitions, or CT transitions (BODIPY → ppy).

To further explore the influence of the dimethylamine group on the photophysical characteristics of the BODIPYs, the absorption spectra of **BD-2** and **BD-4** were also measured after the addition of stoichiometric amounts of hydrochloric acid. This causes the protonation of the amine, interacting with the free electron pair of the nitrogen and decreasing its ability to donate electrons. Figure 3.13 shows the comparison of the spectra of **BD-2** and **BD-4** together with their protonated analogues **BD-2H**$^+$ and **BD-4H**$^+$.

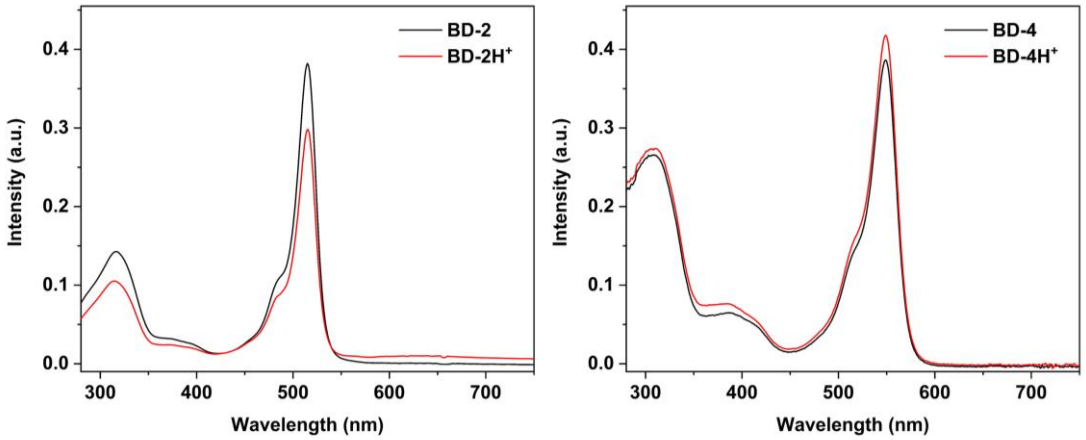

Figure 3.13. Normalized absorption spectra of **BD-2** protonated and unprotonated in THF $5x10^{-6}$ M (left), and of **BD-4** protonated and unprotonated in THF $5x10^{-6}$ M.

The absorption spectra reveal no fundamental differences between the protonated and non-protonated species, maintaining identical absorption maxima and the intense band in the high-energy region at ca. 310 nm. However, theoretical calculations of **BD-2H**$^+$ show a shift in the primary character of the transition at the absorption maximum at 515 nm, indicating an excited state with LE character centered on the BODPIY group, similar to that of **BD-1**. This confirms the possible influence of the free electron pair of the amino group on the CT character of the **BD-2** transition. However, although the calculations reveal this difference (Figure 3.14), the spectra obtained are still very similar for both compounds.

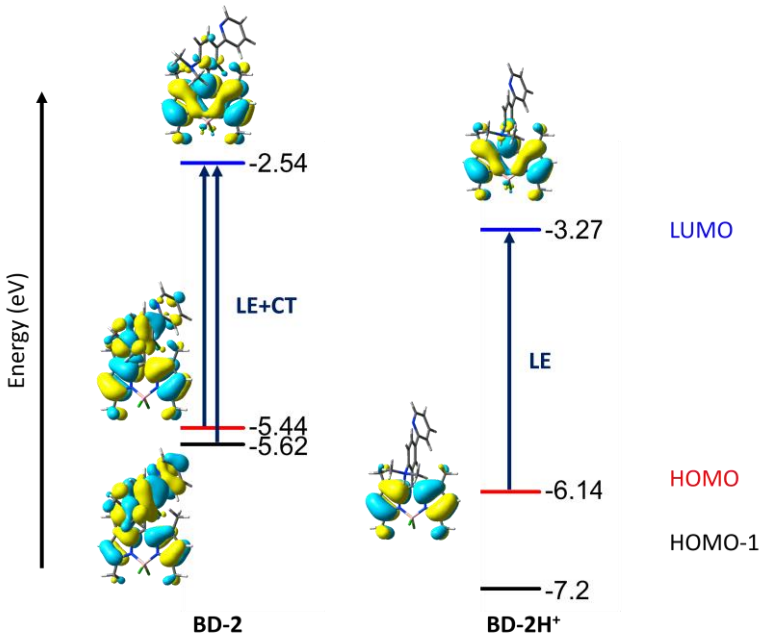

Figure 3.14. Schematic representation of the frontier MOs of **BD-2** and **BD-2H**$^+$.

EMISSION SPECTRA

Emission spectra have been measured for all compounds in $5x10^{-5}$ M THF solutions at both room temperature and 77 K. Additionally, for compound **BD-2** emissions were also measured in dichloromethane and toluene, as well as for its protonated analogue **BD-2H$^+$**. The data can be found in Table 3.2 and Figure 3.15-Figure 3.19.

Table 3.2. Experimental emission data in solid state and solution for the four BODIPY dyes.

Sample	Medium (T/K)	λ_{em}/ nm[a)]	τ/ns (λ_{em})[b)]	τ/μs (λ_{em})[c)]	ϕ/%[d)]
BD-1	THF (298)	527, 560_{sh}	8.38 (527)		95
	THF (77)	540, 570_{sh}			
BD-2	THF (298)	-	-	-	-
	THF (77)	540, 570_{sh}, 630_{sh}			
	DCM (298)	535, 570_{sh}	5.25 (535)	-	1.0
	DCM (77)	-	-	-	-
	Toluene (298)	535, 625	7.29 (535), 10.8 (620)	11.30 (620)	3.9
	Toluene (77)	540, 570_{sh}, 630_{sh}			
BD-2H$^+$	THF (298)	530, 570_{sh}, 635	5.86 (530), 3.76 (570), 6.35 (630)	10.19 (530)	5.0
	THF (77)	530, 570_{sh}			
	DCM (298)	530, 565_{sh}	4.34 (530)	14.70 (550)	11.8
	DCM (77)	-	-	-	-
	Toluene (298)	530, 565_{sh}	4.44 (530), 4.58 (570)	13.89 (570)	27.6
	Toluene (77)	530, 565, 620			
BD-3	THF (298)	580, 620_{sh}	3.35 (580)		0.6
	THF (77)	590, 615			
BD-4	THF (298)	-	-	-	-
	THF (77)	-	-	-	-

a) Data measured with λ_{exc} at 490 nm. Similar emission spectra obtained by excitation in the range 300 – 500 nm. b) Emissions lifetimes calculated as mono-exponential decay or an average of a bi-exponential decay, measuring with a LED lamp of 495 nm. c) Emissions lifetimes calculated as mono-exponential decay, measuring with a pulse lamp set at 490 nm. d) λ_{exc} at 490-500 nm.

Starting with compound **BD-1**, it shows a fluorescent emission typical of BODIPYs that do not undergo ISC (Figure 3.15, a). The spectrum shows a narrow band with a maximum of green emission at 527 nm at RT, a shoulder at 560 nm and a Stokes shift of

15 nm. The expected mirror image profile of the absorption and emission is also observed. This emission, attributed to locally excited (^{1}LE) state centered on the BODIPY part of the molecule, is characterized by a very short lifetime of 8.38 ns and a very high fluorescence quantum yield of 95%. In fact, its high quantum yield and small Stokes shift make the emission easily visible under sun light (Figure 3.15, b). The emission is slightly structured with a vibrational spacing of 1100 cm^{-1}, probably corresponding to a vibrational mode that was assigned in the IR spectrum to the N-B bonds. This structuring of the fluorescence band can be observed in all emission spectra measured for the BODIPYs, but is more pronounced in the low-temperature spectra for **BD-2** and **BD-2H**$^+$. The 77 K spectrum of **BD-1** shows a bathochromic shift of 13 nm, maintaining the same emission profile.

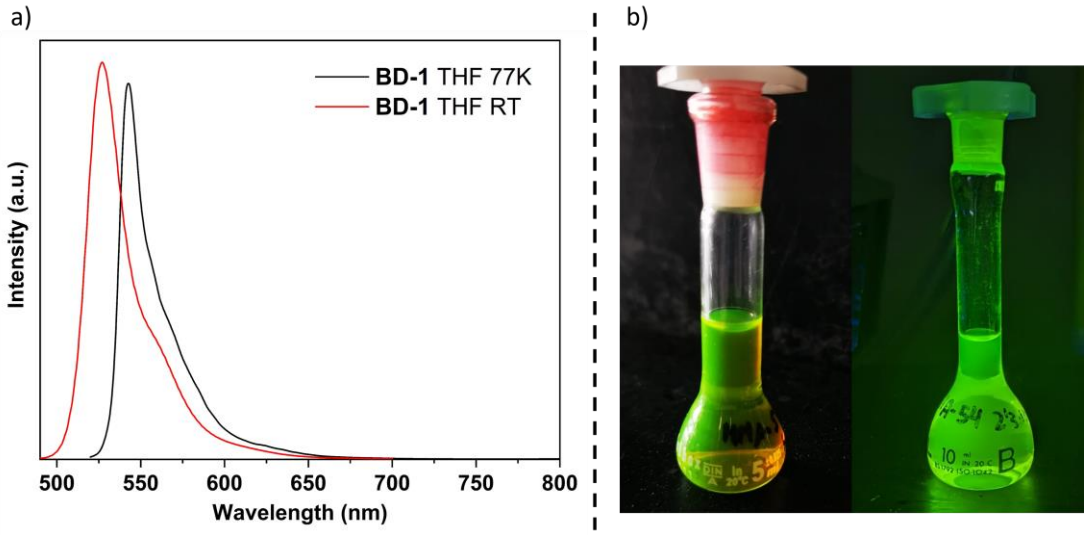

Figure 3.15. a) Emission spectra of **BD-1** in THF 5x10^{-5} M at RT and 77 K. b) Photos of the solution under visible light (left) and under UV light (365 nm, right).

BD-2 and **BD-2H**$^+$ show the highest degree of solvent-induced variation in emission intensity. Nevertheless, the emission maxima remain unchanged in all solvents [λ_{max}(emission) = 535 nm for **BD-2**, and 530 nm for **BD-2H**$^+$], with a slight bathochromic shift at low temperatures in the case of **BD-2**. The normalized and non-normalized emission spectra for this compound can be found in Figure 3.16. **BD-2** shows no emission at RT in THF, while in dichloromethane and toluene a low intensity luminescence can be observed, with 1.0% and 3.9% quantum yields, respectively. The 535 nm maximum band can be assigned to a fluorescence emission, with lifetimes of 5-7 ns and a Stokes shift of 20 nm. The low quantum yields point to non-radiative decay, either from the S_1 state or

from dark triplet states. In the low energy range, a broader band appears in toluene, with a maximum at 625 nm and a lifetime of 11.30 μs. These data suggest a phosphorescence band from a triplet charge transfer (^{3}CT) state, favored by the orthogonal position of the *meso*-substituent. This assignation is also supported by similar cases found in the literature.[156] It is interesting that this band is visible in toluene, and not in dichloromethane or THF, where the charge separation of a CT state would be better stabilized. However, for other BODIPYs with Donor-Acceptor character, the explanation given is that if the CT state becomes excessively stabilized in polar solvents, this could lead to rapid charge recombination to the ground state, or an IC to a lower energy state, leading to deactivation by non-radiative means. This would also explain the lower quantum yield compared with toluene obtained in CH_2Cl_2 or THF compared to toluene. At 77 K, **BD-2** is practically non-emissive in THF and dichloromethane, while in toluene shows a brighter luminescence (as shown in the photographs of Figure 3.18) formed mainly by a structured fluorescence emission at 540 nm and a slight shoulder at 630 nm, probably due to an inefficient ISC at low temperature.

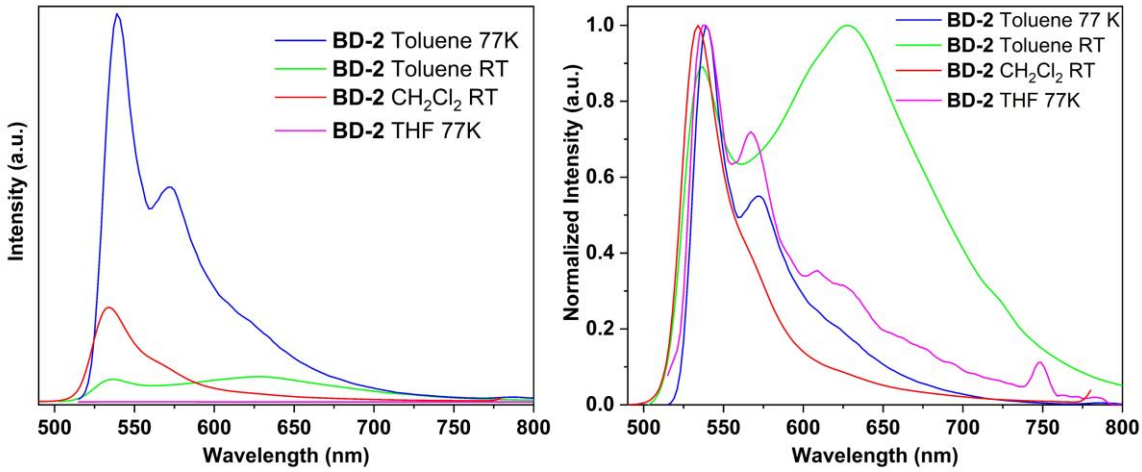

Figure 3.16. Emission spectra of **BD-2** in THF, Toluene and CH_2Cl_2 ($5x10^{-5}$ M) at RT and 77 K (left), and the normalized spectra (right).

At room temperature, **BD-2H$^+$** exhibits a similar but brighter fluorescence pattern than **BD-2** (Figure 3.17), with the maximum at 530 nm (Table 3.2). Notwithstanding, in this case, the emission in THF solution is that which clearly shows a phosphorescence component with a maximum at 635 nm. The quantum yield is 27% in toluene at RT, falling to 11.8% and 5.0% in dichloromethane and THF, respectively. A Stock shift of

15 nm has been calculated. At 77 K, the emissions are less intense than at room temperature (Figure 3.18) or very weak; again mainly due to a more structured fluorescence emission.

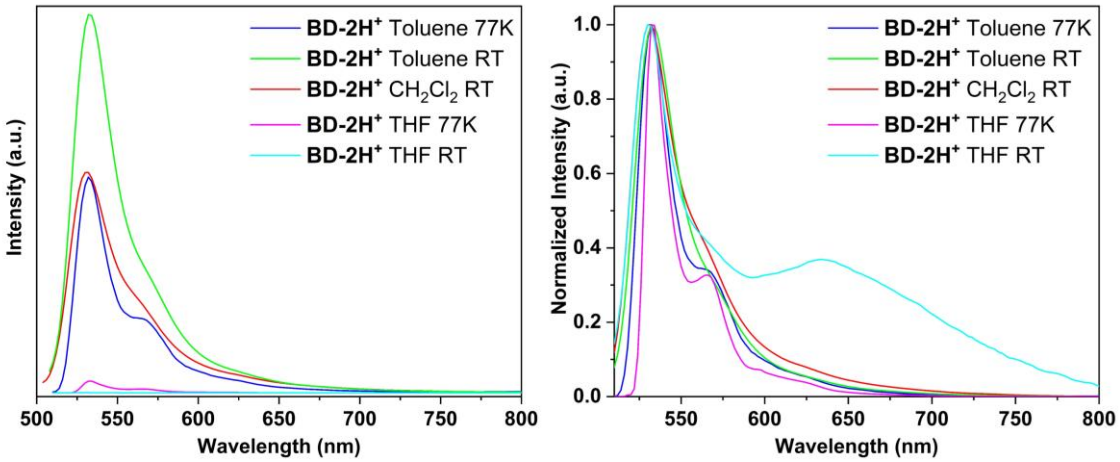

Figure 3.17 Emission spectra of **BD-2H**$^+$ in THF, Toluene and CH_2Cl_2 ($5x10^{-5}$ M) at RT and 77 K (left), and the normalized spectra (right).

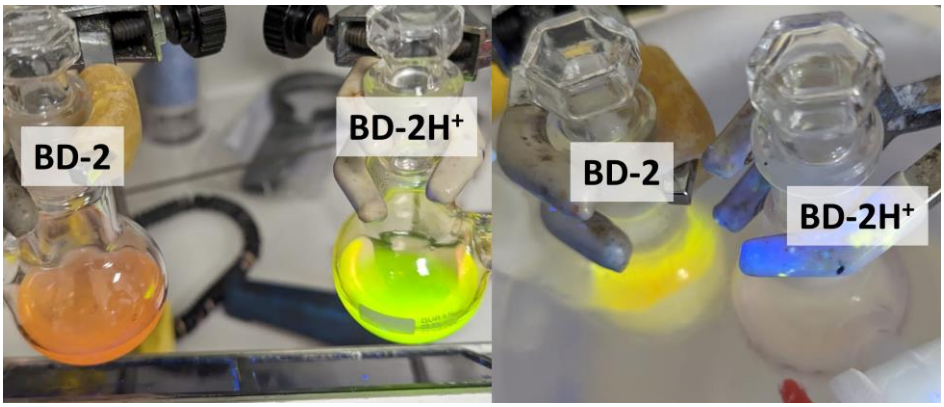

Figure 3.18. Pictures of **BD-2** and **BD-2H**$^+$ in Toluene at RT (left) and 77 K (right).

Initially, the emission behavior suggested a luminescence mainly contributed by a typical fluorescence similar to **BD-1** and **BD-2**, with very short lifetimes, and a low quantum yield due to the ISC to a dark triplet state similar to **BD-2**. However, lifetime measurements between 530 and 570 nm revealed two results: a very short lifetime (4-5 ns) that can be associated with a fluorescence emission, and a much longer lifetime (10-14 μs). To elucidate these results, emission spectrum and quantum yield measurements were performed in toluene after oxygenating the solution for 5 min (Figure

3.19). This solvent was chosen because it has the highest quantum yield for **BD-2H**$^{+}$ at room temperature. Also, deoxygenation was performed using the Freeze-Pump-Thaw technique to ensure complete removal of oxygen from the solvent.

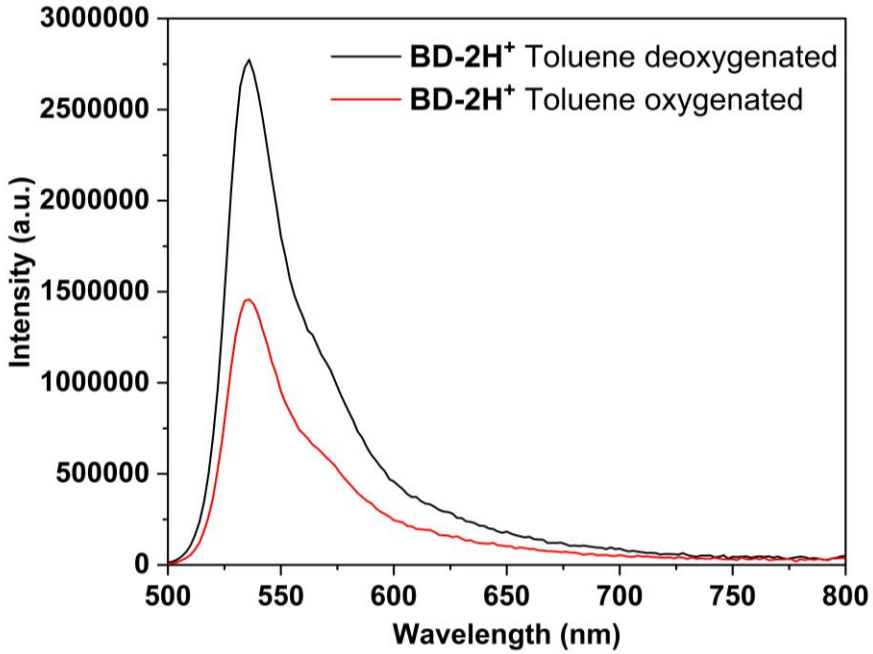

Figure 3.19. Comparison of BD-2 emission in Toluene 5x10^{-5} M in a deoxygenated sample, and after bubbling for 5 minutes with oxygen.

As can be seen in Figure 3.19, the band intensity of the sample decreases drastically after oxygenation, although the relative height of the maximum and shoulder of the band is maintained. This rules out the possibility of a phosphorescence emission with a maximum at 570 nm contributing to the double component lifetime. The quantum yield after oxygenation drops from 27.9% to 5.0%. All these results suggest the existence of some TADF character in the emission, with the band observed in the deoxygenated spectrum representing a mixture of normal and delayed fluorescence. The triplet state is probably a dark state, as observed in many organic molecules, since the phosphorescence of the triplet states is still a spin-forbidden process.[34c] This explanation would also describe the decrease in emission intensity in rigid media, since the decrease in temperature would prevent the reverse intersystem crossing (rISC, Figure 3.20).

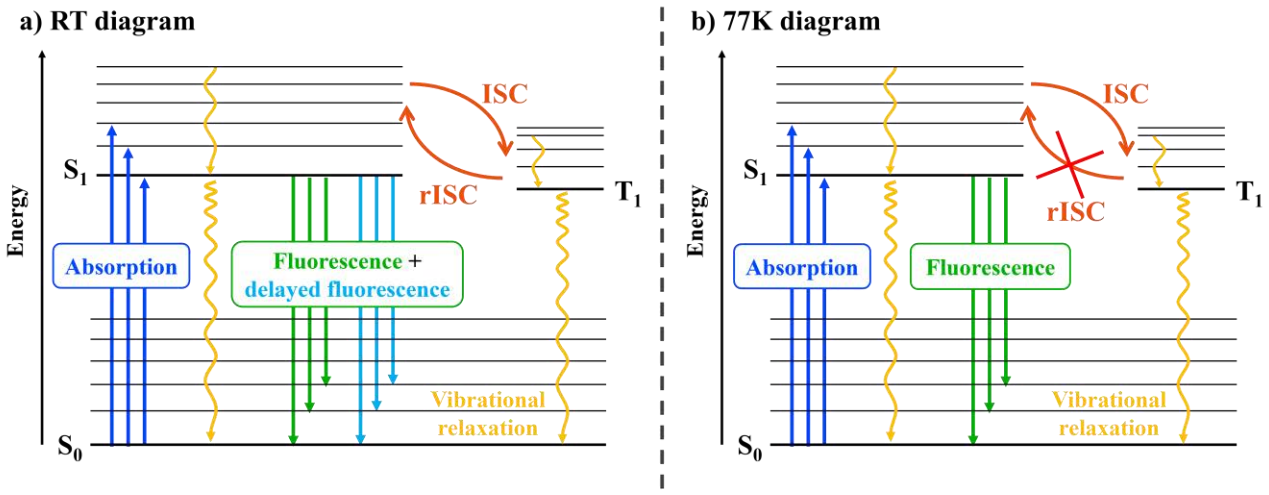

Figure 3.20. Jablonski representation of the processes at RT *vs*. low temperature.

Although the optimization of T_2 or higher states has not been carried out by theoretical calculations, TD-DFT calculations performed for **BD-2H**$^+$ (Anex, Table A.6) provide a rough estimate of its energy, with rISC being more likely to occur from a hot state T_2 or T_3, closer in energy to S_1. Moreover, since the T_1 state is considerably far from T_2 in terms of energy, the return to the S_1 state can compete with non-radiative deactivation. Similar behavior has been found in the literature for BODIPYs with *meso* aromatic substituents featuring dimethylamine groups, although the study of their behavior is not detailed in the article.[157] However, although all the data obtained are suggestive of TADF behavior, it is necessary to complete the study by measuring the lifetimes of this sample at different temperatures, measurements which are expected to be completed in the coming weeks, and before submitting this work for publication.

Finally, compounds **BD-3** and **BD-4** appeared non-emissive in solution in both THF and toluene. Only the emission spectrum for **BD-3** could be recorded in a $5x10^{-5}$ M solution in THF (Figure 3.21). However, the quantum yield at room temperature was less than 1%, which prevented the acquisition of lifetime data. At low temperature, a bathochromic shift similar to that of **BD-1** can be observed, together with a slight band structuring. These observations, combined with the singlet oxygen quantum yield values (see next section), point to an efficient ISC for these compounds, due to the heavy atom effect of the two iodine atoms.

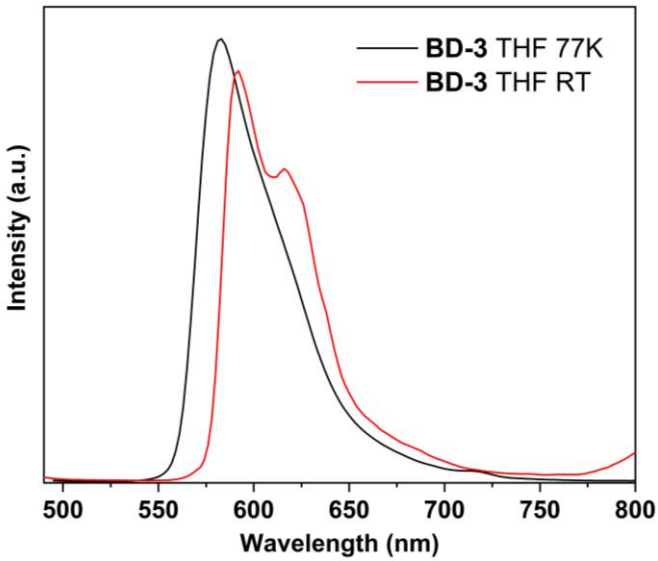

Figure 3.21. Emission spectra of **BD-3** in THF solution ($5x10^{-5}$ M) at RT and 77 K.

SINGLET OXYGEN QUANTUM YIELD

As mentioned earlier in the chapter introduction, singlet oxygen generation serves as another indicator of ISC efficiency in the literature, comparing the ability to generate singlet oxygen with the emission quantum yield. As these molecules emit mainly from the singlet state, low quantum yields together with high singlet oxygen generation point to a very efficient ISC process and to the population of the T_1 state.

THF was chosen as the solvent for these measurements, as only fluorescence-derived bands were observed for all BODIPYs in this solvent at room temperature. The method used consists of varying the absorption intensity of a compound that reacts rapidly with singlet oxygen, generating another invisible species in the visible range. Specifically, 1,3-diphenylisobenzofuran (DPBF) was used, which has an intense absorption with a maximum at 410 nm. Its oxidation reaction is shown in Scheme 3.9. Thus, by mixing the photosensitizer together with DPBF and irradiating with visible light, the variation of the absorption as a function of irradiation time can be obtained (Figure 3.22). By using an external standard with absorptions similar to those of the photosensitizers, and comparing the linear fit, the singlet oxygen quantum yield can be obtained (Figure 3.23). For more details on the procedure, see the Experimental Part.

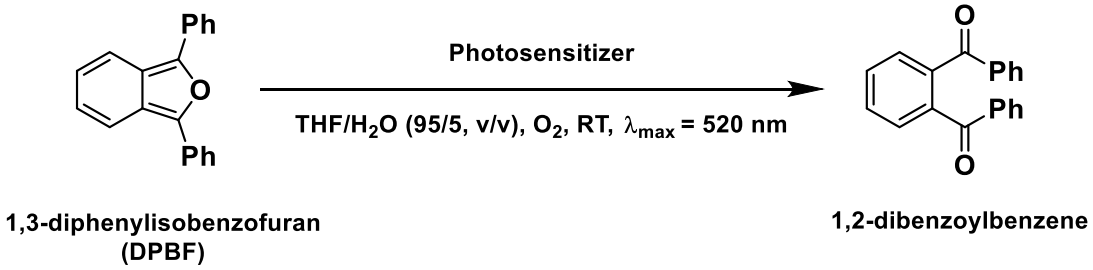

Scheme 3.9. Oxidation reaction of DPBF.

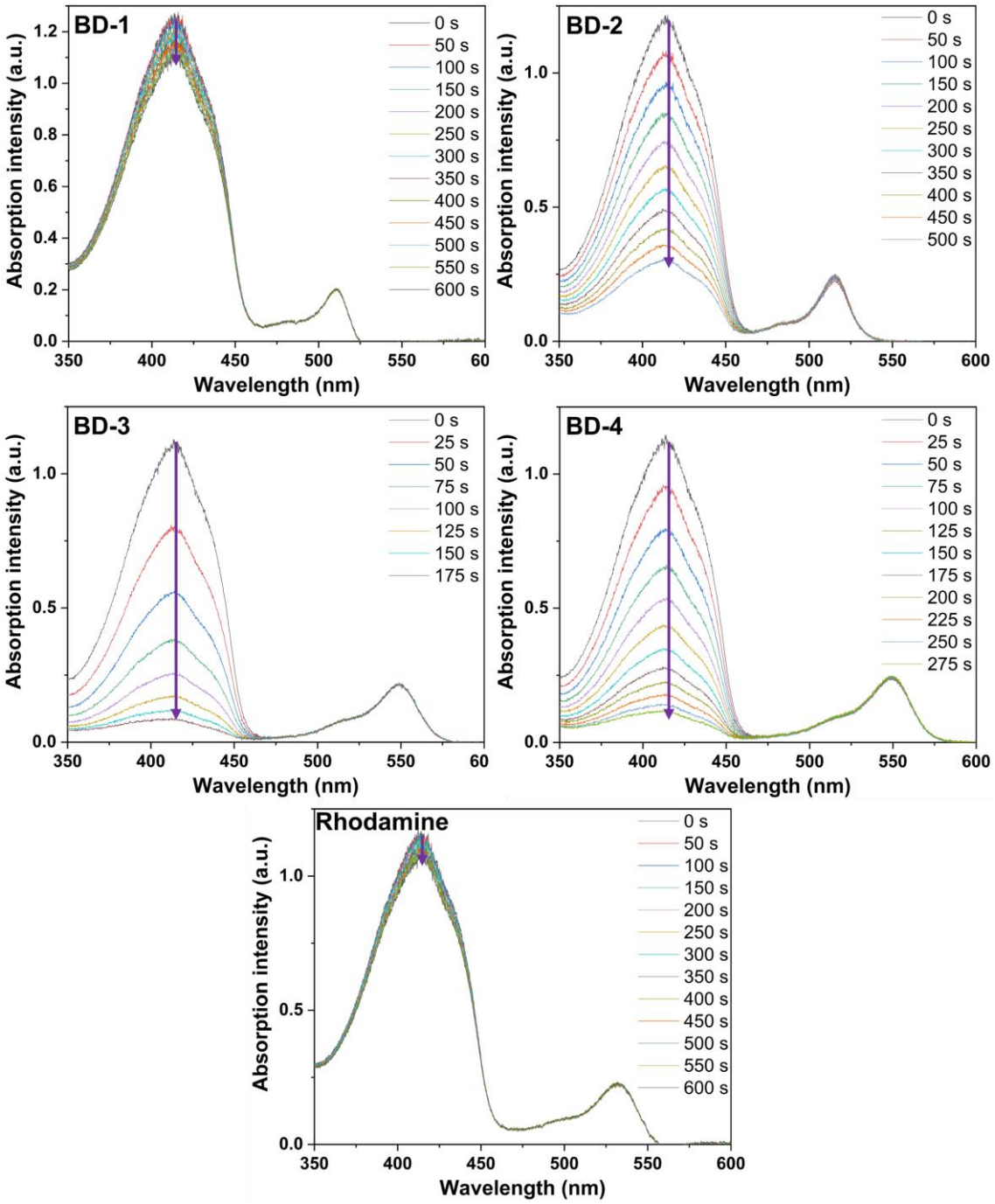

Figure 3.22. Changes in the absorbance at 410 nm of the $^1O_2$ scavenger DPBD in THF solution in the presence of the four BODIPY dyes and the standard (Rhodamine).

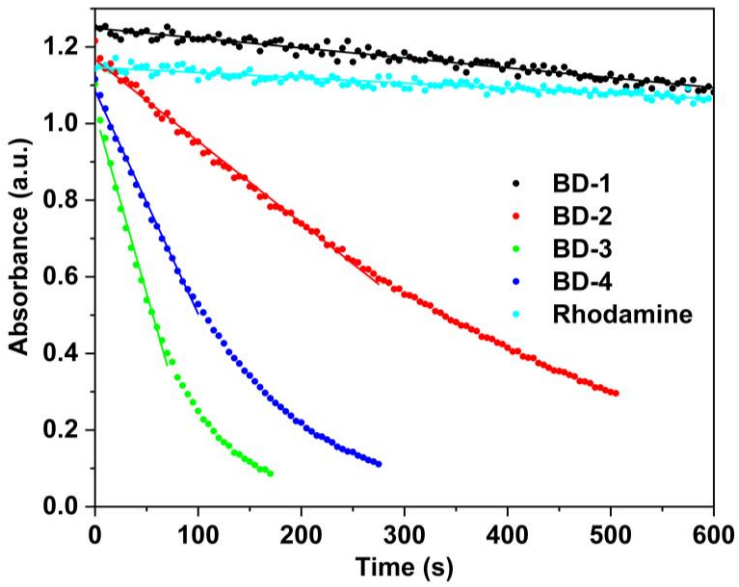

Figure 3.23. Linear fit of the absorbance *vs*. time.

The singlet oxygen quantum yield results (ϕ_Δ^{PC}) can be found in Table 3.3, together with the quantum yield values in THF ($5x10^{-5}$ M). Rhodamine B was chosen as the external standard, because it has very similar absorption to the synthesized BODIPYs and its singlet oxygen quantum yield has been measured, although it is very low.[158]

Table 3.3. Experimental values of the slope of the linear fit, the singlet oxygen quantum yields (ϕ_Δ^{PC}) and the fluorescence quantum yields (ϕ_F).

Sample	Slope	ϕ_Δ^{PC} (%)	ϕ_F (%)
Rhodamine B	-1.37E-04	0.016	-
BD-1	-2.59E-04	5.2	95.0
BD-2	-2.13E-03	35.9	0
BD-3	-9.43E-03	93.6	5.0
BD-4	-5.82E-03	59.0	0.6

As expected, **BD-1** has a very low singlet oxygen quantum yield of 5.2%, in line with its high fluorescence quantum yield of 95.0%. The absence of heavy atoms or orthogonality at the *meso*-position substituent means a minimal ISC in this BODIPY. However, for compound **BD-2** a ϕ_Δ^{PC} value of 35.9% is obtained, although no emission is observed at room temperature in THF. This highlights the donor-acceptor effect in the ISC, facilitated by the aforementioned orthogonality, which allows this molecule to function as a triplet photosensitizer.

The highest ϕ_{Δ}^{PC} values are obtained for BODIPYs **BD-3** and **BD-4**, with values of 93.6% and 59.0% respectively, attributable to the heavy atom effect. Moreover, their fluorescence quantum yield values are very low, confirming a very efficient ISC towards the triplet state. Interestingly, although **BD-4** possesses both heavy atom and donor-acceptor characteristics, its ϕ_{Δ}^{PC} is lower than that of **BD-3**. This discrepancy could be attributed to the polar nature of the solvent in the THF measurements, which stabilizes the possible CT state, as seen in its analogue **BD-2** without iodine. This solvent-induced stabilization could lead to a competition between oxygen sensitization and non-radiative deactivation, the latter being potentially more efficient in this medium. The influence of the solvent is further examined in the photocatalysis studies described in the next section.

3.3 Photocatalytic studies

The ability of the synthesized BODIPYs to generate singlet oxygen in the photocatalytic oxidation of dibenzylamine was also evaluated (Scheme 3.10).

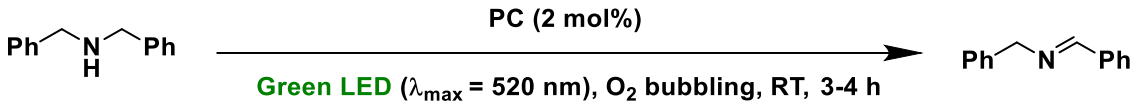

Scheme 3.10. Photocatalytic oxidation of dibenzylamine.

The reactions were carried out using a green LED of ~17 W power (λ_{max} = 520 nm) as irradiation source, with a photocatalyst ratio of 2 mol%. A constant oxygen flow was maintained during the irradiation. More detailed information of the experimental setup is given in the Experimental Part. The progress of the reaction was followed by ^{1}H-NMR spectroscopy and the conversion ratio was determined from the integrals of the signals shown in Figure 3.24.

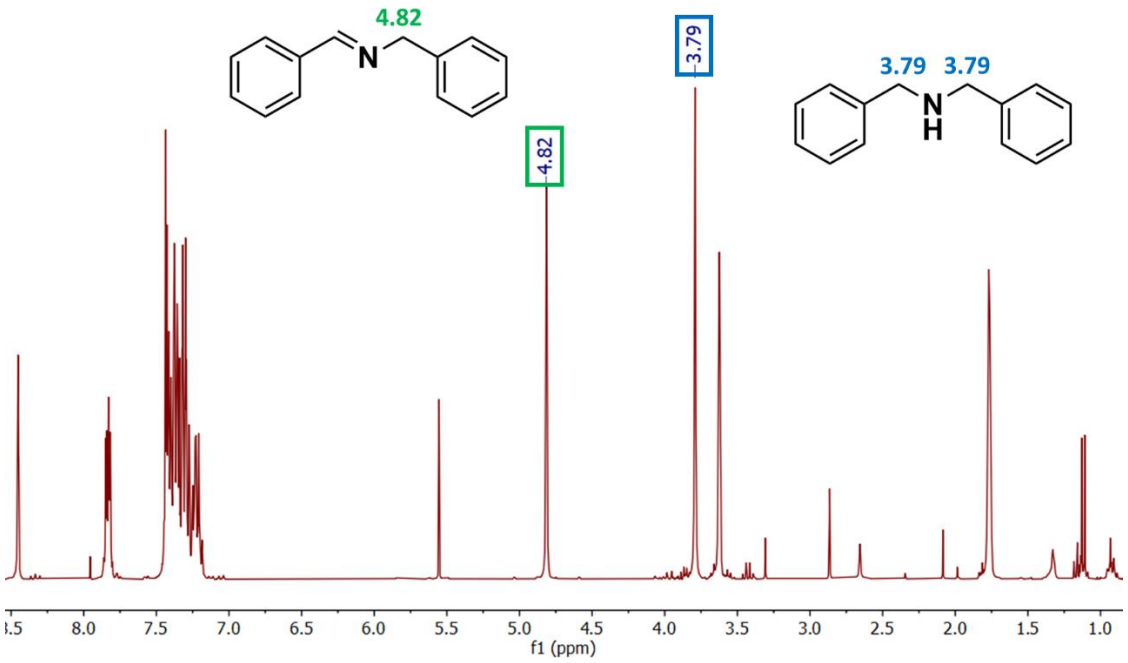

Figure 3.24. ^{1}H-NMR signals used to follow the conversion of the reaction.

Table 3.4 shows the conversion results, with the solvents used for each compound. Mainly toluene-d_8 and THF-d_8 have been used, with an additional test in deuterated chloroform for **BD-2**. The quantum yield values for singlet oxygen (ϕ_Δ^{PC}) in THF are also

included in Table 3.4. It should also be noted that background tests performed in the absence of photocatalyst, light or in an inert atmosphere did not yield conversion values.

Table 3.4. Results of the photocatalytic activity of the four synthetized BODIPYs in different solvents.

Photocatalyst	Solvent	% Conversion		ϕ_{Δ}^{PC} (%) in THF
		2h	4h	
BD-1	Tol-d_8	3	6	5.2
BD-2	Tol-d_8	31	59	35.9
	THF-d_8	11	27	
	$CDCl_3$	24	54	
BD-3	Tol-d_8	100	-	93.6
	THF-d_8	100 (75 min)	-	
BD-4	Tol-d_8	58	96	59.0
	THF-d_8	83	100 (3 h)	

The results show a direct correlation between the ϕ_{Δ}^{PC} of the photocatalysts and the reaction rate. **BD-1**, with minimal ISC, showed a conversion of less than 6% after 4 hours of irradiation. However, **BD-2** showed a significantly variable conversion depending on the solvent used. In THF, where the compound shows no emission and has a ϕ_{Δ}^{PC} of 35.9%, a conversion of 27% was observed after 4 hours, while in chloroform and toluene the conversion increased to almost 60%, pointing to a better sensitization to singlet oxygen in these solvents. **BD-3** and **BD-4** gave the most favorable results in both THF and toluene, showing superior conversion in THF.

As these two compounds showed the best results, the kinetic constants of the reaction were measured in both THF and toluene. For these experiments, the reaction set-up was maintained as before, but the irradiation was stopped every 15 minutes to perform an ^{1}H-NMR measurement. The reaction was repeated consistently three times for each photocatalyst and solvent, with the average values used for the analysis and the standard deviation as weight in the fitting process. The results are shown in Figure 3.25, where the k'(min^{-1}) (slope) and R^2 values are also given. **BD-3** showed the highest kinetic constants in both solvents, two and three times higher than **BD-4** in toluene and THF, respectively. This fact may indicate a certain negative synergy between the heavy atom effect and the orthogonalization of the phenylpyridine group in **BD-4**. Notwithstanding, **BD-4** also

displayed very good values, reaching 80% and 60% conversion in THF and toluene after two hours.

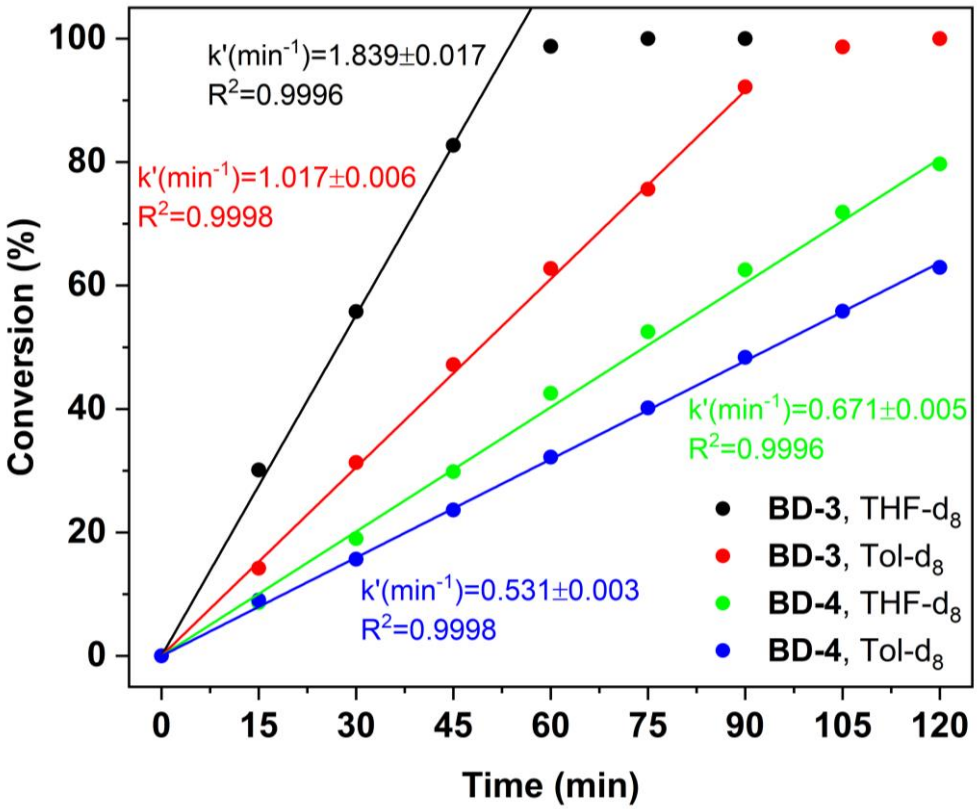

Figure 3.25. Linear fit of the conversion (%) *vs*. time (min) for the oxidation of dibenzylamine in THF-d_8 and Tol-d_8 using **BD-3** and **BD-4** as photocatalysts. k'(min^{-1}) is the 1st order reaction rate pseudophotocatalytic constant of the reaction.

Our donor-acceptor system in **BD-2** showed good efficacy for ISC, as demonstrated by all the data presented in this chapter. These results present **BD-2** as a competent photosensitizer without the need of heavy atoms. Moreover, the protonation of its dimethylamine group suggests the possibility of a BODIPY with TADF behavior. However, as shown by the singlet oxygen quantum yields and photocatalysis results, the best method for efficient ISC in our photosensitizers is the incorporation of iodine atoms at the α positions of the BODIPY core.

Summary and conclusions

Resumen y conclusiones

Summary

The great development experienced in recent years in the use of photocatalytic reactions in the synthesis of highly relevant organic compounds, together with the progressive application of these reactions in industry, has made it desirable to search for sustainable photocatalysts, maintaining the properties of the commonly used transition metal compounds. Although several strategies are being explored, in the context of this thesis two main ones have been studied: the heterogenization of emissive organometallic iridium(III) complexes, and the use of organic photocatalysts.

In **Chapter 1**, we have carried out the synthesis of five silica-based materials incorporating the iridium(III) complex [Ir(dfppy)$_2$(*dasipy*)]PF$_6$, which has two triethoxysilane groups in its structure. These materials have been obtained by different synthesis and functionalization techniques. By means of post-synthetic functionalization methods, a material formed by mesoporous silica nanoparticles with the complex incorporated by superficial covalent bonding (grafting) techniques has been synthesized (**NP_G**). Four other materials have been obtained by *in-situ* functionalization methods. Three of them are hybrid silica gels (**SiO$_2$_N**, **SiO$_2$_B** and **SiO$_2$_OD**), with different morphology that influence the degree of exposure of the complex to the medium, while the fourth is formed by discrete nanoparticles (**NP_IS**). After studying their textural and photophysical properties, their photocatalytic activity has been evaluated in the *trans*-stilbene isomerization reaction, which takes place through an EnT mechanism. Once the reaction conditions were optimized, and the kinetic constant for each material was obtained, the recoverability of the five materials was studied, analyzing the influence of the morphology and the functionalization method on their reusability.

In **Chapter 2** a new material was synthesized, based on the same cationic complex used in chapter 1. However, for the synthesis of this material no additional source of silica was added, resulting in a new kind of ionic material composed entirely of covalently bonded molecules of the complex. After studying the textural and photophysical properties of the material, it was used as a photocatalyst in two photoredox reactions, the photocatalytic dehalogenation of 2-bromoacetophenone, and the synthesis of phenanthridine from acyloximes. As with the materials synthesized in chapter 1, after optimizing the reaction conditions, the recovery and recyclability of the material in successive catalytic cycles was also studied.

Finally, in **Chapter 3**, we have developed the synthesis of four compounds based on the structure of BODIPYs with phenylpyridine groups in the *meso*-position. For the synthesized BODIPYs, two methods to improve the ISC efficiency have been studied. Firstly, the well-known influence of iodination of the alpha positions of the BODIPY fragment and, secondly, the possibility of orthogonalization of the phenylpyridine group at the *meso* position of the BODIPY, with formation of a D-A system. The photophysical properties of the four BODIPYs have been measured, and theoretical calculations were carried out to perform a better assignment of the transitions. To better establish the efficiency of the ISC, the singlet oxygen quantum yield of the four BODIPYs was measured, as well as their use in the photocatalytic reaction of the oxidation of dibenzylamine.

Conclusions

The conclusions drawn from the thesis are presented below, separated by their respective chapters for a better understanding:

Chapter 1

- The functionalization methods employed have successfully achieved the incorporation of the iridium complex in hybrid silica materials of different morphologies while preserving their photophysical properties.

- The differences in the photocatalytic activity of the materials for the *trans*-stilbene isomerization reaction can be attributed to a mixture between their emissive properties and the accessibility of the iridium complex to the medium. The material with the highest photoactivity is the nanoparticles functionalized by post-synthetic techniques (**NP_G**).

- The recoverability of the materials and their reusability is higher for materials synthesized by *in-situ* techniques.

- For the rational design of heterogeneous hybrid photocatalysts, it is necessary to find a balance between the accessibility of the chromophore to the medium, as well as its integration and protection in the material, and the mimicry of the emissive properties of the chromophore in solution. Of all the materials tested, **NP_IS** presents the best balance.

- Organometallic-silica hybrid materials have proven to be very stable heterogeneous photocatalysts for energy transfer processes under visible irradiation.

Chapter 2

- The synthesis of organometallo-ionosilicas has proven to be a very efficient method for the heterogenization of photocatalysts. The **SC-1** material is very versatile, being able to act as both a photooxidant and as a photoreductor.

- The recovery of the material can be adapted to the needs of each reaction, adding the necessary washing steps in each case.

- The recoverability values are very good, probably due to the possibility of accessing new layers of heterogeneous complex as leaching occurs.

- The irradiation time plays a very important role in the stability of the materials, as well as in their recoverability.

Chapter 3

- The orthogonality caused by the dimethylamine group in the BODIPYs **BD-2** and **BD-4** has been related by theoretical calculations with a charge transfer character in their excited states. Thanks to this feature, **BD-2** is a BODIPY with a good ISC efficiency thanks to the D-A system, being favored or hindered depending on the solvent.

- **BD-3** and **BD-4**, however, show the highest ISC efficiency, due to the heavy-atom effect of the two iodinated alpha positions.

- In the case of **BD-4**, some negative synergy between the heavy atom effect and the D-A system has also been detected, with a large variation in singlet oxygen quantum yields depending on the solvent used.

- All four BODIPYs have been successfully employed as organic photocatalysts, also using a green LED as irradiation source, instead of the more energetic blue light used in the previous two chapters.

- A greater influence on the ISC efficiency has been observed for BODIPYs with heavy atoms than for those with a D-A system.

- **BD-2H**$^{+}$ has been found to have very interesting photophysical properties of its own. All the experiments performed so far suggest a TADF behavior, which would be one of the first observed and studied in BODIPYs.

Resumen

El gran desarrollo que ha experimentado en los últimos años el empleo de reacciones fotocatalíticas en síntesis de compuestos orgánicos de gran relevancia, junto con la progresiva aplicación de estas reacciones en la industria ha hecho deseable la búsqueda de fotocatalizadores sostenibles, que mantengan las propiedades de los compuestos de metales de transición empleados habitualmente como fotocatalizadores. Aunque varias estrategias están siendo exploradas, en el contexto de esta tesis se han estudiado principalmente dos: la heterogeneización de complejos organometálicos luminiscentes de iridio(III), y el empleo de fotocatalizadores orgánicos.

En el **capítulo 1**, se ha llevado a cabo la síntesis de cinco materiales de base silícea, incorporando en su estructura el complejo de iridio(III) $[Ir(dfppy)_2(dasipy)]PF_6$, que cuenta en su estructura con dos grupos trietoxisilano. Estos materiales han sido obtenidos empleando diferentes técnicas de síntesis y funcionalización. Mediante métodos de funcionalización post-sintéticas, se ha sintetizado un material formado por nanopartículas mesoporosas de sílica con el complejo incorporado mediante técnicas de unión covalente o *grafting* (**NP_G**). Mediante métodos de funcionalización *in-situ*, se han obtenido cuatro materiales, tres de tipo gel (**SiO_2_N**, **SiO_2_B** y **SiO_2_OD**), con distinta morfología que afecta al grado de exposición del complejo al medio, y un cuarto que presenta nanopartículas discretas (**NP_IS**). Tras estudiar sus propiedades texturales y fotofísicas, su actividad fotocatalítica ha sido evaluada en la reacción de isomerización del *trans*-estilbeno, reacción que tiene lugar mediante un mecanismo de transferencia energética (EnT). Una vez optimizadas las condiciones de reacción, y obtenida la constante cinética para cada material, se estudió la recuperabilidad de los cinco materiales, observando la influencia de la morfología y el método de funcionalización en la capacidad de reutilización de los mismos.

En el **capítulo 2** se sintetizó un nuevo material, basado en el mismo complejo catiónico empleado en el capítulo 1. Sin embargo, para la síntesis de este material no se añadió ninguna fuente adicional de sílica, obteniéndose un nuevo tipo de material iónico formado exclusivamente por moléculas de complejo enlazadas de forma covalente entre sí. Tras estudiar las propiedades texturales y fotofísicas del material, se empleó como fotocatalizador en dos reacciones fotoredox, la deshalogenación fotocatalítica de la 2-bromoacetofenona, y la obtención de fenantridina a partir de aciloximas. Al igual que

con los materiales sintetizados en el capítulo 1, tras optimizar las condiciones de reacción, se estudió su recuperación y reciclabilidad en sucesivos ciclos catalíticos.

Por último, en el **capítulo 3**, se llevó a cabo la síntesis de cuatro compuestos basados en la estructura de BODIPYs, con grupos fenilpiridinas en la posición *meso*. En las BODIPYs sintetizadas, se han estudiado dos métodos para mejorar la eficacia del cruce intersistema (ISC). En primer lugar, la conocida influencia de la yodación de las posiciones alfa del fragmento BODIPY y, en segundo lugar, la posibilidad de ortogonalización del grupo fenilpiridina en la posición *meso* de la BODIPY, con formación de un sistema D-A. Se han medido las propiedades fotofísicas de las cuatro BODIPYs, y se realizaron cálculos teóricos para poder llevar a cabo una mejor asignación de las transiciones. Para terminar de establecer la eficacia del ISC, se midió el rendimiento cuántico de oxígeno singlete de las cuatro BODIPYs, así como su uso en la reacción de fotocatálisis de oxidación de la dibencilamina.

Conclusiones

Las conclusiones extraídas de la tesis se exponen a continuación, separadas por sus respectivos capítulos para una mayor comprensión:

Capítulo 1

- Los métodos de funcionalización empleados han conseguido con éxito la incorporación del complejo de iridio en materiales híbridos de sílica con distintas morfologías, preservando sus propiedades fotofísicas.

- Las diferencias en la actividad fotocatalítica de los materiales para la reacción de isomerización del *trans*-estilbeno se puede atribuir a una mezcla entre la accesibilidad del complejo al medio y sus propiedades emisivas. El material con mayor fotoactividad son las nanopartículas funcionalizadas mediante técnicas post-sintéticas **NP_G**.

- La recuperabilidad de los materiales y su capacidad de reutilizarlos es mayor en los materiales sintetizados mediante técnicas *in-situ*.

- Para el diseño racional de fotocatalizadores híbridos heterogéneos, es necesario encontrar un equilibrio entre la accesibilidad del cromóforo al medio, así como su integración y protección en el material, y la imitación de las propiedades emisivas del cromóforo en disolución. De todos los materiales probados, el que mejor equilibrio presenta es el **NP_IS**.

- Los materiales híbridos organometalo-sílicas han demostrado ser fotocatalizadores heterogéneos muy estables para procesos de transferencia energética bajo iluminación visible.

Capítulo 2

- La síntesis de organometalo-ionosílicas ha demostrado ser un método muy eficaz para la heterogeneización de fotocatalizadores. Además, el material **SC-1** es muy versátil, pudiendo actuar tanto como fotooxidante como fotoreductor.

- La recuperación del material se puede adaptar a las necesidades de cada reacción, añadiendo los pasos de lavado necesarios en cada caso.

- Los valores de recuperabilidad son muy buenos, posiblemente gracias a poder acceder a nuevas capas de complejo heterogéneo a medida que se produce lixiviación.

- El tiempo de irradiación puede jugar un papel muy importante en la estabilidad de los materiales, así como en su capacidad de recuperación.

Capítulo 3

- La ortogonalidad causada por el grupo dimetilamino en las BODIPYs **BD-2** y **BD-4** se ha relacionado mediante cálculos teóricos a un carácter de transferencia de carga en sus estados excitados. Gracias a esta característica, **BD-2** es una BODIPY que presenta una buena eficacia de ISC gracias al sistema D-A, viéndose favorecida o perjudicada según el disolvente.

- BD-3 y **BD-4** presentan sin embargo la mayor eficacia de ISC, debido al efecto del átomo pesado gracias a las dos posiciones alfa yodadas.

- Para **BD-4** se ha detectado cierta sinergia negativa entre los efectos de átomos pesados, y el sistema D-A, observándose una gran variación en la generación de oxígeno singlete según el disolvente empleado.

- Las cuatro BODIPYs han sido empleadas con éxito como fotocatalizadores orgánicos, empleando además como fuente de irradiación un LED verde, en lugar de la luz azul más energética empleada en los dos capítulos anteriores.

- Se ha observado una mayor influencia en la eficacia del ISC en las BODIPYs con átomos pesados, por encima de aquellas con un sistema D-A.

- BD-2H$^+$ ha resultado tener unas propiedades fotofísicas muy interesantes por sí misma. Todos los experimentos realizados hasta el momento hacen sospechar de un comportamiento TADF, que sería uno de los primeros observados y estudiados en BODIPYs.

Experimental Part

Experimental Part

Instrumental and spectroscopic techniques used in the characterization of both the compounds and materials

Elemental analysis

Elemental analyses were made in a Carlo Erba EA1110 CHNS/O microanalyzer (Chapter 1 and 2) or in a Perkin-Elmer 2400 CHNS/O microanalyzer (Chapter 3).

Mass Spectrometry

Mass spectra were recorded on a Microflex MALDI-TOF Bruker spectrometer operating in the linear and reflector modes using dithranol as the matrix. When recording Electrospray Mass spectra, an ESI/APCI Bruker Microtof-Q spectrometer was used, with positive and negative ion mode with MeOH/H_2O 90/10 and 0.1% formic acid as a mobile phase operating in the negative FAB mode.

Infrared Spectra

IR spectra were recorded both on a Nicolet Nexus FT-IR spectrometer from 4000 to 200 cm^{-1}, where all samples were prepared as KBr pellets, or on a Perkin Elmer FT-IR Spectrometer Spectrum Two with the diamond crystal ATR accessory in the wavenumber range from 4000 to 400 cm^{-1}.

Nuclear Magnetic Resonance (NMR)

NMR spectra were obtained on Bruker ARX-300 and ARX-400 spectrometers using $CDCl_3$ and acetone-d_6 as solvents. Chemical shifts are reported in parts per million (ppm) relative to external standards ($SiMe_4$ for ^1H and $^{13}C\{^1H\}$). All coupling constants are given in hertz (Hz). ^1H and $^{13}C\{^1H\}$ NMR spectra were assigned by means of 2D experiments (^1H-^1H COSY and ^1H-^{13}C HSQC and HMBC).

UV-Vis Spectroscopy

UV-vis spectra in solution were recorded on an Agilent 8453 spectrophotometer, using quartz cuvettes with 1 cm of optical path. Solid-state Diffuse Reflectance UV-vis (DRUV) spectra were acquired using a Shimazdu UV-3600 spectrophotometer with a Harrick Praying Mantis accessory coupled to it, and recalculated following the Kubelka Munk function. The samples were diluted in KBr powder for complexes and BODIPY dyes, and silica for the self-condensed material. The materials from Chapter 1 were recorded without diluting the samples and using silica as background.

Luminescence spectroscopy, lifetimes and quantum yields

The excitation and emission spectra for compounds in Chapter 1 were obtained on a Jobin-Yvon Horiba Fluorolog 3-11 Tau-3 spectrofluorimeter. For compounds in Chapter 2 and 3, the spectra were measured on an Edinburgh FLS 1000 spectrofluorimeter. The lifetime measurements were performed on either an Edinburgh FLS 1000 spectrofluorimeter with a μF2 pulse lamp (Power: 100 W, Fuse: 3.15 Amp A/S), or in a Datastation HUB-B with a nanoLED controller ad software DAS6 for shorter lifetimes. The nano-LEDs employed for these measurements were of wavelengths between 400 and 500 nm with pulse lengths of 0.8-1.4 ns. Quantum yields were measured using a Hamamatsu Absolute PL Quantum Yield Measurement System.

X-Ray Crystallography (Structure determination of BD-4)

Adequate pale-violet monocrystals of **BD-4** were obtained by slow evaporation of a solution of the compound in $CDCl_3$. X-ray diffraction intensity data were collected with a Bruker D8 QUEST (PHOTON 100 CMOS) area-detector diffractometer at 100 K, using graphite-monochromatic Mo-K_α radiation with an Oxford Cryosystem temperature controller. The images were collected and processed using Bruker APEX3 and SAINT programs,[159] carrying out the absorption correction at this point by semi-empirical methods using SADABS.[159] The structures were solved by intrinsic phasing using SHELXT,[160] and refined by full-matrix least squares on F^2 with SHELXL,[161] using the WINGX program suite.[162] All non-hydrogen atoms were assigned anisotropic displacement parameters.

Theoretical Calculations

Calculations of all compounds were carried out with the Gaussian 09[163] package (Chapter 1) or Gaussian 16[164] (Chapter 3) using Becke's three-parameter functional combined with Lee-Yang-Parr's correlation functional (B3LYP) in the singlet state (S_0) and the unrestricted U-B3LYP in the triplet state (T_1).[165] The basis set used was the LanL2DZ effective core potential for Ir and I atoms and 6-31G(d,p) for the ligand atoms.[166]

In Chapter 1, optimization of **1** on the singlet state (S_0) was performed by Cintia Ezquerro using a modelized geometry. Dyes in Chapter 3 were also optimized using a modelized geometry. The S_0 geometries of all molecules were characterized as a true minimum since no negative frequencies were found in the vibrational frequency study of the final geometry. DFT and TD-DFT calculations were carried out including the solvent effect of THF, using the PCM approach.[167] The MO diagrams and the orbital contributions were generated with Gaussian 09/16 software and Gauss-Sum[168] program, respectively. The emission energies were calculated as the difference of the DFT-optimized T_1 geometry for both states. The results were visualized with GaussView.

Physical Gas Adsorption

All measured materials were centrifuged and air dried before their textural characterization. The porous texture of the samples was characterized by nitrogen adsorption/desorption measurements at 77 K on an AUTOSORB-6 apparatus. The samples were previously degassed at 373 K for 4 h and 5×10^{-5} bars using an AUTOSORB DEGASSER (both apparatus from Quantachrome). The adsorption data obtained were analyzed using the software QuadraWinTM (version 6.0) of Quantachrome Instruments. The BET surface area was estimated by using multipoint BET method, analyzing the adsorption data at the relative pressure (P/P_0) range of 0.05-0.30. Cumulative pore volumes and pore-size distribution curves were obtained by applying a non-local density functional theory (NLDFT) method developed silica with cylindrical pores to the adsorption branch of the nitrogen isotherm at 77 K.[169] The total pore volume and the mesopore volume were read directly from the adsorption branch of the isotherm at 0.99 and 0.8, respectively, while the micropore volume was determined by using t-plot method and found to be 0.

Transmission (TEM) and Field Emission Scanning (FESEM) Electron Microscopy

The morphology of the mesoporous materials was investigated by transmission electron microscopy (TEM) and field emission scanning electron microscopy (FESEM). Samples were prepared by dipping a sonicated suspension of the sample on ethanol on a carbon-coated copper grid. TEM images were performed using a JEM-2010 microscope (JEOL, 200 kV, 0.14 nm of resolution), with a detector of Si(Li) (area of 30 mm^2 and resolution of 142 eV). The digital analysis of the TEM micrographs was performed using DigitalMicrographTM 3.6.1. by Gatan. SEM analyses were carried out in a field emission scanning electron microscope (FESEM) Merlin VP Compact (Zeiss, 1.6 nm of resolution at 1 kV).

High Resolution Inductively Coupled Plasma Mass spectrometry (HR-ICP-MS)

The metal contents of the materials were determined by high resolution inductively coupled plasma mass spectrometry (HR-ICP-MS) using a Thermo Scientific ELEMENT XR spectrometer. The samples were dissolved in a mixture of 3,5 mL HCl + 1 mL HNO_3 + 1 mL HF + 5 mL H_3BO_3 (5%), digested in a microwave (260ºC, 45 bar) and filtered off (0.45 µm) prior to analysis. This treatment allows for the complete dissolution of the samples.

Singlet Oxygen Quantum Yield

Singlet-oxygen quantum yields (ϕ_Δ^{PC}) were recorded using a method described in the bibliography,[170] with a homemade-assembled setup comprising a Quantum Northwest qpod-2e thermostatic sample holder, a green 10 W LED as a light source, and an Ocean Optics USB4000 UV-vis spectrometer for data acquisition. The sample holder is a Peltier temperature-controlled system, offering the capability as well to attach a LED for simultaneous sample irradiation and UV-vis spectra acquisition.

The singlet-oxygen conversion is calculated by monitoring the oxidation of 1,3-diphenylisobenzofuran (DPBF, yellow) to 1,2-dibenzoylbenzene (colorless) by UV-visible spectroscopy (Scheme E.1).

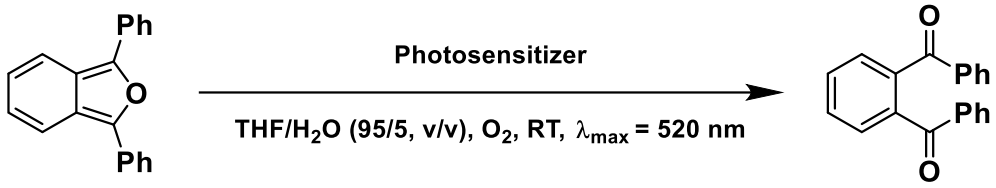

1,3-diphenylisobenzofuran (DPBF)

1,2-dibenzoylbenzene

Scheme E.1. Oxidation reaction of DPBF

This reaction is very fast in the presence of singlet oxygen. A stock solution of $8x10^{-5}$ M of DPBF was prepared. From this stock solution, 3 ml were transferred into a quartz cuvette, and the absorbance was adjusted to 1.2 at 410 nm. Next, a few drops of a solution containing $1\text{-}3x10^{-4}$ M of the different photosensitizers were added incrementally until an absorbance value of 0.2 was reached. Throughout the experiments, the solution was stirred at 20°C to ensure sample homogeneity. The mixture was then irradiated using a 10 W green LED (λ_{max}=520 nm) for a total of 10 minutes, with absorption spectra recorded every 0.5 seconds. The same experimental procedure was repeated for the four BODIPY dyes, and Rhodamine was used as the standard. To confirm the photostability of DPBF under the same irradiation conditions, a background test was conducted in the absence of a photosensitizer (10 minutes).

The decrease in the absorption band at 410 nm, which corresponds to DPBF, was plotted against the irradiation time. The experimental data obtained during the initial minutes of irradiation were fitted to a straight line.

The ϕ_Δ^{BD} were calculated using the equation (1), considering the value of Rhodamine as the reference for $^1O_2$ photosensitization in THF (ϕ_Δ^R=0.016).[158]

$$\phi_\Delta^{BD} = \frac{I^R}{I^{BD}} \times \frac{k^{BD}}{k^R} \times \phi_\Delta^R \text{ (eq. 1)}$$

Where *I* is the absorbance intensity of the photosensitizer, which is calculated as the area under the absorption spectrum ranging from 480 nm to 600 nm. This range is selected to incorporate the full range of irradiation wavelengths of the LED used in the experiment. The slope of the linear fit is denoted as *k*. Superscripts *R* and *BD* stand for Rhodamine and BODIPY dyes respectively.

Synthesis of starting materials

The starting materials were prepared following the reported procedures:

$[Ir(dfppy)_2(\mu\text{-}Cl)]_2$[171]

$[Ir(dfppy)_2(MeCN)_2]PF_6$[172]

N,N'-dipropiltriethoxysilane-2,2'-bipyridine-4,4'-dicarboxamide[173] (*dasipy*)

2,6-difluoro-3-(pyridin-2-yl)benzaldehyde[174] (**L1**)

(E)-Biphenyl-2-carbaldehyde O-4-(trifluoromethyl)benzoyl oxime[96]

The other reagents were obtained from commercial sources and used without further purification.

Synthesis of an iridium(III) complex and new BODIPY dyes

Synthesis of $[Ir(dfppy)_2(dasipy)]PF_6$ (1)

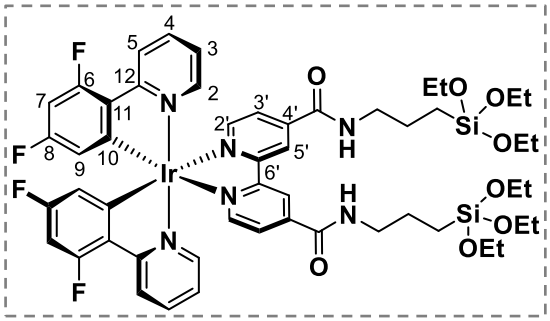

Complex **1** has been prepared as previously reported.[40a] A solution of 0.2 g (0.25 mmol) of $[Ir(dfppy)_2(MeCN)_2]PF_6$ in 30 ml of dichloromethane was treated with 0.21 g (0.33 mmol) of *dasipy*. The yellow mixture was stirred for 6 h at RT, and the resulting solution was evaporated to dryness. The resultant yellow solid was treated with diethylether and kept under Ar atmosphere.

Yield: 0.27 g, 0.20 mmol, 81%.

Elemental analysis (%): Anal Calc. for $C_{52}F_{10}H_{62}IrN_6O_8PSi_2$: C, 47.59; H, 4.76; N, 6.40. Best analyses found: C, 43.06; H, 4.89; N, 6.40 (fits well with **1**·$2CH_2Cl_2$).

ESI (+): $^m/_z$ 1223 $[M]^+$ (100%); 1195 $[M\text{-}Et + H]^+$ (23%).

IR (KBr, cm^{-1}): ν(N-H) 3280 (m, broad); ν(C-H aromatic) 3070 (m); ν(C-H aliphatic) 2959 (m), 2930 (m), 2875 (m); ν(C=O) 1670 (s); ν(C-H aromatic) 1604 (vs), 1558 (vs), 1479 (s), 1430 (s), 1405 (vs); ν(C-F) 1261 (s); ν(Si-O-C) 1163 (s), 1074 (vs), 953 (s); ν(Si-O) 1102 (vs), 991(s); ν(P-F) 840 (vs); ν(Ir-N) 555 (vs).

^{1}H NMR (400 MHz, $CDCl_3$, δ): 8.91 (s, 2H, $H^{5'}{}_{bpy}$); 8.68 (s broad, 2H, N*H*); 8.34 (d, $J_{H\text{-}H}$ = 8.7 Hz, 2H, $H^2{}_{dfppy}$); 8.05 (d, $J_{H\text{-}H}$ = 5.5 Hz, 2H, $H^{2'}{}_{bpy}$ or $H^{3'}{}_{bpy}$); 7.97 (dd, $J_{H\text{-}H}$ = 5.3 Hz, $J_{H\text{-}H}$ = 1.4 Hz, 2H, $H^{2'}{}_{bpy}$ or $H^{3'}{}_{bpy}$); 7.83 (pst, $J_{H\text{-}H}$ = 6.6 Hz, 2H, $H^3{}_{dfppy}$); 7.45 (d, $J_{H\text{-}H}$ = 5.5 Hz, 2H, $H^5{}_{dfppy}$); 7.08 (pst, $J_{H\text{-}H}$ = 6.2 Hz, 2H, $H^4{}_{dfppy}$); 6.60 (pst, $J_{F\text{-}H} \approx 10$ Hz, 2H, $H^7{}_{dfppy}$); 5.67 (dd, $J_{F\text{-}H} \approx 8$ Hz, $J_{H\text{-}H}$ = 2.3 Hz, 2H, $H^9{}_{dfppy}$); 3.82 (c, $J_{H\text{-}H}$ = 7.3 Hz, 12H, OCH_2CH_3); 3.52 (m, 4H, $CH_2CH_2CH_2Si$); 1.81 (m, 4H, $CH_2CH_2CH_2Si$); 1.20 (t, $J_{H\text{-}H}$ = 7.0 Hz, 18H, OCH_2CH_3); 0.72 (t, $J_{H\text{-}H}$ = 8.4 Hz, 4H, $CH_2CH_2CH_2Si$).

$^{13}C\{^{1}H\}$ NMR (100.6 MHz, $CDCl_3$, δ): 165.5 (s, C^{10}_{dfppy}); 164.3 (s, C^{12}_{dfppy}); 164.1 (d, J_{F-C} = 230 Hz, C^{8}_{dfppy}); 163.5 (s, CO); 161.5 (d, J_{F-C} = 233 Hz, C^{6}_{dfppy}); 155.8 (s, $C^{4'}_{bpy}$ or $C^{6'}_{bpy}$); 150.8 (s, $C^{2'}_{bpy}$ or $C^{3'}_{bpy}$); 148.6 (s, C^{5}_{dfppy}); 146.5 (s, $C^{4'}_{bpy}$ or $C^{6'}_{bpy}$); 139.6 (s, C^{3}_{dfppy}); 128.1 (s, $C^{2'}_{bpy}$ or $C^{3'}_{bpy}$); 127.5 (s broad, C^{11}_{dfppy}); 124.0 (m, C^{2}_{dfppy} or C^{4}_{dfppy}); 122.6 (s, $C^{5'}_{bpy}$); 114.2 (d, $^{2}J_{C-F} \approx 18$ Hz, C^{9}_{dfppy}); 99.9 (pst, $J_{C-F} \approx 27$ Hz, C^{7}_{dfppy}); 58.6 (s, O-*C*$H_2$$CH_3$); 43.5 (s, *C*$H_2$$CH_2$$CH_2$-Si); 22.8 (s, CH_2*C*$H_2$$CH_2$-Si); 18.4 (s, O-$CH_2$*C*$H_3$); 7.9 (s, $CH_2$$CH_2$*C*$H_2$-Si).

$^{19}F\ \{^{1}H\}$ NMR (376.5 MHz, $CDCl_3$, δ): -71.40 (d, $^{1}J_{F-P}$ = 712 Hz, 6F, P*F*$_6$); -104.73 (d, J_{F-F} = 11.3 Hz, 2F, F^{6}); -107.91 (d, J_{F-F} = 11.2 Hz, 2F, F^{8}).

Synthesis of 2-fluoro-6-(N,N-dimethylamine)-3-(2-pyridinyl) benzaldehyde (L2)

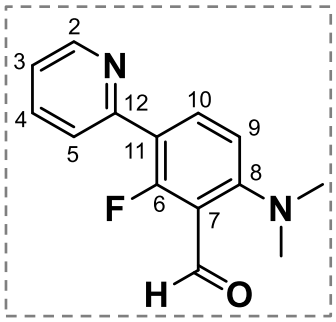

3.20 g (17 mmol) of 2-(2′,4′-difluorophenyl)pyridine were dissolved in 55 ml of dry THF, and the solution was cooled to -80 °C. Then, 6.7 ml of a solution of n-butyllithium 2.5 M (17 mmol) were added dropwise while maintaining constant stirring. After an additional 20 minutes, 5 ml of anhydrous N,N-dimethylformamide were added dropwise, and the solution was allowed to return to RT for other 20 minutes. Then, 10 ml of distilled water were added, and the product was collected by extraction with dichloromethane (100 ml) and washed with water (2x50 ml). The organic phase was dried over anhydrous $MgSO_4$ and the solvent was removed using a rotary evaporator. The residue was purified by silica gel column chromatography using ethyl acetate/hexane (2/3, v/v) as the eluent. The product was obtained as a yellow solid, together with another fraction of a white solid corresponding to 2,6-difluoro-3-(pyridin-2-yl)benzaldehyde **L1**, which was obtained as a pure compound.

Yield: **L2**=2.0 g, 8.19 mmol, 49%; **L1**=2.0 g, 9.12 mmol, 49%.

Elemental analysis: Anal. Calc. for $C_{14}H_{13}FN_2O$: C, 68.84; H, 5.36; N, 11.47. Best analyses found: C, 70.69; H, 5.53; N, 11.21.

ESI (+): $^{m}/_{z}$ 245 $[\mathbf{L2}+H]^+$ (100%).

^{1}H NMR (300 MHz, $CDCl_3$, δ): 10.35 (s, 1H, -CO*H*), 8.70 (ddd, $J_{H\text{-}H}$ = 4.9, 1.7, 1.1 Hz, 1H, H^2), 8.12 (t, $J_{H\text{-}H}$ = 9.0 Hz, 1H, H^{10}), 7.84 – 7.69 (m, 2H, H^5, H^4), 7.23 (ddd, $J_{H\text{-}H}$ = 6.8, 4.8, 2.0 Hz, 1H, H^3), 6.89 (d, $J_{H\text{-}H}$ = 9.0 Hz, 1H, H^9), 3.02 (s, 6H).

^{13}C{^{1}H} NMR (75 MHz, $CDCl_3$, δ): 186.3 (d, $^3J_{C\text{-}F}$ = 12.1 Hz, -*C*OH), 163.6 (d, $^1J_{C\text{-}F}$ = 262.4 Hz, C^6), 155.0 (d, $^3J_{C\text{-}F}$ = 4.4 Hz, C^{12}), 152.7 (d, $^3J_{C\text{-}F}$ = 1.9 Hz, C^8), 149.6 (s, C^2), 136.4 (s, C^4), 136.1 (d, $^3J_{C\text{-}F}$ = 7.2 Hz, C^{10}), 124.1 (d, $J_{C\text{-}F}$ = 10.2 Hz, C^5), 121.8 (s, C^3), 117.2 (d, $^2J_{C\text{-}F}$ = 12.2 Hz, C^{11}), 113.4 (d, $^2J_{C\text{-}F}$ = 8.2 Hz, C^7), 112.7 (d, $^4J_{C\text{-}F}$ = 3.2 Hz, C^9), 44.6 (s, -N(CH_3)$_2$).

^{19}F {^{1}H} NMR (282 MHz, $CDCl_3$, δ): -122.63 (s, 1F, F^6).

Synthesis of 1,3,5,7-tetramethyl-8-(2,6-difluoro-3-(pyridin-2-yl)phenyl)-4,4-difluoroboradiazaindacene (BD-1)

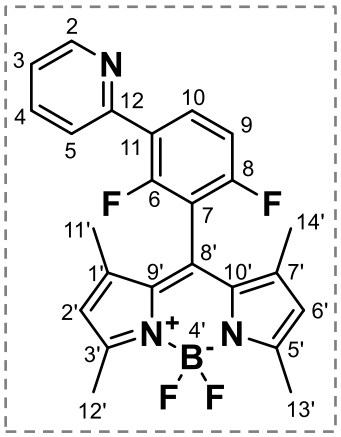

0.66 ml (6.36 mmol) of 2,4-dimethylpyrrole were dissolved in 20 ml of dichloromethane under an Ar atmosphere and in darkness. To this solution, 0.70 g (3.18 mmol) of **L1** were added. The mixture was stirred overnight at RT. Then, 0.9 g of *p*-chloranil were dissolved in dichloromethane and added to the reaction mixture. After 1 hour, 3.2 ml of NEt_3 were slowly added dropwise, followed by the gradual addition of 6 ml of $BF_3{\cdot}OEt_2$ (47.8 mmol, excess). The mixture was stirred for an additional 12 hours and then neutralized with a saturated $NaHCO_3$ solution until pH=7-8. The organic layer was collected, and the aqueous layer was further washed with CH_2Cl_2 until the red color disappeared. The organic layer was dried over anhydrous $MgSO_4$. The crude was purified by silica gel column chromatography using CH_2Cl_2/hexane (8/2, v/v). After the first impurity eluted, the gradient was adjusted by gradually increasing the proportion of CH_2Cl_2. The product was further purified using a filtration setup with a 2 cm silica layer and washed with CH_2Cl_2. After solvent evaporation, a red solid exhibiting green iridescence was obtained.

Yield: 0.37 g, 0.84 mmol, 26%.

Elemental analysis: Anal. Calc. for $C_{24}H_{20}F_4BN_3$: C, 65.93; H, 4.61; N, 9.61. Best analyses found: C, 64.58; H, 5.36; N, 7.94 (Elemental analyses fit well for **BD-1** + 0.5 hexane. $C_{27}H_{27}BClF_4N_3$: C, 67.51; H, 5.67; N, 8.75).

ESI (+): $^{m}/_{z}$ 438 [**BD-1**+H]$^+$ (100%).

IR (cm-1): ν(C-H aromatic) 3095 (vw); ν(C-H aliphatic) 2961 (vw), 2924 (vw), 2855 (vw); 1625 (vw); 1597 (vw); ν(B-F) 1547 (s); 1508 (s); 1465 (s); 1436 (s); 1408 (m); ν(C-F aromatic) 1307 (s); 1277 (m); 1256 (s); 1243 (w); 1188 (s); 1154 (vs); 1078 (s); 1040 (s); 1013 (vs); ν(N-B) 970 (vs); 812 (s); 789 (vs); 746 (s); 723 (s); 626 (s); 567 (s); 475 (vs).

^{1}H NMR (400 MHz, $CDCl_3$, δ): 8.74 (d, J_{H-H} = 4.5 Hz, 1H, H^{2}), 8.24 (ptd, J_{F-H} = 8.7, J_{H-H} =6.5 Hz, 1H, H^{10}), 7.82 – 7.72 (m, 2H, H^{4} and H^{5}), 7.29 (q, J_{H-H} = 4.5 Hz, 1H, H^{3}), 7.20 (pt, J_{F-H} = 8.1 Hz, 1H, H^{9}), 6.02 (s, 2H, $H^{2'}$ and $H^{6'}$), 2.57 (s, 6H, -C$H_3^{12'}$ and -C$H_3^{13'}$), 1.63 (s, 6H, -C$H_3^{11'}$ and -C$H_3^{14'}$).

^{13}C{^{1}H} NMR (100.6 MHz, $CDCl_3$, δ): 159.8 (dd, $^{1}J_{C-F}$ = 252.2 Hz, $^{3}J_{C-F}$ = 5.9 Hz, C^{8}), 157.4 (dd, $^{1}J_{C-F}$ = 253.0 Hz, $^{3}J_{C-F}$ = 6.0 Hz, C^{6}), 156.7 (s, $C^{3'}$ and $C^{5'}$), 151.8 (d, $^{3}J_{C-F}$ = 2.9 Hz, C^{12}), 150.2 (s, C^{2}), 142.2 (s, $C^{1'}$ and $C^{7'}$), 136.9 (s, C^{4}), 133.2 (dd, J = 9.5, 4.6 Hz, C^{10}), 131.5 (s, $C^{9'}$ and $C^{10'}$), 127.4 (s, $C^{8'}$), 124.7 (dd, $^{2}J_{C-F}$ = 12.3 Hz, $^{4}J_{C-F}$ = 3.9 Hz, C^{11}), 124.4 (d, J = 10.3 Hz, C^{5}), 123.1 (s, C^{3}), 121.8 (s, $C^{2'}$ and $C^{6'}$), 112.8 (dd, $^{2}J_{C-F}$ = 21.4 Hz, $^{4}J_{C-F}$= 3.8 Hz, C^{9}), 112.5 (pt, $^{2}J_{C-F}$ = 21.5 Hz, C^{7}), 14.9 (s, $C^{12'}$ and $C^{13'}$), 13.8 (s, $C^{11'}$ and $C^{14'}$).

^{19}F{^{1}H} NMR (376.5 MHz, $CDCl_3$, δ): -110.62 (d, J_{F-F} = 6.4 Hz, 1F, F^{6}), -114.63 (d, J_{F-F} = 6.2 Hz, 1F, F^{8}), -146.22 (q, $^{1}J_{F-B}$ = 32.6 Hz, 2F, -BF_2).

Synthesis of 1,3,5,7-tetramethyl-8-(2-fluoro-6-(N,N-dimethylamine)-3-(pyridin-2-yl)phenyl)-4,4-difluoroboradiazaindacene (BD-2)

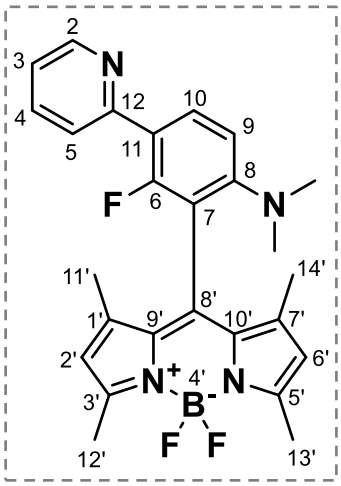

The synthesis is similar to **BD-1**. 0.85 ml (8.20 mmol) of 2,4-dimethylpyrrole was dissolved in 20 ml of dry dichloromethane under an Ar atmosphere and in darkness. Subsequently, 1.00 g (4.10 mmol) of **L2** were added to the solution. The reaction was stirred overnight at RT, and 0.5 g of *p*-chloranil previously dissolved in dichloromethane were added to the medium. After 1 hour, 2.30 ml of NEt_3 were added dropwise, followed by 4.20 ml of $BF_3{\cdot}OEt_2$ (33.4 mmol, excess) after an additional 15 minutes. The reaction mixture was stirred for over an hour, and additional 2.30 ml of NEt_3 and 4.20 ml of $BF_3{\cdot}OEt_2$ were added following the same procedure. After 3 hours of agitation at RT, the color of the solution changed to black. The mixture was then neutralized with 30 ml of a saturated $NaHCO_3$ solution. The organic layer was collected, and the aqueous layer was washed with CH_2Cl_2 fractions. The organic layer was dried over anhydrous $MgSO_4$, and the crude was purified through silica gel column chromatography using CH_2Cl_2/MeOH (9.9/0.1, v/v), yielding a bright red solid with red luminescence.

Yield: 405.2 mg, 0.88 mmol, 21%.

Elemental analysis: Anal. Calc. for $C_{26}H_{26}F_3BN_4$: C, 67.55; H, 5.67; N, 12.12. Best analyses found: C, 64.47; H, 5.41; N, 10.62 (Elemental analyses fit well for **BD-2**+0.5 CH_2Cl_2. $C_{26.5}H_{27}F_3ClBN_4$: C, 63.05; H, 5.39; N, 11.10).

MALDI (-): $^m/_z$ 463 [**BD-2**+H]$^+$ (100%).

IR (cm-1): ν(C-H aromatic) 3092 (vw); ν(C-H aliphatic) 2959 (vw), 2924 (vw), 2868 (vw), 2850 (vw), 2800 (vw); 1622 (w); 1586 (w); 1567 (w); ν(B-F) 1539 (s); 1505 (s); 1468 (s); 1431 (s); 1408 (s); 1367 (m); 1346 (m); ν(C-F) 1300 (s); 1183 (s); 1153 (vs); 1054 (s); 1017 (s); ν(N-B) 970 (vs); 885 (m); 811 (vs); 791 (vs); 752 (m); 720 (s); 664 (m); 630 (s); 579 (m); 549 (s); 475 (vs).

^{1}H NMR (400 MHz, $CDCl_3$, δ): 8.68 (d, J_{H-H} = 4.9 Hz, 1H, H^{2}), 8.09 (t, J_{H-H} = 9.0 Hz, 1H, H^{10}), 7.72 (d, J_{H-H} = 7.6 Hz, 1H, H^{5}), 7.67 (pt, J_{H-H} = 7.4 Hz, 1H, H^{4}), 7.19 (pdt, J_{H-H} = 6.9, 4.9 Hz, 1H, H^{3}), 6.86 (d, J_{H-H} = 8.9 Hz, 1H, H^{9}), 6.00 (s, 2H, $H^{2'}$ and $H^{6'}$), 2.85 (s, 6H, -N(CH_3)$_2$), 2.56 (s, 6H, -$CH_3^{12'}$ and -$CH_3^{13'}$), 1.67 (s, 6H, -$CH_3^{11'}$ and -$CH_3^{14'}$).

^{13}C{^{1}H} NMR (100.6 MHz, $CDCl_3$, δ): 157.8 (d, $^{1}J_{C-F}$ = 246.9 Hz, C^{6}), 155.6 (s, $C^{3'}$ and $C^{5'}$), 153.0 (d, $^{3}J_{C-F}$ = 3.1 Hz, C^{12}), 152.3 (d, $^{3}J_{C-F}$ = 4.8 Hz, C^{8}), 149.7 (s, C^{2}), 142.4 (s, $C^{1'}$ and $C^{7'}$), 136.6 (s, C^{4}), 134.75 (d, $^{3}J_{C-F}$ = 3.8 Hz, $C^{8'}$), 132.1 (d, $^{3}J_{C-F}$ = 5.7 Hz, C^{10}), 132.0 (s, $C^{9'}$ and $C^{10'}$), 124.1 (d, J_{C-F} = 11.3 Hz, C^{5}), 122.0 (s, C^{3}), 121.4 (s, $C^{2'}$ and $C^{6'}$), 119.0 (d, $^{2}J_{C-F}$ = 13.0 Hz, C^{11}), 113.6 (d, $^{4}J_{C-F}$ = 2.7 Hz, C^{9}), 112.6 (d, $^{2}J_{C-F}$ = 20.1 Hz, C^{7}), 43.0 (s, -N(CH_3)$_2$), 14.8 (s, $C^{12'}$ and $C^{13'}$), 14.2 (s, $C^{11'}$ and $C^{14'}$).

^{19}F{^{1}H} NMR (376.5 MHz, $CDCl_3$, δ): -115.04 (s, 1F, F^{6}), -145.80 (dq, $^{2}J_{F-F}$ = 109.4, $^{1}J_{F-B}$ = 32.9 Hz, 1F, -BF_2), -147.25 (dq, $^{2}J_{F-F}$ = 109.6, $^{1}J_{F-B}$ = 32.9 Hz, 1F, -BF_2).

Synthesis of 2,6-diiodo-1,3,5,7-tetramethyl-8-(2,6-difluoro-3-(pyridin-2-yl)phenyl)-4,4-difluoroboradiazaindacene (BD-3)

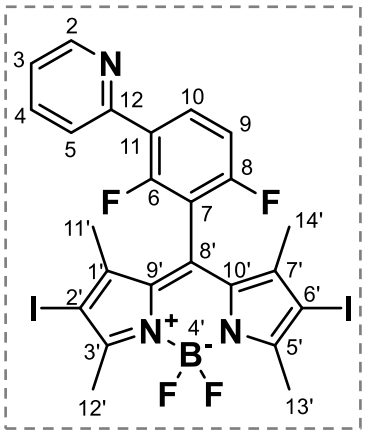

0.08 g (0.18 mmol) of **BD-1** were dissolved in 25 ml of dry dichloromethane, and 0.17 g of N-iodosuccinimide (0.73 mmol) were added. The colour of the solution changed from red to dark violet. The reaction was stirred at RT and followed by TLC. After 30 minutes, a small excess of N-iodosuccinimide (~15 mg, 0.07 mmol) was added, and the reaction was stirred for other 2 hours. After removing the solvent, the compound was purified by silica gel chromatography column using CH_2Cl_2/hexane (9/1 v/v), obtaining a dark violet solid.

Yield: 95.7 mg, 0.14 mmol, 76%.

Elemental analysis: Anal. Calc. for $C_{24}H_{18}BF_4I_2N_3$: C, 41.84; H, 2.63; N, 6.10. Best analyses found: C, 38.38; H, 3.01; N, 4.66 (Elemental analyses fit well for **BD-3**+ CH_2Cl_2. $C_{25}H_{20}BCl2F_4I_2N_3$: C, 38.80; H, 2.60; N, 5.43).

MALDI (+): $^m/_z$ 689 [**BD-3**] (100%).

IR (cm-1): ν(C-H aromatic) 3072 (vw); ν(C-H aliphatic) 2958 (vw), 2922 (vw), 2852 (vw); 1622 (w); 1593 (w); ν(B-F) 1537 (s); 1484 (m); 1466 (m); 1438 (s); 1399 (m); 1341 (s); ν(C-F) 1311 (s); 1263 (w); 1243 (w); 1178 (vs); 1120 (s); 1098 (s); 1083 (s); 1059 (m); 1045 (m); ν(N-B) 994 (vs); 914 (s); 865 (m); 795 (s); 753 (m); 724 (s); 630 (m); 588 (s); 566 (s); ν(C-I) 527 (vs); 486 (m); 462 (m).

^{1}H NMR (400 MHz, $CDCl_3$, δ): 8.75 (d, $J_{H\text{-}H}$ = 4.8 Hz, 1H, H^2), 8.30 (ptd, $J_{F\text{-}H}$ = 8.8, $J_{H\text{-}H}$ =6.7 Hz, 1H, H^{10}), 7.83 – 7.72 (m, 2H, H^4 and H^5), 7.33 (pt, $J_{H\text{-}H}$ = 6.1 Hz, 1H, H^3), 7.23 (pt, $J_{F\text{-}H}$ = 8.6 Hz, 1H, H^9), 2.67 (s, 6H, -C$H_3^{11'}$ and -C$H_3^{14'}$), 1.65 (s, 6H, -C$H_3^{12'}$ and -C$H_3^{13'}$).

^{13}C{^{1}H} NMR (100.6 MHz, $CDCl_3$, δ): 159.6 (dd, $^1J_{C\text{-}F}$ = 257.8 Hz, $^3J_{C\text{-}F}$ = 5.0 Hz, C^8), 157.1 (dd, $^1J_{C\text{-}F}$ = 255.0 Hz, $^3J_{C\text{-}F}$ = 6.4 Hz, C^6), 158.1 (s, $C^{3'}$ and $C^{5'}$), 151.3 (s, C^{12}), 150.1 (s, C^2), 144.5 (s, $C^{1'}$ and $C^{7'}$), 137.2 (s, C^4), 133.9 (dd, J = 10.0, 4.7 Hz, C^{10}), 131.3 (s, $C^{9'}$ and $C^{10'}$), 127.3 (s, $C^{8'}$), 124.8 (dd, $^2J_{C\text{-}F}$ = 11.7 Hz, $^4J_{C\text{-}F}$ = 4.7 Hz, C^{11}), 124.5 (d,

J = 10.1 Hz, C^5), 123.3 (s, C^3), 113.1 (dd, $^2J_{C\text{-}F}$ = 25.7 Hz, $^4J_{C\text{-}F}$= 3.6 Hz, C^9), 112.6 (pt, $^2J_{C\text{-}F}$ = 21.5 Hz, C^7), 86.5 (s, $C^{2'}$ and $C^{6'}$), 16.3 (s, $C^{11'}$, $C^{12'}$, $C^{13'}$ and $C^{14'}$).

$^{19}F\{^1H\}$ NMR (376.5 MHz, $CDCl_3$, δ): -110.29 (d, $J_{F\text{-}F}$ = 5.7 Hz, 1F, F^6), -114.36 (d, $J_{F\text{-}F}$ = 5.6 Hz, 1F, F^8), -145.59 (q, $^1J_{F\text{-}B}$ = 32.0 Hz, 2F, -BF_2).

Synthesis of 2,6-diiodo-1,3,5,7-tetramethyl-8-(2-fluoro-6-(N,N-dimethylamine)-3-(pyridin-2-yl)phenyl)-4,4-difluoroboradiazaindacene (BD-4)

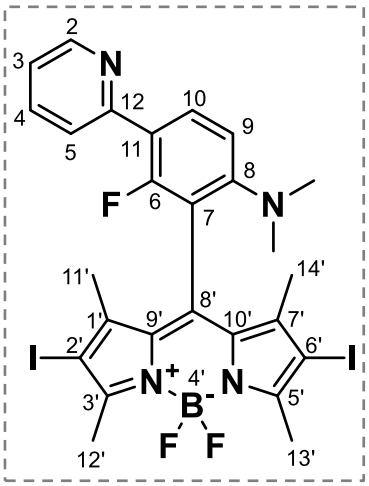

0.10 g (0.221 mmol) of **BD-2** were dissolved in 25 ml of dry dichloromethane, and 0.20 mg (0.89 mmol) of N-iodosuccinimide were added. After 30 minutes of agitation at RT, the colour of the solution changed from orange to dark violet. The reaction was followed by proton NMR, and after two hours the solvent was removed, and the product was purified by a silica gel chromatographic column using CH_2Cl_2/MeOH (9/1, v/v). A dark purple solid was obtained after the removal of the solvent.

Yield: 65.6 mg, 0.09 mmol, 42%.

Elemental analysis: Anal. Calc. for $C_{26}H_{24}BF3I_2N_4$: C, 43.73; H, 3.39; N, 7.85. Best analyses found: C, 43.60; H, 3.55; N, 7.25.

MALDI (-): $^m/_z$ 714 [**BD-4**] (100%).

IR (cm-1): ν(C-H aromatic) 3090 (vw), 3054 (vw); ν(C-H aliphatic) 2951 (vw), 2915 (vw), 2860 (vw), 2837 (vw), 2792 (vw); 1615 (w); 1586 (w); 1571 (w); ν(B-F) 1525 (s); 1471 (m); 1429 (m); 1396 (m); 1369 (m); 1343 (s); ν(C-F) 1303 (s); 1214 (w); 1170 (vs); 1116 (s); 1080 (s); ν(N-B) 986 (vs); 912 (m); 818 (m); 791 (s); 773 (m); 758 (m); 742 (m); 724 (s); 700 (m); 665 (w); 636 (m); 622 (m); 588 (s); 569 (m); 545 (w); ν(C-I) 523 (vs); 487 (s).

^{1}H NMR (400 MHz, $CDCl_3$, δ): 8.69 (d, J_{H-H} = 4.8 Hz, 1H, H^2), 8.18 (t, J_{H-H} = 9.0 Hz, 1H, H^{10}), 7.72-7.64 (m, 2H, H^4 and H^5), 7.21 (pdt, J_{H-H} = 4.9, 3.4 Hz, 1H, H^3), 6.90 (d, J_{H-H} = 8.9 Hz, 1H, H^9), 2.84 (s, 6H, -N(CH_3)$_2$), 2.66 (s, 6H, -$CH_3^{12'}$ and -$CH_3^{13'}$), 1.70 (s, 6H, -$CH_3^{11'}$ and -$CH_3^{14'}$).

^{13}C{^{1}H} NMR (100.6 MHz, $CDCl_3$, δ): 157.5 (d, $^1J_{C-F}$ = 247.3 Hz, C^6), 156.8 (s, $C^{3'}$ and $C^{5'}$), 152.6 (d, $^3J_{C-F}$ = 2.9 Hz, C^{12}), 152.1 (d, $^3J_{C-F}$ = 4.5 Hz, C^8), 149.7 (s, C^2), 144.4 (s, $C^{1'}$ and $C^{7'}$), 136.5 (s, C^4), 134.7 (d, $^3J_{C-F}$ = 3.6 Hz, $C^{8'}$), 132.6 (d, $^3J_{C-F}$ = 5.6 Hz, C^{10}),

131.7 (s, $C^{9'}$ and $C^{10'}$), 123.9 (d, J_{C-F} = 11.1 Hz, C^5), 122.0 (s, C^3), 119.2 (d, $^2J_{C-F}$ = 13.2 Hz, C^{11}), 113.8 (d, $^4J_{C-F}$ = 2.8 Hz, C^9), 112.4 (d, $^2J_{C-F}$ = 19.7 Hz, C^7), 85.9 (s, $C^{2'}$ and $C^{6'}$), 43.0 (s, -N(CH_3)$_2$), 16.6 (s, $C^{12'}$ and $C^{13'}$), 16.2 (s, $C^{11'}$ and $C^{14'}$).

$^{19}F\{^1H\}$ NMR (376.5 MHz, $CDCl_3$, δ): -114.83 (s, F^6), -145.33 (dq, $^2J_{F-F}$ = 105.3, $^1J_{F-B}$ = 32.7 Hz, 1F, -BF_2), -146.38 (dq, $^2J_{F-F}$ = 105.3, $^1J_{F-B}$ = 31.0 Hz, 1F, -BF_2).

Synthesis of hybrid silica-based materials

The synthesis of the *in-situ* hybrid materials involved the co-condensation of the iridium complex **1** with the silica precursor (TEOS). The chosen nominal metal concentrations were 1 wt% for **SiO_2_N**, **SiO_2_B** and **SiO_2_OD** and 0.2 wt% for **NP_IS**.

SiO_2_N

A solution containing 53 mg of **1** (0.04 mmol) in 3 mL of THF were added to 2 mL of TEOS. The resulting mixture was stirred for an hour at room temperature, and then 30 mL of distilled water were incorporated. After an additional hour of stirring, 1.4 mL of a solution of NaF in H_2O (0.05 M) were added, and the mixture was left for 24 hours at room temperature under agitation. The resulting yellow precipitate was filtrated and washed with water, ethanol and acetone. Once dried, the solid was grinded to yield a yellow powder.

Yield: 0.51 g, 88%.

Molar ratio of the synthesis gel: 1.0 TEOS : 182 H_2O : 4 THF : $7.7 \cdot 10^{-3}$ F^-.

Nominal metal concentration: 1 wt%.

IR (KBr, cm^{-1}): ν(O-H) 3460 (s broad), 1640 (m); ν(N-H) 3280 (m, broad); ν(C-H) 2930 (w); ν(Si-O-Si) 1220, 1090 (s broad), 800 (m), 460 (s); ν(Si-O) 950 (m).

SiO_2_B

53 mg of **1** (0.04 mmol) were dissolved in 2 mL of absolute ethanol, and 2 mL of TEOS were added to the solution. After 1 hour of stirring, a solution containing 93 µL of NaF 0.05 M and 25 µL of NH_3 25% in 5.1 mL water:ethanol (2.4:1) was added dropwise, and the mixture was left to stir for 24 hours. 25 mL of ethanol were then added, and after a few minutes, the mixture was filtrated to obtain a yellow solid that was washed with ethanol, water and acetone. The dry solid was grinded to yield a yellow powder.

Yield: 0.52 g, 89%.

Molar ratio in the synthesis gel: 1.0 TEOS : 24 H_2O : 5.6 EtOH : 5.1 x 10^{-5} F^-: 0.03 NH_4OH.

Nominal metal concentration: 1 wt%.

IR (KBr, cm^{-1}): ν(O-H) 3435 (s broad), 1635 (m); ν(N-H) 3270 (m, broad); ν(C-H) 2962 (w), 2923 (w), 2850 (w); ν(ring) 1560 (w), 1480 (w), 1430 (w), 1408 (w), 1385 (w); ν(Si-O-Si) 1220, 1090 (s broad), 800 (m), 465 (s); ν(Si-O) 960 (m).

SiO_2_OD

A solution of 53 mg of **1** (0.04 mmol) in 4 mL of ethanol were added dropwise at a regular rate for 20 minutes, to another solution containing 1.00 g of CTAB (hexadecyltrimethylammonium bromide) and 156 µL of TEA (triethanolamine) dissolved in 65 mL of distilled water. After two hours of agitation at room temperature, 2 mL of TEOS were added dropwise over 20 minutes, and the solution was then stirred for an additional two hours at RT. Afterward, 2 mL of NH_3 25% were added dropwise, and the reaction mixture was allowed to stir for 24 hours. The resulting yellow suspension was centrifugated at 15000 rpm for 20 minutes and washed with distilled water and ethanol. Finally, the surfactant was removed by ionic exchange with a saturated NH_4NO_3 solution.

Yield: 0.46 g, 79%.

Molar ratio of the synthesis gel: 1.0 TEOS : 408 H_2O : 7.5 EtOH : 0.3 CTAB : 0.13 TEA : 2.3 NH_4OH.

Nominal metal concentration: 1 wt%.

IR (KBr, cm^{-1}): ν(O-H) 3450 (s broad), 1640 (m); ν(N-H) 3280 (m, broad); ν(C-H) 2930 (w), 2860 (w); ν(ring) 1550 (w), 1460 (w), 1385 (m); ν(Si-O-Si) 1228, 1085 (s broad), 800 (m), 460 (s); ν(Si-O) 960 (m).

NP_IS

0.20 g of CTAB were added to a mixture of 13.1 mL of distilled water and 31.4 µL of TEA. The resulting suspension was heated to 80°C and stirred for 1 hour. Simultaneously, a solution containing complex **1** (7.6 mg, 0.006 mmol) in 3 mL of absolute ethanol and 2 mL (9.12 mmol) of TEOS was stirred at room temperature. This last solution was added to the first one at 80°C. After allowing the mixture to react for 10 minutes, 0.21 mL of diethoxydimethylsilane (DMDES, 1.22 mmol) were added and the mixture was stirred for another 2 hours at 80°C. The suspension was cooled to room temperature, the particles were separated through centrifugation (20 min at 20000 rpm) and subsequently washed with distilled water and ethanol. Finally, the surfactant was removed by ionic exchange with a saturated NH_4NO_3 solution, obtaining the material as a pale-yellow powder.

Yield: 0.36 g, 82%.

Molar ratio of the synthesis gel: 1.0 TEOS : 80 H_2O : 5.6 EtOH : 0.06 CTAB : 0.03 TEA : 0.14 DMDES.

Nominal metal concentration: 0.2 wt%.

IR (KBr, cm^{-1}): ν(O-H) 3440 (s broad), 1640 (m); ν(N-H) 3275 (m, broad); ν(C-H) 2970 (m), 2928 (w), 2852 (w); ν(ring) 1452 (w), 1405 (w); ν(Si-CH_3) 1265 (m), 850 (m); ν(Si-O-Si) 1220, 1080 (s broad), 800 (m), 460 (s); ν(Si-O) 950 (m).

Synthesis of grafted mesoporous organometallo-silica nanoparticles (NP_G)

Complex-free mesoporous silica nanoparticles (**MSN**) were prepared by dissolving 0.20 g of CTAB and 31.4 µL of TEA in 13.1 ml of distilled water. Then, 2 mL of TEOS were added, and the mixture was allowed to stir at room temperature for 24 hours. The resultant white suspension was centrifuged for 15 minutes at 18000 rpm and washed with distilled water and ethanol. The surfactant was removed by ionic exchange with a saturated NH_4NO_3 solution.

Yield: 0.41 g, 76%.

Molar ratio of the synthesis gel: 1.0 TEOS : 80 H_2O : 0.06 CTAB : 0.03 TEA.

NP_G were obtained by dropwise addition of a solution of 17.5 mg (0.013 mmol) of complex **1** in 3 mL of ethanol to a suspension of 0.25 g (6.67 mmol) of the complex-free silica nanoparticles in 30 mL of ethanol. The resulting mixture was stirred for 2 hours, and 0.7 mL of an aqueous solution 0.05 M of NaF were added. The reaction was kept under magnetic stirring for 24 hours at room temperature. The obtained yellow solid was separated by centrifugation and washed with ethanol.

Yield: 0.26 g, 99%.

IR (KBr, cm^{-1}): ν(O-H) 3435 (s broad), 1640 (m); ν(N-H) 3280 (m, broad); ν(C-H) 2960 (w), 2925 (w), 2855 (w); ν(ring) 1550 (w), 1480 (w); ν(Si-O-Si) 1220, 1090 (s broad), 800 (m), 470 (s); ν(Si-O) 960 (m).

Synthesis of self-condensed material (SC-1)

0.15 g of complex **1** were dissolved in 5 ml of absolute ethanol and added to 13.1 ml of distilled water. After stirring for 1 hour at RT, 0.7 ml of an aqueous solution of NaF (0.05 M) were added, the reaction mixture was heated to 80°C and allowed to react for 96 hours. After that time, the reaction was cooled to RT, the material was separated by centrifugation at 18000 rpm for 15 minutes, and washed with distilled water and ethanol. The obtained yellow solid was air dried.

Yield: 94.4 mg, 74%.

Elemental analysis: Anal. Calc. for $C_{44}F_{10}H_{42}IrN_6O_6PSi_2$: C, 43.27; H, 3.47; N, 6.89. Best analyses found: C, 41.06; H, 3.30; N, 6.70.

MALDI (+): $^{m}/_{z}$ 1073 [**1** – 2Et – 2(-OEt)-2H]$^{+}$ (11%); 823 [**1** – {$(CH_2)_3Si(OEt)_3$} – {$NH_2(CH_2)_3Si(OEt)_3$} +3H]$^{+}$ (100%); 573 [**1** – (*dasipy*)]$^{+}$ (51%).

IR (cm^{-1}): ν(N-H) 3330 (broad); ν(C-H aromatic) 3086 (w); ν(C-H aliphatic) 2939 (w), 2878 (w); ν(C=O) 1661 (m); ν(C-H aromatic) 1604 (vs), 1575 (s), 1557 (s), 1479 (s), 1431 (s), 1406 (s); ν(C-F) 1296 (s); ν(Si-O-C) 1165 (m), 1071 (m); ν(Si-O) 1105 (s), 989(s); ν(P-F) 842 (vs); ν(Ir-N) 557 (s).

Photocatalytic methods

Photo-isomerization of trans-stilbene

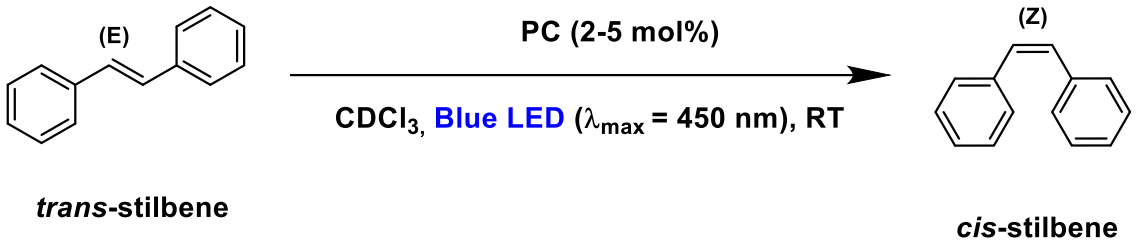

Scheme E.2. Photo-isomerization of *trans*-stilbene.

The photocatalytic reactions were carried out by mixing the *trans*-stilbene with the corresponding amount of either complex **1** or the different hybrid materials, and irradiated with blue light emitted by an RGB LED of 50 W. The chosen molar ratio of *trans*-stilbene:photocatalyst was kept at 1:0.05 for all materials, except for **NP_IS**, where the nominal percentage of iridium was 0.2 wt% instead of 1 wt%. For this photocatalyst in particular, a molar ratio of 1:0.02 was chosen.

The samples were prepared as follows for each photocatalyst:

1: In an NMR tube, 10 mg (0.055 mmol) of *trans*-stilbene were combined with the corresponding amount of the iridium complex (3.8 mg or 0.003 mmol for a 1:0.05 molar ratio; and 1.5 mg or 0.001 mmol for a 1:0.02 molar ratio), and 0.6 mL of $CDCl_3$ were added. The NMR tubes were kept in constant agitation during the irradiation period. The reaction was monitored using ^{1}H-NMR spectra.

SiO_2_N, **SiO_2_B**, **SiO_2_OD**, **NP_G:** The same procedure was followed; for 5 mg (0.028 mmol) of *trans*-Stilbene, 26.6 mg of each material were added to separate NMR tubes (1:0.05 molar ratio).

NP_IS: For 26.6 mg of material, 2.5 mg (0.014 mmol) of *trans*-Stilbene were added (1:0.02 molar ratio).

Before irradiation, and under dark conditions, all the tubes containing *trans*-stilbene and the corresponding catalyst underwent 30 minutes of sonication, followed by 30 minutes of additional agitation. Each reaction was then carried out under blue light until the maximum conversion was achieved (Figure E.1). For the purpose of recyclability

studies, the materials were recovered by centrifugation at 13000 rpm for 10 minutes, treated with 2 mL of dry dichloromethane and subjected to 10 minutes of sonication. After a further centrifugation cycle, the materials were vacuum dried, and used in the successive reaction.

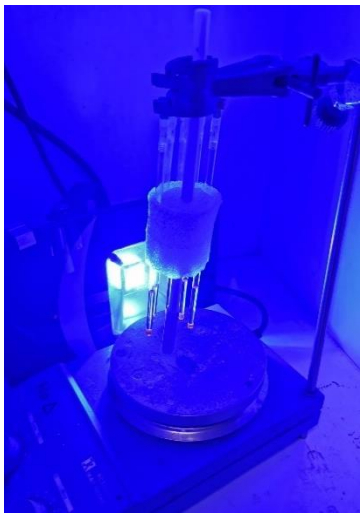

Figure E.1. Set-up of the photocatalytic reaction.

Throughout each reaction, the isomerization rate was measured by ^{1}H NMR spectroscopy, following the changes in the intensity of the alkene proton signals observed at 7.15 ppm for the *trans*-stilbene and 6.60 ppm for the *cis*-stilbene.

Photocatalytic dehalogenation of 2-bromoacetophenone

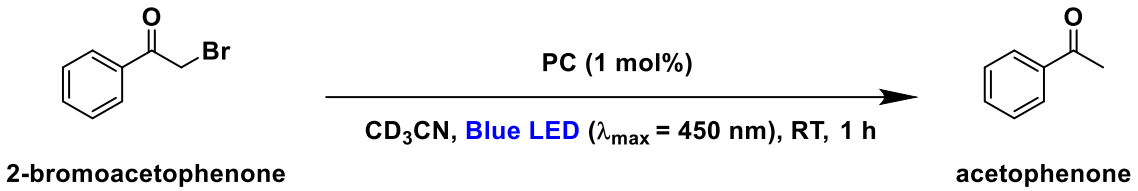

Scheme E.3. Photocatalytic dehalogenation reaction.

In NMR tube: 2-bromoacetophenone (15 mg, 0.075 mmol, 1 equiv.), triethanolamine (30 µl, 0.23 mmol, 3 equiv.) and the corresponding amount of photocatalyst (**1**: 1.00 mg, 0.75 µmol; **SC-1**: 0.92 mg, 0.75 µmol; 0.01 equiv.) were dissolved in 0.8 ml of deuterated acetonitrile. Under dark, the tubes were degassed by nitrogen bubbling for 5 minutes, and for the heterogeneous reactions the tubes were sonicated for 1 minute. The reaction was then irradiated with a 50 W Blue LED (λ_{max} = 450 nm) for 5-90 minutes under agitation. The reaction was followed by ^{1}H-NMR, adding 1,3,5-trimethoxybenzene as internal standard (~0.06 mmol) to determine the yield of the reaction.

In a round bottom flask (for recyclability studies): 2-bromoacetophenone (650 mg, 3.3 mmol, 1 equiv.), **SC-1** (40 mg, 0.033 mmol, 0.01 equiv.) and 15 ml of acetonitrile previously degassed (20 minutes of nitrogen bubbling) were added under nitrogen to a 50 ml round bottom flask. After sonicating the mixture for one minute, triethanolamine (1.3 ml, 9.8 mmol, 3 equiv.) was also incorporated, and the flask was irradiated under agitation using a 50 W Blue LED (λ_{max}=450 nm) for 90 minutes. After that time, the reaction was centrifuged at 20000 rpm for 15 minutes, and the recovered material was washed (10 minutes of sonication, centrifugation at 20000 rpm for 15 min) with distilled water. The material was then also centrifuged and washed with absolute ethanol. After a new centrifugation step, the solid was treated with dichloromethane to resuspend it and transferred back to the reaction flask. The material was subsequently dried and subjected to vacuum at 100°C to remove any remaining traces of water. The following reactions were set up using the same procedure. Yields were determined by ^{1}H-NMR analysis, with the addition of 1,3,5-trimethoxybenzene as an internal standard.

Photocatalytic synthesis of phenanthridine

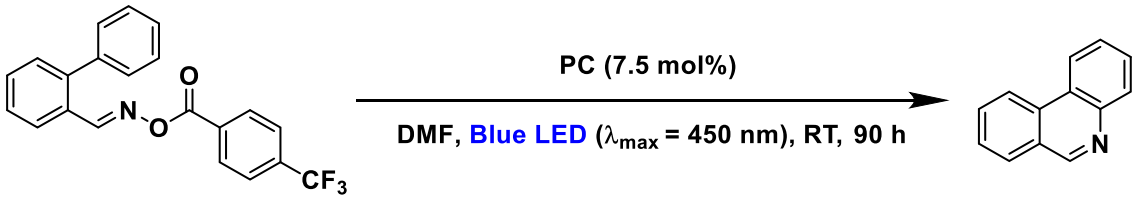

Scheme E.4. Photocatalytic phenanthridine formation from acyloxime.

Homogeneous conditions: (*E*)-Biphenyl-2-carbaldehyde O-4-(trifluoromethyl)benzoyl oxime (36.6 mg, 0.10 mmol, 1 equiv.), 3 ml of dry and degassed DMF and the corresponding amount of photocatalyst were introduced into a round bottom flask under nitrogen. The reaction mixture was then irradiated under stirring, using an RGB LED of 100 W operating only in the blue region (~33 W). After 24-90 hours, the solvent was evaporated, and the conversion was determined by ^{1}H-NMR.

Heterogeneous conditions and recovery study: **SC-1** (10 mg, 8.1 µmol, 0.075 equiv.) was transferred to a round bottom flask and subjected to vacuum at 100°C for 1 hour, without any stirring. Upon cooling to room temperature, (*E*)-Biphenyl-2-carbaldehyde O-4-(trifluoromethyl)benzoyl oxime (40 mg, 0.11 mmol, 1 equiv.) and 3 ml of dry and degassed DMF were added in a dry-box. The reaction was irradiated with blue light at RT while stirring, using an RGB LED of 100 W. After 90 hours, the solid was recuperated through centrifugation at 12500 rpm for 10 minutes. The supernatant was dried, and the conversion was determined using ^{1}H-NMR. The collected material was washed (10 minutes of sonication, centrifugation at 12500 rpm for 10 min) with acidic absolute ethanol (pH=2) and absolute ethanol, and was then transferred back to the reaction flask to start a new catalytic cycle. The material was dried for 1 hour at 100°C under vacuum, and the subsequent cycles were set as described. After the second catalytic cycle, the flask was sonicated under dark for 45 minutes prior to irradiation.

Photocatalytic oxidation of dibenzylamine

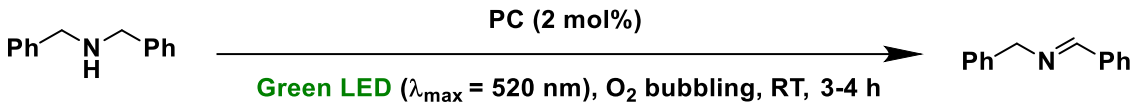

Scheme E.5. Photocatalytic oxidation of dibenzylamine.

In a typical synthesis, 0.070 mmol of dibenzylamine (14.0 mg, 13.6 µl) and the corresponding amount of photocatalyst (**BD-1** to **BD-4**, 1.42 µmol, 2 mol%) were dissolved in 0.8 ml of deuterated solvent (THF-d_8, toluene-d_8). A gentle bubbling with oxygen was initiated, and the reaction was irradiated using the green light of a 50 W RGB LED (λ_{max}=520 nm, ~17 W). The progress of the reaction was monitored by ^{1}H-NMR, with experiments conducted every 15 minutes of irradiation. When necessary, additional deuterated solvent was added during the reaction. The experimental setup for the reaction is depicted in Figure E.2.

Figure E.2. Set-up of the photocatalytic oxidation reaction.

Bibliography

Bibliography

[1] (a) F. Millward, E. Zysman-Colman, *Trends Chem.* **2023**, in press; (b) T. Noël, E. Zysman-Colman, *Chem Catal.* **2022**, *2*, 468-476.

[2] (a) J. M. R. Narayanam, C. R. J. Stephenson, *Chem. Soc. Rev.* **2011**, *40*, 102-113; (b) P. Melchiorre, *Chem. Rev.* **2022**, *122*, 1483-1484; (c) P. Bellotti, H.-M. Huang, T. Faber, F. Glorius, *Chem. Rev.* **2023**, *123*, 4237-4352.

[3] (a) H. Trommsdorff, *Ann. Pharm.* **1834**, *11*, 190-207; (b) A. Natarajan, C. K. Tsai, S. I. Khan, P. McCarren, K. N. Houk, M. A. Garcia-Garibay, *J. Am. Chem. Soc.* **2007**, *129*, 9846-9847.

[4] N. D. Heindel, M. A. Pfau, *J. Chem. Educ.* **1965**, *42*, 383-386.

[5] S. E. Braslavsky, *Pure Appl. Chem.* **2007**, *79*, 293-465.

[6] M. A. Ischay, M. E. Anzovino, J. Du, T. P. Yoon, *J. Am. Chem. Soc.* **2008**, *130*, 12886-12887.

[7] D. A. Nicewicz, D. W. C. MacMillan, *Science* **2008**, *322*, 77-80.

[8] J. M. R. Narayanam, J. W. Tucker, C. R. J. Stephenson, *J. Am. Chem. Soc.* **2009**, *131*, 8756-8757.

[9] K. Gadde, D. De Vos, B. U. W. Maes, *Synthesis* **2022**, *55*, 164-192.

[10] J. Zhao, W. Wu, J. Sun, S. Guo, *Chem. Soc. Rev.* **2013**, *42*, 5323-5351.

[11] G. Farias, C. A. M. Salla, M. Aydemir, L. Sturm, P. Dechambenoit, F. Durola, B. de Souza, H. Bock, A. P. Monkman, I. H. Bechtold, *Chem. Sci.* **2021**, *12*, 15116-15127.

[12] J. R. Lakowicz, *Principles of Fluorescence Spectroscopy*, 3 ed., Springer New York, NY, **2006**.

[13] (a) V. Srivastava, P. K. Singh, P. P. Singh, *J. Photochem. Photobiol. C: Photochem. Rev.* **2022**, *50*, 100488; (b) C. Stephenson, T. Yoon, D. W. C. MacMillan, *Visible Light Photocatalysis in Organic Chemistry*, Wiley-VCH, Weinheim, Germany, **2018**; (c) Q.-Q. Zhou, Y.-Q. Zou, L.-Q. Lu, W.-J. Xiao, *Angew. Chem. Int. Ed.* **2019**, *58*, 1586-1604; (d) F. Meyer, P. S. Halasyamani, G. Masson, *ACS Org. Inorg. Au* **2023**, *3*, 1-3.

[14] (a) J. D. Bell, J. A. Murphy, *Chem. Soc. Rev.* **2021**, *50*, 9540-9685; (b) R. C. McAtee, E. J. McClain, C. R. J. Stephenson, *Trends. Chem.* **2019**, *1*, 111-125; (c) K. Kwon, R. T. Simons, M. Nandakumar, J. L. Roizen, *Chem. Rev.* **2022**, *122*, 2353-2428.

[15] F. Strieth-Kalthoff, M. J. James, M. Teders, L. Pitzer, F. Glorius, *Chem. Soc. Rev.* **2018**, *47*, 7190-7202.

[16] H. Sahoo, *J. Photochem. Photobiol. C: Photochem.* **2011**, *12*, 20-30.

[17] (a) T. Neveselý, M. Wienhold, J. J. Molloy, R. Gilmour, *Chem. Rev.* **2022**, *122*, 2650-2694; (b) F. Strieth-Kalthoff, F. Glorius, *Chem* **2020**, *6*, 1888-1903.

[18] (a) R. Bevernaegie, S. A. M. Wehlin, B. Elias, L. Troian-Gautier, *ChemPhotoChem* **2021**, *5*, 217-234; (b) M. H. Shaw, J. Twilton, D. W. C. MacMillan, *J. Org. Chem.* **2016**, *81*, 6898-6926; (c) C. K. Prier, D. A. Rankic, D. W. C. MacMillan, *Chem. Rev.* **2013**, *113*, 5322-5363.

[19] (a) T. Koike, M. Akita, *Inorg. Chem. Front.* **2014**, *1*, 562-576; (b) V. Mdluli, S. Diluzio, J. Lewis, J. F. Kowalewski, T. U. Connell, D. Yaron, T. Kowalewski, S. Bernhard, *ACS Catal.* **2020**, *10*, 6977-6987.

[20] W. M. Haynes, *CRC handbook of chemistry and physics, 95th Edition*, 95th ed. ed., CRC Press, Hoboken, **2014**.

[21] (a) Y. Y. Loh, K. Nagao, A. J. Hoover, D. Hesk, N. R. Rivera, S. L. Colletti, I. W. Davies, D. W. C. MacMillan, *Science* **2017**, *358*, 1182-1187; (b) G. E. M. Crisenza, P. Melchiorre, *Nat. Commun.* **2020**, *11*, 803; (c) *Nat. Catal.* **2019**, *2*, 735-735.

[22] (a) A. A. Yakushev, A. S. Abel, A. D. Averin, I. P. Beletskaya, A. V. Cheprakov, I. S. Ziankou, L. Bonneviot, A. Bessmertnykh-Lemeune, *Coord. Chem. Rev.* **2022**, *458*, 214331; (b) R. Lindroth, K. L. Materna, L. Hammarström, C.-J. Wallentin, *ACS Org. Inorg. Au* **2022**, *2*, 427-432; (c) A. Jacques, A. Devaux, C. Rubay, F. Pennetreau, A. Desmecht, K. Robeyns, S. Hermans, B. Elias, *ChemCatChem* **2023**, *15*, e202201672.

[23] E. Serrano, N. Linares, J. Garcia-Martinez, J. R. Berenguer, *ChemCatChem* **2013**, *5*, 844-860.

[24] (a) S. Gisbertz, B. Pieber, *ChemPhotoChem* **2020**, *4*, 456-475; (b) L. Zeng, X. Guo, C. He, C. Duan, *ACS Catal.* **2016**, *6*, 7935-7947; (c) T. Zhang, W. Lin, *Chem. Soc. Rev.* **2014**, *43*, 5982-5993.

[25] L. Cao, C. Wang, *ACS Cent. Sci.* **2020**, *6*, 2149-2158.

[26] (a) A. Savateev, M. Antonietti, *ACS Catal.* **2018**, *8*, 9790-9808; (b) D. Franchi, Z. Amara, *ACS Sustainable Chem. Eng.* **2020**, *8*, 15405-15429.

[27] (a) A. Kunzmann, S. Valero, Á. E. Sepúlveda, M. Rico-Santacruz, E. Lalinde, J. R. Berenguer, J. García-Martínez, D. M. Guldi, E. Serrano, R. D. Costa, *Adv. Energy Mater.* **2018**, *8*, 1702583; (b) M. Rico-Santacruz, Á. E. Sepúlveda, C. Ezquerro, E. Serrano, E. Lalinde, J. R. Berenguer, J. García-Martínez, *Appl. Catal. B: Environ.* **2017**, *200*, 93-105.

[28] (a) F. Glaser, O. S. Wenger, *Coord. Chem. Rev.* **2020**, *405*, 213129; (b) B. M. Hockin, C. Li, N. Robertson, E. Zysman-Colman, *Catal. Sci. Technol.* **2019**, *9*, 889-915; (c) C. B. Larsen, O. S. Wenger, *Chem. Eur. J.* **2018**, *24*, 2039-2058; (d) L. H. M. de Groot, A. Ilic, J. Schwarz, K. Wärnmark, *J. Am. Chem. Soc.* **2023**, *145*, 9369-9388.

[29] (a) A. Reichle, O. Reiser, *Chem. Sci.* **2023**, *14*, 4449-4462; (b) S. Engl, O. Reiser, *Chem. Soc. Rev.* **2022**, *51*, 5287-5299.

[30] (a) S. Paria, O. Reiser, in *Visible Light Photocatalysis in Organic Chemistry*, **2018**, pp. 233-251; (b) A. Hossain, A. Bhattacharyya, O. Reiser, *Science* **2019**, *364*, eaav9713.

[31] M. K. Bogdos, E. Pinard, J. A. Murphy, *Beilstein J. Org. Chem.* **2018**, *14*, 2035-2064.

[32] T. Bortolato, S. Cuadros, G. Simionato, L. Dell'Amico, *Chem. Commun.* **2022**, *58*, 1263-1283.

[33] N. A. Romero, D. A. Nicewicz, *Chem. Rev.* **2016**, *116*, 10075-10166.

[34] (a) R. Hojo, A. M. Polgar, Z. M. Hudson, *ACS Sustainable Chem. Eng.* **2022**, *10*, 9665-9678; (b) C. Prentice, J. Morrison, A. D. Smith, E. Zysman-Colman, *Chem. Eur. J.* **2023**, *29*, e202202998; (c) M. A. Bryden, E. Zysman-Colman, *Chem. Soc. Rev.* **2021**, *50*, 7587-7680.

[35] (a) C. Ezquerro, A. E. Sepúlveda, A. Grau-Atienza, E. Serrano, E. Lalinde, J. R. Berenguer, J. García-Martínez, *J. Mater. Chem. C* **2017**, *5*, 9721-9732; (b) C. Ezquerro, E. Fresta, E. Serrano, E. Lalinde, J. García-Martínez, J. R. Berenguer, R. D. Costa, *Mater. Horiz.* **2019**, *6*, 130-136; (c) M. Nieddu, M. Patrian, S. Ferrara, J. P. Fuenzalida Werner, F. Kohler, E. Anaya-Plaza, M. A. Kostiainen, H. Dietz, J. R. Berenguer, R. D. Costa, *Adv. Sci.* **2023**, *10*, 2300069.

[36] (a) T.-Y. Li, J. Wu, Z.-G. Wu, Y.-X. Zheng, J.-L. Zuo, Y. Pan, *Coord. Chem. Rev.* **2018**, *374*, 55-92; (b) A. F. Henwood, E. Zysman-Colman, *Chem. Comm.* **2017**, *53*, 807-826.

[37] A. F. Henwood, A. K. Bansal, D. B. Cordes, A. M. Z. Slawin, I. D. W. Samuel, E. Zysman-Colman, *J. Mater. Chem. C* **2016**, *4*, 3726-3737.

[38] (a) S. Ladouceur, K. N. Swanick, S. Gallagher-Duval, Z. Ding, E. Zysman-Colman, *Eur. J. Inorg. Chem.* **2013**, 5329-5343; (b) K. P. S. Zanoni, B. K. Kariyazaki, A. Ito, M. K. Brennaman, T. J. Meyer, N. Y. Murakami Iha, *Inorg. Chem.* **2014**, *53*, 4089-4099.

[39] (a) K. Mori, H. Yamashita, *Chem. Eur. J.* **2016**, *22*, 11122-11137; (b) A. Eskandari, M. Jafarpour, A. Rezaeifard, M. Salimi, *App. Organomet. Chem.* **2019**, *33*, e5093; (c) Y.-X. Tan, S.-X. Lin, C. Liu, Y. Huang, M. Zhou, Q. Kang, D. Yuan, M. Hong, *Appl. Catal., B* **2018**, *227*, 425-432; (d) M. Wen, K. Mori, Y. Kuwahara, T. An, H. Yamashita, *Chem. Asian J.* **2018**, *13*, 1767-1779; (e) K. Mori, D. Tatsumi, T. Iwamoto, Y. Masui, M. Onaka, H. Yamashita, *Chem. Asian J.* **2018**, *13*, 1348-1356; (f) Y. Zhao, Y. Dong, F. Lu, C. Ju, L. Liu, J. Zhang, B. Zhang, Y. Feng, *J . Mater. Chem. A* **2017**, *5*, 15380-15389.

[40] (a) C. Ezquerro, I. López, E. Serrano, E. Alfaro-Arnedo, E. Lalinde Peña, I. Larráyoz, J. G. Pichel, J. García-Martinez, J. R. Berenguer, *Mater. Adv.* **2022**, *3*, 3582-3592; (b) N. Linares, A. E. Sepulveda, J. R. Berenguer, E. Lalinde, J. Garcia-Martinez, *Microporous Mesoporous Mater.* **2012**, *158*, 300-308.

[41] (a) L. Li, W. Wang, J. Tang, Y. Wang, J. Liu, L. Huang, Y. Wang, F. Guo, J. Wang, W. Shen, L. A. Belfiore, *Nanoscale Res. Lett.* **2019**, *14*, 190; (b) C. C. de Escobar, A. Dallegrave, M. A. Lasarin, J. H. Zimnoch dos Santos, *Colloids Surf., A* **2015**, *486*, 96-105; (c) X. Qian, K. Fuku, Y. Kuwahara, T. Kamegawa, K. Mori, H. Yamashita, *ChemSusChem* **2014**, *7*, 1528-1536.

[42] (a) P. Verma, Y. Kuwahara, K. Mori, R. Raja, H. Yamashita, *Nanoscale* **2020**, *12*, 11333-11363; (b) X. Li, S. Ye, Y. C. Zhang, H. P. Zhao, Y. Huang, B. Zhang, T. Cai, *Nanoscale* **2020**, *12*, 7595-7603; (c) S. M. Soria-Castro, B. Lebeau, M. Cormier, S. Neunlist, T. J. Daou, J.-P. Goddard, *Eur. J. Org. Chem.* **2020**, *2020*, 1572-1578; (d) G. Mohammadi Ziarani, S. Rohani, A. Ziarati, A. Badiei, *RSC Adv.* **2018**, *8*, 41048-41100; (e) M. P. Conley, C. Copéret, C. Thieuleux, *ACS Catalysis* **2014**, *4*, 1458-1469; (f) M. Rimoldi, A. Mezzetti, *Catal. Sci. Technol.* **2014**, *4*, 2724-2740; (g) E. Serrano, N. Linares, J. Garcia-Martinez, J. R. Berenguer, *Chemcatchem* **2013**, *5*, 844-860.

[43] (a) Y. Liang, *Nanoscale Adv.* **2021**, *3*, 6827-6868; (b) M. Abd El Sater, N. Jaber, E. Schulz, *ChemCatChem* **2019**, *11*, 3662-3687; (c) D. González-Muñoz, A. Casado-Sánchez, I. del Hierro, S. Gómez-Ruiz, S. Cabrera, J. Alemán, *J. Catal.* **2019**, *373*, 374-383; (d) A. E. Fernandes, A. M. Jonas, *Catalysis Today* **2019**, *334*, 173-186; (e) H. Heinz, C. Pramanik, O. Heinz, Y. Ding, R. K. Mishra, D. Marchon, R. J. Flatt, I. Estrela-Lopis, J. Llop, S. Moya, R. F. Ziolo, *Surface Science Reports* **2017**, *72*, 1-58; (f) A. Jana, J. Mondal, P. Borah, S. Mondal, A. Bhaumik, Y. Zhao, *Chem. Commun.* **2015**, *51*, 10746-10749; (g) N. Body, C. Lefebvre, P. Eloy, T. Haynes, S. Hermans, O. Riant, *J. Photochem. Photobiol., A* **2023**, *440*, 114648; (h) S. E. Mora-Rodríguez, A. Camacho-Ramírez, J. Cervantes-González, M. A. Vázquez, J. A. Cervantes-Jauregui, A. Feliciano, A. Guerra-Contreras, S. Lagunas-Rivera, *Org. Chem. Front.* **2022**, *9*, 2856-2888; (i) D. González-Muñoz, A. Gómez-Avilés, C. B. Molina, J. Bedia, C. Belver, J. Alemán, S. Cabrera, *J. Mater. Sci. Technol.* **2022**, *103*, 134-143.

[44] N. Linares, A. E. Sepúlveda, M. C. Pacheco, J. R. Berenguer, E. Lalinde, C. Nájera, J. Garcia-Martinez, *New J. Chem.* **2011**, *35*, 225-234.
[45] Y. Duan, C. Ezquerro, E. Serrano, E. Lalinde, J. García-Martínez, J. R. Berenguer, R. D. Costa, *Adv. Funct. Mater.* **2020**, *30*, 2005401.
[46] (a) S. L. Suib, J. Přech, J. Čejka, Y. Kuwahara, K. Mori, H. Yamashita, *Mater. Today* **2020**, *32*, 244-259; (b) N. Linares, E. Serrano, M. Rico, A. Balu, E. Losada, R. Luque, J. García-Martínez, *Chem. Commun.* **2011**, *47*, 9024-9035.
[47] K. Feng, R.-Y. Zhang, L.-Z. Wu, B. Tu, M.-L. Peng, L.-P. Zhang, D. Zhao, C.-H. Tung, *J. Am. Chem. Soc.* **2006**, *128*, 14685-14690.
[48] (a) K. Mori, K. Watanabe, M. Kawashima, M. Che, H. Yamashita, *J. Phys. Chem. C* **2011**, *115*, 1044-1050; (b) K. Mori, M. Tottori, K. Watanabe, M. Che, H. Yamashita, *J. Phys. Chem. C* **2011**, *115*, 21358-21362.
[49] R. Rojas-Luna, M. Castillo-Rodríguez, J. R. Ruiz, C. Jiménez-Sanchidrián, D. Esquivel, F. J. Romero-Salguero, *Dalton Trans.* **2022**, *51*, 18708-18721.
[50] A. E. McCalley, S. Kaja, A. J. Payne, P. Koulen, *Molecules* **2014**, *19*, 7327-7340.
[51] M. Hara, S. Samori, X. Cai, M. Fujitsuka, T. Majima, *J. Phys. Chem. A* **2005**, *109*, 9831-9835.
[52] D. H. Song, H. Y. Yoo, J. P. Kim, *Dyes Pigm.* **2007**, 727-731.
[53] D. Cameron, S. Eisler, *J. Phys. Org. Chem.* **2018**, *31*, e3858.
[54] (a) A. W. H. Speed, T. J. Mann, R. V. O'Brien, R. R. Schrock, A. H. Hoveyda, *J. Am. Chem. Soc.* **2014**, *136*, 16136-16139; (b) Z. Huang, E.-i. Negishi, *J. Am. Chem. Soc.* **2007**, *129*, 14788-14792; (c) B. Tomassy, A. Zwierzak, *Synth. Commun.* **1998**, *28*, 1201-1214.
[55] N. Hoffmann, *Chem. Rev.* **2008**, *108*, 1052-1103.
[56] G. S. Hammond, J. Saltiel, A. A. Lamola, N. J. Turro, J. S. Bradshaw, D. O. Cowan, R. C. Counsell, V. Vogt, C. Dalton, *J. Am. Chem. Soc.* **1964**, *86*, 3197-3217.
[57] J. Saltiel, G.-E. Khalil, K. Schanze, *Chem. Phys. Lett.* **1980**, *70*, 233-235.
[58] C. Ezquerro, Universidad de La Rioja (Doctoral Thesis in Universidad de La Rioja), **2019**.
[59] K. Zhang, N. Xu, M. Jia, R. Li, M. Huang, *J. Appl. Phys.* **2019**, *125*, 183101.
[60] S. El Hankari, A. Bouhaouss, P. Hesemann, *Microporous Mesoporous Mater.* **2013**, *180*, 196-208.
[61] (a) J. G. Croissant, X. Cattoën, M. Wong Chi Man, J.-O. Durand, N. M. Khashab, *Nanoscale* **2015**, *7*, 20318-20334; (b) H. Li, D. Shen, H. Lu, F. Wu, X. Chen, R. Pleixats, J. Pan, *Sep. Purif. Technol.* **2021**, *277*, 119453; (c) S. Inagaki, S. Guan, Y. Fukushima, T. Ohsuna, O. Terasaki, *J. Am. Chem. Soc.* **1999**, *121*, 9611-9614.
[62] B. Karimi, N. Ganji, O. Pourshiani, W. R. Thiel, *Prog. Mater. Sci.* **2022**, *125*, 100896.
[63] P. Hesemann, L. Viau, A. Vioux, in *The Sol-Gel Handbook, Vol. 2*, **2015**, pp. 487-518.
[64] P. Hesemann, T. P. Nguyen, S. E. Hankari, *Materials* **2014**, *7*, 2978-3001.
[65] (a) M. Braun, U. D. Thach, B. Prelot, P. Hesemann, D. Esposito, *J. Chem. Technol. Biotechnol.* **2017**, *92*, 2229-2235; (b) A. Duarte Rodrigues, M. Jacob, V. Gauchou, J.-O. Durand, P. Trens, P. Hesemann, *Molecules* **2020**, *25*, 5987.
[66] (a) U. D. Thach, P. Trens, B. Prelot, J. Zajac, P. Hesemann, *J. Phys. Chem. C* **2016**, *120*, 27412-27421; (b) N. Abdou, B. Alonso, N. Brun, P. Landois, A. Taubert, P. Hesemann, A. Mehdi, *Mater. Chem. Front.* **2022**, *6*, 939-947.
[67] (a) U. D. Thach, B. Prelot, P. Hesemann, *Sep. Purif. Technol.* **2018**, *196*, 217-223; (b) H. Wu, P. Hesemann, P. Trens, G. Silly, F. Salles, J. Zajac, *J. Chem. Eng.*

2020, *398*, 125634; (c) B. Mezghrani, L. M. A. Ali, S. Richeter, J.-O. Durand, P. Hesemann, N. Bettache, *ACS Appl. Mater. Interfaces* **2021**, *13*, 29325-29339; (d) B. Mezghrani, L. M. A. Ali, N. Cubedo, M. Rossel, P. Hesemann, J.-O. Durand, N. Bettache, *Int. J. Pharm.* **2023**, *641*, 123083; (e) B. Mezghrani, L. M. A. Ali, S. Jakimoska, F. Cunin, P. Hesemann, J.-O. Durand, N. Bettache, *ChemPlusChem* **2023**, *88*, e202300021; (f) T. Tran Duy, A. Duarte Rodrigues, G. Vo-Thanh, P. Hesemann, *Green Energy Environ.* **2020**, *5*, 130-137.

[68] (a) C. DeCastro, E. Sauvage, M. H. Valkenberg, W. F. Hölderich, *J. Catal.* **2000**, *196*, 86-94; (b) M. H. Valkenberg, C. deCastro, W. F. Hölderich, *Green Chem.* **2002**, *4*, 88-93.

[69] (a) L. F. Bobadilla, T. Blasco, J. A. Odriozola, *Phys. Chem. Chem. Phys.* **2013**, *15*, 16927-16934; (b) H. Zhao, N. Yu, J. Wang, D. Zhuang, Y. Ding, R. Tan, D. Yin, *Microporous Mesoporous Mater.* **2009**, *122*, 240-246; (c) T. Sasaki, M. Tada, C. Zhong, T. Kume, Y. Iwasawa, *J. Mol. Catal. A-Chem.* **2008**, *279*, 200-209; (d) E. N. Kusumawati, D. Nishio-Hamane, T. Sasaki, *Catal. Today* **2018**, *309*, 109-118; (e) M. G. Ahmad, K. Chanda, *Coord. Chem. Rev.* **2022**, *472*, 214769.

[70] (a) M. Shimizu, K. Michikawa, Y. Maegawa, S. Inagaki, K.-i. Fujita, *ACS Appl. Nano Mater.* **2020**, *3*, 2527-2535; (b) H. Matsukawa, M. Yoshida, T. Tsunenari, S. Nozawa, A. Sato-Tomita, Y. Maegawa, S. Inagaki, A. Kobayashi, M. Kato, *Sci. Rep.* **2019**, *9*, 15151; (c) M. Waki, Y. Maegawa, K. Hara, Y. Goto, S. Shirai, Y. Yamada, N. Mizoshita, T. Tani, W.-J. Chun, S. Muratsugu, M. Tada, A. Fukuoka, S. Inagaki, *J. Am. Chem. Soc.* **2014**, *136*, 4003-4011.

[71] (a) M. Martínez-Aguirre, E. Serrano, C. Ezquerro, E. Lalinde, J. R. Berenguer, J. García-Martínez, M. A. Rodríguez, *Catal. Today* **2023**, *422*, 114213; (b) M. Cheng, L. Zhou, J. Ma, J. Mu, C. Yi, M.-J. Li, *Mater. Sci. Eng. C* **2019**, *104*, 109972; (c) H. Takeda, M. Ohashi, Y. Goto, T. Ohsuna, T. Tani, S. Inagaki, *Adv. Funct. Mater.* **2016**, *26*, 5068-5077; (d) S. Liu, J. Zhang, D. Shen, H. Liang, X. Liu, Q. Zhao, W. Huang, *Chem. Commun.* **2015**, *51*, 12839-12842.

[72] (a) G. Ekineker, C. Nguyen, S. Bayır, S. Dominguez Gil, Ü. İşci, M. Daurat, A. Godefroy, L. Raehm, C. Charnay, E. Oliviero, V. Ahsen, M. Gary-Bobo, J.-O. Durand, F. Dumoulin, *Chem. Commun.* **2019**, *55*, 11619-11622; (b) C. Mauriello Jimenez, D. Aggad, J. G. Croissant, K. Tresfield, D. Laurencin, D. Berthomieu, N. Cubedo, M. Rossel, S. Alsaiari, D. H. Anjum, R. Sougrat, M. A. Roldan-Gutierrez, S. Richeter, E. Oliviero, L. Raehm, C. Charnay, X. Cattoën, S. Clément, M. Wong Chi Man, M. Maynadier, V. Chaleix, V. Sol, M. Garcia, M. Gary-Bobo, N. M. Khashab, N. Bettache, J.-O. Durand, *Adv. Funct. Mater.* **2018**, *28*, 1800235.

[73] (a) Y.-L. Li, A.-J. Li, S.-L. Huang, J. J. Vittal, G.-Y. Yang, *Chem. Soc. Rev.* **2023**, *52*, 4725-4754; (b) T. Luo, L. Gilmanova, S. Kaskel, *Coord. Chem. Rev.* **2023**, *490*, 215210.

[74] (a) D. I. Ugwu, J. Conradie, *J. Mol. Struct.* **2023**, *1293*, 136275; (b) J. Á. Martín-Illán, D. Rodríguez-San-Miguel, F. Zamora, *Coord. Chem. Rev.* **2023**, *495*, 215342.

[75] (a) J. W. Beatty, J. J. Douglas, K. P. Cole, C. R. Stephenson, *Nat. Commun.* **2015**, *6*, 7919; (b) J. W. Tucker, Y. Zhang, T. F. Jamison, C. R. J. Stephenson, *Angew. Chem. Int. Ed.* **2012**, *51*, 4144-4147; (c) D. Cambié, C. Bottecchia, N. J. W. Straathof, V. Hessel, T. Noël, *Chem. Rev.* **2016**, *116*, 10276-10341; (d) K. P. Cole, J. J. Douglas, T. Hammerstad, C. R. J. Stephenson, *Org. Process Res. Dev.* **2023**, *27*, 399-408.

[76] S. D. A. Zondag, D. Mazzarella, T. Noël, *Annu. Rev. Chem. Biomol. Eng.* **2023**, *14*, 283-300.
[77] M. Yan, J. C. Lo, J. T. Edwards, P. S. Baran, *J. Am. Chem. Soc.* **2016**, *138*, 12692-12714.
[78] L. Fensterbank, J.-P. Goddard, C. Ollivier, in *Visible Light Photocatalysis in Organic Chemistry* (Ed.: J. Sons), **2018**, pp. 25-71.
[79] (a) C. Prentice, J. Morrisson, A. D. Smith, E. Zysman-Colman, *Beilstein J. Org. Chem.* **2020**, *16*, 2363-2441; (b) M. Silvi, P. Melchiorre, *Nature* **2018**, *554*, 41-49; (c) T. E. Schirmer, B. König, *J. Am. Chem. Soc.* **2022**, *144*, 19207-19218.
[80] H. F. Piedra, C. Valdés, M. Plaza, *Chem. Sci.* **2023**, *14*, 5545-5568.
[81] (a) P. Knochel, W. Dohle, N. Gommermann, F. F. Kneisel, F. Kopp, T. Korn, I. Sapountzis, V. A. Vu, *Angew. Chem. Int. Ed.* **2003**, *42*, 4302-4320; (b) W. F. Bailey, J. J. Patricia, *J. Organomet. Chem.* **1988**, *352*, 1-46.
[82] W. P. Neumann, *Synthesis* **1987**, *1987*, 665-683.
[83] (a) M. R. Medeiros, L. N. Schacherer, D. A. Spiegel, J. L. Wood, *Org. Lett.* **2007**, *9*, 4427-4429; (b) A. Krief, A.-M. Laval, *Chem. Rev.* **1999**, *99*, 745-778.
[84] Y. Kwon, J. Lee, Y. Noh, D. Kim, Y. Lee, C. Yu, J. C. Roldao, S. Feng, J. Gierschner, R. Wannemacher, M. S. Kwon, *Nat. Commun.* **2023**, *14*, 92.
[85] S. Fukuzumi, S. Mochizuki, T. Tanaka, *J. Phys. Chem.* **1990**, *94*, 722-726.
[86] (a) A. Santiago-Portillo, H. G. Baldoví, E. Carbonell, S. Navalón, M. Álvaro, H. García, B. Ferrer, *J. Phys. Chem. C* **2018**, *122*, 29190-29199; (b) W. Zhang, D. Wang, Q. Xie, C. Xu, G. Kuang, J. Tang, C. Pan, G. Yu, *Macromolecules* **2023**, *56*, 4022-4029; (c) X. Li, S. Yu, Z. Shen, R. Wang, W. Zhang, A. Núñez-Delgado, N. Han, L.-B. Xing, *J. Colloid Interface Sci.* **2022**, *617*, 118-128; (d) K. L. Materna, L. Hammarström, *Chem. Eur. J.* **2021**, *27*, 16966-16977.
[87] (a) T. Ishikawa, *Med. Res. Rev.* **2001**, *21*, 61-72; (b) P. Lasák, K. Motyka, V. Kryštof, J. Stýskala, *Molecules* **2018**, *23*; (c) A. Nandikolla, Y. M. Khetmalis, B. Venkata Siva Kumar, A. Chandu, B. Karan Kumar, G. Shetye, R. Ma, S. Murugesan, S. G. Franzblau, K. V. G. Chandra Sekhar, *RSC Med. Chem.* **2023**, *14*, 1549-1561.
[88] (a) M. Zhang, L. Liu, H. Xiao, T. Zhao, L. Yang, X. Xu, *J. Heterocyclic Chem.* **2016**, *53*, 234-240; (b) F. Meng, G. Zuo, X. Hao, G. Wang, H. Xiao, J. Zhang, G. Xu, *J. Ethnopharmacol.* **2009**, *125*, 494-496.
[89] D.-Z. Chen, S.-R. Fan, B.-J. Yang, H.-C. Yao, Y.-T. Wang, J.-Y. Cai, C.-X. Jing, Z.-H. Pan, M. Luo, Y.-Q. Yuze, G.-J. Liu, X.-J. Hao, *J. Nat. Prod.* **2021**, *84*, 1175-1184.
[90] (a) A. Krasiński, Z. Radić, R. Manetsch, J. Raushel, P. Taylor, K. B. Sharpless, H. C. Kolb, *J. Am. Chem. Soc.* **2005**, *127*, 6686-6692; (b) A. D. C. Parenty, L. V. Smith, K. M. Guthrie, D.-L. Long, J. Plumb, R. Brown, L. Cronin, *J. Med. Chem.* **2005**, *48*, 4504-4506; (c) I. Kock, D. Heber, M. Weide, U. Wolschendorf, B. Clement, *J. Med. Chem.* **2005**, *48*, 2772-2777; (d) Q. A. Khan, J. Lu, S. M. Hecht, *J. Nat. Prod.* **2009**, *72*, 438-442; (e) I. Azad, R. Ahmad, T. Khan, M. Saquib, F. Hassan, Y. Akhter, A. R. Khan, M. Nasibullah, *Future Med. Chem.* **2020**, *12*, 709-739.
[91] Y. Ding, D. Qu, K.-M. Zhang, X.-X. Cang, Z.-N. Kou, W. Xiao, J.-B. Zhu, *J. Asian Nat. Prod. Res.* **2017**, *19*, 53-100.
[92] V. Talukdar, A. Vijayan, N. Kumar Katari, K. V. Radhakrishnan, P. Das, *Adv. Synth. Catal.* **2021**, *363*, 1202-1245.

[93] (a) N. Ramkumar, R. Nagarajan, *J. Org. Chem.* **2013**, *78*, 2802-2807; (b) T. Nishiyama, S. Takaiwa, R. Kotouge, S. Tani, R. Yoshinaga, E. Hamada, M. Endo, Y. Sugino, N. Hatae, S. Hibino, T. Choshi, *Tetrahedron Lett.* **2019**, *60*, 151278.
[94] (a) R. Alonso, P. J. Campos, B. García, M. A. Rodríguez, *Org. Lett.* **2006**, *8*, 3521-3523; (b) R. Alonso, P. J. Campos, M. A. Rodríguez, D. Sampedro, *J. Org. Chem.* **2008**, *73*, 2234-2239.
[95] R. Alonso, A. Caballero, P. J. Campos, M. A. Rodríguez, *Tetrahedron* **2010**, *66*, 8828-8831.
[96] H. Jiang, X. An, K. Tong, T. Zheng, Y. Zhang, S. Yu, *Angew. Chem. Int. Ed.* **2015**, *54*, 4055-4059.
[97] L. Khouchaf, K. Boulahya, P. P. Das, S. Nicolopoulos, V. K. Kis, J. L. Lábár, *Materials* **2020**, *13*, 4393.
[98] G. Sun, M. Zuo, W. Qian, J. Jiao, X.-Y. Hu, L. Wang, *Green Synth. Catal.* **2021**, *2*, 32-37.
[99] (a) C. Yang, F. Mehmood, T. L. Lam, S. L.-F. Chan, Y. Wu, C.-S. Yeung, X. Guan, K. Li, C. Y.-S. Chung, C.-Y. Zhou, T. Zou, C.-M. Che, *Chem. Sci.* **2016**, *7*, 3123-3136; (b) C.-F. Leung, S.-M. Ng, C.-C. Ko, W.-L. Man, J. Wu, L. Chen, T.-C. Lau, *Energy Environ. Sci.* **2012**, *5*, 7903-7907.
[100] (a) A. Vega-Penaloza, J. Mateos, X. Companyo, M. Escudero-Casao, L. Dell'Amico, *Angew. Chem. Int. Ed.* **2021**, *60*, 1082-1097; (b) Q. Liu, C. Huo, Y. Fu, Z. Du, *Org. Biomol. Chem.* **2022**, *20*, 6721-6740.
[101] B. G. McCarthy, R. M. Pearson, C.-H. Lim, S. M. Sartor, N. H. Damrauer, G. M. Miyake, *J. Am. Chem. Soc.* **2018**, *140*, 5088-5101.
[102] S. Sasaki, G. P. C. Drummen, G.-i. Konishi, *J. Mater. Chem. C* **2016**, *4*, 2731-2743.
[103] Y. Wu, D. Kim, T. S. Teets, *Synlett* **2021**, *33*, 1154-1179.
[104] I. Ghosh, B. König, *Angew. Chem. Int. Ed.* **2016**, *55*, 7676-7679.
[105] (a) J. Zhang, L. Wang, Q. Liu, Z. Yang, Y. Huang, *Chem. Commun.* **2013**, *49*, 11662-11664; (b) R. W. Redmond, J. N. Gamlin, *Photochem. Photobiol.* **1999**, *70*, 391-475.
[106] (a) D. P. Hari, B. König, *Chem. Commun.* **2014**, *50*, 6688-6699; (b) A. Srivastava, P. K. Singh, A. Ali, P. P. Singh, V. Srivastava, *RSC Adv.* **2020**, *10*, 39495-39508.
[107] N. J. Turro, V. Ramamurthy, J. C. Scaiano, *Principles of molecular photochemistry: an introduction*, University science books, **2009**.
[108] (a) M. Singh, A. K. Yadav, L. D. S. Yadav, R. K. P. Singh, *Tetrahedron Lett.* **2017**, *58*, 2206-2208; (b) I. K. Sideri, E. Voutyritsa, C. G. Kokotos, *Org. Biomol. Chem.* **2018**, *16*, 4596-4614.
[109] F. D. Lewis, R. E. Dykstra, I. R. Gould, S. Farid, *J. Phys. Chem.* **1988**, *92*, 7042-7043.
[110] M. J. P. Mandigma, J. Kaur, J. P. Barham, *ChemCatChem* **2023**, *15*, e202201542.
[111] T.-Y. Shang, L.-H. Lu, Z. Cao, Y. Liu, W.-M. He, B. Yu, *Chem. Commun.* **2019**, *55*, 5408-5419.
[112] H. Uoyama, K. Goushi, K. Shizu, H. Nomura, C. Adachi, *Nature* **2012**, *492*, 234-238.
[113] J. Luo, J. Zhang, *ACS Catal.* **2016**, *6*, 873-877.
[114] E. Speckmeier, T. G. Fischer, K. Zeitler, *J. Am. Chem. Soc.* **2018**, *140*, 15353-15365.
[115] S. Fukuzumi, H. Kotani, K. Ohkubo, S. Ogo, N. V. Tkachenko, H. Lemmetyinen, *J. Am. Chem. Soc.* **2004**, *126*, 1600-1601.

[116] (a) A. Joshi-Pangu, F. Lévesque, H. G. Roth, S. F. Oliver, L.-C. Campeau, D. Nicewicz, D. A. DiRocco, *J. Org. Chem.* **2016**, *81*, 7244-7249; (b) B. Zilate, C. Fischer, C. Sparr, *Chem. Commun.* **2020**, *56*, 1767-1775; (c) A. Tlili, S. Lakhdar, *Angew. Chem. Int. Ed.* **2021**, *60*, 19526-19549.
[117] H. van Willigen, G. Jones, M. S. Farahat, *J. Phys. Chem.* **1996**, *100*, 3312-3316.
[118] C. Tanielian, C. Wolff, *J. Phys. Chem.* **1995**, *99*, 9831-9837.
[119] K. Bergmann, C. T. O'Konski, *J. Phys. Chem.* **1963**, *67*, 2169-2177.
[120] (a) S. P. Pitre, C. D. McTiernan, H. Ismaili, J. C. Scaiano, *J. Am. Chem. Soc.* **2013**, *135*, 13286-13289; (b) T. Shen, Z.-G. Zhao, Q. Yu, H.-J. Xu, *J. Photochem. Photobiol., A* **1989**, *47*, 203-212.
[121] A. Treibs, F.-H. Kreuzer, *Justus Liebigs Ann. Chem.* **1968**, *718*, 208-223.
[122] (a) V. Lakshmi, M. Rajeswara Rao, M. Ravikanth, *Org. Biomol. Chem.* **2015**, *13*, 2501-2517; (b) G. Ulrich, R. Ziessel, A. Harriman, *Angew. Chem. Int. Ed.* **2008**, *47*, 1184-1201.
[123] R. Ziessel, G. Ulrich, A. Harriman, *New J. Chem.* **2007**, *31*, 496-501.
[124] (a) N. Boens, B. Verbelen, M. J. Ortiz, L. Jiao, W. Dehaen, *Coord. Chem. Rev.* **2019**, *399*, 213024; (b) P. K. Singh, P. Majumdar, S. P. Singh, *Coord. Chem. Rev.* **2021**, *449*, 214193; (c) D. Wang, X. Wang, S. Zhou, P. Gu, X. Zhu, C. Wang, Q. Zhang, *Coord. Chem. Rev.* **2023**, *482*, 215074.
[125] B. M. Squeo, M. Pasini, *Supramol. Chem.* **2020**, *32*, 56-70.
[126] (a) V.-N. Nguyen, Z. Zhao, B. Z. Tang, J. Yoon, *Chem. Soc. Rev.* **2022**, *51*, 3324-3340; (b) Z. Mao, J. H. Kim, J. Lee, H. Xiong, F. Zhang, J. S. Kim, *Coord. Chem. Rev.* **2023**, *476*, 214908; (c) M. C. Malacarne, M. B. Gariboldi, E. Caruso, *Int. J. Mol. Sci.* **2022**, *23*, 10198; (d) A. Kamkaew, S. H. Lim, H. B. Lee, L. V. Kiew, L. Y. Chung, K. Burgess, *Chem. Soc. Rev.* **2013**, *42*, 77-88.
[127] (a) S. Kolemen, E. U. Akkaya, *Coord. Chem. Rev.* **2018**, *354*, 121-134; (b) P. Kaur, K. Singh, *J. Mater. Chem. C* **2019**, *7*, 11361-11405.
[128] (a) E. Fresta, A. Charisiadis, L. M. Cavinato, N. Palandjian, K. Karikis, V. Nikolaou, G. Charalambidis, A. G. Coutsolelos, R. D. Costa, *Adv. Photonics Res.* **2021**, *2*, 2000188; (b) M. Poddar, R. Misra, *Coord. Chem. Rev.* **2020**, *421*, 213462.
[129] (a) P. Wang, S. Guo, H.-J. Wang, K.-K. Chen, N. Zhang, Z.-M. Zhang, T.-B. Lu, *Nat. Commun.* **2019**, *10*, 3155; (b) H. Yang, J. Wang, J. Ma, H. Yang, J. Zhang, K. Lv, L. Wen, T. Peng, *J. Mater. Chem. A* **2019**, *7*, 10439-10445.
[130] L. Collado, T. Naranjo, M. Gomez-Mendoza, C. G. López-Calixto, F. E. Oropeza, M. Liras, J. Marugán, V. A. de la Peña O'Shea, *Adv. Funct. Mater.* **2021**, *31*, 2105384.
[131] (a) J. Miao, Y. Wang, J. Liu, L. Wang, *Chem. Soc. Rev.* **2022**, *51*, 153-187; (b) L. Bucher, N. Desbois, E. N. Koukaras, C. H. Devillers, S. Biswas, G. D. Sharma, C. P. Gros, *J. Mater. Chem. A* **2018**, *6*, 8449-8461.
[132] (a) P. Rana, N. Singh, P. Majumdar, S. Prakash Singh, *Coord. Chem. Rev.* **2022**, *470*, 214698; (b) P. De Bonfils, L. Péault, P. Nun, V. Coeffard, *Eur. J. Org. Chem.* **2021**, *2021*, 1809-1824; (c) A. Turksoy, D. Yildiz, E. U. Akkaya, *Coord. Chem. Rev.* **2019**, *379*, 47-64; (d) E. Bassan, A. Gualandi, P. G. Cozzi, P. Ceroni, *Chem. Sci.* **2021**, *12*, 6607-6628.
[133] T. Yogo, Y. Urano, Y. Ishitsuka, F. Maniwa, T. Nagano, *J. Am. Chem. Soc.* **2005**, *127*, 12162-12163.
[134] X.-F. Zhang, *J. Photochem. Photobiol. A: Chem.* **2018**, *355*, 431-443.
[135] (a) N. J. L. K. Davis, R. W. MacQueen, S. T. E. Jones, C. Orofino-Pena, D. Cortizo-Lacalle, R. G. D. Taylor, D. Credgington, P. J. Skabara, N. C. Greenham,

J. Mater. Chem. C **2017**, *5*, 1952-1962; (b) S.-C. Yeh, L.-J. Wang, H.-M. Yang, Y.-H. Dai, C.-W. Lin, C.-T. Chen, R.-J. Jeng, *Chem. Eur. J.* **2017**, *23*, 14747-14759; (c) V.-N. Nguyen, Y. Yim, S. Kim, B. Ryu, K. M. K. Swamy, G. Kim, N. Kwon, C.-Y. Kim, S. Park, J. Yoon, *Angew. Chem. Int. Ed.* **2020**, *59*, 8957-8962.

[136] Z. Wang, L. Huang, Y. Yan, A. M. El-Zohry, A. Toffoletti, J. Zhao, A. Barbon, B. Dick, O. F. Mohammed, G. Han, *Angew. Chem. Int. Ed.* **2020**, *59*, 16114-16121.

[137] Y.-F. Kang, W.-K. Chen, K.-X. Teng, L.-Y. Wang, X.-C. Xu, L.-Y. Niu, G. Cui, Q.-Z. Yang, *CCS Chem.* **2022**, *4*, 3516-3528.

[138] J. Zhao, K. Xu, W. Yang, Z. Wang, F. Zhong, *Chem. Soc. Rev.* **2015**, *44*, 8904-8939.

[139] W. Li, L. Li, H. Xiao, R. Qi, Y. Huang, Z. Xie, X. Jing, H. Zhang, *RSC Adv.* **2013**, *3*, 13417-13421.

[140] (a) B. Bertrand, K. Passador, C. Goze, F. Denat, E. Bodio, M. Salmain, *Coord. Chem. Rev.* **2018**, *358*, 108-124; (b) Y. Wang, S. Wang, Q. Wang, W. Tang, L. Lin, T. Zhang, M. Hu, X. Wang, *J. Inorg. Biochem.* **2023**, *242*, 112160; (c) W.-W. Feng, B.-F. Liang, B.-H. Chen, Q.-Y. Liu, Z.-Y. Pan, Y.-J. Liu, L. He, *Dyes Pigm.* **2023**, *211*, 111077; (d) S. Paul, P. Kundu, P. Kondaiah, A. R. Chakravarty, *Inorg. Chem.* **2021**, *60*, 16178-16193; (e) H. S. Jung, S. Koo, M. Won, S. An, H. Park, J. L. Sessler, J. Han, J. S. Kim, *Chem. Sci.* **2023**, *14*, 1808-1819; (f) C. Liu, Y. Jiang, J. Xiang, C. Xiang, H. Li, H. Li, F. Wei, J. Huang, R. Li, K. Man-Chung Wong, P. Gong, *Dyes Pigm.* **2023**, *209*, 110900; (g) S. Paul, S. Sahoo, S. Sahoo, C. Jayabaskaran, A. R. Chakravarty, *Eur. J. Inorg. Chem.* **2022**, e202200487.

[141] B. Liu, J. Jiao, W. Xu, M. Zhang, P. Cui, Z. Guo, Y. Deng, H. Chen, W. Sun, *Adv. Mater.* **2021**, *33*, 2100795.

[142] S. Pordel, R. N. Pickens, J. K. White, *Organometallics* **2021**, *40*, 2983-2994.

[143] J. Sun, F. Zhong, X. Yi, J. Zhao, *Inorg. Chem.* **2013**, *52*, 6299-6310.

[144] J. M. Lee, J. M. Park, H. K. Lee, H. M. Kim, J. H. Kim, J. P. Kim, *Dyes Pigms.* **2021**, *196*, 109662.

[145] (a) J. P. Celli, B. Q. Spring, I. Rizvi, C. L. Evans, K. S. Samkoe, S. Verma, B. W. Pogue, T. Hasan, *Chem. Rev.* **2010**, *110*, 2795-2838; (b) D. E. J. G. J. Dolmans, D. Fukumura, R. K. Jain, *Nat Rev Cancer* **2003**, *3*, 380-387.

[146] (a) B. Aziz, I. Aziz, A. Khurshid, E. Raoufi, F. N. Esfahani, Z. Jalilian, M. R. Mozafari, E. Taghavi, M. Ikram, *Biomedicines* **2023**, *11*, 224; (b) R. Stuhr, P. Bayer, A. J. von Wangelin, *ChemSusChem* **2022**, *15*, e202201323.

[147] (a) E. L. Clennan, A. Pace, *Tetrahedron* **2005**, *61*, 6665-6691; (b) A. A. Gorman, M. A. J. Rodgers, *Chem. Soc. Rev.* **1981**, *10*, 205-231.

[148] (a) M. C. DeRosa, R. J. Crutchley, *Coord. Chem. Rev.* **2002**, *233-234*, 351-371; (b) J. Al-Nu'airat, I. Oluwoye, N. Zeinali, M. Altarawneh, B. Z. Dlugogorski, *Chem. Rec.* **2021**, *21*, 315-342.

[149] L. Huang, J. Zhao, S. Guo, C. Zhang, J. Ma, *J. Org. Chem.* **2013**, *78*, 5627-5637.

[150] N. Okamura, T. Nakamura, S. Yagi, T. Maeda, H. Nakazumi, H. Fujiwara, S. Koseki, *RSC Adv.* **2016**, *6*, 51435-51445.

[151] A. Loudet, K. Burgess, *Chem. Rev.* **2007**, *107*, 4891-4932.

[152] A. D. Lama, B. Bartolomei, C. Rosso, G. Filippini, M. M. Martínez, L. A. Sarandeses, M. Prato, *Eur. J. Org. Chem.* **2022**, *2022*, e202200622.

[153] H. He, L. Si, Y. Zhong, M. Dubey, *Chem. Commun.* **2012**, *48*, 1886-1888.

[154] M. Farfán-Paredes, O. González-Antonio, D. E. Tahuilan-Anguiano, J. Peón, A. Ariza, P. G. Lacroix, R. Santillan, N. Farfán, *New J. Chem.* **2020**, *44*, 19459-19471.

[155] R. Lara, G. Millán, M. T. Moreno, E. Lalinde, E. Alfaro-Arnedo, I. P. López, I. M. Larráyoz, J. G. Pichel, *Chem. Eur. J.* **2021**, *27*, 15757-15772.
[156] A. Uddin, S. R. Allen, A. K. Rylski, C. J. O'Dea, J. T. Ly, T. A. Grusenmeyer, S. T. Roberts, Z. A. Page, *Angew. Chem. Int. Ed.* **2023**, *62*, e202219140.
[157] L. Quan, W. Lin, T. Sun, Z. Xie, Y. Huang, X. Jing, *Catal Lett* **2014**, *144*, 308-313.
[158] F. Wilkinson, W. P. Helman, A. B. Ross, *J. Phys. Chem. Ref. Data.* **1993**, *22*, 113-262.
[159] Bruker AXS Inc., Madison, Wisconsi, USA, **2017**.
[160] G. Sheldrick, *Acta Crystallogr. Sect. A* **2015**, *71*, 3-8.
[161] G. M. Sheldrick, *Acta crystallogr., Sect. C* **2015**, *71*, 3-8.
[162] L. J. Farrugia, *J. Appl. Crystallogr* **1999**, *32*, 837-838.
[163] G. W. T. M. J. Frisch, H. B. Schlegel, G. E. Scuseria, M. A. Robb, J. R. Cheeseman, G. Scalmani, V. Barone, G. A. Petersson, H. Nakatsuji, X. Li, M. Caricato, A. Marenich, J. Bloino, B. G. Janesko, R. Gomperts, B. Mennucci, H. P. Hratchian, J. V. Ortiz, A. F. Izmaylov, J. L. Sonnenberg, D. Williams-Young, F. Ding, F. Lipparini, F. Egidi, J. Goings, B. Peng, A. Petrone, T. Henderson, D. Ranasinghe, V. G. Zakrzewski, J. Gao, N. Rega, G. Zheng, W. Liang, M. Hada, M. Ehara, K. Toyota, R. Fukuda, J. Hasegawa, M. Ishida, T. Nakajima, Y. Honda, O. Kitao, H. Nakai, T. Vreven, K. Throssell, J. A. Montgomery, Jr., J. E. Peralta, F. Ogliaro, M. Bearpark, J. J. Heyd, E. Brothers, K. N. Kudin, V. N. Staroverov, T. Keith, R. Kobayashi, J. Normand, K. Raghavachari, A. Rendell, J. C. Burant, S. S. Iyengar, J. Tomasi, M. Cossi, J. M. Millam, M. Klene, C. Adamo, R. Cammi, J. W. Ochterski, R. L. Martin, K. Morokuma, O. Farkas, J. B. Foresman, and D. J. Fox, *Gaussian 09, Revision B.01, Gaussian, Inc., Wallingford CT* **2010**.
[164] M. J. Frisch, Trucks, G.W., et al., *Gaussian 16 Revision A* **2016**, *3*.
[165] (a) A. D. Becke, *Phys. Rev. A* **1988**, *38*, 3098-3100; (b) A. D. Becke, *J. Chem. Phys.* **1993**, *98*, 5648-5652; (c) C. Lee, W. Yang, R. G. Parr, *Phys. Rev. B* **1988**, *37*, 785-789.
[166] P. J. Hay, W. R. Wadt, *J. Chem. Phys.* **1985**, *82*, 299-310.
[167] V. Barone, M. Cossi, *J. Phys. Chem. A* **1998**, *102*, 1995-2001.
[168] N. M. O'Boyle, A. L. Tenderholt, K. M. Langner, *J. Comput. Chem.* **2008**, *29*, 839-845.
[169] K. A. Cychosz, R. Guillet-Nicolas, J. García-Martínez, M. Thommes, *Chem. Soc. Rev.* **2017**, *46*, 389-414.
[170] (a) L. V. Lutkus, S. S. Rickenbach, T. M. McCormick, *J. Photochem. Photobiol. A: Chem.* **2019**, *378*, 131-135; (b) M. Hoebeke, X. Damoiseau, *Photochem. Photobiol. Sci.* **2002**, *1*, 283-287.
[171] F. Lafolet, S. Welter, Z. Popović, L. D. Cola, *J. Mater. Chem.* **2005**, *15*, 2820-2828.
[172] Y. Zhou, W. Li, Y. Liu, M. Zhou, *ChemPlusChem* **2013**, *78*, 413-418.
[173] G. M. Greenway, A. Greenwood, P. Watts, C. Wiles, *Chem. Commun.* **2006**, 85-87.
[174] N. Okamura, T. Nakamura, S. Yagi, T. Maeda, H. Nakazumi, H. Fujiwara, S. Koseki, *RSC Advances* **2016**, *6*, 51435-51445.

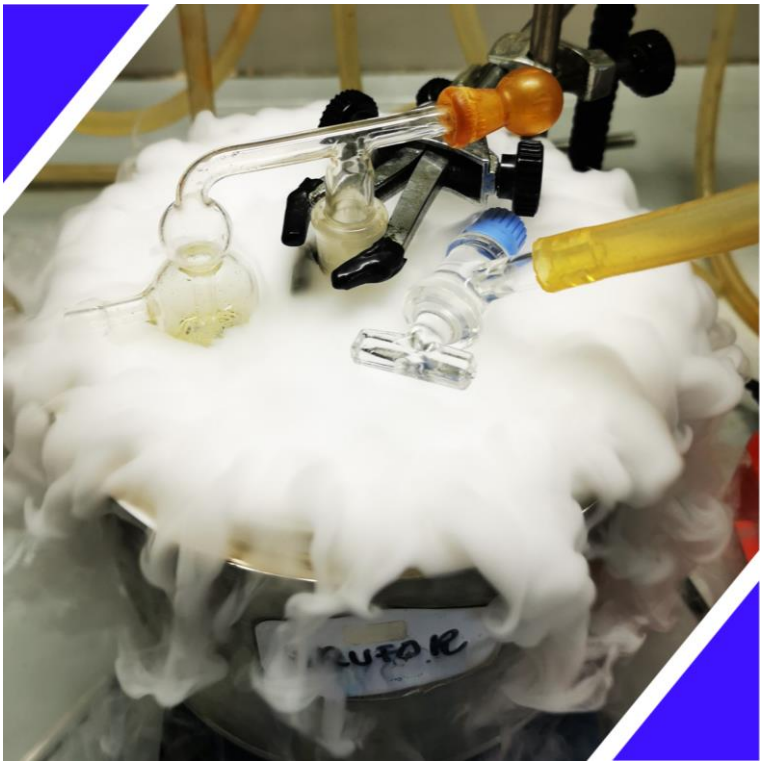

Annex

Annex

Table A.1. Selected distances (Å) and angles (º) for **BD-4**.

BD-4			
B1-F1	1.392(3)	**B1-N1**	1.546(3)
B1-F2	1.388(2)	**B1-N2**	1.553(3)
I1-C2	2.071(2)	**C5-C15**	1.493(3)
I2-C9	2.068(2)		
F1-B1-F2	109.55(16)	**N1-B1-N2**	106.44(15)
F1-B1-N1	110.40(17)	**F2-B1-N2**	110.39(17)
C16-N4-C26	119.37(17)	**C26-N4-C27**	111.51(17)
C16-N4-C27	117.59(17)	**C4-C5-C6**	120.97(17)

Table A.2. X-ray Crystallographic Data for **BD-4**.

Empirical formula	$C_{26}H_{24}BF_3I_2N_4$
F_w	714.10
T (K)	100(1)
Wavelength	0.71073 Å
Crystal system	Triclinic
Space group	P -1
a(Å)	8.718(2)
b(Å)	10.088(2)
c(Å)	14.919(4)
α(deg)	101.77(1)
β(deg)	92.78 (2)
γ(deg)	95.42(1)
Volume (A^3)	1275.6(6)
Z	2
Crystal size	0.494 x 0.244 x 0.140 mm^3
D_{calcd} (Mg/m^3)	1.859
Absorption coefficient (mm^{-1})	2.511
F(000)	692
θ range for data collection (deg)	2.245 to 29.127
No of data // restraints // parameters	6847 // 0 // 325
Goodness-of-fit on $F^{2(a)}$	1.068
Final R indexes [I>2σ(I)][(a)]	R_1 = 0.0209
	wR_2 = 0561
R indexes (all data)[(a)]	R_1 = 0.0249
	wR_2 = 0.0578
Largest diff peak and hole ($e \cdot Å^{-3}$)	0.782 and -0.816

(a) $R_1 = \Sigma(||F_o| - |F_c||)/\Sigma|F_o|$; $wR_2 = [\Sigma w(F_o^2 - F_c^2)^2/\Sigma wF_o^2]^{1/2}$; goodness of fit $= \{\Sigma[w(F_o^2 - F_c^2)^2]/(N_{obs} - N_{param})\}^{1/2}$; $w = [\sigma^2(F_o) + (g_1P)^2 + g_2P]^{-1}$; $P = [\max(F_o^2;0 + 2F_c^2]/3$.

BD-1	
S_0	**T_1**
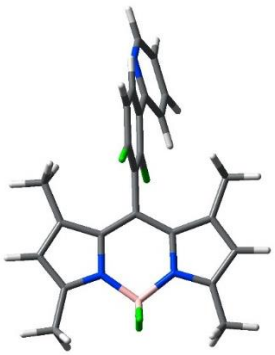	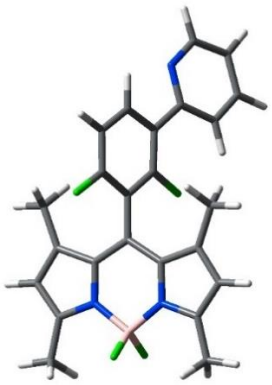
BD-2	
S_0	**T_1**
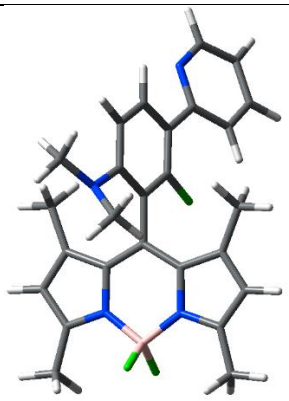	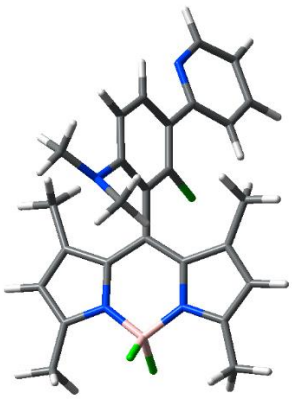
BD-2-H^+	
S_0	**T_1**
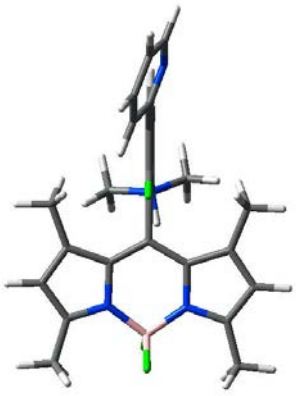	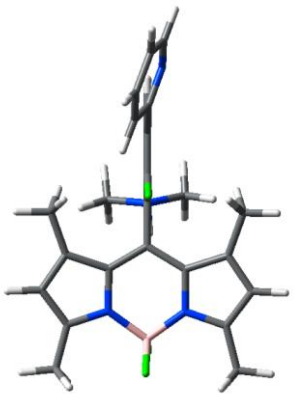

Figure A.1. Optimized structures of S_0 and T_1 states of **BD-1**, **BD-2** and **BD-2H$^+$** in THF.

BD-3	
S_0	T_1
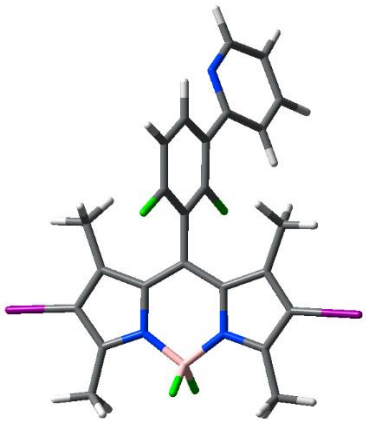	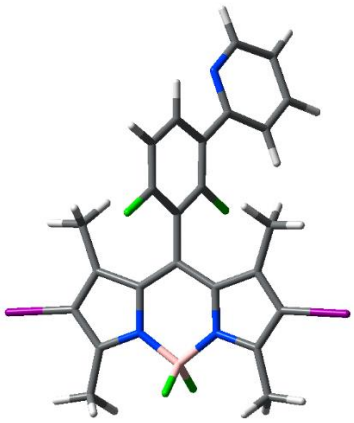
BD-4	
S_0	T_1
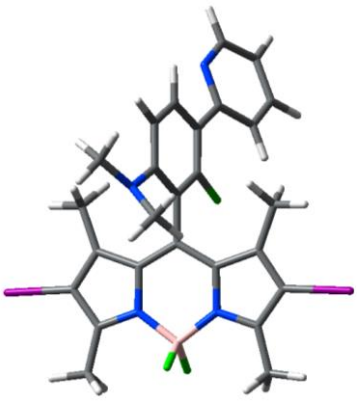	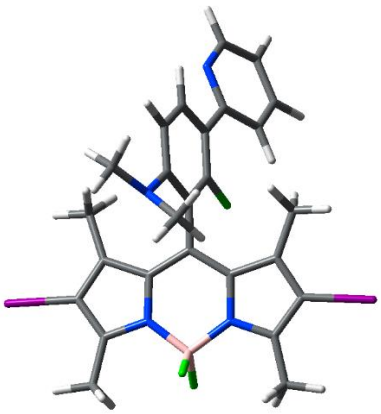

Figure A.2. Optimized structures of S_0 and T_1 states of **BD-3** and **BD-4** THF.

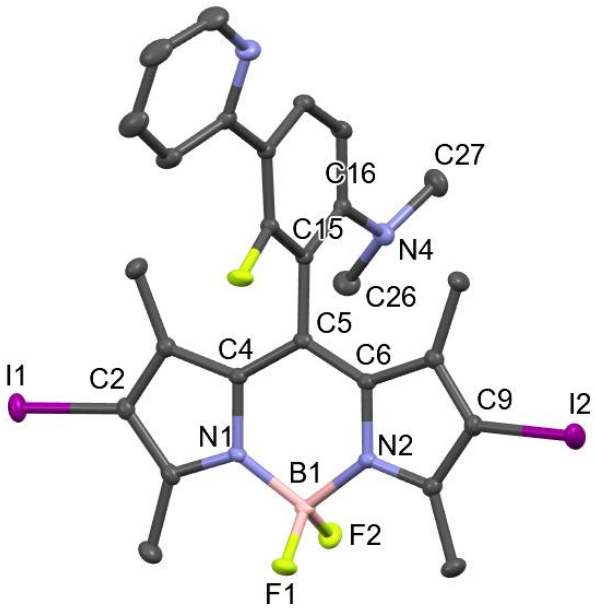

Figure A.3. Molecular structure of **BD-4** with ellipsoids drawn at the 50% probability level.

Table A.3. DFT optimized geometries for ground state and triplet state of BODIPYs **BD-1**, **BD-2**, **BD-H$^+$**, **BD-3** and **BD-4** in THF.

	BD-1		**BD-2**		**BD-2H$^+$**	
	S_0	**T_1**	**S_0**	**T_1**	**S_0**	**T_1**
B1-F1	1.400	1.403	1.400	1.403	1.392	1.394
B1-F2	1.399	1.402	1.401	1.404	1.398	1.399
B1-N1	1.552	1.544	1.550	1.543	1.557	1.551
B1-N2	1.552	1.544	1.551	1.545	1.557	1.551
C5-C15	1.493	1.486	1.498	1.490	1.498	1.493
F1-B1-F2	109.65	109.12	109.56	108.98	110.31	110.04
F1-B1-N1	110.18	110.45	110.17	110.34	110.03	110.07
F2-B1-N2	110.15	110.41	110.27	110.55	110.12	110.44
N1-B1-N2	106.53	106.05	106.48	106.07	106.22	105.61
C4-C5-C6	121.29	118.35	120.77	118.09	121.54	117.92
C16-N4-C26			119.45	117.78	112.55	112.95
C16-N4-C27			117.68	117.36	113.64	113.23
C26-N4-C27			111.31	111.39	111.48	111.72

	BD-3		**BD-4**		
	S_0	**T_1**	**S_0**	**T_1**	**X-ray**
B1-F1	1.395	1.399	1.394	1.399	1.392
B1-F2	1.395	1.399	1.398	1.400	1.388
I1-C2	2.118	2.113	2.119	2.115	2.071
I2-C9	2.118	2.113	2.118	2.115	2.068
B1-N1	1.556	1.548	1.553	1.546	1.546
B1-N2	1.556	1.548	1.555	1.548	1.553
C5-C15	1.492	1.486	1.496	1.488	1.493
F1-B1-F2	110.21	109.56	110.13	109.48	109.55
F1-B1-N1	110.32	110.42	110.20	110.36	110.40
F2-B1-N2	110.33	110.36	110.22	110.51	110.39
N1-B1-N2	106.31	105.83	106.27	105.87	106.44
C4-C5-C6	121.23	118.39	120.70	118.15	120.97
C16-N4-C26			119.60	117.77	119.37
C16-N4-C27			117.68	117.38	117.59
C26-N4-C27			111.26	111.52	111.51

Table A.4. Composition (%) of frontier molecular orbitals (MOs) of **BD-1**, **BD-2**, **BD-3** and **BD-4**.

BD-1

MO	eV	dfppy	BODIPY
L+5	0.82	12	88
L+4	0.51	87	13
L+3	-0.50	97	3
L+2	-0.77	98	2
L+1	-1.44	99	1
LUMO	-2.61	4	97
HOMO	-5.55	0	100
H-1	-6.46	95	5
H-2	-6.68	5	95
H-3	-6.87	0	99
H-4	-7.15	97	3
H-5	-7.26	93	7
H-6	-7.77	86	14
H-7	-7.86	26	74
H-8	-8.12	94	6

BD-2

MO	eV	ppy	BODIPY	NMe_2
L+3	-0.24	93	5	1
L+2	-0.59	99	1	0
L+1	-1.26	95	1	4
LUMO	-2.54	4	96	0
HOMO	-5.44	16	67	17
H-1	-5.62	39	33	28
H-2	-6.61	2	97	1
H-3	-6.81	10	89	0
H-4	-6.83	75	19	6
H-5	-7.00	78	2	19
H-6	-7.06	98	1	0
H-7	-7.70	10	87	3
H-8	-7.75	96	2	3

BD-3

MO	eV	dfppy	BODIPY
L+5	-0.56	96	4
L+3	-0.84	93	7
L+1	-1.50	99	1
LUMO	-2.92	4	96
HOMO	-5.77	0	100
H-1	-6.52	91	9
H-2	-6.66	8	92
H-3	-6.70	1	99
H-4	-7.20	98	2
H-5	-7.32	85	14
H-8	-7.77	30	70

BD-4

MO	eV	ppy	BODIPY	NMe_2
L+5	-0.33	93	6	1
L+4	-0.63	97	3	0
L+1	-1.32	94	1	5
LUMO	-2.85	4	96	1
HOMO	-5.60	39	26	35
H-1	-5.77	16	75	9
H-2	-6.60	1	99	0
H-3	-6.66	2	98	0
H-4	-6.91	82	8	10
H-6	-7.10	98	2	0
H-9	-7.68	7	91	2

$BD\text{-}2H^+$

MO	eV	ppy	BODIPY	NMe2
L+3	-1.04	99	1	0
L+2	-1.46	95	4	1
L+1	-2.28	96	1	3
LUMO	-3.27	3	97	1
HOMO	-6.14	0	99	0
H-1	-7.20	43	57	1
H-2	-7.25	56	44	1
H-3	-7.43	0	99	0
H-4	-7.62	100	0	0
H-5	-8.02	94	6	0
H-6	-8.25	100	0	0
H-7	-8.50	5	93	1

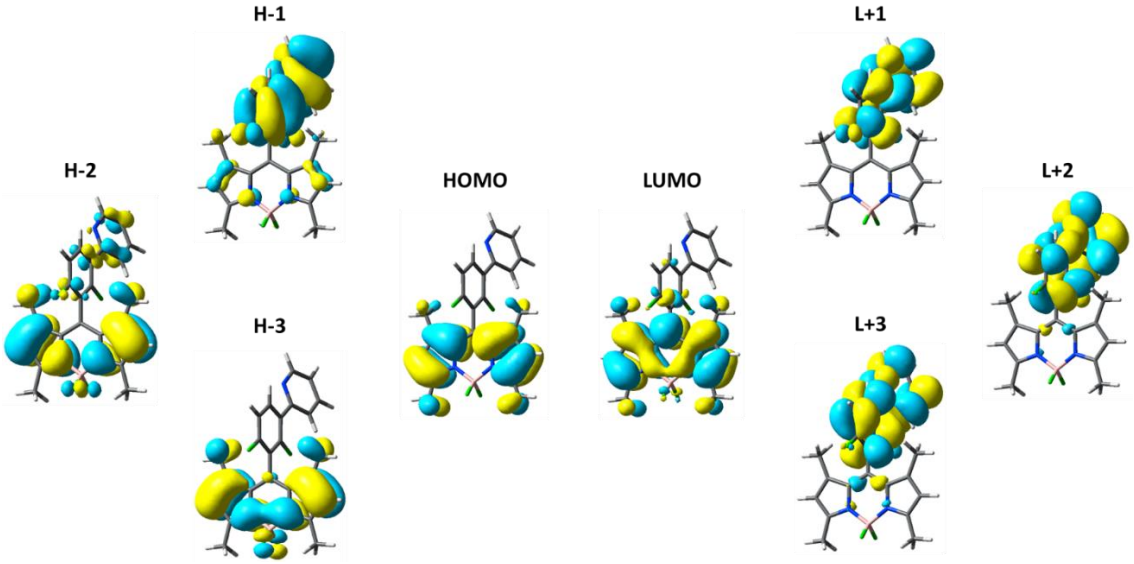

Figure A.4. BD-1 selected frontier MOs in the ground state.

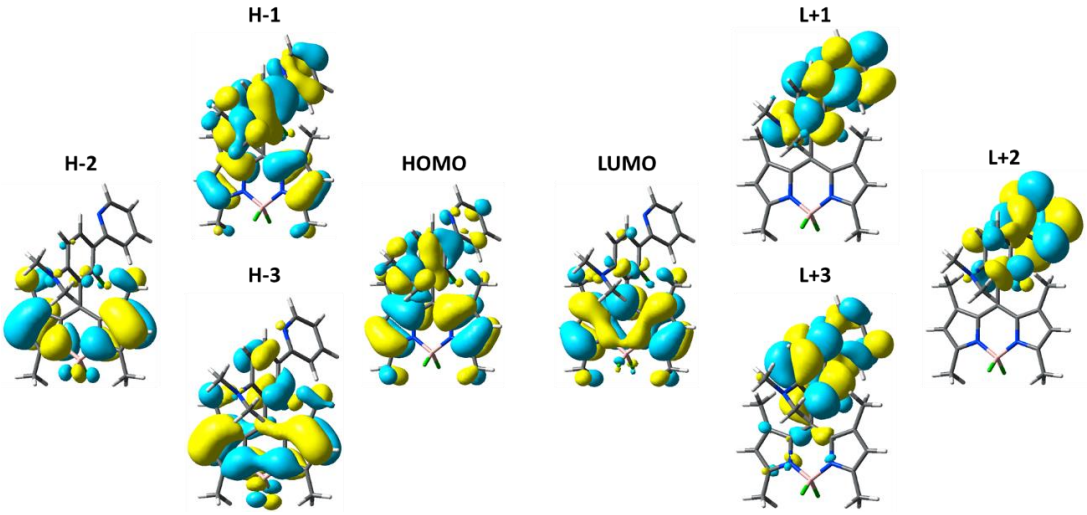

Figure A.5. BD-2 selected frontier MOs in the ground state.

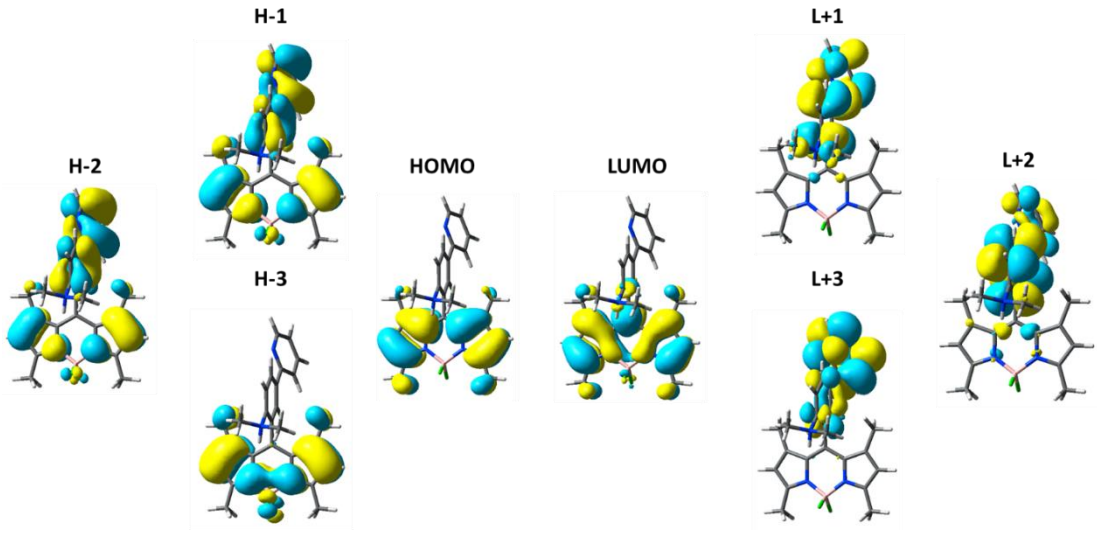

Figure A.6. BD-2H$^+$ selected frontier MOs in the ground state.

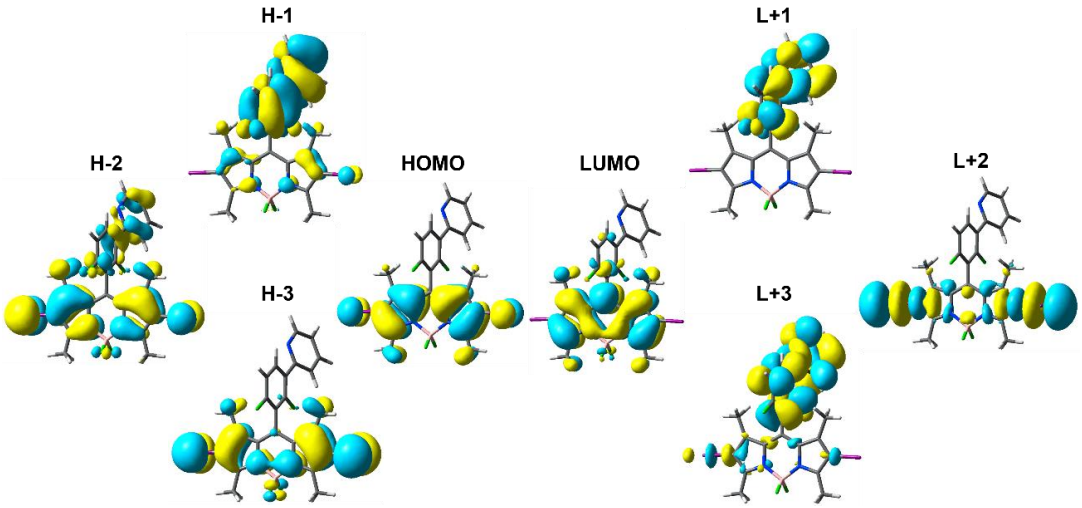

Figure A.7. BD-3 selected frontier MOs in the ground state.

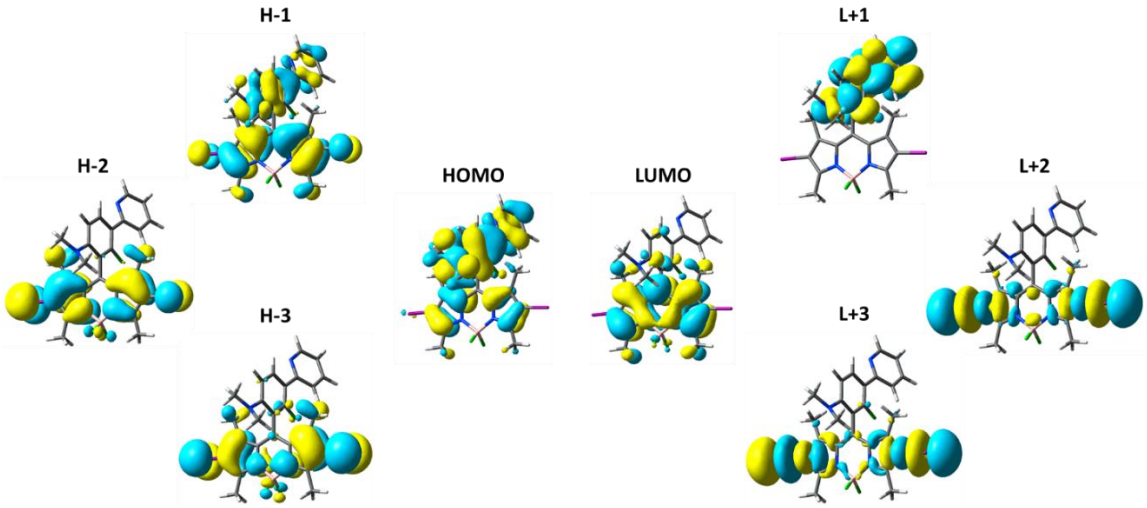

Figure A.8. BD-4 Frontier MOs in the ground state.

Table A.5. Selected vertical excitation energies singlets and first triplets computed by TD-DFT/SCRF(THF) with the orbitals involved for **BD-1** and **BD-2**.

BD-1				
State	**λ/nm**	**f**	**Transition (% Contribution)**	**Main character**
T_1	850.66	-	HOMO→LUMO (101%)	LE (BODIPY)
T_2	461.40	-	H-2→LUMO (88%)	LE (BODIPY)
T_3	433.22	-	H-3→LUMO (94%)	LE (BODIPY)
S_1	433.27	0.5749	HOMO→LUMO (98%)	LE (BODIPY)
S_3	364.65	0.0554	H-2→LUMO (92%)	LE (BODIPY)
S_4	344.00	0.0321	H-3→LUMO (95%)	LE (BODIPY)
S_6	322.90	0.0400	H-5→LUMO (40%), H-4→LUMO (58%)	CT (ppy→BODIPY)
S_9	272.86	0.5689	H-1→L+1 (84%)	LE (ppy)
S_{13}	260.78	0.0320	H-2→L+1 (96%)	CT (BODIPY→ ppy)
S_{14}	255.89	0.1650	H-7→LUMO (16%), H-5→L+1 (26%), H-1→L+2 (31%)	LE (ppy), CT (BODIPY→ ppy)
S_{15}	252.14	0.1201	H-7→LUMO (59%)	LE (ppy), CT (BODIPY→ ppy)
BD-2				
State	**λ/nm**	**f**	**Transition (% Contribution)**	**Main character**
T_1	838.07	-	H-1→LUMO (23%), HOMO→LUMO (78%)	CT (ppy→BODIPY), LE (BODIPY)
T_2	536.70	-	H-1→LUMO (76%), HOMO→LUMO (21%)	CT (ppy→BODIPY), LE (BODIPY)
T_3	458.01	-	H-2→LUMO (95%)	LE (BODIPY)
S_1	529.75	0.0167	H-1→LUMO (52%), HOMO→LUMO (47%)	CT (ppy→BODIPY), LE (BODIPY)
S_2	432.72	0.5283	H-1→LUMO (47%), HOMO→LUMO (52%)	CT (ppy→BODIPY), LE (BODIPY)
S_3	367.28	0.0537	H-2→LUMO (96%)	LE (BODIPY)
S_4	348.98	0.0218	H-4→LUMO (68%), H-3→LUMO (26%)	CT (ppy→BODIPY), LE (BODIPY)
S_5	343.05	0.0500	H-4→LUMO (26%), H-3→LUMO (73%)	CT (ppy→BODIPY), LE (BODIPY)
S_6	334.75	0.1120	HOMO→L+1 (96%)	CT (BODIPY→ ppy)
S_7	316.83	0.2439	H-5→LUMO (44%), H-1→L+1 (52%)	LE (ppy), CT (BODIPY→ ppy)
S_8	316.57	0.2922	H-5→LUMO (52%), H-1→L+1 (43%)	LE (ppy), CT (BODIPY→ ppy)
S_{10}	288.14	0.0686	HOMO→L+2 (62%)	CT (BODIPY→ ppy)
S_{12}	272.86	0.0341	HOMO→L+2 (14%), HOMO→L+3 (55%)	CT (BODIPY→ ppy)
S_{13}	267.75	0.0229	H-6→L+1 (87%)	LE (ppy)
S_{15}	260.38	0.0397	H-8→LUMO (76%), H-7→LUMO (19%)	CT (ppy→BODIPY), LE (BODIPY)
S_{16}	258.42	0.2889	H-8→LUMO (19%), H-7→LUMO (57%)	CT (ppy→BODIPY), LE (BODIPY)

Table A.6. Selected vertical excitation energies singlets and first triplets computed by TD-DFT/SCRF(THF) with the orbitals involved for **BD-2H$^+$** and **BD-3**.

BD-2H$^+$				
State	**λ/nm**	**f**	**Transition (% Contribution)**	**Main character**
T_1	905.12	-	HOMO→LUMO (102%)	LE (BODIPY)
T_2	481.90	-	H-2→LUMO (40%), H-1→LUMO (57%)	LE (BODIPY), CT (ppy→BODIPY)
T_3	447.69	-	H-3→LUMO (95%)	LE (BODIPY)
S_1	439.21	0.5527	HOMO→LUMO (98%)	LE (BODIPY)
S_2	380.88	0.0689	H-2→LUMO (30%), H-1→LUMO (65%)	LE (BODIPY), CT (ppy→BODIPY)
S_5	355.33	0.0377	H-3→LUMO (93%)	LE (BODIPY)
S_8	305.33	0.0137	HOMO→L+2 (90%)	CT (BODIPY→ ppy)
S_{10}	281.54	0.0747	H-2→L+1 (16%), H-1→L+1 (83%)	LE (ppy)
S_{11}	277.06	0.5993	H-2→L+1 (78%)	LE (ppy), CT (BODIPY→ ppy)
S_{15}	255.90	0.0547	H-5→L+1 (51%), H-2→L+2 (19%), H-1→L+2 (22%)	LE (ppy), CT (BODIPY→ ppy)
S_{16}	253.88	0.2171	H-7→LUMO (85%)	LE (ppy), CT (BODIPY→ ppy)
BD-3				
State	**λ/nm**	**f**	**Transition (% Contribution)**	**Main character**
T_1	857.72	-	HOMO→LUMO (98%)	LE (BODIPY)
T_2	502.02	-	H-2→LUMO (80%), H-1→LUMO (11%)	LE (BODIPY), CT (ppy→BODIPY)
T_3	470.19	-	H-3→LUMO (91%)	LE (BODIPY)
S_1	468.04	0.5861	HOMO→LUMO (92%)	LE (BODIPY)
S_2	409.21	0.0215	H-1→LUMO (98%)	CT (ppy→BODIPY)
S_3	386.51	0.2153	H-2→LUMO (88%)	LE (BODIPY)
S_4	384.80	0.0680	H-3→LUMO (95%)	LE (BODIPY)
S_5	342.76	0.0341	H-5→LUMO (56%), H-4→LUMO (41%)	CT (ppy→BODIPY)
S_6	327.03	0.0053	HOMO→L+1 (99%)	CT (BODIPY→ppy)
S_7	317.14	0.0074	H-5→LUMO (42%), H-4→LUMO (58%)	CT (ppy→BODIPY)
S_{12}	285.08	0.0875	H-8→LUMO (81%)	CT (BODIPY→ppy), LE (ppy)
S_{13}	282.56	0.0221	HOMO→L+3 (78%)	CT (BODIPY→ppy)
S_{15}	271.63	0.3646	H-4→L+1 (16%), H-1→L+1 (69%)	LE (ppy)
S_{16}	271.47	0.0650	H-5→L+1 (16%), H-4→L+1 (67%)	LE (ppy)
S_{18}	264.44	0.0426	H-2→L+1 (94%)	CT (BODIPY→ppy)
S_{24}	254.76	0.1266	H-5→L+1 (35%), H-1→L+3 (32%)	LE (ppy)

Table A.7. Selected vertical excitation energies singlets and first triplets computed by TD-DFT/SCRF(THF) with the orbitals involved for **BD-4**.

BD-4				
State	**λ/nm**	**f**	**Transition (% Contribution)**	**Main character**
T_1	843.22	-	H-1→LUMO (59%), HOMO→LUMO (39%)	LE (BODIPY), CT (ppy→BODIPY)
T_2	594.05	-	H-1→LUMO (39%), HOMO→LUMO (59%)	LE (BODIPY), CT (ppy→BODIPY)
T_3	495.97	-	H-2→LUMO (91%)	LE (BODIPY)
S_1	585.43	0.0163	H-1→LUMO (15%), HOMO→LUMO (84%)	LE (BODIPY), CT (ppy→BODIPY)
S_2	465.09	0.5598	H-1→LUMO (79%), HOMO→LUMO (14%)	LE (BODIPY), CT (ppy→BODIPY)
S_3	387.41	0.1966	H-2→LUMO (87%)	CT (BODIPY→ ppy)
S_4	381.98	0.0805	H-3→LUMO (95%)	CT (BODIPY→ ppy)
S_5	370.62	0.0185	H-4→LUMO (88%)	LE (ppy)
S_8	323.27	0.3715	HOMO→L+1 (95%)	LE (ppy), CT (BODIPY→ ppy)
S_9	310.93	0.2678	H-1→L+1 (95%)	CT (BODIPY→ ppy)
S_{14}	288.15	0.1001	H-9→LUMO (41%), HOMO→L+4 (34%)	LE (BODIPY), CT (BODIPY→ ppy)
S_{16}	283.44	0.0227	H-9→LUMO (49%), HOMO→L+4 (27%)	LE (BODIPY), CT (BODIPY→ ppy)
S_{19}	270.22	0.0256	HOMO→L+4 (22%), HOMO→L+5 (43%)	CT (BODIPY→ ppy)
S_{21}	268.04	0.0176	H-6→L+1 (57%), H-1→L+4 (25%)	LE (ppy), CT (BODIPY→ ppy)

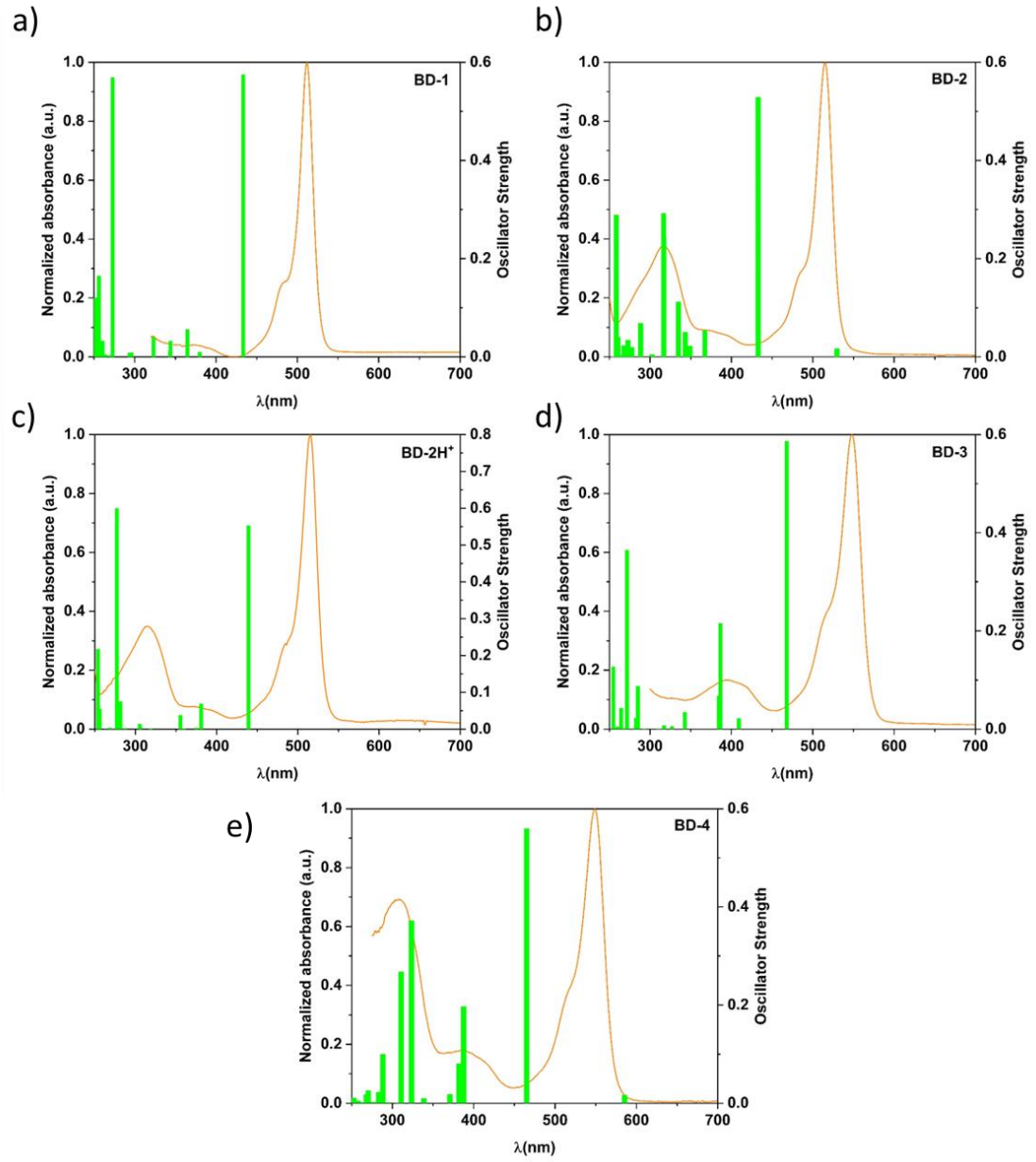

Figure A.9. Calculated stick absorption spectra of BODIPYs **BD-1** (a), **BD-2** (b), **BD-2H**$^{+}$ (c), **BD-3** (d) and **BD-4** (e) in THF compared with the experimental ones (THF, 5x10^{-6} M).

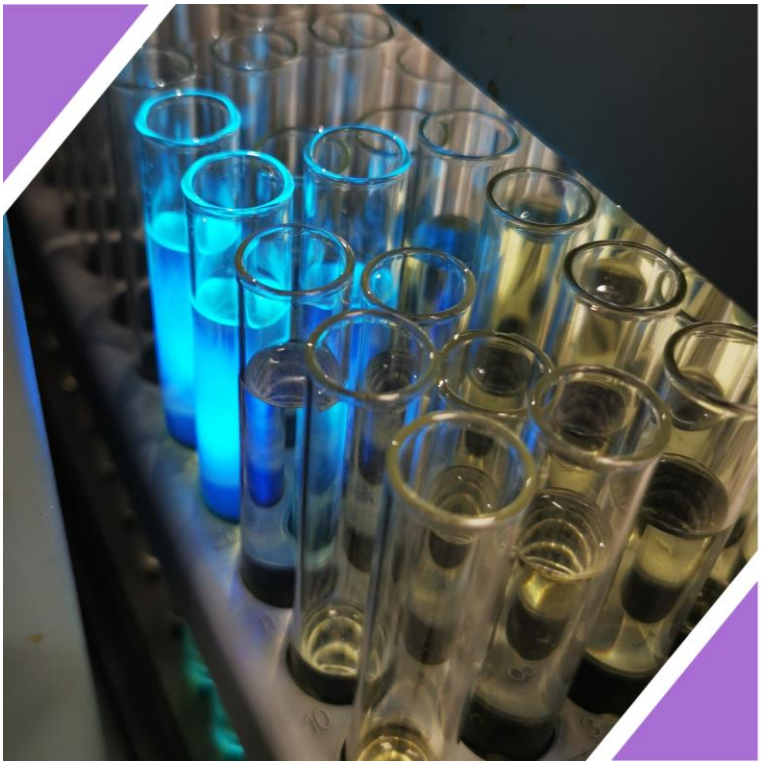

Research at the Eli

Zysman-Colman group

Research at the Eli Zysman-Colman group

During the third year of my doctoral research, I spent four months in the research group of Prof. Eli Zysman-Colman at the University of St. Andrews, Scotland. The main objective of my stay was to further extend the heterogenization of photocatalysts by incorporating a compound used in that group as an organic PC into silica nanoparticles developed in our group. Furthermore, I tested some copper complexes and derived materials previously synthesized in our group as photocatalysts, taking advantage of the previous experience of the EZC group in photocatalysis with copper complexes.

Here, I present a summary of the research carried out during my stay.

In the first project, I succeeded in functionalizing a compound called **DiKTa** with a terminal alkyne. This compound, which has been extensively studied in the EZC group, exhibits multiresonant thermally activated delayed fluorescence (MR-TADF) in solution, with a fluorescence emission with maximum at 453 nm in toluene at RT [$\phi_{PL}(\phi_{DF})$ = 26(1)%, τ_p = 5.1 ns, τ_d = 23 μs]. This compound has previously been used as a photocatalyst in the EZC group. Functionalization with the terminal alkyne allowed its subsequent grafting onto nanoparticles previously decorated with azide groups through click chemistry reactions. The scheme of the nanoparticles structure, as well as photographs of them in the solid state can be found in Figure R.1.

The synthesized nanoparticles were analyzed by spectroscopic techniques to determine their photophysical properties. However, no TADF behavior could be observed in the nanoparticles (t = 7.0 ns, broad emission with maximum at 505 nm), in tests performed both in solid state and in suspension. Furthermore, an attempt was made to reproduce some of the photocatalytic reactions tested with the **DiKTa** compound under homogeneous conditions. However, the nanoparticles showed a much lower photocatalytic activity in isomerization reactions (Figure R.1 c), and with a significant drop in their activity when trying to recover and reuse them in successive reactions (yield from 35% to 25% at the second cycle). To check whether the modification in the structure of the molecule is the cause of the decrease in the photocatalytic activity, we tried to synthesize the molecular compound related to **DiKTa**, but containing a triazole group similar to that in **DiKTa-NP**. Unfortunately, it was possible to obtain this compound in the laboratory, but there was not enough time to carry out further studies with it.

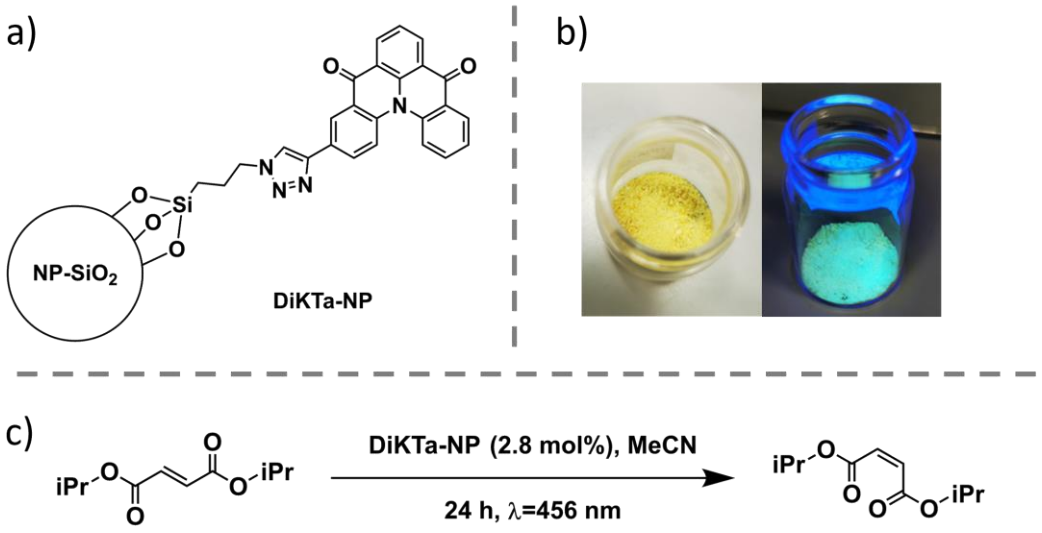

Figure R.1. a) Schematic representation of the nanoparticles functionalized with the **DiKTa** compound. b) Photos of **DiKTa-NP** in solid state under visible light (left) and UV light (right). c) Photocatalytic isomerization reaction studied.

In the second project, several copper(I) based compounds and materials that I had previously synthetized in the laboratory were used to test their efficacy as photocatalysts. The main copper complex I used ([Cu(*dasipy*)(xantphos)]PF_6, (**2**) and its ionic self-condensed material (**SC-2**) are shown in the Figure R.2. An atom transfer radical addition (ATRA) reaction was tested, as it has been studied in the literature with copper complexes as photocatalysts (Scheme R.1).

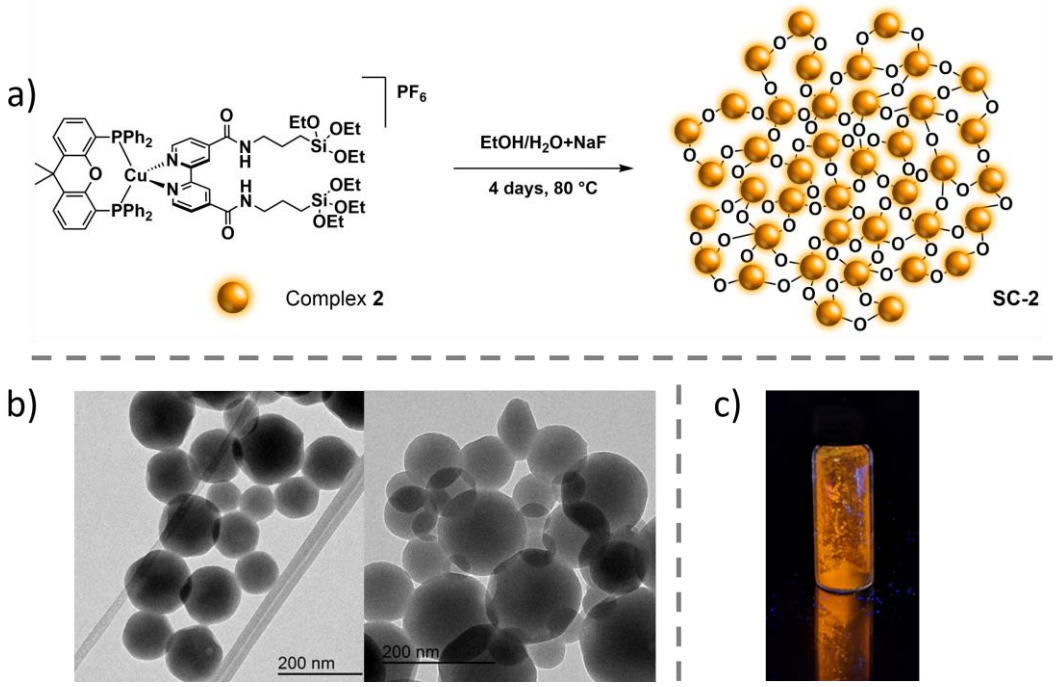

Figure R.2. a) Schematic representation of the self-condensation of the material (**SC-2**). b) TEM pictures of the material. c) Photo of **SC-2** under UV light.

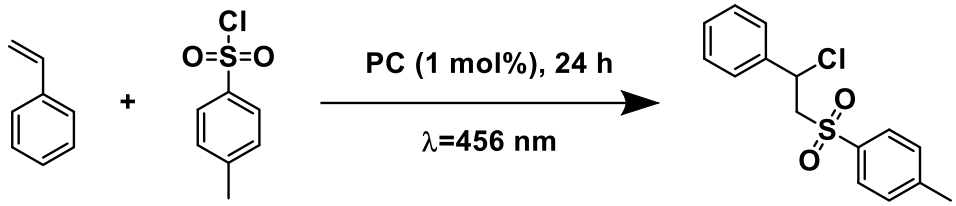

Scheme R.1. Photocatalytic ATRA reaction.

The results of these tests in MeCN showed that, although very good results are obtained with the copper complex used in the literature [Cu(dmp)(xantphos)]PF_6 (dmp = 2,9-dimethyl-1,10-phenanthroline; **3**), the copper complexes synthesized by our research group are not stable under these conditions and degrade before good yields can be obtained (Table R.1). In fact, the characteristic yellow color of these compounds turns to a blue/green color after the irradiation, indicating an oxidation from copper(I) to copper(II). It was also found that the solvent influences the stability of these complexes, since the yield of the reaction increases when the reaction is repeated in a less coordinating solvent such as DCM, but without reaching the value of the standard complex.

Table R.1. Photocatalytic results of the ATRA reaction.

Photocatalyst	Yield in MeCN	Yield in DCM
[Cu(dmp)(xantphos)]PF_6 (**3**)	100%	100%
[Cu(*dasipy*)(xantphos)]PF_6 (**2**)	5%	45%
SC-2	11%	14%

The stability of [Cu(dmp)(xantphos)]PF_6 is probably due to the two methyl groups at the 2 and 9 positions of the phenanthroline, which prevent the pseudo Jahn–Teller distortion of the copper center after excitation. After the results obtained with the photocatalytic tests, the strategy was changed to try to modify the neocuproine ligand in order to add the functionalization that would allow its subsequent heterogenization in different types of materials. I worked on this modification during the last month of my stay, which led to the synthesis of the ligand showed in the Scheme R.2. This ligand is now being used in our research group to prepare new copper complexes, both homoleptic and heteroleptic, in order to incorporate them into materials like silicas or titanias, both for photocatalysis applications and OLEDs.

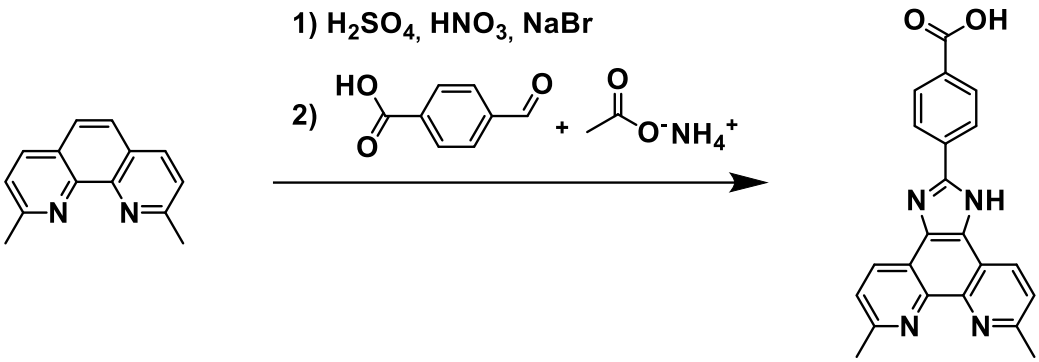

Scheme R.2. Modification of the neocuproine.